Phenomenology of Dark Matter Annihilation and Non-Minimal Flavour Violation in the MSSM

Björn Herrmann

LPSC-08-47

Université Joseph Fourier – Grenoble I
École Doctorale de Physique

Thèse de Doctorat
Spécialité: Physique théorique des particules et astroparticules

présentée par
Björn Herrmann

en vue de l'obtention du grade de
Docteur en Sciences
de l'Université Joseph Fourier

Phenomenology of Dark Matter Annihilation and Non-Minimal Flavour Violation in the MSSM

préparée au
Laboratoire de Physique Subatomique et de Cosmologie Grenoble

soutenue le 10 septembre 2008 devant le jury composé de:

Prof. Willem de Boer	Examinateur
Dr. Laura Covi	Examinateur
Prof. Michael Klasen	Directeur de thèse
Prof. François Montanet	Président du jury
Prof. Jean Orloff	Rapporteur
Dr. Tilman Plehn	Rapporteur

"Physics is not the most important thing in the world. Love is."
Richard P. Feynman

To Aurélie
who encouraged me during the preparation of this Thesis
with her support, her councils, her patience,
and, above all, her love.

Acknowledgements

First of all, I would like to express my gratitude to my supervisor Michael Klasen for giving me the possibility to prepare this Thesis and for guiding me through the three years of its preparation. Thank you also for your encouragements, your patience, and your gentleness.

Second, I thank Benjamin Fuks and Karol Kovařìk, who have not only been my closest collaborators during the last three years, but also have become good friends. Without you guys and our numerous discussions this Thesis would not exist in its present form.

My sincere appreciation goes to my referees, Jean Orloff and Tilman Plehn, and the other members of the evaluation committee, Wim de Boer, Laura Covi, and François Montanet, for carefully reading the manuscript and for their comments and suggestions.

Scientific research lives from exchanges. In this context, I would like to thank the rest of the LPSC theory group, in particular Giuseppe Bozzi, Jonathan Debove, Sabine Kraml, Markus Haider, Ingo Schienbein, and Carole Weydert for active and lively discussions. Thanks go also to Benoît Clement, Bertrand Martin dit Latour, Julien Morel, Julien Labbé, Guillaume Pignol, and Maud Versteegen from the experimental groups, as well as Jonathan Aumont, Lauranne Fauvet, and Antje Putze from the astrophysics and cosmology group for fruitful exchanges.

Let me also warmly acknowledge Johann Collot and Serge Kox, successive directors of the LPSC, and Jaume Carbonell, head of the theory group, for their constant support, as well as Anic, Audrey, and Cécile from the administration for organizing my numerous missions.

During my Thesis I also made my first steps in teaching. I am grateful to Yannick Arnoud, Alain Drillat, Christophe Furget, and Monique Giroud for guiding me on this way and sharing their experience with me. Further thanks go to the members of our vulgarization workshop. Preparing and presenting the “particle train” was certainly one of my personal highlights during the three years.

Finally, I am indebted to my parents for giving me the possibility to go to university and concentrate on my studies. The last, but not least, thanks go to Aurélie for her support and her love.

Résumé

Le Modèle Standard de la physique des particules est basé sur le groupe de jauge $SU(3) \times SU(2) \times U(1)$ et inclut les interactions forte et électrofaible. Son contenu en particules est expérimentalement bien établi à l'exception du boson de Higgs. Celui-ci est nécessaire dans la description de la brisure de la symétrie électrofaible mais, jusqu'à présent, non observé auprès des collisionneurs actuels. Malgré le grand succès expérimental de ses prédictions, le Modèle Standard souffre de certaines inconsistences théoriques et expérimentales. Les arguments cités le plus souvent sont le problème de hierarchie, qui est lié aux corrections de boucles fermioniques à la masse du boson de Higgs, ainsi que l'unification des constantes de couplages requise par des théories de grande unification mais non réalisée dans le Modèle Standard. Du côté cosmologique le Modèle Standard n'inclut pas de candidat pour la matière noire dans l'univers, ce qui constitue un argument supplémentaire pour la physique au delà du Modèle Standard. Parmi les extensions proposées, la Supersymétrie (SUSY), et en particulier le Modèle Supersymétrique Standard Minimal (MSSM), est la théorie la plus économique et la mieux étudiée. Basée sur une symétrie entre bosons et fermions, elle prédit des superpartenaires pour les particules du Modèle Standard. L'absence d'observation directe des superpartenaires aux collisionneurs actuels implique que la Supersymétrie doit être brisée à l'échelle électrofaible. Le Lagrangien à basse énergie inclut alors des termes donnant une masse aux superpartenaires, ce qui implique un total de 124 paramètres liés au mécanisme exact de la brisure. Il est alors essentiel de contraindre l'espace des paramètres à l'échelle électrofaible ainsi qu'à l'échelle de la brisure de la Supersymétrie. Selon les différents mécanismes de la brisure, des termes violant la saveur peuvent être introduits dans le Lagrangien. Ceci implique la nécessité d'étudier la possibilité de violation non-minimale de la saveur dans le contexte des contraintes. La conservation de la R-parité implique que la particule supersymétrique la plus légère (LSP) soit stable. Si cette dernière est électriquement neutre et un singlet de couleur, elle constitue un excellent candidat pour la particule de matière noire. Le fait de pouvoir calculer sa densité relique pour un modèle donné constitue une possibilité intéressante d'obtenir des contraintes supplémentaires par rapport aux expériences auprès des collisionneurs ou des mesures de précisions électrofaibles.

Dans la première partie de cette thèse, nous avons étudié les différentes contraintes qui peuvent être imposées sur le MSSM à l'échelle électrofaible, tout en considérant la possibilité de violation non-minimale de la saveur. En particulier, nous avons imposé les limites expérimentales du rapport d'embranchement $b \to s\gamma$, du paramètre électrofaible $\Delta\rho$, et du moment magnétique anomal du muon a_μ, ainsi que les limites sur la densité relique $\Omega_{\rm CDM}h^2$ de matière noire obtenues par la mission WMAP et d'autres mesures cosmologiques. En ce qui concerne les modèles de supergravité minimale (mSUGRA) où la violation de la saveur est naturellement présente due à la médiation par la gravité, nous avons commencé par identifier les régions exclues ou favorisées par les différentes contraintes grâce à des "scans" détaillés de l'espace des paramètres. Basés sur cette analyse, nous avons défini des scénarios "benchmark" qui permettent une violation de la saveur importante entre les squarks de deuxième et troisième génération, qui sont en accord avec toutes les contraintes, et qui n'impliquent pas de masses trop élevées pour les superpartenaires qui seront alors observables aux collisionneurs actuels ou futurs. Une étude détaillée des contraintes a ensuite permis d'identifier les limites pour le paramètre introduisant le mélange de saveur dans la matrice de masses des squarks et de comprendre la phénoménologie introduite par ce mélange.

Dans un deuxième temps, nous avons effectué une analyse similaire pour des modèles de

brisure de Supersymétrie par médiation de jauge (GMSB). Dans les modèles GMSB minimaux, les régions caractérisées par des petites masses ou des masses intermédiaires masses de superpartenaires sont exclues par la contrainte sévère due à la désintegration $b \to s\gamma$. La violation de saveur dans le secteur des squarks peut être introduite ici si l'on tient compte d'un possible mélange entre les champs de messagers et les champs de matière. Nous avons montré que cette introduction d'un mélange de saveur permet de satisfaire les contraintes de basse énergie et électrofaible également pour les scénarios incluant des masses de superpartenaires découvrables aux collisionneurs. Nous avons alors pu définir des scénarios "benchmark" également pour les modèles GMSB et discuter en détail leur phénoménologie qui est très similaire à celle des points choisis en mSUGRA. Comme dans les modèles GMSB le gravitino est toujours la LSP et le candidat de matière noire, des contraintes supplémentaires doivent être prises en compte, comme par exemple le temps de vie de la particule la deuxième plus légère (NLSP), ou la température du réchauffement à laquelle la leptogenèse impose une limite inférieure. Pour ces scénarios, nous avons analysé ces contraintes supplémentaires afin de déterminer l'ordre de grandeur de la masse du gravitino.

La deuxième partie de cette thèse est consacrée à une étude de l'annihilation d'une paire de neutralinos, candidat potentiel pour la matière noire, en une paire de quark-antiquark. Ce processus domine dans des larges régions de l'espace des paramètres des modèles mSUGRA. Dans un premier temps nous avons consideré la région appelée "A-funnel", où quasiment le seul diagram contribuant est l'annihilation en paire de quarks beau par l'échange d'un boson de Higgs pseudoscalaire. Pour ce canal d'annihilation, nous avons calculé les corrections de diagrammes à une boucle en QCD et SUSY-QCD. Ceci a été réalisé par l'application des techniques de renormalisation et de resommation des corrections dominantes au couplage de Yukawa, et par la méthode de la soustraction de dipôles pour l'implémentation des corrections réelles. Nous avons ensuite montré numériquement que ces corrections ont un impact important sur la section efficace d'annihilation. En particulier, l'implémentation de la masse "running" du quark beau et les effets de la resommation en SUSY-QCD sont non négligeables et peuvent diminuer la section efficace par jusqu'a 75 pour cent. Nous avons implémenté les nouvelles corrections dans le code public `DarkSUSY` qui calcule la densite relique de matière noire pour un scenario supersymétrique donné. Nous avons ainsi montré que la prédiction de la densité relique de matière noire reçoit également des corrections significatives, au moins dans cette région particulière de l'espace des paramètres. La région préférée par rapport aux données cosmologiques est décalée vers des masses des particules supersymétriques plus petites, ce qui compense la section efficace plus faible.

Ensuite, nous avons généralisé ces résultats pour l'annihilation de neutralinos en une paire de quark-antiquark en tenant compte de tous les canaux possibles, c'est-à-dire l'échange d'un boson Z, d'un boson de Higgs neutre ou d'un squark. Pour commencer, nous avons identifié les régions dans l'espace des paramètres mSUGRA qui sont en accord avec les limites cosmologiques sur la densité relique et qui sont caractérisées par une contribution importante de tels états finals. Il s'est avéré que, en mSUGRA, les quarks "légers" (up, down, charme et étrange) ne jouent un rôle important que dans les régions expérimentalment défavorisées. En conséquence, nous nous sommes concentrés sur les états finals qui contiennent des quarks beau ou top. En applicant les mêmes techniques que pour la région "A-funnel", les corrections virtuelles et réelles en QCD et SUSY-QCD ont été calculées et implémentées dans un code numérique. Ce dernier a ensuite été inclu dans le code public `micrOMEGAs` afin d'étudier l'impact des nouvelles contributions. Comme pour la région "A-funnel", les nouvelles contributions ont un impact significatif sur la section efficace d'annihilation et, en conséquence, sur

la prédiction de la densité relique de matière noire dans notre univers. La région favorisée par la cosmologie est alors modifiée, ce qui montre que ces corrections doivent être prises en compte si l'on souhaite obtenir des prédiction plus précises.

Dans la troisième partie du travail nous avons finalement consideré la production des particules supersymétriques au futur Large Hadron Collider (LHC) du CERN. Afin d'inclure des effets de violation non-minimale de la saveur, les couplages doivent être généralisés pour prendre en compte les matrices de masses modifiées. Nous avons présenté des expressions analytiques pour la section efficace partonique de production de squarks, jauginos et gravitinos. Ceux-ci sont ensuite numériquement convolués avec des densités partoniques universelles pour obtenir des prédictions numériques des sections efficaces au LHC. Nous avons effectué une étude détaillee en ce concerne la production de squarks et jauginos pour nos scénarios "benchmark" dans des modèles GMSB avec violation de la saveur dans le secteur des squarks. En particulier, nous avons discuté la phénoménologie impliquée par cette violation non-minimale de la saveur, qui entraîne des effets interéssants au niveau des sections efficaces. Concernant la production de gravitinos, qui serait *a priori* intéressante dans des modèles GMSB où le gravitino est la particule supersymétrique la plus légère, nos scénarios incluent des gravitinos relativement lourds afin de satisfaire les contraintes cosmologiques. En conséquence, les sections efficaces de production sont numériquement trop faibles pour être observables au LHC. Il est à noter que seulement un gravitino très léger permetterait d'obtenir une production détectable. Nous argumentons que ce cas n'est pas réalisable dans nos modèles GMSB avec violation de la saveur introduite par un mélange des champs de messager avec des champs de matière.

En conclusion, la Supersymétrie est une extension attractive du Modèle Standard de la physique des particules. Elle adresse le problème de hierarchie, mène à l'unification des constantes de couplages et inclut des candidats intéressants pour la matière noire dans l'univers. Comme perspectives, il serait intéressant d'élargir les études présentées dans cette thèse. En ce qui concerne la violation non-minimale de la saveur, on pourrait par exemple relaxer les simplifications faites pour cette première étude ou analyser d'autres mécanismes de brisure de la Supersymétrie. Il serait également intéressant de calculer des corrections QCD et SUSY-QCD pour la production des particules supersymétriques dans ces scénarios. Pour les processus d'annihilation de neutralinos, on pourrait étudier l'impact des corrections dans le contexte de la détection directe ou indirecte de matière noire. Dans un modèle plus général que mSUGRA on pourrait trouver des régions avec une forte contribution des quarks légers, qui recevraient *a priori* des corrections importantes en QCD en SUSY-QCD. Comme la production de gravitinos peut inclure des effets dus à la violation de la saveur, il serait intèressant de l'ètudier dans un scenario avec un gravitino lèger et violation de la saveur dans le secteur des squarks.

Abstract

In absence of direct experimental evidence, it is essential to constrain the parameter space of the Minimal Supersymmetric Standard Model (MSSM) both at the Supersymmetry breaking and the electroweak scale. After a brief introduction to Supersymmetry (SUSY), we present an extensive analysis of electroweak, low energy, and cosmological constraints in minimal supergravity (mSUGRA) and gauge-mediated SUSY-breaking (GMSB) scenarios. We include the possibility of non-minimal flavour violation (NMFV) in the squark sector and define "collider-friendly" benchmark points based on detailed scans of the parameter space. We then consider neutralino pair annihilation into quark-antiquark pairs that dominates wide ranges of the mSUGRA parameter space. We present the corresponding full one-loop QCD and SUSY-QCD calculation and show numerically that the loop diagrams have an important impact on the annihilation cross section and, in consequence, in the prediction of the dark matter relic density, resulting in a modification of the preferred regions of the parameter space. We finally present analytical expressions and numerical predictions for squark, gaugino, and gravitino production cross sections at the LHC in GMSB with NMFV. We also discuss the phenomenology of flavour mixing and cosmological implications on the gravitino mass within this context.

Contents

Chapter 1

Supersymmetry and the MSSM

Interesting extensions have been proposed for the Standard Model of particle physics, that suffers from several conceptual problems and from discrepancies when it is confronted to precision measurements. In this work, we focus on Supersymmetry, which is an attractive solution and probably the most popular and best studied of these extensions. This first Chapter is devoted to an introductional overview of Supersymmetry and its features. We start by discussing the motivations for physics beyond the Standard Model, then present the formal and phenomenological aspects of the Minimal Supersymmetric Standard Model (MSSM) and show how it can solve the problems of the Standard Model. We thereby also focus on flavour violation and dark matter issues, which will be the main topics of this Thesis.

1.1 Motivation

Including the electroweak [1–4] and strong [5–7] gauge interactions based on the symmetry group $SU(3) \times SU(2) \times U(1)$, the Standard Model of particle physics successfully describes a wide range of phenomena. It greatly deals with the interactions of the particles that have been discovered so far, and nearly all of its predictions have been experimentally verified at very high precision. At present, the only experimentally missing piece is the Higgs boson, originating from an isodoublet scalar field [8–12]. The latter is responsible for electroweak symmetry breaking and for the fermion masses through its Yukawa couplings. However, there are several strong hints that the Standard Model is not complete and has to be extended in order to describe physics at arbitrarily high energies. In this context, the Standard Model is rather supposed to be some effective low-energy limit of a more fundamental theory.

Strong arguments arise from the particle physics side, where the most cited one is the so-called "hierarchy problem" related to the mass of the Higgs boson itself. The latter receives corrections through fermion loops involving integrals, that diverge quadratically. In consequence, the correction to the Higgs mass is of the order of the cutoff scale squared, which is used to regularize the loop integral. However, for that large Higgs masses, the Higgs self-coupling would become too strong and the could no longer be used to explain electroweak symmetry breaking. In addition, the expectation for the Higgs vacuum expectation value, that governs the masses of gauge bosons and fermions, is of the order of a few 100 GeV, well below an eventual cutoff scale [13, 14]. A second argument concerns the unification of gauge interactions. It is well-known that, within the Standard Model, the running weak, electromagnetic, and strong coupling constants do not meet in one single point at some high energy

scale, which should be the case if the three corresponding forces unify. Third, the Standard Model does not include gravity, which cannot be ignored at energies near the Planck scale. Finally, there is also the hope to clarify some "unaesthetic" points in the Standard Model. Its large number of arbitrary parameters for instance, like the number of colours or lepton families, might be explained by embedding it into some larger framework.

Further important hints come from cosmology. First evidence for a dark component in our Universe has been found in 1933 [15]. Since then, indirect and direct evidence for the presence of Dark Matter have been accumulating on all astrophysical scales. On galactic scales, the strongest argument are the rotation curves of spiral galaxies, which have a flat behaviour at large distances [16–18]. Without involving modified gravity, this is well explained only after including a dark halo surrounding the galaxy. Other hints pointing to the existence of Dark Matter come from weak or strong gravitational lensing of galaxies or clusters [19, 20] or the velocity dispersion of dwarf spheroidal or spiral satellite galaxies [21, 22]. Recently, the first direct proof for the existence of Dark Matter has been delivered by observations of the Bullet cluster, where astronomers could for the first time separate the baryonic and dark matter contributions after the collision of two clusters of galaxies [23]. On cosmological scales, strong evidence comes from precision measurements of the anisotropies of the Cosmic Microwave Background (CMB) by the satellites `COBE` and `WMAP` [24–27]. From those measurements, combined with further cosmological data, e.g. from supernovae [28] and baryon acoustic oscillations [29], it is clear today that we live in a flat Universe dominated by Dark Energy which accounts for about 75% of its energy content. Only about 4% are made of baryonic matter, while radiation accounts for about 0.001%. The remaining 25% of the matter-energy content of our Universe are non-baryonic Dark Matter, that is supposed to consist of so-called weakly interacting massive particles (WIMPs). In addition, simulations of large structure formation suggest that the main part of the Dark Matter should be highly non-relativistic, i.e. "cold" Dark Matter [30]. As no particle within the Standard Model is suitable to play that role[1], the presence of cold Dark Matter in our Universe is also strongly pointing to physics beyond the Standard Model.

1.2 The Supersymmetry Algebra

Supersymmetry has first been introduced into particle physics in 1974 [31, 32]. Its basic idea is to postulate an additional symmetry between bosonic and fermionic degrees of freedom, needed in order to cancel the fermionic contributions to the Higgs boson mass. Thus, a supersymmetric transformation operator $\mathcal{Q}$ is an anticommutating spinor that transforms a bosonic state into a fermionic one, and vice versa. A simple and elegant formulation of Supersymmetry transformations is obtained in Euclidean space extended by two Grassmanian coordinates θ_α and $\bar{\theta}_{\dot{\alpha}}$ with $\{\theta_\alpha, \theta_\beta\} = 0$ for $\alpha, \beta = 1, 2$, that defines the so-called superspace. The spinorial generator $\mathcal{Q}$ and its hermitian conjugate $\mathcal{Q}^\dagger$ are then given by

$$\mathcal{Q}_\alpha \;=\; \frac{\partial}{\partial\theta_\alpha} - i\sigma^\mu_{\alpha\dot{\beta}}\bar{\theta}^{\dot{\beta}}\frac{\partial}{\partial x^\mu} \qquad \text{and} \qquad \mathcal{Q}^\dagger_{\dot{\alpha}} \;=\; -\frac{\partial}{\partial\bar{\theta}_{\dot{\alpha}}} + i\theta^\beta\sigma^\mu_{\beta\dot{\alpha}}\frac{\partial}{\partial x^\mu}. \tag{1.1}$$

In principle, there can be $N \geq 1$ distinct sets of generators, the theoretical upper limit is $N \leq 4J$, where J denotes the maximal spin of the particles involved in the theory. However,

[1] Neutrinos are relativistic particles, so that they can only account for hot Dark Matter. Additionally, they are not massive enough to account for the rather important observed amount of Dark Matter in our Universe.

since only the case $N = 1$ is of phenomenological interest, we do not consider models with $N > 1$ for the rest of this Thesis. The generators are related to the generator of spacetime translations P^μ through

$$\left\{\mathcal{Q}_\alpha, \mathcal{Q}^\dagger_{\dot\beta}\right\} \;=\; 2\sigma^\mu_{\alpha\dot\beta} P_\mu, \tag{1.2}$$

which underlines the spacetime character of Supersymmetry. Here, σ^i denote the Pauli matrices, and $\sigma^0 = \mathbf{1}$. Furthermore, the operators $\mathcal{Q}$ and $\mathcal{Q}^\dagger$ obey the commutation and anti-commutation relations

$$\left\{\mathcal{Q}_\alpha, \mathcal{Q}_\beta\right\} \;=\; \left\{\mathcal{Q}^\dagger_{\dot\alpha}, \mathcal{Q}^\dagger_{\dot\beta}\right\} \;=\; \left[P^\mu, \mathcal{Q}_\alpha\right] \;=\; \left[P^\mu, \mathcal{Q}^\dagger_{\dot\alpha}\right] \;=\; 0. \tag{1.3}$$

The particle states lie in the irreducible representations of the above superalgebra, that are called supermultiplets. Each of them contains an equal number of fermionic and bosonic states, which are called superpartners of each other. The Supersymmetry generators commute both with the squared mass operator P^2 and the generators of the gauge transformations. Thus, in exact Supersymmetry, particles in the same supermultiplet have equal mass, electric charge, weak isospin, and colour quantum numbers.

Only two kinds of supermultiplets are relevant. The first possibility is a single Weyl fermion together with a complex scalar field, which accounts for two fermionic and two bosonic degrees of freedom. This is called a chiral supermultiplet. The second possibility is a gauge multiplet that contains a massless spin-1 vector boson together with a Weyl fermion, which accounts also for two fermionic and bosonic degrees of freedom. In $N = 1$ Supersymmetry, further combinations of particles can always be reduced to combinations of chiral and vector supermultiplets.

In order to preserve Supersymmetry when going off-shell, an additional complex scalar field is introduced into the chiral supermultiplets. This auxiliary field without a kinetic term counterbalances the two additional real fermionic degrees of freedom that a Weyl fermion acquires when becoming off-shell. When going on-shell, the auxiliary field is eliminated through its equations of motion. In the same way, an auxiliary field with one real bosonic degree of freedom restores Supersymmetry in the gauge supermultiplets.

1.3 The Minimal Supersymmetric Standard Model (MSSM)

The Minimal Supersymmetric Standard Model (MSSM) is the minimal supersymmetric theory that includes the Standard Model. Tab. 1.1 shows its particle content, organized in chiral and vector supermultiplets. The quarks and leptons obtain the squarks and sleptons as scalar superpartners, while those of the gluon, the electroweak gauge and the Higgs bosons are called gluino, gauginos, and higgsinos. A particularity is the necessity of two complex Higgs doublets in contrast to only one in the Standard Model. We also indicate the graviton and its superparner the gravitino, that are present in theories with local Supersymmetry including gravity.

In order to describe the interactions within the MSSM, we will denote the complex scalar and Weyl fermions within the chiral supermultiplets by ϕ and ψ, while the gauge bosons and their fermionic superpartners from the gauge supermultiplets are denoted by A_μ and λ. We further denote the auxiliary fields of the chiral and gauge supermultiplets by F and D. We

SM Particles		Spin		Spin		Superpartners
Quarks	$(u_L \;\; d_L)$	1/2	Q	0	$(\tilde{u}_L \;\; \tilde{d}_L)$	Squarks
	$u_R^\dagger$	1/2	$\bar{u}$	0	$\tilde{u}_R^*$	
	$d_R^\dagger$	1/2	$\bar{d}$	0	$\tilde{d}_R^*$	
Leptons	$(\nu \;\; e_L)$	1/2	L	0	$(\tilde{\nu} \;\; \tilde{e}_L)$	Sleptons
	$e_R^\dagger$	1/2	$\bar{e}$	0	$\tilde{e}_R^*$	
Higgs	$(H_u^+ \;\; H_u^0)$	0	H_u	1/2	$(\tilde{H}_u^+ \;\; \tilde{H}_u^0)$	Higgsinos
	$(H_d^0 \;\; H_d^-)$	0	H_d	1/2	$(\tilde{H}_d^0 \;\; \tilde{H}_d^-)$	
Gluon	g	1		1/2	$\tilde{g}$	Gluino
W bosons	$W^0, W^\pm$	1		1/2	$\tilde{W}^0, \tilde{W}^\pm$	Winos
B boson	B^0	1		1/2	$\tilde{B}^0$	Bino
Graviton	G	2		3/2	$\tilde{G}$	Gravitino

Table 1.1: Chiral (upper part) and gauge (lower part) supermultiplets in the MSSM.

finally introduce the covariant derivatives

$$\begin{aligned}
\mathcal{D}_\mu \phi_i &= \partial_\mu \phi_i - igA_\mu^a \big(T^a \phi\big)_i, && (1.4)\\
\mathcal{D}_\mu \phi_i^* &= \partial_\mu \phi_i^* + igA_\mu^a \big(\phi^* T^a\big)_i, && (1.5)\\
\mathcal{D}_\mu \psi_i &= \partial_\mu \psi_i - igA_\mu^a \big(T^a \psi\big)_i, && (1.6)\\
\mathcal{D}_\mu \lambda^a &= \partial_\mu \lambda^a + gf^{abc} A_\mu^b \lambda^c, && (1.7)
\end{aligned}$$

that will render the Lagrangian invariant under gauge transformations. The hermitian matrices T^a correspond to the representation under which the chiral supermultiplets transform under the gauge group, related by the totally antisymmetric structure constants f^{abc} through $[T^a, T^b] = if^{abc}T^c$. The Lagrangian of a renormalizable supersymmetric field theory can then be written as

$$\mathcal{L}_{\text{SUSY}} = \mathcal{L}_{\text{chiral}} + \mathcal{L}_{\text{gauge}} - \sqrt{2}g\big(\phi^* T^a \psi\big)\lambda^a - \sqrt{2}g\lambda^{\dagger a}\big(\psi^\dagger T^a \phi\big) + g\big(\phi^* T^a \phi\big)D^a. \qquad (1.8)$$

The kinetic terms and gauge interactions of the chiral and gauge multiplets are contained in the parts

$$\begin{aligned}
\mathcal{L}_{\text{chiral}} &= -\mathcal{D}^\mu \phi^{*i} \mathcal{D}_\mu \phi_i - i\psi^{\dagger i}\bar{\sigma}^\mu \mathcal{D}_\mu \psi_i - \frac{1}{2}\big(W^{ij}\psi_i\psi_j + W_{ij}^*\psi^{\dagger i}\psi^{\dagger j}\big) - W^i W_i^*, && (1.9)\\
\mathcal{L}_{\text{gauge}} &= -\frac{1}{4}F_{\mu\nu}^a F^{\mu\nu a} - i\lambda^{\dagger a}\bar{\sigma}^\mu \mathcal{D}_\mu \lambda^a + \frac{1}{2}D^a D^a. && (1.10)
\end{aligned}$$

The superpotential W is an analytic function of the complex fields ϕ and contains the interactions between the chiral and gauge supermultiplets through its derivatives

$$W^i = \frac{\partial W}{\partial \phi_i} \qquad \text{and} \qquad W^{ij} = \frac{\partial^2 W}{\partial \phi_i \partial \phi_j}, \qquad (1.11)$$

while $F_{\mu\nu}^a = \partial_\mu A_\nu^a - \partial_\nu A_\mu^a + gf^{abc}A_\mu^b A_\nu^c$ is the usual Yang-Mills field strength tensor. The matrices $\bar{\sigma}$ are related to the Pauli matrices σ through $\bar{\sigma}^0 = \sigma^0$ and $\bar{\sigma}^i = -\sigma^i$ for $i = 1, 2, 3$.

Suppressing all gauge and family indices, the superpotential of the MSSM in terms of the chiral superfields Q, L, $\bar{u}$, $\bar{d}$, $\bar{e}$, H_u, and H_d is given by

$$W_{\text{MSSM}} \;=\; \bar{u}\mathbf{y}_{\text{u}}QH_u - \bar{d}\mathbf{y}_{\text{d}}QH_d - \bar{e}\mathbf{y}_{\text{e}}LH_d + \mu H_u H_d. \tag{1.12}$$

The first three terms correspond to the Yukawa couplings in family space, while the μ-term is related to the masses of the Higgs bosons and the Higgsinos.

As two side remarks, let us note that the auxiliary fields F_i appear in the Lagrangian only through the derivatives of the superpotential W_i, to which they are related through the equations of motion $F_i = -W_i^*$ and $F^{i*} = -W^i$. Second, the Lagrangian of Eq. (1.8) is, of course, invariant under global Supersymmetry transformations. For rather complete reviews on Supersymmetry and in particular the MSSM see Refs. [33–35].

1.4 Supersymmetry Breaking

As no superpartners of the Standard Model particles have been observed so far, it is obvious that Supersymmetry must be a broken symmetry in the vacuum stage chosen by Nature. However, there is no consensus on the exact breaking mechanism. It only seems to be accepted that Supersymmetry should be broken via "soft" terms in the Lagrangian, i.e. terms with positive mass dimension. Otherwise, new quadratic divergences would be introduced and Supersymmetry could no longer be a viable solution to the Hierarchy problem.

The possible Supersymmetry breaking terms are included in the Lagrangian at low energy,

$$\begin{aligned}
\mathcal{L}_{\text{soft}} \;=\; & -\frac{1}{2}\Big(M_1\tilde{B}\tilde{B} + M_2\tilde{W}\tilde{W} + M_3\tilde{g}\tilde{g} + \text{h.c.}\Big) \\
& -\Big(\tilde{Q}^\dagger \mathbf{m}_{\mathbf{Q}}^{\mathbf{2}}\tilde{Q} + \tilde{u}\mathbf{m}_{\bar{\mathbf{u}}}^{\mathbf{2}}\tilde{u}^\dagger + \tilde{\bar{d}}\mathbf{m}_{\bar{\mathbf{d}}}^{\mathbf{2}}\tilde{\bar{d}}^\dagger + \tilde{L}^\dagger \mathbf{m}_{\mathbf{L}}^{\mathbf{2}}\tilde{L} + \tilde{e}\mathbf{m}_{\bar{\mathbf{e}}}^{\mathbf{2}}\tilde{\bar{e}}^\dagger\Big) \\
& -\Big(m_{H_u}^2 H_u^* H_u + m_{H_d}^2 H_d^* H_d + b\big(H_u H_d + \text{h.c.}\big)\Big) \\
& -\Big(\tilde{\bar{u}}\mathbf{a}_{\mathbf{u}}\tilde{Q}H_u - \tilde{\bar{d}}\mathbf{a}_{\mathbf{d}}\tilde{Q}H_d - \tilde{\bar{e}}\mathbf{a}_{\mathbf{e}}\tilde{L}H_e + \text{h.c.}\Big).
\end{aligned} \tag{1.13}$$

Here, the mass terms for gluino, winos, bino, squarks, sleptons, and the Higgs bosons, are contained in the first three lines. The last line of $\mathcal{L}_{\text{soft}}$ involves the trilinear scalar interactions $\mathbf{a_u}$, $\mathbf{a_d}$, and $\mathbf{a_e}$. The latter are 3×3 matrices in generation space, as are the matrices $\mathbf{m_i^2}$ for $i = Q, L, \bar{u}, \bar{d}, \bar{e}$.

Most models assume that Supersymmetry breaking occurs at a scale $\langle F \rangle$ in some "hidden" or "secluded" sector, while the Standard model particles as well as their superpartners dwell in the so-called "visible" or "observable" sector. Couplings between the particles contained in the two sectors are supposed to be small and the mediation of Supersymmetry breaking to the visible sector is realized through a shared interaction. After a brief discussion of the super-Higgs mechanism, we will review two different scenarios that are relevant within this work.

1.4.1 The Super-Higgs Mechanism and the Gravitino

As in the case of electroweak symmetry breaking, the spontaneous breaking of Supersymmetry implies the existence of a Nambu-Goldstone boson, that is called the goldstino. Taking into account gravity, Supersymmetry becomes a local symmetry and the resulting theory is called

supergravity. The spin-2 graviton has then as its fermionic superpartner with spin 3/2 the gravitino, which can be considered as the gauge field of local Supersymmetry transformations. After the spontaneous breaking of Supersymmetry, the gravitino acquires a mass through the so-called super-Higgs mechanism in an analogous way as the ordinary Higgs mechanism in the context of electroweak symmetry breaking. The gravitino absorbs the goldstino, the latter becoming its longitudinal components with spin 1/2. The so acquired gravitino mass is of the order of

$$m_{\tilde{G}} \;=\; \frac{\langle F \rangle}{\sqrt{3} M_{\mathrm{P}}}, \tag{1.14}$$

related to the Supersymmetry breaking scale $\langle F \rangle$ and the reduced Planck mass M_{P}.

After overlapping with the goldstino field, the gravitino has in principle four helicity states. However, in collider phenomenology, the only gravitationally interacting "original" gravitino components can generally be neglected with respect to the inherited goldstino modes that feature non-gravitational interactions. Note that the gravitino plays an important role in cosmology, not only as a possible dark matter candidate, but also in the context of the abundances of light elements in our Universe. Cosmological constraints on the MSSM, and in particular on the gravitino mass, are discussed in Sec. 2.2.

1.4.2 Constrained MSSM and Minimal Supergravity

The most popular framework is probably the constrained MSSM (cMSSM) [36–38]. In this framework, often also called minimal supergravity (mSUGRA), the shared interaction that mediates Supersymmetry breaking into the MSSM is gravity. The soft terms in Eq. (1.13) are determined by only five universal parameters at the Supersymmetry breaking scale. These are the common scalar and gaugino masses, m_0 and $m_{1/2}$, the universal trilinear coupling A_0, as well as the ratio of the vacuum expectation values of the Higgs doublets, $\tan\beta$, and the sign of the Higgsino mass parameter, $\mathrm{sgn}(\mu)$, for the Higgs sector. From the relations at high scale,

$$M_3 \;=\; M_2 \;=\; M_1 \;=\; m_{1/2}, \tag{1.15}$$

$$\mathbf{m_Q^2} \;=\; \mathbf{m_{\bar{u}}^2} \;=\; \mathbf{m_{\bar{d}}^2} \;=\; \mathbf{m_L^2} \;=\; \mathbf{m_{\bar{e}}^2} \;=\; m_0^2 \mathbf{1}, \tag{1.16}$$

$$m_{H_u}^2 \;=\; m_{H_d}^2 \;=\; m_0^2, \tag{1.17}$$

$$\mathbf{a}_i \;=\; A_0 \mathbf{y}_i \qquad \text{for } i = u, d, e, \tag{1.18}$$

the parameters at low energy are obtained through renormalization group running, i.e. their numerical evolution down to the electroweak scale. The weak-scale parameters of the Higgs sector are discussed in Sec. 1.5.1.

Note that the mediation of Supersymmetry breaking through the flavour-depending gravitational interaction may give rise to important flavour violating terms in the Lagrangian at low energy, i.e. important flavour changing neutral currents (FCNC). Being in contrast to current measurements this fact is often called the "flavour problem" in Supersymmetry. However, rather stringent constraints can be imposed on the flavour breaking elements of the Lagrangian. For a detailed discussion of flavour violation in the MSSM see Secs. 1.6, 2.3, and 2.4.

1.4.3 Gauge Mediated Supersymmetry Breaking

Gauge-mediated SUSY breaking (GMSB) [39–42] is a second attractive scenario, that presents a quite different phenomenology. As the name indicates, Supersymmetry breaking is mediated to the visible sector through the usual gauge interactions, whereas gravity-mediated contributions are suppressed. This is realized by introducing an additional messenger sector, containing a chiral superfield S as well as n_q quark-like and n_l lepton-like messenger fields. The scalar and auxiliary components of the superfield S acquire vacuum expectation values $\langle S\rangle$ and $\langle F_S\rangle$. Through Yukawa couplings to S the messenger fields acquire a mass $M_{\rm mes} \simeq \langle S\rangle$, while $\langle F_S\rangle$ generates the mass splitting of the messenger fields. The two vacuum expectation values are usually re-expressed in terms of an effective Supersymmetry breaking scale, $\Lambda = \langle F_S\rangle/\langle S\rangle$. The gauge interactions being flavour-blind, minimal GMSB provides a natural suppression of flavour violation in the MSSM and thus an attractive possibility to avoid the "flavour-problem" arising e.g. in minimal supergravity.

The soft Supersymmetry breaking terms are generated through virtual loops of messengers. The gaugino masses stem from one-loop diagrams, while the scalar masses are due to two-loop diagrams. At the messenger scale $M_{\rm mes}$, the corresponding expressions read

$$M_i = \frac{\alpha_i(M_{\rm mes})}{4\pi}\Lambda\; g\!\left(\frac{\Lambda}{M_{\rm mes}}\right)\big(N_5 + 3N_{10}\big), \tag{1.19}$$

$$m_{\tilde j}^2 = 2\big(N_5 + 3N_{10}\big)\Lambda^2\; f\!\left(\frac{\Lambda}{M_{\rm mes}}\right)\sum_{i=1}^{3}\frac{\alpha_i^2(M_{\rm mes})}{16\pi^2}C_j^i, \tag{1.20}$$

where the C_j^i are Casimir invariants and N_i the multiplicity of the messengers in the $\mathbf{5}+\bar{\mathbf{5}}$ and $\mathbf{10}+\overline{\mathbf{10}}$ vector-like supermultiplets. The threshold functions

$$f(x) = \frac{1+x}{x^2}\left[\log(1+x) - 2{\rm Li}_2\frac{x}{1+x} + \frac{1}{2}{\rm Li}_2\frac{2x}{1+x}\right] + \big\{x\to -x\big\}, \tag{1.21}$$

$$g(x) = \frac{1}{x^2}\Big[\big(1+x\big)\log(1+x)\Big] + \big\{x\to -x\big\}, \tag{1.22}$$

are of the order of one for $x \in [0;1]$, i.e. for the relevant region where $\Lambda < M_{\rm mes}$. Note that configurations with $\Lambda > M_{\rm mes}$ do not lead to physical solutions of the renormalization group equations. Since the trilinear couplings are generated at the two-loop level, they can be neglected with respect to the masses generated by one-loop diagrams, so that

$$\mathbf{a_u} = \mathbf{a_d} = \mathbf{a_e} = 0 \tag{1.23}$$

at the messenger scale.

The phenomenology of the minimal GMSB model is then determined by the effective Supersymmetry breaking scale Λ, the messenger mass scale $M_{\rm mes}$, and the numbers of messenger fields, n_q and n_l. The Higgs sector is again parametrized by the ratio of the vacuum expectation values of the two Higgs doublets, $\tan\beta$, and the sign of the higgsino mass parameter, ${\rm sgn}(\mu)$. Another free parameter is the gravitino mass $m_{\tilde G}$, that is related to the Supersymmetry breaking scale $\langle F\rangle$ as shown in Eq. (1.14). However, the suppression of gravity with respect to gauge interactions implies that the gravitino is the lightest supersymmetric particle.

1.5 Mass Eigenstates of the MSSM

An important feature of Supersymmetry is the mixing of supersymmetric particles. When $SU(2)\times U(1)$ is spontaneously broken, particles having equal quantum numbers mix, as do also the neutral B^0 and W^0 bosons in the Standard Model. Thus, the gauge eigenstates presented in Tab. 1.1 are not the mass eigenstates of the theory, the latter being superpositions of gauge eigenstates having equal quantum numbers. In the following, the particle mixing between gauge and mass eigenstates and the resulting mass spectrum of the MSSM is discussed.

1.5.1 Higgs Sector

As already mentioned above, two complex Higgs doublets, H_u and H_d, are needed in Supersymmetry. They couple, and thus give mass, to the up- and down-type (s)quarks and (s)leptons, respectively. Limiting the MSSM to only one doublet would spoil the cancellation of chiral anomalies, since the sum of the hypercharges of all chiral fermions should be zero. Another reason for the presence of the second doublet is that the superpotential should only involve the superfields and not their conjugates, which cannot be fulfilled with one single doublet.

After rotating away the vacuum expectation values of the charged Higgs fields using $SU(2)_L$ gauge transformations, i.e. after setting $\langle H_u^+\rangle = \langle H_d^-\rangle = 0$, the scalar potential of the MSSM can be written as

$$\begin{aligned} V &= \big(|\mu|^2 + m_{H_u}^2\big)|H_u^0|^2 + \big(|\mu|^2 + m_{H_d}^2\big)|H_d^0|^2 - b\big(H_u^0 H_d^0 + \text{h.c.}\big) \\ &\quad + \frac{1}{8}\big(g^2 + g'^2\big)\big(|H_u^0|^2 - |H_d^0|^2\big)^2 \end{aligned} \tag{1.24}$$

where the parameter b can be chosen to be real and positive. The neutral components of the Higgs fields develop vacuum expectation values $\langle H_u^0\rangle = v_u/\sqrt{2}$ and $\langle H_d^0\rangle = v_d/\sqrt{2}$. Their ratio is traditionally denoted

$$\tan\beta \;=\; \frac{v_u}{v_d} \;=\; \frac{\langle H_u^0\rangle}{\langle H_d^0\rangle} \tag{1.25}$$

with $\beta \in [0;\pi/2]$. This nomenclature anticipates the fact that the so introduced angle β will turn out to parametrize the rotation of the gauge eigenstates into the mass eigenstates. The variable $\tan\beta$ is one of the key parameters of the Higgs sector and the phenomenology of the whole MSSM.

In order to provide electroweak symmetry breaking, the potential in Eq. (1.24) has to present a minimum. It can be shown that this is the case if the conditions

$$\big(|\mu|^2 + m_{H_u}^2\big) + \big(|\mu|^2 + m_{H_d}^2\big) \;>\; 2b \qquad \text{and} \qquad \big(|\mu|^2 + m_{H_u}^2\big)\big(|\mu|^2 + m_{H_d}^2\big) \;<\; b^2 \tag{1.26}$$

are satisfied simultaneously. It is interesting to note that this cannot be achieved in exact Supersymmetry, where $m_{H_u}^2 = m_{H_d}^2$, and therefore electroweak symmetry breaking automatically also implies Supersymmetry breaking.

The two complex Higgs doublets contain eight real scalar degrees of freedom. After electroweak symmetry breaking, three of them become the massless Nambu-Goldstone bosons G^0 and $G^\pm$, that are absorbed by the electroweak gauge bosons that become massive. The remaining five scalar degrees of freedom correspond to physical particles: two CP-even neutral

(h^0, H^0), two charged ($H^\pm$), and one CP-odd (A^0) Higgs boson. These are related to the gauge eigenfields through

$$\begin{pmatrix} G^0 \\ A^0 \end{pmatrix} = \sqrt{2}\begin{pmatrix} \sin\beta & -\cos\beta \\ \cos\beta & \sin\beta \end{pmatrix}\begin{pmatrix} \Im\{H_u^0\} \\ \Im\{H_d^0\} \end{pmatrix}, \tag{1.27}$$

$$\begin{pmatrix} G^+ \\ H^+ \end{pmatrix} = \begin{pmatrix} \sin\beta & -\cos\beta \\ \cos\beta & \sin\beta \end{pmatrix}\begin{pmatrix} H_u^+ \\ H_d^{-*} \end{pmatrix}, \tag{1.28}$$

$$\begin{pmatrix} h^0 \\ H^0 \end{pmatrix} = \sqrt{2}\begin{pmatrix} \cos\alpha & \sin\alpha \\ -\sin\alpha & \cos\alpha \end{pmatrix}\begin{pmatrix} \Re\{H_u^0\} - v_u \\ \Re\{H_d^0\} - v_d \end{pmatrix}. \tag{1.29}$$

The masses of the five physical Higgs bosons are obtained by expanding the potential around its minimum. At the tree level, they are given by

$$m^2_{h^0,H^0} = \frac{1}{2}\left(m_A^2 + m_Z^2 \mp \sqrt{\left(m_A^2 + m_Z^2\right)^2 - 4m_A^2 m_Z^2 \cos 2\beta}\right), \tag{1.30}$$

$$m_A^2 = \frac{2b}{\sin 2\beta}, \tag{1.31}$$

$$m^2_{H^\pm} = m_A^2 + m_W^2, \tag{1.32}$$

while the mixing angles $\alpha \in [-\pi/2; 0]$ and β are related through

$$\frac{\tan 2\alpha}{\tan 2\beta} = \frac{m_A^2 + m_Z^2}{m_A^2 - m_Z^2} \qquad \text{and} \qquad \frac{\sin 2\alpha}{\sin 2\beta} = \frac{m^2_{h^0} + m^2_{H^0}}{m^2_{h^0} - m^2_{H^0}}. \tag{1.33}$$

Note that only two variables are needed to parametrize the Higgs sector at the tree level, e.g. m_A and $\tan\beta$. For more detailed reviews of electroweak symmetry breaking and the Higgs sector in the MSSM, see e.g. Refs. [43–46].

1.5.2 Gaugino Sector

When $SU(2) \times U(1)$ is spontaneously broken, the neutral higgsinos, bino, and wino mix, resulting in the four neutralinos $\tilde{\chi}_i^0$ ($i = 1, 2, 3, 4$). The corresponding mass matrix is given by

$$\mathcal{M}_{\tilde{\chi}^0} = \begin{pmatrix} M_1 & 0 & -m_Z s_W \cos\beta & m_Z s_W \sin\beta \\ 0 & M_2 & m_Z c_W \cos\beta & -m_Z c_W \sin\beta \\ -m_Z s_W \cos\beta & m_Z c_W \cos\beta & 0 & -\mu \\ m_Z s_W \sin\beta & -m_Z c_W \sin\beta & -\mu & 0 \end{pmatrix}, \tag{1.34}$$

where $s_W = \sin\theta_W$ and $c_W = \cos\theta_W$. Its diagonalization involves the unitary matrix $\mathcal{N}$ and leads to four neutral mass eigenstates, the neutralino fields

$$\tilde{\chi}_i^0 = \mathcal{N}_{i1}\tilde{B}^0 + \mathcal{N}_{i2}\tilde{W}^0 + \mathcal{N}_{i3}\tilde{H}_d^0 + \mathcal{N}_{i4}\tilde{H}_u^0, \tag{1.35}$$

while the mass eigenvalues, by convention ordered according to $m_{\tilde{\chi}_1^0} < ... < m_{\tilde{\chi}_4^0}$, are obtained through

$$\mathrm{diag}(m_{\tilde{\chi}_1^0}, m_{\tilde{\chi}_2^0}, m_{\tilde{\chi}_3^0}, m_{\tilde{\chi}_4^0}) = \mathcal{N}^* \mathcal{M}_{\tilde{\chi}^0} \mathcal{N}^{-1}. \tag{1.36}$$

In the context of neutralino dark matter, it is useful to introduce the gaugino and higgsino fractions of the lightest neutralino, usually defined as $f_G = |\mathcal{N}_{11}|^2 + |\mathcal{N}_{12}|^2$ and $f_H = |\mathcal{N}_{13}|^2 +$

$|\mathcal{N}_{14}|^2$. The lightest neutralino is then called "gaugino-like" if $f_G > 0.5$ and "higgsino-like" if $f_H > 0.5$, its nature influencing the coupling strenghts to gauge and Higgs bosons.

In the same way, the charged higgsinos and winos also mix, resulting in four charginos $\tilde{\chi}_i^{\pm}$ $(i = 1, 2)$. In contrast to the neutralino case, the chargino mass matrix

$$\mathcal{M}_{\tilde{\chi}^{\pm}} \;=\; \begin{pmatrix} M_2 & \sqrt{2} m_W \sin\beta \\ \sqrt{2} m_W \cos\beta & \mu \end{pmatrix} \tag{1.37}$$

is asymmetric, so that two unitary matrices $\mathcal{U}$ and $\mathcal{V}$ are needed for its diagonalization. The mass eigenvalues, ordered according to $m_{\tilde{\chi}_1^{\pm}} < m_{\tilde{\chi}_2^{\pm}}$, are then given by

$$\mathrm{diag}(m_{\tilde{\chi}_1^{\pm}}, m_{\tilde{\chi}_2^{\pm}}) \;=\; \mathcal{U}^* \mathcal{M}_{\tilde{\chi}^{\pm}} \mathcal{V}^{-1}. \tag{1.38}$$

while the chargino mass eigenstates are obtained through

$$\left(\tilde{\chi}_1^-, \tilde{\chi}_2^-\right)^T \;=\; \mathcal{U} \left(\tilde{W}^-, \tilde{H}_d^-\right)^T \quad \text{and} \quad \left(\tilde{\chi}_1^+, \tilde{\chi}_2^+\right)^T \;=\; \mathcal{V} \left(\tilde{W}^+, \tilde{H}_u^+\right)^T. \tag{1.39}$$

Being the superpartner of the gluon, the gluino is the only fermion in a colour octet and therefore cannot mix with other particles. In models with minimal supergravity or gauge mediated Supersymmetry breaking, and up to one-loop level, its mass parameter M_3 is related to the ones of the bino and wino at any scale through

$$\frac{M_3}{g_3} \;=\; \frac{M_2}{g_2} \;=\; \frac{M_1}{g_1}, \tag{1.40}$$

where the g_i denote the coupling constants of the three gauge groups. This relation implies that the gluino is usually much heavier than the other gauginos. This is yet emphasized by the fact that the gluino is strongly interacting, and the dependence of M_3 on the energy scale is therefore more important than those of M_1 and M_2.

Note that the neutralinos and the gluino are, in contrast to the charged charginos, Majorana fermions. The matrices $\mathcal{N}, \mathcal{U}$, and $\mathcal{V}$ naturally appear in the expressions for the couplings of neutralinos and charginos, respectively.

1.5.3 Sfermion Sector

In the sfermion sector, the mass eigenstates are superpositions of the left- and right-handed sfermions gauge eigenstates. Assuming constrained minimal flavour violation, the squared mass matrix for each sfermion flavour is given by

$$\mathcal{M}_{\tilde{f}}^2 \;=\; \begin{pmatrix} M_{\tilde{L}_f}^2 & m_f X_f \\ m_f X_f^* & M_{\tilde{R}_f}^2 \end{pmatrix}. \tag{1.41}$$

Denoting $M_{\tilde{L}}$, $M_{\tilde{E}}$, $M_{\tilde{Q}}$, $M_{\tilde{U}}$, and $M_{\tilde{D}}$ the soft Supersymmetry breaking mass terms for left- and right-handed sleptons and squarks, and m_q, m_l, e_q, e_l, T_q^3 and T_l^3 the mass, electric charge, and weak isospin quantum number of the squarks q and leptons l, the diagonal entries are given by

$$M_{\tilde{L}_q}^2 \;=\; M_{\tilde{Q}_q}^2 + m_q^2 + m_Z^2 \left(T_q^3 - e_q \sin^2\theta_W\right) \cos 2\beta, \tag{1.42}$$

$$M_{\tilde{R}_q}^2 \;=\; M_{\tilde{U}_q}^2 + m_q^2 + m_Z^2 e_q \sin^2\theta_W \cos 2\beta \qquad \text{for up} - \text{type squarks}, \tag{1.43}$$

$$M_{\tilde{R}_q}^2 \;=\; M_{\tilde{D}_q}^2 + m_q^2 + m_Z^2 e_q \sin^2\theta_W \cos 2\beta \qquad \text{for down} - \text{type squarks}, \tag{1.44}$$

for squarks ($q = u, d, c, s, t, b$) and by

$$M^2_{\tilde{L}_l} = m^2_{\tilde{L}} + m^2_l + m^2_Z\big(T^3_l - e_l \sin^2\theta_W\big)\cos 2\beta, \tag{1.45}$$

$$M^2_{\tilde{R}_l} = m^2_{\tilde{E}} + m^2_l + m^2_Z e_l \sin^2\theta_W \cos 2\beta, \tag{1.46}$$

for sleptons ($l = e, \nu_e, \mu, \nu_\mu, \tau, \nu_\tau$). The helicity mixing is generated by the off-diagonal elements

$$X_f = A^*_f - \mu \begin{cases} \cot\beta & \text{for up}-\text{type sfermions,} \\ \tan\beta & \text{for down}-\text{type sfermions,} \end{cases} \tag{1.47}$$

involving the trilinear couplings A_f.

Note that helicity mixing is proportional to the associated fermion mass, so that the off-diagonal elements are usually neglected for the first and second generations of sfermions. Mixing between the interaction eigenstates is then only relevant for the third generation, i.e. the tau slepton as well as the bottom and top squarks. In order to obtain the physical mass eigenstates, the mass matrix is diagonalized by a unitary matrix $\mathcal{R}^{\tilde{f}}$ according to

$$\mathrm{diag}(m^2_{\tilde{f}_1}, m^2_{\tilde{f}_2}) = \mathcal{R}^{\tilde{f}} \mathcal{M}_{\tilde{f}} \mathcal{R}^{\tilde{f}\dagger} \qquad \text{and} \qquad \big(\tilde{f}_1, \tilde{f}_2\big)^T = \mathcal{R}^{\tilde{f}}\big(\tilde{f}_L, \tilde{f}_R\big)^T, \tag{1.48}$$

where by convention $m_{\tilde{f}_1} < m_{\tilde{f}_2}$. The mass eigenvalues themselves are at the tree level given by

$$m^2_{\tilde{f}_{1,2}} = \frac{1}{2}\Big(M^2_{\tilde{L}_f} + M^2_{\tilde{R}_f} \mp \sqrt{\big(M^2_{\tilde{L}_f} - M^2_{\tilde{R}_f}\big)^2 + 4m^2_f X^2_f}\Big) \tag{1.49}$$

and the diagonalizing matrix can be expressed in terms of a mixing angle $\theta_{\tilde{f}} \in [0; \pi/2]$,

$$\mathcal{R}^{\tilde{f}} = \begin{pmatrix} \cos\theta_{\tilde{f}} & \sin\theta_{\tilde{f}} \\ -\sin\theta_{\tilde{f}} & \cos\theta_{\tilde{f}} \end{pmatrix} \qquad \text{with} \qquad \tan 2\theta_{\tilde{f}} = \frac{2m_f X_f}{M^2_{\tilde{L}_f} - M^2_{\tilde{R}_f}}. \tag{1.50}$$

In the absence left-handed eigenstates, no diagonalizing matrix is necessary for sneutrinos. A more detailed discussion of the squark sector including the possibility of flavour violation is given in the following Section.

1.6 Flavour Violation in the Squark Sector

The squark mass matrices are usually expressed in the super-CKM basis [47]. At the weak scale, their squares are given by

$$\mathcal{M}^2_{\tilde{u}} = \left(\begin{array}{ccc|ccc} M^2_{\tilde{L}_u} & \Delta^{uc}_{\mathrm{LL}} & \Delta^{ut}_{\mathrm{LL}} & m_u X_u & \Delta^{uc}_{\mathrm{LR}} & \Delta^{ut}_{\mathrm{LR}} \\ \Delta^{cu*}_{\mathrm{LL}} & M^2_{\tilde{L}_c} & \Delta^{ct}_{\mathrm{LL}} & \Delta^{cu*}_{\mathrm{RL}} & m_c X_c & \Delta^{ct}_{\mathrm{LR}} \\ \Delta^{tu*}_{\mathrm{LL}} & \Delta^{tc*}_{\mathrm{LL}} & M^2_{\tilde{L}_t} & \Delta^{tu*}_{\mathrm{RL}} & \Delta^{tc*}_{\mathrm{RL}} & m_t X_t \\ \hline m_u X^*_u & \Delta^{uc}_{\mathrm{RL}} & \Delta^{ut}_{\mathrm{RL}} & M^2_{\tilde{R}_u} & \Delta^{uc}_{\mathrm{RR}} & \Delta^{ut}_{\mathrm{RR}} \\ \Delta^{cu*}_{\mathrm{LR}} & m_c X^*_c & \Delta^{ct}_{\mathrm{RL}} & \Delta^{cu*}_{\mathrm{RR}} & M^2_{\tilde{R}_c} & \Delta^{ct}_{\mathrm{RR}} \\ \Delta^{tu*}_{\mathrm{LR}} & \Delta^{tc*}_{\mathrm{LR}} & m_t X^*_t & \Delta^{tu*}_{\mathrm{RR}} & \Delta^{tc*}_{\mathrm{RR}} & M^2_{\tilde{R}_t} \end{array}\right) \tag{1.51}$$

and

$$\mathcal{M}^2_{\tilde{d}} = \left(\begin{array}{ccc|ccc} M^2_{\tilde{L}_d} & \Delta^{ds}_{\mathrm{LL}} & \Delta^{db}_{\mathrm{LL}} & m_d X_d & \Delta^{ds}_{\mathrm{LR}} & \Delta^{db}_{\mathrm{LR}} \\ \Delta^{sd*}_{\mathrm{LL}} & M^2_{\tilde{L}_s} & \Delta^{db}_{\mathrm{LL}} & \Delta^{sd*}_{\mathrm{RL}} & m_s X_s & \Delta^{sb}_{\mathrm{LR}} \\ \Delta^{bd*}_{\mathrm{LL}} & \Delta^{bs*}_{\mathrm{LL}} & M^2_{\tilde{L}_b} & \Delta^{bd*}_{\mathrm{RL}} & \Delta^{bs*}_{\mathrm{RL}} & m_b X_b \\ \hline m_d X^*_d & \Delta^{ds}_{\mathrm{RL}} & \Delta^{db}_{\mathrm{RL}} & M^2_{\tilde{R}_d} & \Delta^{ds}_{\mathrm{RR}} & \Delta^{db}_{\mathrm{RR}} \\ \Delta^{sd*}_{\mathrm{LR}} & m_s X^*_s & \Delta^{sb}_{\mathrm{RL}} & \Delta^{sd*}_{\mathrm{RR}} & M^2_{\tilde{R}_s} & \Delta^{sb}_{\mathrm{RR}} \\ \Delta^{bd*}_{\mathrm{LR}} & \Delta^{bs*}_{\mathrm{LR}} & m_b X^*_b & \Delta^{bd*}_{\mathrm{RR}} & \Delta^{bs*}_{\mathrm{RR}} & M^2_{\tilde{R}_b} \end{array}\right) \tag{1.52}$$

for up- and down-type squarks, respectively. The expressions of their diagonal entries $M^2_{\tilde{L}_q}$ and $M^2_{\tilde{R}_q}$ as well as the squark helicity mixing elements X_q are given in Eqs. (1.42) – (1.44) and Eq. (1.47), respectively.

In the Standard Model, the only source of flavour violation arises through the rotation of the quark interaction eigenstates into the basis of physical mass eigenstates. This rotation diagonalizes the quark Yukawa matrices and renders the charged-current interactions proportional to the unitary CKM-matrix [48, 49]. In the super-CKM basis, the squark eigenstates undergo the same rotations at high energy scale as their quark counterparts, so that their charged-current interactions are also proportional to the Standard Model CKM-matrix. However, different renormalizations of quarks and squarks introduce a mismatch of quark and squark field rotations at low energies and lead to additional flavour violation at the weak scale through renormalization group running [50–53]. In minimal flavour violating (MFV) Supersymmetry, the flavour violating non-diagonal entries $\Delta^{qq'}_{ij}$ stem only from the trilinear Yukawa couplings of the fermion and Higgs supermultiplets, and can therefore be deduced from the CKM-matrix. In the "usual" MSSM, these are often neglected. In the so-called constrained minimal flavour violation (cMFV) models, the off-diagonal entries $\Delta^{qq'}_{ij}$ are then set to zero.

However, when embedding Supersymmetry in larger structures such as grand unification theories (GUTs), new sources of flavour violation can appear [54]. For example, local gauge symmetry allows for R-parity violating terms in the SUSY Lagrangian, but these terms are today severely constrained by proton decay and collider searches. Additional sources of flavour violation are included in the squark mass matrices at the weak scale. In contrast to MFV, their flavour violating off-diagonal entries cannot be deduced from the CKM-matrix alone. Non-minimal flavour violation (NMFV) is therefore conveniently parametrized in the super-CKM basis by considering the elements $\Delta^{qq'}_{ij}$ of the squared squark mass matrix as free parameters. They are usually normalized to the diagonal entries according to

$$\Delta^{qq'}_{ij} = \lambda^{qq'}_{ij} M_{\tilde{i}_q} M_{\tilde{j}'_q} \tag{1.53}$$

so that NMFV is governed by 24 dimensionless variables $\lambda^{qq'}_{ij}$ [55]. Note that $SU(2)$ gauge invariance relates the $\Delta^{qq'}_{ij}$ of up- and down-type squarks through the CKM-matrix, implying that a large difference between them is not allowed.

To diagonalize the mass matrices $\mathcal{M}^2_{\tilde{u}}$ and $\mathcal{M}^2_{\tilde{d}}$, a generalization of the rotation matrices to two 6×6 matrices $\mathcal{R}^{\tilde{u}}$ and $\mathcal{R}^{\tilde{d}}$ is now required. The mass eigenstates are then obtained

through

$$\begin{aligned} \mathrm{diag}\big(m^2_{\tilde{u}_1}, m^2_{\tilde{u}_2}, m^2_{\tilde{u}_3}, m^2_{\tilde{u}_4}, m^2_{\tilde{u}_5}, m^2_{\tilde{u}_6}\big) &= \mathcal{R}^{\tilde{u}} \mathcal{M}^2_{\tilde{u}} \mathcal{R}^{\tilde{u}\dagger}, & (1.54) \\ \mathrm{diag}\big(m^2_{\tilde{d}_1}, m^2_{\tilde{d}_2}, m^2_{\tilde{d}_3}, m^2_{\tilde{d}_4}, m^2_{\tilde{d}_5}, m^2_{\tilde{d}_6}\big) &= \mathcal{R}^{\tilde{d}} \mathcal{M}^2_{\tilde{d}} \mathcal{R}^{\tilde{d}\dagger}, & (1.55) \end{aligned}$$

where the masses are now ordered by convention according to $m_{\tilde{q}_1} < ... < m_{\tilde{q}_6}$ for $q = u, d$. The physical mass eigenstates are given by

$$\begin{aligned} \big(\tilde{u}_1, \tilde{u}_2, \tilde{u}_3, \tilde{u}_4, \tilde{u}_5, \tilde{u}_6\big)^T &= \mathcal{R}^{\tilde{u}} \left(\tilde{u}_L, \tilde{c}_L, \tilde{t}_L, \tilde{u}_R, \tilde{c}_R, \tilde{t}_R\right)^T, & (1.56) \\ \big(\tilde{d}_1, \tilde{d}_2, \tilde{d}_3, \tilde{d}_4, \tilde{d}_5, \tilde{d}_6\big)^T &= \mathcal{R}^{\tilde{d}} \left(\tilde{d}_L, \tilde{s}_L, \tilde{b}_L, \tilde{d}_R, \tilde{s}_R, \tilde{b}_R\right)^T. & (1.57) \end{aligned}$$

All relevant, i.e. squark-involving, couplings then have to be generalized, involving the rotation matrices $\mathcal{R}^{\tilde{u}}$ and $\mathcal{R}^{\tilde{d}}$. For a listing of couplings in non-minimal flavour violating Supersymmetry, see App. A. In the limit of vanishing off-diagonal parameters $\Delta^{qq'}_{ij}$ (or $\lambda^{qq'}_{ij}$) the matrices $\mathcal{R}^{\tilde{q}}$ become again flavour-diagonal, leaving only the well-known helicity mixing already present in (c)MFV. For a detailed review of flavour violation in the MSSM, see e.g. Ref. [56].

1.7 R-Parity and Dark Matter

Originally motivated by the non-observation of proton decay, that might become possible within Supersymmetry, an additional symmetry has been introduced into the MSSM. This so-called R-parity is related to baryon and lepton number conservation and is for each particle defined as

$$P_R \;=\; (-1)^{3(B-L)+2s} \;=\; \begin{cases} +1 & \text{for Standard Model particles,} \\ -1 & \text{for their superpartners,} \end{cases} \qquad (1.58)$$

where B and L denote the baryon and lepton numbers, respectively, and s the spin of the particle.

Within this work, we suppose the MSSM to conserve R-parity, which leads to important implications[2]. As a first consequence, only vertices with a pair number of supersymmetric particles are allowed. The latter can then only be produced by pairs and may decay only into final states containing an odd number of superpartners. As a further consequence, the lightest supersymmetric particle (LSP) cannot decay and must therefore be stable.

As discussed above, the Standard Model has no particle that can account for the cold Dark Matter in our Universe. In Supersymmetry, a natural candidate for this purpose is the stable LSP [57]. Additionally, in order to be a viable candidate, it has to be electrically neutral and a colour singlet. Therefore, a supersymmetric scenario may be ruled out, if it does not include a cosmologically suiting LSP. Promising Dark Matter candidates are the lightest neutralino $\tilde{\chi}^0_1$, which is the LSP in a wide range of the cMSSM or mSUGRA parameter space, or the gravitino $\tilde{G}$, which is the LSP in scenarios with gauge-mediated Supersymmetry breaking (GMSB) and can, depending on its mass, be either cold, warm, or hot Dark Matter.

[2]Nevertheless we should note that R-parity violation also leads to an interesting phenomenology, in particular in connection with neutrino physics.

1.8 Beyond the Minimal Model

Although Supersymmetry, and in particular the MSSM presented above, addresses successfully the hierarchy problem by stabilizing the Higgs mass due to the new scalar loop contributions, leads to unification of the gauge couplings [58], and includes a suitable candidate for cold Dark Matter [57], several open questions remain, leading to the assumption that the minimal MSSM should be extended in one or several sectors. As a first example, the "flavour problem" can conveniently be addressed by considering gauge-mediated instead of gravity-mediated Supersymmetry breaking or by including the possibility of non-minimal flavour violation as discussed in Sec. 1.6.

Another question arises through the Supersymmetry conserving higgsino mass parameter μ, that appears in the scalar potential of Eq. (1.24) together with the Supersymmetry breaking masses m_{H_u} and m_{H_d}. The two mass scales should then lie within a few orders of magnitude with respect to the electroweak scale, whereas they are *a priori* unrelated. A possible solution to this so-called "μ-problem" consists of introducing an additional gauge singlet [59, 60]. In those next-to-minimal Supersymmetric Standard Models (NMSSM), the μ-term is absent at the tree-level before Supersymmetry breaking and arises only from the vacuum expectation values from the new field. Recently, an NMSSM scenario based on gauge-mediated Supersymmetry breaking has been proposed [61].

Further examples of Supersymmetric models beyond the MSSM are the CP-violating MSSM [62], that includes explicit or spontaneous CP-violation in order to address the "strong CP-problem", or models with R-parity violation [63]. Except for the inclusion of non-minimal flavour violation in the squark sector, these models are, however, beyond the scope of this Thesis.

Chapter 2

Constraints and Benchmark Points for the MSSM

The Minimal Supersymmetric Standard Model (MSSM) depends on 124 *a priori* free soft Supersymmetry-breaking parameters at the electroweak scale, that are often restricted to a few universal parameters imposed at the unification scale. In the absence of direct experimental evidence for supersymmetric particles, a large variety of data can be used to constrain the parameter space of the MSSM both at the weak and the high scale.

Mass limits for superpartners of Standard Model particles can be obtained from searches of charginos, neutralinos, gluinos, stops and other squarks, and sleptons at colliders. In Tab. 2.1 the current most important lower limits are summarized, obtained from different measurements or combinations of measurements [64]. Note that all of these limits have been obtained assuming a neutralino LSP in the mSUGRA case, R-parity conservation, and constrained minimal flavour violation (cMFV). Further constraints on the MSSM parameter space can be obtained through electroweak precision, low-energy, and cosmological constraints. The first ones are particularly important in the case of non-minimal flavour violation, while cosmology is less sensitive to flavour mixing, but may involve parameters from outside the MSSM.

In this Chapter, we first discuss the different constraints that can be imposed on the MSSM including non-minimal flavour violation (NMFV). Based on systematic scans of the parameter space, we then work out benchmark scenarios for minimal supergravity (mSUGRA) and gauge mediation (GMSB) scenarios, that allow for non-minimal flavour violation as discussed in Sec. 1.6 [65, 66].

2.1 Low Energy and Electroweak Precision Constraints

For non-minimal flavour violation (NMFV), rather strong constraints can be obtained from low-energy and electroweak precision observables. Upper limits from the neutral kaon sector, on B- and D-meson oscillations, various rare decays, and electric dipole moments can be used to impose constraints on non-minimal flavour mixing in the squark and slepton sectors. In several works [55, 68–70], rather complete analysis have been performed. The obtained limits on the flavour mixing parameters $\lambda_{ij}^{qq'}$ are summarized in Tab. 2.2, pointing out that only mixing between the second- and third-generation squarks can be substantial, and this only in the left-left or right-right chiral sectors. Note that in gravity mediation models the latter is disfavoured by its scaling with the Supersymmetry-breaking mass [54].

Neutralinos	$m_{\tilde{\chi}_1^0} \geq 36 - 59$ GeV	in mSUGRA from combined LEP2 results
	$m_{\tilde{\chi}_1^0} \geq 93$ GeV	in GMSB from combined LEP2 results
	$m_{\tilde{\chi}_2^0} \geq 59$ GeV	in mSUGRA from combined LEP2 results
Charginos	$m_{\tilde{\chi}_1^\pm} \geq 45 - 85$ GeV	in mSUGRA from Z width and comb. LEP2 results
	$m_{\tilde{\chi}_1^\pm} \geq 150$ GeV	in GMSB from DØ
Stop	$m_{\tilde{t}_1} \geq 95 - 96$ GeV	in mSUGRA from combined LEP2 results
Sbottom	$m_{\tilde{b}_1} \geq 96$ GeV	in mSUGRA from combined LEP2 results
Other squarks	$m_{\tilde{q}} \geq 300$ GeV	for gluinos of equal mass from CDF
Selectron	$m_{\tilde{e}_1} \geq 99$ GeV	in mSUGRA from combined LEP2 results
Smuon	$m_{\tilde{\mu}_1} \geq 95$ GeV	in mSUGRA from combined LEP2 results
Stau	$m_{\tilde{\tau}_1} \geq 80 - 86$ GeV	in mSUGRA or GMSB from combined LEP2 results
Sneutrino	$m_{\tilde{\nu}_1} \geq 43$ GeV	from measurements of the Z width
Gluino	$m_{\tilde{g}} \geq 195$ GeV	for any squark masses from CDF
Gravitino	$m_{\tilde{G}} \geq 1.1 \cdot 10^{-5}$ eV	for heavy sparticles from CDF
	$m_{\tilde{G}} \geq 1.3 \cdot 10^{-5}$ eV	for $m_{\tilde{q}}, m_{\tilde{g}} \sim 200$ GeV from Ref. [67]

Table 2.1: Current limits at 95% confidence level for supersymmetric particle masses, as given in Ref. [64], and assuming constrained minimal flavour violation and R-parity conservation. Note that some of the limits depend on the imposed Supersymmetry breaking scenario and mass hierarchies at the electroweak scale.

In this study, we take implicitly into account all of the previously mentioned constraints by restricting ourselves to the case of flavour-mixing between the second and third generation squarks and consequently to only one real NMFV-parameter. Depending on the sector that includes flavour violation, this parameter is either

$$\lambda_{\rm LL} \equiv \lambda_{\rm LL}^{sb} = \lambda_{\rm LL}^{ct} \qquad \text{or} \qquad \lambda_{\rm RR} \equiv \lambda_{\rm RR}^{sb} = \lambda_{\rm RR}^{ct}, \tag{2.1}$$

while all other $\lambda_{ij}^{qq'}$ are zero, respectively. Allowed regions for this parameter are then obtained by imposing explicitly a number of low-energy, electroweak precision, and cosmological constraints. Note that the equality $\lambda_{\rm LL,RR}^{sb} = \lambda_{\rm LL,RR}^{ct}$ is justified by the fact that $SU(2)$ gauge invariance relates these values and implies that a large difference between them is not allowed.

A rather stringent constraint comes from the theoretically robust inclusive branching ratio

$$\mathrm{BR}(b \to s\gamma) \;=\; \big(3.55 \pm 0.26\big) \cdot 10^{-4}, \tag{2.2}$$

obtained from the combined measurements of BaBar, Belle, and CLEO [71], which affects directly the allowed squark mixing between the second and third generation. The above limit is imposed at the 2σ confidence level on the two-loop QCD / one-loop SUSY-QCD calculation [70, 72]. Like the Standard Model contributions, squarks enter the calculation of this branching ratio already at the one-loop level, so that its dependence on the NMFV-parameters $\lambda_{\rm LL}$ and $\lambda_{\rm RR}$ is rather important.

A second important consequence of NMFV in the MSSM is the generation of large splittings between squark mass eigenvalues. The splitting within the isospin doublets influences the Z- and W-boson self-energies at zero momentum $\Sigma_{Z,W}(0)$ in the electroweak ρ-parameter

$$\Delta\rho \;=\; \frac{\Sigma_Z(0)}{m_Z^2} - \frac{\Sigma_W(0)}{m_W^2} \tag{2.3}$$

qq' / ij	LL	LR	RL	RR
12	$1.4 \cdot 10^{-2}$	$9.0 \cdot 10^{-5}$	$9.0 \cdot 10^{-5}$	$9.0 \cdot 10^{-3}$
13	$9.0 \cdot 10^{-2}$	$1.7 \cdot 10^{-2}$	$1.7 \cdot 10^{-2}$	$7.0 \cdot 10^{-2}$
23	$1.6 \cdot 10^{-1}$	$4.5 \cdot 10^{-3}$	$6.0 \cdot 10^{-3}$	$2.2 \cdot 10^{-1}$

Table 2.2: The 95% probability bounds on the NMFV-parameters $|\lambda_{ij}^{qq'}|$ for down-type squarks obtained in Ref. [68].

and consequently the W-boson mass m_W and the squared sine of the electroweak mixing angle $\sin^2\theta_W$. The latest combined fits of the Z-boson mass, width, pole asymmetry, W-boson, and top quark mass constrain new physics contributions to $T = -0.13 \pm 0.11$ [64] or

$$\Delta\rho \;=\; -\alpha T \;=\; \big(1.02 \pm 0.86\big) \cdot 10^{-3} \tag{2.4}$$

for $\alpha^{-1}(m_Z) = 127.918$. This value is then imposed at the 2σ-level on the one-loop NMFV and two-loop cMFV SUSY calculation [73].

The anomalous magnetic moment of the muon $a_\mu = (g_\mu - 2)/2$ represents a third observable that is sensitive to SUSY loop contributions. Recent BNL data and the Standard Model prediction disagree by [64]

$$\Delta a_\mu \;=\; a_\mu^{\rm exp} - a_\mu^{\rm SM} \;=\; \big(29.2 \pm 8.6\big) \cdot 10^{-10}. \tag{2.5}$$

We take into account SM and MSSM contributions up to two loops [74, 75] and require them to agree with the region above within two standard deviations. Here, squarks are involved only at the two-loop level, so that their contribution is suppressed with respect to the slepton one-loop diagrams. Concerning our analysis within non-minimal flavour violation, we should note that the one-loop SUSY contributions are approximately given by [76]

$$a_\mu^{\rm SUSY,1-loop} \;\simeq\; 13 \cdot 10^{-10} \left(\frac{100\ {\rm GeV}}{M_{\rm SUSY}}\right)^2 \tan\beta\ {\rm sgn}(\mu), \tag{2.6}$$

if the relevant SUSY particles have a common mass $M_{\rm SUSY}$. In consequence, negative values of μ then increase, not decrease, the disagreement between the experimental measurements and the theoretical SM value of a_μ, so that the region $\mu < 0$ is strongly disfavoured in all supersymmetric models.

2.2 Cosmological Constraints

As already mentioned in the previous Chapter, Supersymmetry provides an interesting candidate for the cold dark matter in our Universe. It is the lightest supersymmetric particle (LSP), which is stable if R-parity is conserved. In order to have a suitable candidate for non-baryonic cold dark matter (WIMP), it is first of all required to be electrically neutral and a colour singlet [57].

Since we can then compute the relic abundance of the lightest supersymmetric particle for a given scenario, the calculation of the relic density $\Omega_{\rm CDM}h^2$ allows to put additional constraints on the MSSM parameter space with respect to collider, low-energy, and electroweak precision

data. Cosmologically (dis)favoured regions are identified by comparing to the rather narrow interval

$$0.095 < \Omega_{\rm CDM} h^2 < 0.136. \tag{2.7}$$

This limit at 2σ (95%) confidence level has recently been obtained from the three-year data of the WMAP satellite, combined with the SDSS and SNLS survey and Baryon Acoustic Oscillation data and interpreted within an eleven-parameter inflationary model [77], which is more general than the usual six-parameter "vanilla" concordance model of cosmology. Note that this range is well compatible with the older, independently obtained range of $0.094 < \Omega_{\rm CDM} h^2 < 0.129$ [78].

2.2.1 Neutralino Dark Matter

One natural candidate for cold dark matter within supersymmetric models is the lightest of the four neutralinos. It is only gravitationally and weakly interacting and massive enough to account for the cold dark matter density observed in our Universe. In particular in models with minimal supergravity, the LSP is usually a neutralino.

The evolution of the number density of the relic particle with mass $m_{\tilde\chi}$ is governed by the Boltzmann equation

$$\frac{dn}{dt} \;=\; -3Hn - \langle\sigma_{\rm ann} v\rangle\big(n^2 - n_{\rm eq}^2\big), \tag{2.8}$$

where the first term on the right-hand side corresponds to a dilution due to the expansion of the Universe, and the second one to a decrease due to annihilations and coannihilations. Here, H denotes the Hubble expansion parameter and $n_{\rm eq}$ the density of the relic particle in thermal equilibrium. Knowing the effective (co)annihilation cross section $\sigma_{\rm ann}$, the Boltzmann equation can be integrated numerically from $t = 0$ (Big Bang) to $t = t_0$ (today). The energy density of the relic particle with mass $m_{\tilde\chi}$ is then directly proportional to the present number density n_0,

$$\Omega_{\rm CDM} h^2 \;=\; \frac{m_{\tilde\chi} n_0}{\rho_c} \;\propto\; \frac{1}{\langle\sigma_{\rm ann} v\rangle}, \tag{2.9}$$

$\rho_c = 3H_0^2/(8\pi G_{\rm N})$ being the critical density of our Universe, H_0 the present Hubble parameter, and $G_{\rm N}$ the gravitational constant [79].

The effective cross section $\sigma_{\rm ann}$ involves all annihilation and coannihilation processes of the relic particle into Standard Model particles. The notation $\langle\sigma_{\rm ann} v\rangle$ stands for the thermal average of the cross section multiplied by the relative particle velocity v, which can in the case of neutralino pairs and for a given temperature T be calculated by [80, 81]

$$\langle\sigma_{\rm ann} v\rangle \;=\; \frac{1}{4T m_{\tilde\chi}^4 K_2^2(m_{\tilde\chi}/T)} \int {\rm d}s\; s\beta_{\tilde\chi}(s) K_1(\sqrt{s}/T)\sigma_{\rm ann}(s) \;\equiv\; \int {\rm d}s\; f_v(s)\; \sigma_{\rm ann}(s). \tag{2.10}$$

Here, K_1 and K_2 denote the modified Bessel functions of the first and second kind, respectively, $\beta_{\tilde\chi}$ the neutralino velocity, and $\sigma_{\rm ann}(s)$ is the annihilation cross section as a function of the squared centre-of-momentum energy s. The most important processes contributing to $\sigma_{\rm ann}$ are those that have two-particle final states and that occur at the tree level [82]. In the case of neutralino (co)annihilation, possible final states include those with fermion-antifermion pairs as well as with combinations of gauge ($W^\pm$, Z^0) and Higgs (h^0, H^0, A^0, $H^\pm$) bosons, depending on the region of the parameter space. Processes producing fermions or antifermions may be detectable either directly or through their annihilation into photons.

In addition, these channels are always open (for b-quarks if $m_{\tilde{\chi}_1^0} \geq 4.5$ GeV) in contrast to the other channels, which may be suppressed or even closed [79, 82].

Several public codes perform a calculation of the cold dark matter relic density within supersymmetric models. The most developed and most popular ones are `DarkSUSY` [83] and `micrOMEGAs` [84]. All relevant annihilation and co-annihilation processes are implemented in these codes, but for most of them no (or at least not the full) higher order corrections are included. For a compilation of all contributing processes see e.g. Ref. [79]. A more detailed discussion of processes with quarks in the final state is given in Chaps. 3 and 4.

2.2.2 Gravitino Dark Matter

Another promising candidate for the cold dark matter in our Universe is the gravitino, that is present in local supersymmetric theories and acquires its mass through the super-Higgs mechanism. In certain scenarios, in particular in the case of gauge-mediated Supersymmetry breaking (GMSB), the gravitino is the lightest supersymmetric particle. Depending on its mass, the gravitino can account either for cold ($m_{\tilde{G}} \gtrsim 100$ keV), warm (1 keV $\lesssim m_{\tilde{G}} \lesssim$ 100 keV), or hot ($m_{\tilde{G}} \lesssim 1$ keV) dark matter. The constraints for gravitino dark matter are similar, while somewhat more complex, than in the neutralino case.

Today's gravitino abundance in our Universe has two contributions. First, gravitinos are produced by thermal scattering in the very early Universe. Their corresponding energy density [85–87]

$$\Omega_{\tilde{G}}^{\mathrm{th}} h^2 \;\simeq\; 0.27 \left(\frac{T_{\mathrm{R}}}{10^{10}\ \mathrm{GeV}}\right)\left(\frac{100\ \mathrm{GeV}}{m_{\tilde{G}}}\right)\left(\frac{m_{\tilde{g}}}{1\ \mathrm{TeV}}\right)^2 \tag{2.11}$$

involves the gluino mass $m_{\tilde{g}}$ at low energy and the reheating temperature T_{R}. The latter is the temperature of the Universe after inflation, for which at present no convincing constraints exist. However, values of $T_{\mathrm{R}} \gtrsim 10^9$ GeV are preferred in scenarios that feature leptogenesis in order to explain the cosmic baryon asymmetry [88, 89].

Second, there is non-thermal production through decay of the next-to-lightest supersymmetric particle (NLSP) into the gravitino. As each NLSP will decay into its Standard Model partner and one gravitino, the resulting gravitino energy density can be obtained through

$$\Omega_{\tilde{G}}^{\mathrm{non-th}} h^2 \;=\; \frac{m_{\tilde{G}}}{m_{\mathrm{NLSP}}} \Omega_{\mathrm{NLSP}}^{\mathrm{th}} h^2, \tag{2.12}$$

where $\Omega_{\mathrm{NLSP}}^{\mathrm{th}} h^2$ is the thermal freeze-out relic density the NLSP would have if it did not decay. The calculation of $\Omega_{\mathrm{NLSP}}^{\mathrm{th}} h^2$ can be done in the same way as for the neutralino, i.e. by solving the Boltzmann equation (2.8). This can be done numerically for any NLSP using the public code `micrOMEGAs`, whereas `DarkSUSY` is only adapted to the neutralino case. Note that for low values of $m_{\tilde{G}}$ and high reheating temperatures T_{R} thermal production dominates, whereas for high values of $m_{\tilde{G}}$ it is negligible with respect to the contribution from NLSP decay.

Of course, as in the neutralino case, to be a viable candidate for cold dark matter the total energy density of the gravitino should be within the experimental limits in Eq. (2.7), or at least not exceed the upper limit[1]. Since for a given supersymmetric scenario $\Omega_{\tilde{G}} h^2 = \Omega_{\tilde{G}}^{\mathrm{th}} h^2 + \Omega_{\tilde{G}}^{\mathrm{non-th}} h^2$ does not only depend on $m_{\tilde{G}}$ but also on the reheating temperature, we can put upper limits on the latter by evaluating the gravitino relic density.

[1] Note that, in GMSB models with gravitino warm or hot dark matter, the lightest messenger particle can play the role of cold dark matter required by the constraints coming from large structure formation.

Another constraint for scenarios with gravitino dark matter arises from the fact that the NLSP can spoil the abundances of light elements in our Universe, such as Li, if it does not decay rapidly enough [86]. The lifetime of a supersymmetric particle decaying into its Standard Model partner and a gravitino is given by the inverse of the corresponding decay rate,

$$\Gamma_{\rm NLSP} \;=\; \frac{1}{48\pi M_{\rm P}^2}\frac{m_{\rm NLSP}^5}{m_{\tilde{G}}^2}\left(1-\frac{m_{\tilde{G}}^2}{m_{\rm NLSP}^2}\right)^4. \tag{2.13}$$

Given the cosmological uncertainties, we have here neglected any flavour violation and supersymmetric particle mixing, which only would have minor effects on the resulting limits for the gravitino mass. Inserting the value of the reduced Planck mass $M_{\rm P} = \sqrt{8\pi G_{\rm N}}$, Eq. (2.13) can be rewritten as

$$\tau_{\rm NLSP} \;=\; \left(6.1\cdot 10^3\,{\rm s}\right)\left(\frac{1\ {\rm TeV}}{m_{\rm NLSP}}\right)^5\left(\frac{m_{\tilde{G}}}{100\ {\rm GeV}}\right)^2\left(1-\frac{m_{\tilde{G}}^2}{m_{\rm NLSP}^2}\right)^{-4}. \tag{2.14}$$

In order to preserve the abundances of the light elements, that are well explained by primordial nucleosynthesis, the lifetime of the NLSP should be shorter than $\tau_{\rm NLSP} \lesssim 2\cdot 10^3$ seconds [86]. In consequence, this last constraint favours scenarios having a light gravitino and/or a heavy NLSP. Note that this might enter in conflict with the thermal production preferring a rather high reheating temperature and therefore also a rather high gravitino mass, as can be seen from Eq. (2.11).

2.3 Non-Minimal Flavour Violation in mSUGRA Scenarios

The previously discussed experimental limits are now imposed on the constrained Minimal Supersymmetric Standard Model (cMSSM), or minimal supergravity (mSUGRA) model, with five free parameters m_0, $m_{1/2}$, A_0, $\tan\beta$, and ${\rm sgn}(\mu)$ at the grand unification scale. Since our analysis depends very little on the trilinear coupling A_0, we set it to zero in the following. For the ratio of the Higgs vacuum expectation values, we fix a small ($\tan\beta = 10$), intermediate (30), and large (50) value. The impact of the sign of the off-diagonal Higgs mass parameter μ is investigated for $\tan\beta = 10$ only, before we set it to $\mu > 0$ for $\tan\beta = 30$ and $\tan\beta = 50$.

With these boundary conditions at the grand unification scale, we solve the renormalization group equations numerically to two-loop order using the computer programme `SPheno 2.2.3` [90] and compute the soft SUSY-breaking masses at the electroweak scale with the complete one-loop formulas, supplemented by two-loop contributions in the case of the neutral Higgs bosons and the μ-parameter. At this point we generalize the squark mass matrices as described in Sec. 1.6 in order to account for flavour mixing between the second- and third-generation squarks, diagonalize these mass matrices, and compute the low-energy and electroweak precision observables with the computer programme `FeynHiggs 2.5.1` [91]. As already mentioned, flavour violation in the right-right chiral sector is here disfavoured due to the scaling of the flavour-violating entries $\Delta_{ij}^{qq'}$ with the Supersymmetry breaking scale, implying a hierarchy $\Delta_{\rm LL} \gg \Delta_{\rm LR,RL} \gg \Delta_{\rm RR}$ [54]. Within mSUGRA, we therefore concentrate on flavour mixing in the left-left sector, implemented through the parameter $\lambda_{\rm LL}$, while $\lambda_{\rm RR}$ is set to zero. The neutralino relic density is computed by a modified version of `DarkSUSY 4.1`, that takes into account the six-dimensional squark helicity and flavour mixing. For the Standard Model input parameters, we use the current values of Ref. [64], summarized in App. B.

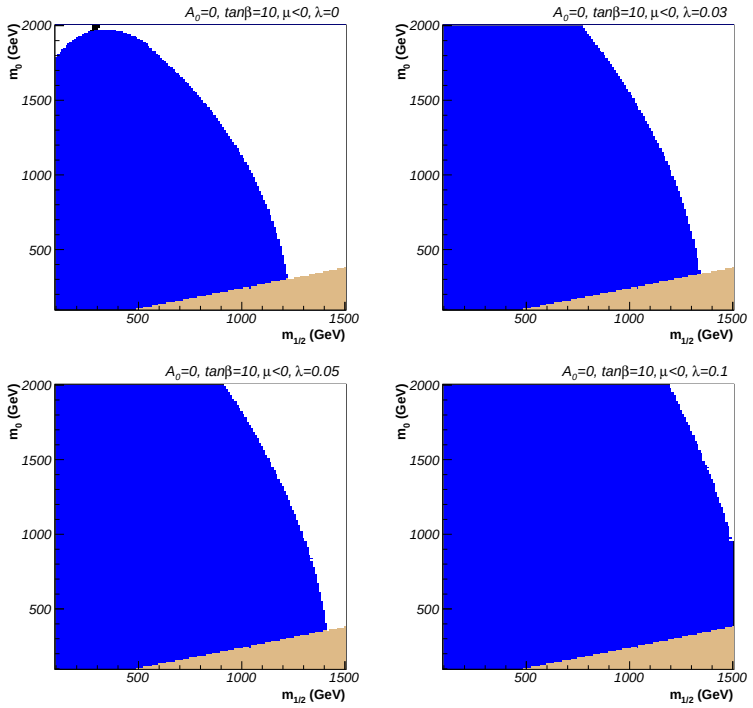

Figure 2.1: The m_0-$m_{1/2}$ planes for $\tan\beta = 10$, $A_0 = 0$, $\mu < 0$, and $\lambda_{\rm LL} = 0,\ 0.03,\ 0.05,$ and 0.1. We show WMAP favoured (black) as well as $b \to s\gamma$ (blue) and charged LSP (beige) excluded regions of the mSUGRA parameter space in constrained minimal ($\lambda_{\rm LL} = 0$) and (non-)minimal ($\lambda_{\rm LL} > 0$) flavour violation.

2.3.1 Scans of the mSUGRA parameter space and benchmark points

Typical scans of the cMSSM parameter space in m_0 and $m_{1/2}$ with a relatively small value of $\tan\beta = 10$ and $A_0 = 0$ are shown in Figs. 2.1 and 2.2 for $\mu < 0$ and $\mu > 0$, respectively. All experimental limits described in Secs. 2.1 and 2.2 are imposed at the 2σ-level. As expected, the $b \to s\gamma$ excluded region depends strongly on flavour mixing, while the regions favoured by $(g-2)_\mu$ and the dark matter relic density are quite insensitive to variations of the NMFV parameter $\lambda_{\rm LL}$. $\Delta\rho$ constrains the parameter space only for very heavy scalar masses $m_0 >$ 2000 GeV and heavy gaugino masses $m_{1/2} > 1500$ GeV, so that the corresponding excluded regions are not shown. In addition to the fact that $\mu < 0$ is strongly disfavoured due to Δa_μ, the measured $b \to s\gamma$ branching ratio excludes virtually all of the region favoured by the dark matter relic density, except for very high SUSY masses. We therefore do not consider negative values of μ in the rest of this analysis.

In Figs. 2.3 and 2.4, we show the m_0-$m_{1/2}$ planes for larger $\tan\beta$, namely $\tan\beta = 30$ and $\tan\beta = 50$, and for $\mu > 0$. The regions which are favoured both by the anomalous magnetic moment of the muon and by the cold dark matter relic density, and which are not excluded by the $b \to s\gamma$ measurements, are stringently constrained and do not allow for large flavour violation.

We now inspect the m_0–$m_{1/2}$ planes in Figs. 2.2 – 2.4 for mSUGRA scenarios that are allowed/favoured by low-energy, electroweak precision and cosmological constraints, and that permit non-minimal flavour violation among left-chiral squarks of the second and third gen-

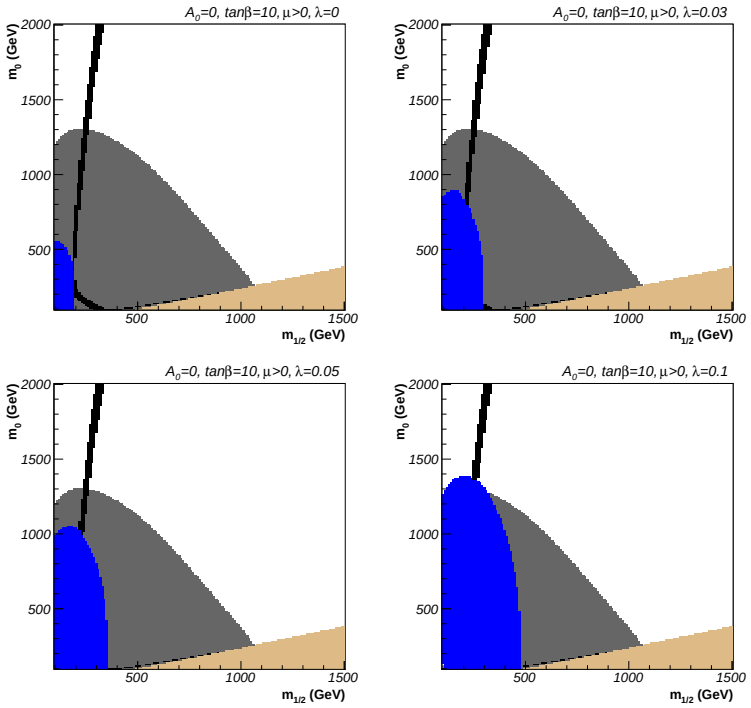

Figure 2.2: The m_0-$m_{1/2}$ planes for $\tan\beta = 10$, $A_0 = 0$, $\mu > 0$, and $\lambda_{\rm LL} = 0,\ 0.03,\ 0.05$, and 0.1. We show a_μ (grey) and WMAP favoured (black) as well as $b \to s\gamma$ (blue) and charged LSP (beige) excluded regions of the mSUGRA parameter space in constrained minimal ($\lambda_{\rm LL} = 0$) and (non-)mininal ($\lambda_{\rm LL} > 0$) flavour violation.

eration up to $\lambda_{\rm LL} \leq 0.1$. Additionally, we require them at the same time to be "collider-friendly", i.e. to have relatively low values of m_0 and $m_{1/2}$. Our choices are presented in Tab. 2.3, together with the nearest pre-WMAP Snowmass Points (and Slopes, SPS) [92, 93] and the nearest post-WMAP scenarios (BDEGOP) proposed in Ref. [94]. The benchmark scenarios are also valid in (constrained) minimal flavour violation. We have also verified that in the case of MFV the hierarchy $\Delta^{qq'}_{\rm LL} \ll \Delta^{qq'}_{\rm LR,RL} \ll \Delta^{qq'}_{\rm RR}$ and the equality $\lambda^{sb}_{\rm LL} = \lambda^{ct}_{\rm LL}$ are still reasonably well fulfilled numerically with the values of $\lambda^{sb}_{\rm LL} \approx \lambda^{ct}_{\rm LL}$ ranging from zero to $5 \cdot 10^{-3} \ldots 1 \cdot 10^{-2}$ for our different benchmark points.

Starting with Fig. 2.2 and $\tan\beta = 10$, the bulk region of equally low scalar and fermion masses is all but excluded by the $b \to s\gamma$ branching ratio. This leaves as a favoured region first the so-called focus point region of low fermion masses $m_{1/2}$, where the lightest neutralinos are relatively heavy, have a significant higgsino component, and annihilate dominantly into pairs of electroweak gauge bosons. Our benchmark point A lies in this region, albeit at smaller masses than SPS 2 ($m_0 = 1350$ GeV, $m_{1/2} = 300$ GeV) and BDEGOP E' ($m_0 = 1530$ GeV, $m_{1/2} = 300$ GeV), which lie outside the favoured region by $(g-2)_\mu$ and lead to collider-unfriendly squark and gaugino masses.

The second favoured region for small $\tan\beta$ is the coannihilation branch of low scalar masses m_0, where the lighter tau-slepton mass eigenstate is not much heavier than the lightest neutralino and the two have a considerable coannihilation cross section. This is where we have chosen our benchmark point B, which differs from the points SPS 3 ($m_0 = 90$ GeV,

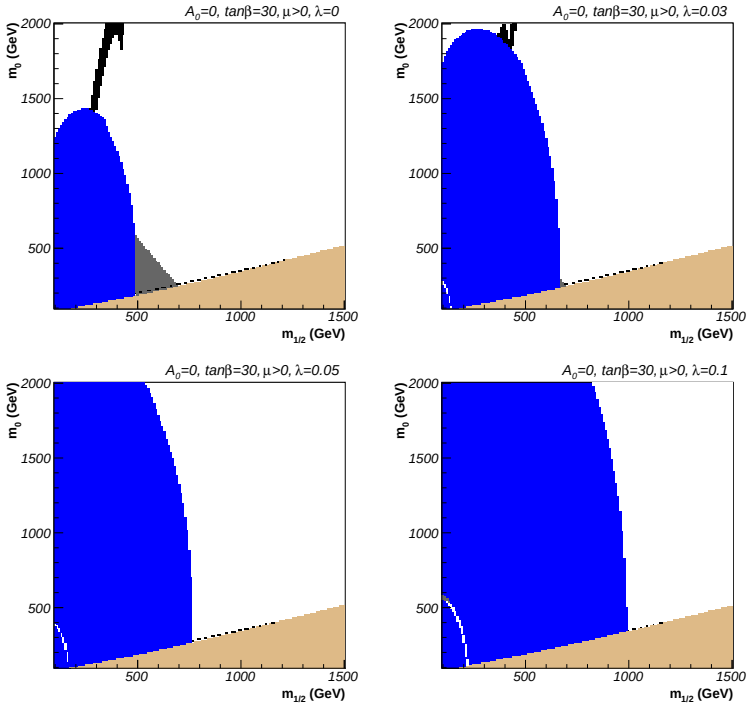

Figure 2.3: Same as Fig. 2.2 for $\tan\beta = 30$, $A_0 = 0$, $\mu > 0$.

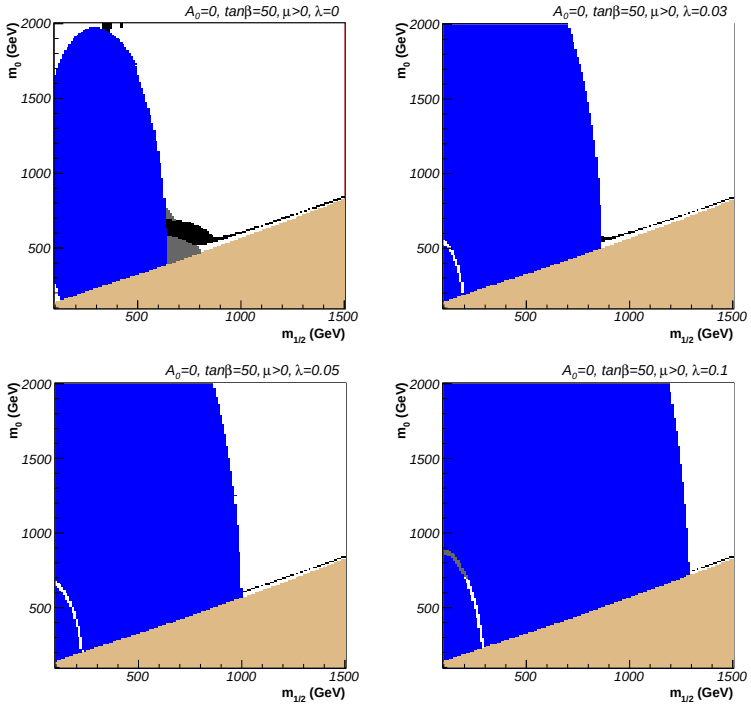

Figure 2.4: Same as Fig. 2.2 for $\tan\beta = 50$, $A_0 = 0$, $\mu > 0$.

	m_0 [GeV]	$m_{1/2}$ [GeV]	A_0	$\tan\beta$	sgn(μ)	SPS	BDEGOP	Cosmol. region
A	700	200	0	10	+	2	E'	Focus point
B	100	400	0	10	+	3	C'	Co-annihilation
C	230	590	0	30	+	1b	I'	Co-annihilation
D	600	700	0	50	+	4	L'	Bulk/Higgs funnel

Table 2.3: Benchmark point allowing for flavour violation among the second and third generations for $A_0 = 0$, $\mu > 0$, and three different values of $\tan\beta$. For comparison we also show the nearest pre-WMAP SPS [92,93] and post-WMAP BDEGOP [94] benchmark points and indicate the relevant cosmological regions.

$m_{1/2} = 400$ GeV) and BDEGOP C' ($m_0 = 85$ GeV, $m_{1/2} = 400$ GeV) only very little in the scalar mass. This minor difference may be traced to the fact that we use `DarkSUSY 4.1` [83] instead of the private dark matter code `SSARD` of Ref. [94].

At larger values of $\tan\beta = 30$ in Fig. 2.3, only the coannihilation region survives the constraints coming from $b \to s\gamma$ decays. Here we choose our point C, which has slightly higher masses than both SPS 1b ($m_0 = 200$ GeV, $m_{1/2} = 400$ GeV) and BDEGOP I' ($m_0 = 175$ GeV, $m_{1/2} = 350$ GeV), due to the ever more stringent constraints from the B-decay.

Finally, for the large value of $\tan\beta = 50$ in Fig. 2.4, the bulk region reappears at relatively high scalar and fermion masses. Here, the couplings of the heavier scalar and pseudoscalar Higgs bosons H^0 and A^0 to bottom quarks and tau leptons and the charged Higgs coupling to top-bottom quark pairs are significantly enhanced, resulting e.g. in increased dark matter annihilation cross sections through s-channel Higgs exchange into bottom-quark final states. So as $\tan\beta$ increases further ($\tan\beta \sim 54$, see Chap. 3), the so called Higgs-funnel region eventually makes its appearance on the diagonal of large scalar and fermion masses. We choose our point D in the concentrated (bulky) region favoured by cosmology and $(g-2)_\mu$. The corresponding masses are slightly higher than those of SPS 4 ($m_0 = 400$ GeV, $m_{1/2} = 300$ GeV) and BDEGOP L' ($m_0 = 300$ GeV, $m_{1/2} = 450$ GeV). We do so in order to escape again from the constraints of the $b \to s\gamma$ decay, which are stronger today than they were a few years ago. In this scenario, squarks and gluinos are very heavy with masses over 1 TeV.

2.3.2 Dependence of Observables and Mass Eigenvalues on Flavour Violation

Let us now turn to the dependence of the precision variables discussed in the previous Section on the flavour violating parameter $\lambda_{\rm LL}$ in the four benchmark scenarios defined above. Our numerical analysis confirms the expected weak dependence of the leptonic observable $(g-2)_\mu$ on the squark sector. We find the constant values of $a_\mu^{\rm SUSY} = 6 \cdot 10^{-10}$, $14 \cdot 10^{-10}$, $16 \cdot 10^{-10}$, and $13 \cdot 10^{-10}$ for our benchmark points A, B, C, and D, respectively. Note that the benchmark points have been defined based on the older experimental limits $\Delta a_\mu = \big(22 \pm 10\big) \cdot 10^{-10}$. Our points B, C, and D lie well within 2σ of both the older and the current experimentally favoured range of Eq. (2.5). The point A, however, lies now outside the 2σ interval with respect to the "new" limits, so that a redefinition would be necessary [95].

In the first diagrams of Figs. 2.5 – 2.8 we show the dependence of the most stringent low-energy constraint coming from the good agreement between the measurements of the $b \to s\gamma$ branching ratio and the two-loop Standard Model prediction, on the NMFV parameter

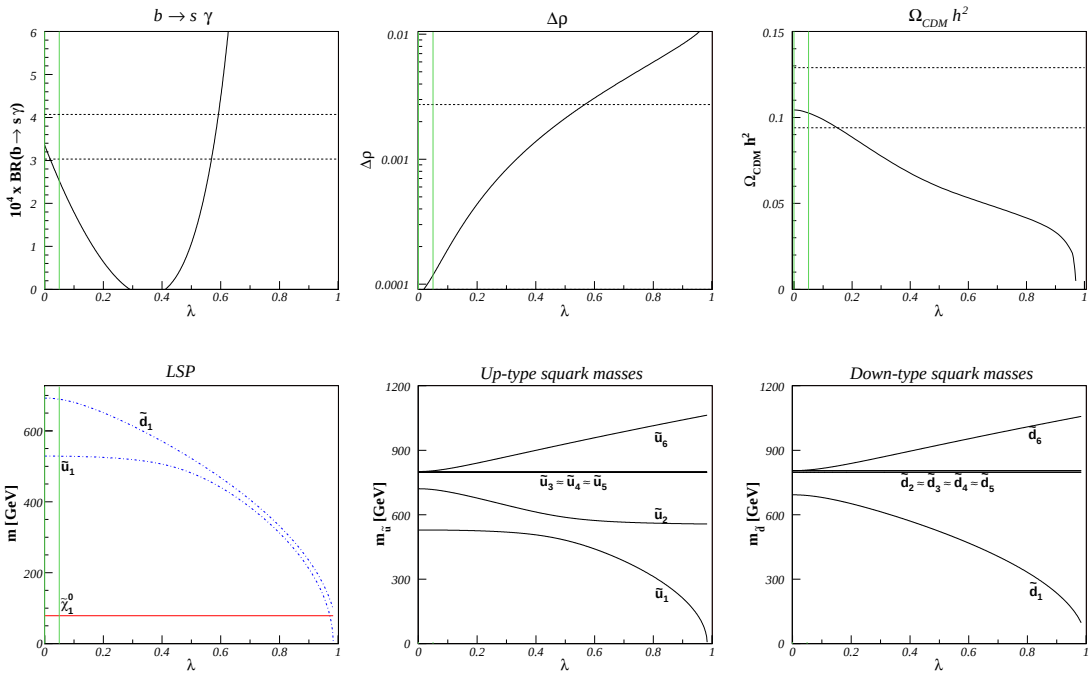

Figure 2.5: Dependence of the precision observables BR($b \to s\gamma$), $\Delta\rho$, and the cold dark matter relic density $\Omega_{\rm CDM}h^2$ as well as the lightest SUSY-particle, up- and down-type squark masses on the NMFV parameter $\lambda_{\rm LL}$ in our benchmark scenario A. The experimentally allowed/favoured ranges (within 2σ) are indicated by horizontal dashed lines.

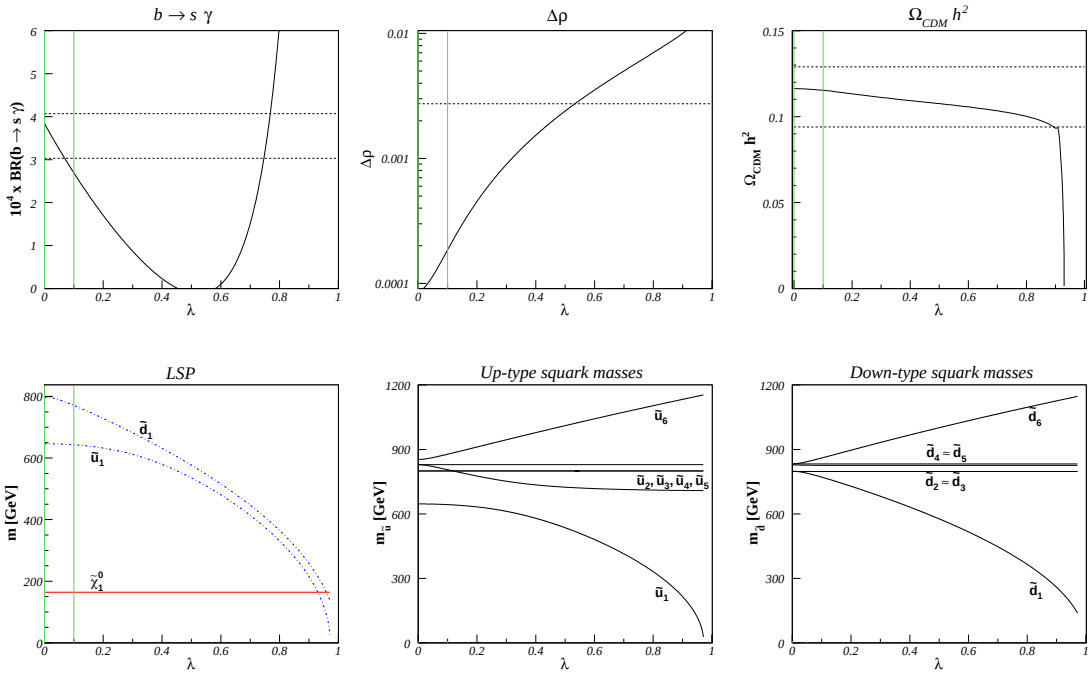

Figure 2.6: Same as Fig. 2.5 for our benchmark scenario B.

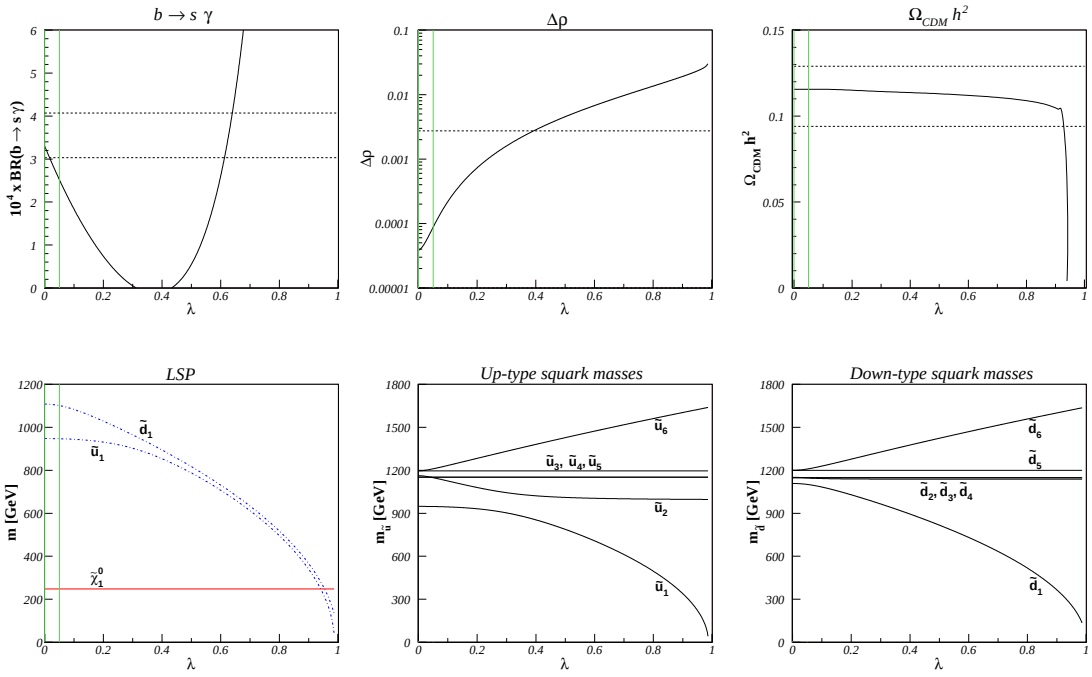

Figure 2.7: Same as Fig. 2.5 for our benchmark scenario C.

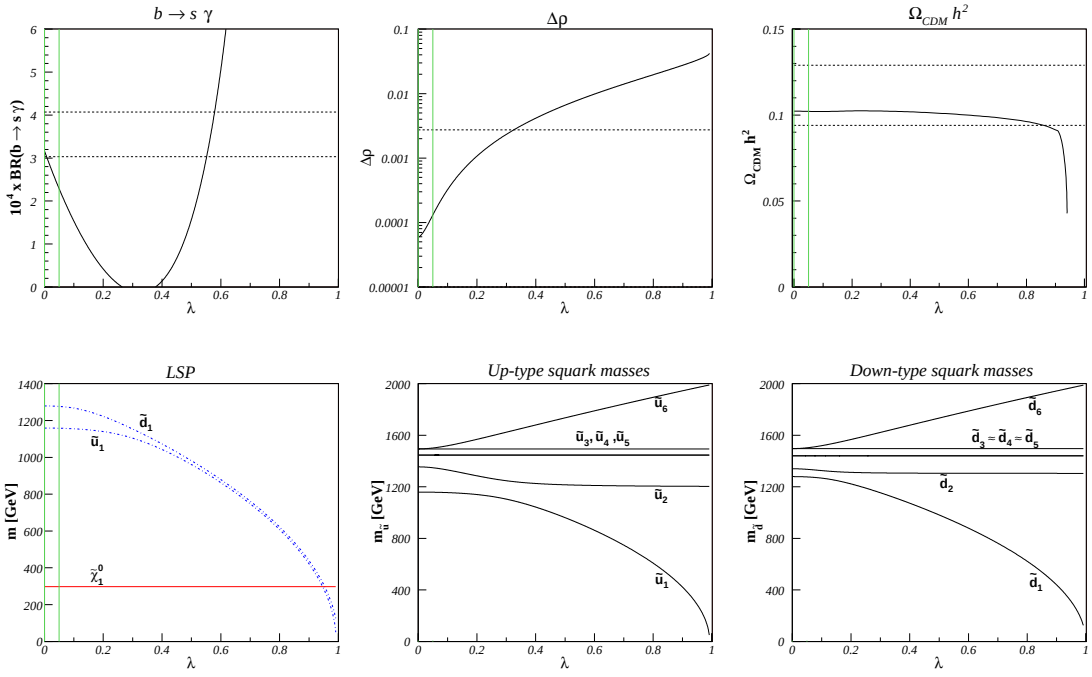

Figure 2.8: Same as Fig. 2.5 for our benchmark scenario D.

$\lambda_{\rm LL}$. The horizontal dashed lines indicate the favoured region at 2σ and exhibit two allowed intervals, one close to $\lambda_{\rm LL} = 0$ (green line), the second at higher values of $\lambda_{\rm LL} \leq 0.5$. The latter is, however, disfavoured by $B \to X_s\mu^+\mu^-$ data constraining the sign of the $b \to s\gamma$ amplitude to be the same as in the Standard Model [96]. We therefore limit ourselves to the regions in the vicinity of (constrained) minimal flavour violation, i.e. $\lambda_{\rm LL} \leq 0.05$ for the points A, C, and D, and $\lambda_{\rm LL} \leq 0.1$ for the point B.

The electroweak precision observable $\Delta\rho$ is shown in the second diagrams of Figs. 2.5 – 2.8 for our four benchmark scenarios. Again, the horizontal band corresponds to the experimentally allowed range, for which only the upper bound is visible. The self-energies diagrams of the electroweak gauge bosons depend strongly on the helicities, flavours, and mass eigenvalues of the squarks in the loop. However, the sufficiently small SUSY masses in our scenarios combined with the rather large experimental error still allow for relatively large values of $\lambda_{\rm LL} \leq 0.57$, 0.52, 0.38, and 0.32 for the benchmark points A, B, C, and D, respectively. As mentioned above, $\Delta\rho$ constrains SUSY models in cMFV only for $m_0 \gtrsim 2000$ GeV and $m_{1/2} \gtrsim 1500$ GeV.

In the next diagrams of Figs. 2.5 – 2.8, we show the cold dark matter relic density $\Omega_{\rm CDM}h^2$ as a function of the NMFV parameter $\lambda_{\rm LL}$. Here, only the lower bound of the indicated favoured range of Eq. (2.7) is relevant, as the relic density falls with increasing $\lambda_{\rm LL}$. In our model A, the lightest neutralino has a sizable higgsino component, so that squark exchanges contribute significantly to its annihilation cross section. Since the squark masses are generally larger in our models B, C, and D, there is less sensitivity of $\Omega_{\rm CDM}h^2$ to the NMFV parameter, except for very large $\lambda_{\rm LL} \leq 1$.

This rapid fall-off of the relic density for very large $\lambda_{\rm LL}$, can be understood by looking at the resulting lightest up- and down-type squark mass eigenvalues, as shown in the fourth diagrams of Fig. 2.5 – 2.8. For higher values of $\lambda_{\rm LL}$ the off-diagonal elements of the squared squark mass matrices get more important, and in consequence the mass splitting between lightest and heaviest up- and down-type squarks increases. As a further consequence, the lightest squark mass eigenvalue approaches and finally falls below the mass of the lightest neutralino. Coannihilation processes and light squark propagators then lead to a rapidly falling dark matter relic density and finally to the case of a squark LSP, that is cosmologically excluded.

An interesting phenomenon of level reordering between neighbouring states can be observed in the remaining diagrams of Fig. 2.5 – 2.8 for the two lowest mass eigenvalues of up- and down-type squarks. With increasing $\lambda_{\rm LL}$ the mass splitting between the lightest and heaviest mass eigenstates gets larger, while the intermediate squark masses are practically degenerate and insensitive to $\lambda_{\rm LL}$. For up-type squarks, it is first the second-lowest mass that decreases up to intermediate values of $\lambda_{\rm LL} \sim 0.2 - 0.5$ while the lowest mass is constant, and only at this point the second-lowest mass becomes constant and the lowest squark mass starts to decrease further with $\lambda_{\rm LL}$. These "avoided crossings" are a common phenomenon for Hermitian matrices, that depend continuously on one single real parameter. At the point where the two levels should cross, the corresponding squark eigenstates mix and change character. For our scenario C, the phenomenon occurs even a second time with an additional avoided crossing between the states $\tilde{u}_2$ and $\tilde{u}_3$ at $\lambda_{\rm LL} \simeq 0.05$. For scenario B, this takes place at $\lambda_{\rm LL} \simeq 0.1$ and there is even another crossing at $\lambda_{\rm LL} \simeq 0.02$. For down-type squarks, the level reordering phenomenon is not so pronounced.

2.4 GMSB Scenarios and Non-Minimal Flavour Violation

In contrast to the cMSSM or mSUGRA model, where flavour violation naturally arises from the fact that Supersymmetry breaking is mediated by gravity, flavour mixing is naturally suppressed in the minimal gauge mediation scenarios, since the gauge interactions are flavour-blind. However, it has been shown that flavour breaking terms can reappear at the electroweak scale in models beyond the minimal one [42, 97, 98]. For squarks, flavour violation can then arise in the left-left and the right-right chiral sectors. In this Section, we discuss the possibility of non-minimal flavour violation induced through the possible mixing of messenger and matter fields [98]. We show that this is an interesting possibility to relax the stringent electroweak precision constraints, that virtually exclude the minimal GMSB scenario.

2.4.1 Scans of the Minimal GMSB Parameter Space

We first impose the experimental limits discussed in Sec. 2.1 at the 2σ confidence level on the minimal gauge mediated SUSY breaking (GMSB) model with five free parameters Λ, $M_{\rm mes}$, $N_{\rm mes}$, $\tan\beta$, and $\mathrm{sgn}(\mu)$ at the GUT scale. A further free parameter is the gravitino mass $m_{\tilde{G}}$ at the weak scale, that will be discussed later in connection with the cosmological constraints. The physical mass spectrum at the electroweak scale is again computed using the combination of `SPheno 2.2.3` and `FeynHiggs 2.6.4` as described in Sec. 2.3. Since we assume here constrained minimal flavour violation (cMFV), all off-diagonal entries $\lambda_{ij}^{qq'}$ of the squared squark mass matrices are set to zero. For the numerical values of the Standard Model input parameters, see App. B.

In Fig. 2.9 we show typical scans of the minimal GMSB parameter space in Λ and $M_{\rm mes}$ for $\mu > 0$ and different values of $N_{\rm mes}$ (1 and 3) and $\tan\beta$ (15, 30, and 50). The six panels reveal that these scenarios are strongly disfavoured by the measurements of the $b \to s\gamma$ branching ratio. In particular, the Snowmass Points [92] SPS 7 ($\Lambda = 40$ TeV, $M_{\rm mes} = 80$ TeV, $\tan\beta = 15$, $\mu > 0$, and $N_{\rm mes} = 3$) and SPS 8 ($\Lambda = 100$ TeV, $M_{\rm mes} = 200$ TeV, $\tan\beta = 15$, $\mu > 0$, and $N_{\rm mes} = 1$) lead to values of $\mathrm{BR}(b \to s\gamma) = 4.86 \cdot 10^{-4}$ and $4.57 \cdot 10^{-4}$, which are excluded at the 5σ and 4σ level, respectively, even if both of these points lie well within 1σ of the experimentally allowed range for the anomalous magnetic moment of the muon, with $a_\mu^{\rm SUSY} = 22.8 \cdot 10^{-10}$ and $a_\mu^{\rm SUSY} = 16.3 \cdot 10^{-10}$.

Recently, a detailed study of electroweak precision observables, including scenarios with minimal GMSB, has been published [99]. Scanning also over $\tan\beta$ and allowing for higher values of $N_{\rm mes} \leq 8$, the authors show that experimentally favoured scenarios can be achieved at low messenger scales, which, however, implies a certain amount of fine tuning at the electroweak scale, especially in the Higgs sector. Note that for $N_{\rm mes} \gtrsim 8$ problems with perturbativity of the gauge interactions arise at very high scales [42].

2.4.2 GMSB Models with Non-Minimal Flavour Violation

Minimal gauge-mediated Supersymmetry breaking is known to suppress flavour-changing neutral currents (FCNC) as suggested by measurements and thus avoid the so-called "flavour-problem" naturally arising in models where Supersymmetry breaking is mediated by gravity. Although the gauge interactions are flavour-blind, it has been shown that considering models beyond the minimal GMSB can reintroduce flavour breaking terms at the electroweak scale in the slepton and squark sectors. For example, for very high messenger scales $M_{\rm mes} \sim 10^{15}$ GeV

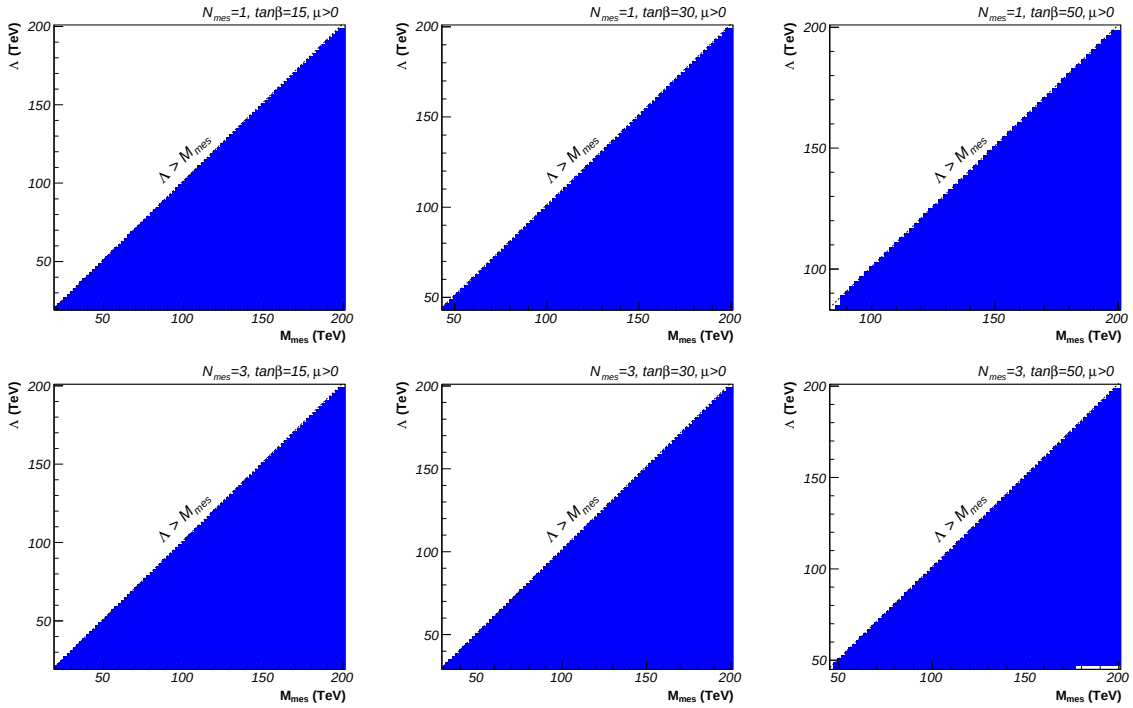

Figure 2.9: The Λ-$M_{\rm mes}$ planes for $\tan\beta = 15$, 30, and 50, $N_{\rm mes} = 1$ and 3, $\mu > 0$. We show the $b \to s\gamma$ excluded (dark blue) regions in constrained minimal flavour violation (cMFV). The region $\Lambda > M_{\rm mes}$ above the diagonal is theoretically excluded due to non-physical solutions to the renormalization group equations.

gravity is no longer negligible with respect to the flavour blind gauge interactions [42]. In consequence, flavour violating terms are reintroduced through gravity mediating as in mSUGRA models. However, scenarios with that high messenger scales are rather unattractive from a phenomenological point of view due to the resulting very high sparticle masses. Second, flavour violation can be induced from heavy right-handed neutrinos participating in leptogenesis [97]. If these are lighter than the messenger scale, flavour off-diagonal mass terms are introduced into the slepton mass matrices. A third possibility might be to consider broken messenger number invariance, that implies that the lightest messenger is not stable, but introduces flavour violating terms in the Lagrangian at the weak scale [42]. A disadvantage of this model is that the now unstable lightest messenger may not be a viable candidate for cold dark matter, if the too light gravitino cannot account for the observed relic abundance.

For our study, we focus on the model proposed in Ref. [98], based on the introduction of a mixing between messenger and matter fields. In the case of fundamental messenger multiplets, belonging to **5** and $\overline{\mathbf{5}}$ representations of $SU(5)$, the messengers carry the quantum numbers of left-handed leptons and right-handed down-type quarks. In consequence, flavour violation is introduced into the chiral sectors of right-handed sleptons and left-handed up- and down-type squarks. In our analysis of squark flavour violation, this corresponds to the case already discussed for minimal supergravity including a variation of the parameter $\lambda_{\rm LL}$, while $\lambda_{\rm RR}$ is set to zero. Also investigated is an alternative model with antisymmetric messenger multiplets, belonging to **10** and $\overline{\mathbf{10}}$ representations. In this case, the messengers share quantum numbers

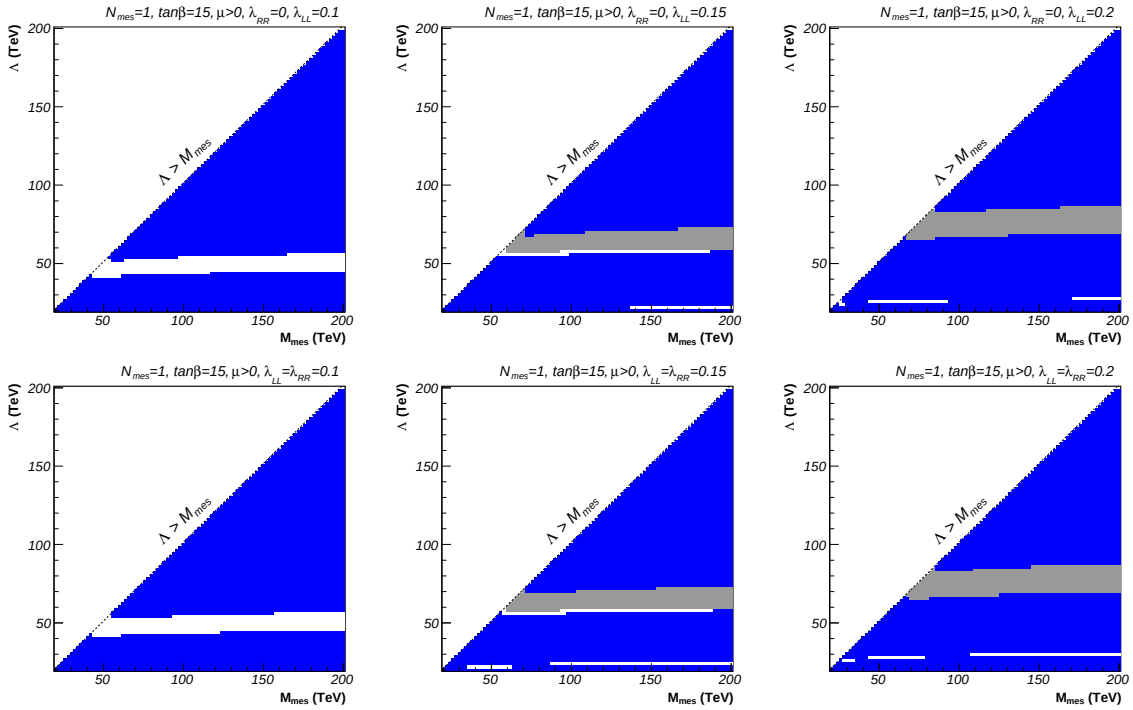

Figure 2.10: The Λ-$M_{\rm mes}$ planes for $\tan\beta = 15$, $N_{\rm mes} = 1$, and $\mu > 0$. We show a_μ favoured (grey) and $b \to s\gamma$ excluded (dark blue) regions in non-minimal flavour violation (NMFV) with squark mixing between the second and third generations in the left-left sector ($\lambda_{\rm RR} = 0, \lambda_{\rm LL} > 0$) or both the left-left and right-right sector ($\lambda_{\rm LL} = \lambda_{\rm RR} > 0$). The region $\Lambda > M_{\rm mes}$ above the diagonal is theoretically excluded due to non-physical solutions of the renormalization group equations.

with right-handed leptons, left-handed up- and down-type type quarks, and right-handed up-type quarks, leading to flavour mixing for left-handed sleptons as well as for both left- and right-handed up- and down-type squarks. Contrary to minimal supergravity, GMSB allows thus for important flavour mixing in the right-right chiral sector. Note that, in this antisymmetric scenario, flavour mixing in the sector of right-handed down-type squarks may be parametrized independently of the other squarks. In our analysis however, we use for simplicity the same flavour violation parameter $\lambda_{\rm LL} = \lambda_{\rm RR}$ for both chiral sectors. This is also motivated by $SU(2)$ gauge invariance not allowing a large difference between them. In both scenarios flavour violation is thus completely governed by the parameter $\lambda_{\rm LL}$.

2.4.3 Benchmark Points for GMSB with Flavour Violation

We now re-investigate the low-energy and electroweak precision constraints including non-minimal flavour violation as discussed above. Allowed regions for the parameters Λ, $M_{\rm mes}$, $N_{\rm mes}$, $\tan\beta$, $\mathrm{sgn}(\mu)$, $\lambda_{\rm LL}$, and $\lambda_{\rm RR}$ are obtained by explicitly imposing the constraints from $b \to s\gamma$, $\Delta\rho$, and a_μ, that are sensitive to flavour violating terms. The renormalization group running is again performed with `SPheno 2.2.3`. The flavour violating terms $\lambda_{\rm LL}$ and $\lambda_{\rm RR}$ are included in the squark mass matrices at the electroweak scale before computing the mass spectrum and the low-energy and electroweak precision observables with `FeynHiggs 2.6.4`.

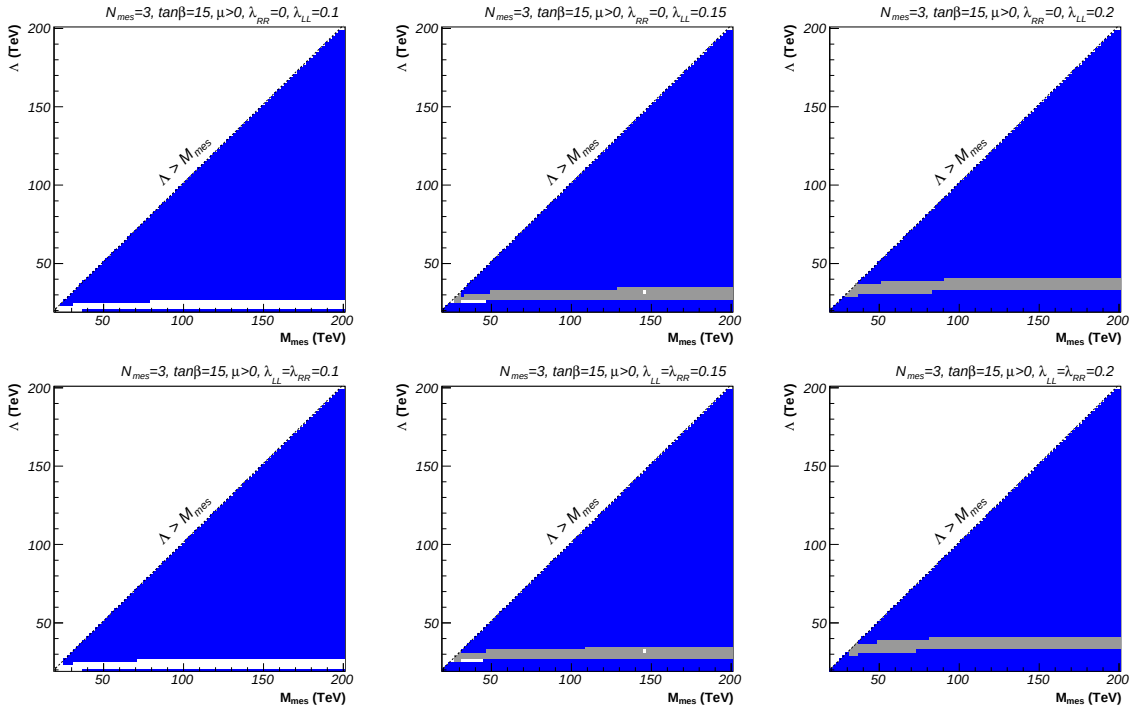

Figure 2.11: Same as Fig. 2.10 for $N_{\rm mes} = 3$, $\tan\beta = 15$, and $\mu > 0$.

In Figs. 2.10 – 2.15 we show scans of the Λ-$M_{\rm mes}$ plane for $\mu > 0$ and the same values $N_{\rm mes} = 1,\ 3$ and $\tan\beta = 15,\ 30,\ 50$ as in Sec. 2.4.1. In each figure, the upper panels correspond to the case of matter mixing with fundamental messengers and flavour mixing only in the left-left chiral sector ($\lambda_{\rm RR} = 0$), while the lower panels represent the case of antisymmetric messengers leading to flavour mixing in the left-left and right-right chiral squark sectors ($\lambda_{\rm RR} = \lambda_{\rm LL}$). For the same reasons as in mSUGRA scenarios, the region favoured by the anomalous magnetic moment of the muon a_μ is quite insensitive to variations of the parameter $\lambda_{\rm LL}$. As expected, the region excluded by the inclusive branching ration BR($b \to s\gamma$) depends strongly on flavour mixing. It is, in particular, also affected by the mixing scenario, inducing a slight but visible difference in the excluded regions. The constraint coming from $\Delta\rho$ does not play a role for the moderate sparticle masses corresponding to our region of interest, so that the excluded regions are not shown. It becomes clear that, if we allow for flavour mixing between the second and third generation squarks, windows in the parameter space both favoured by a_μ and not excluded by the stringent constraint from $b \to s\gamma$ make their appearance for small and moderate SUSY masses.

Within these regions, we propose six benchmark scenarios permitting non-minimal flavour violation and not yielding too high sparticle masses ("collider-friendly"), so that possible SUSY signals should be observable at present and/or future hadron colliders. Our choices are presented in Tab. 2.4, labeled starting at the point E due to our four benchmark proposals for mSUGRA scenarios including non-minimal flavour violation in Sec. 2.2. Note that, in contrast to the mSUGRA case, these scenarios are not valid in constrained minimal flavour violation ($\lambda_{\rm LL} = \lambda_{\rm RR} = 0$), so that we indicate the valid range for the flavour mixing parameters. We have also checked that these scenarios are cosmologically allowed, see Sec. 2.4.5.

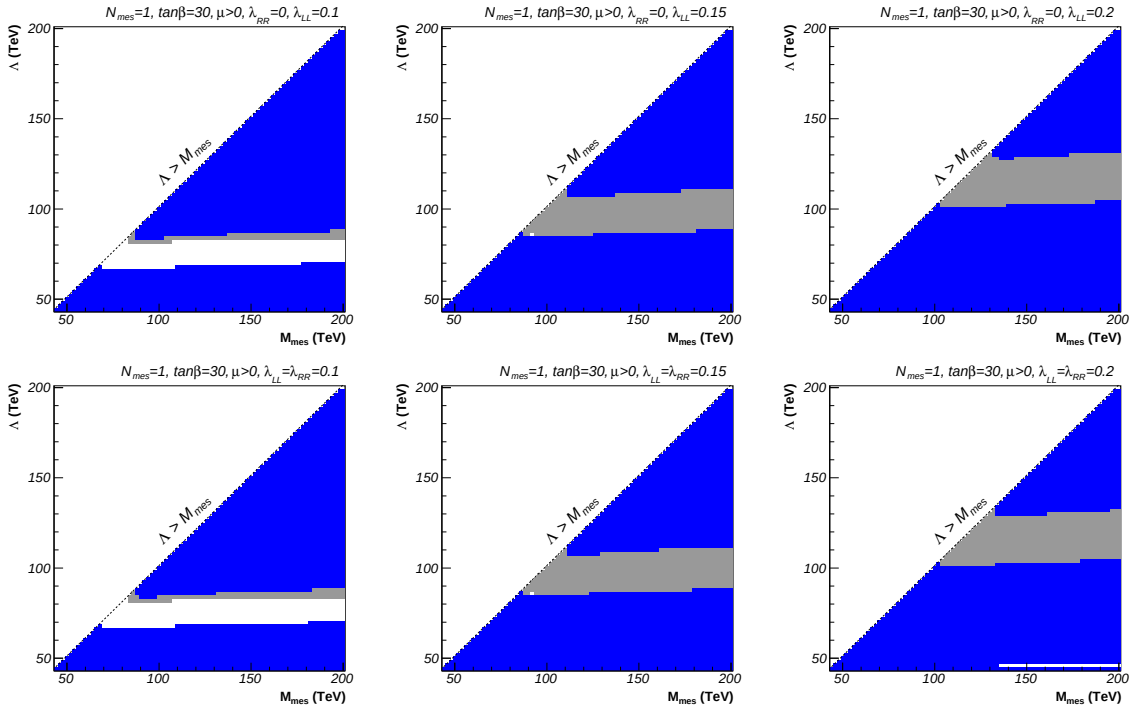

Figure 2.12: Same as Fig. 2.10 for $N_{\rm mes} = 1$, $\tan\beta = 30$, and $\mu > 0$.

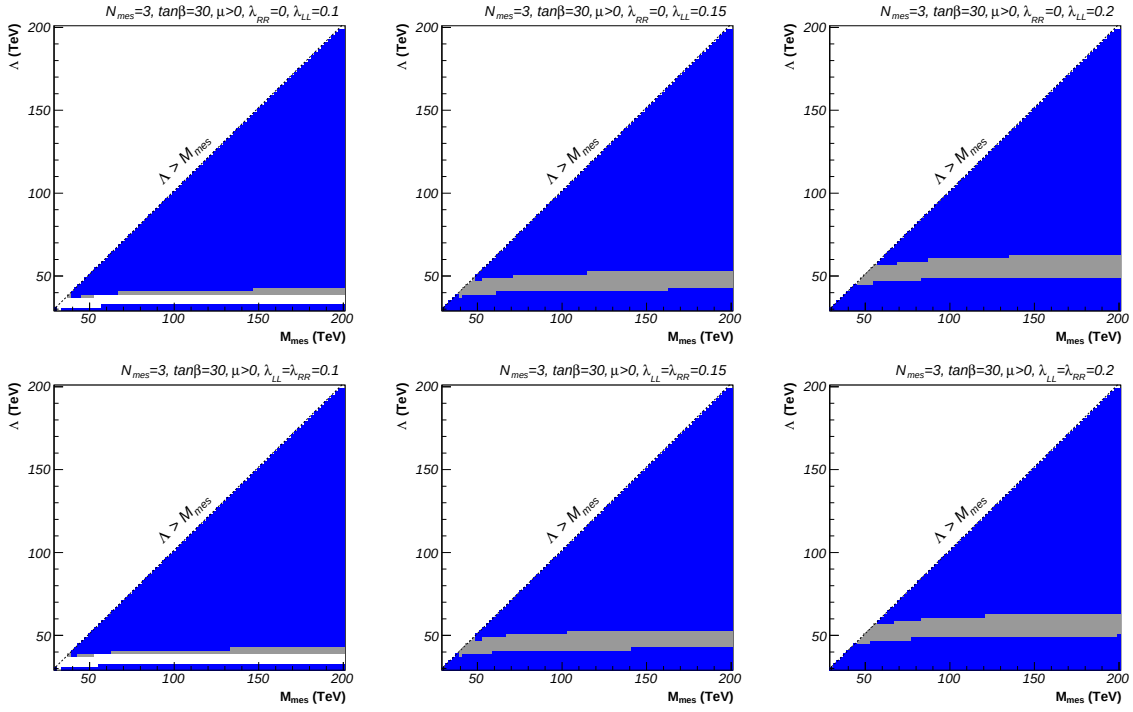

Figure 2.13: Same as Fig. 2.10 for $N_{\rm mes} = 3$, $\tan\beta = 30$, and $\mu > 0$.

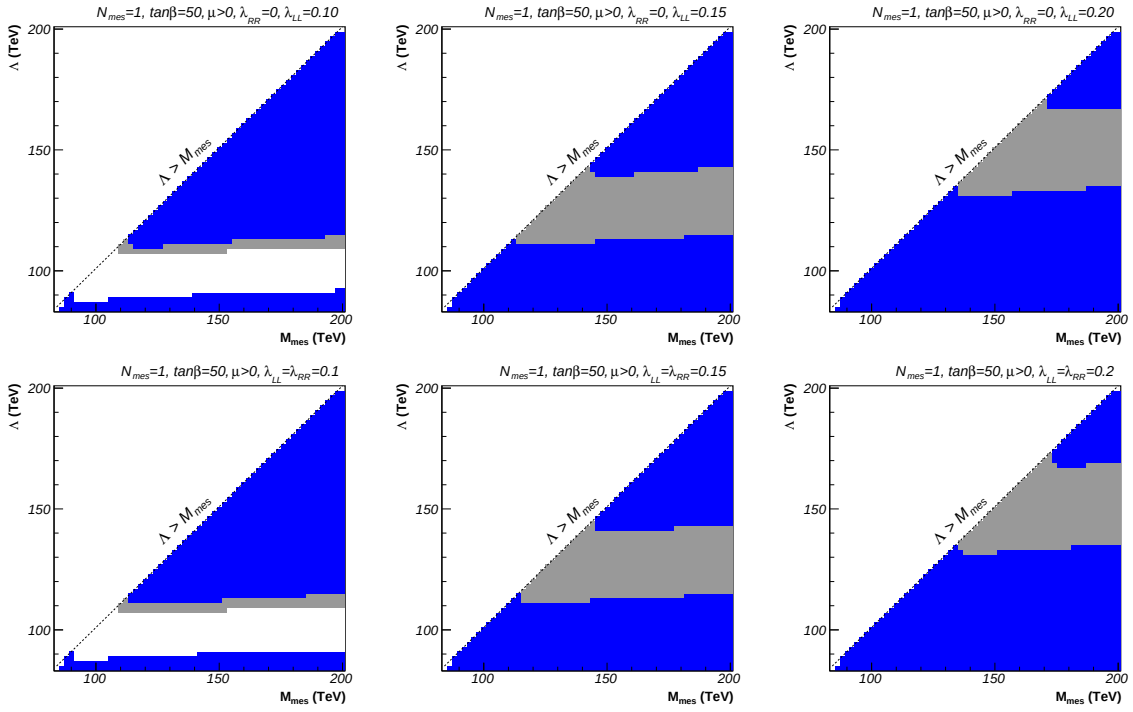

Figure 2.14: Same as Fig. 2.10 for $N_{\rm mes} = 1$, $\tan\beta = 50$, and $\mu > 0$.

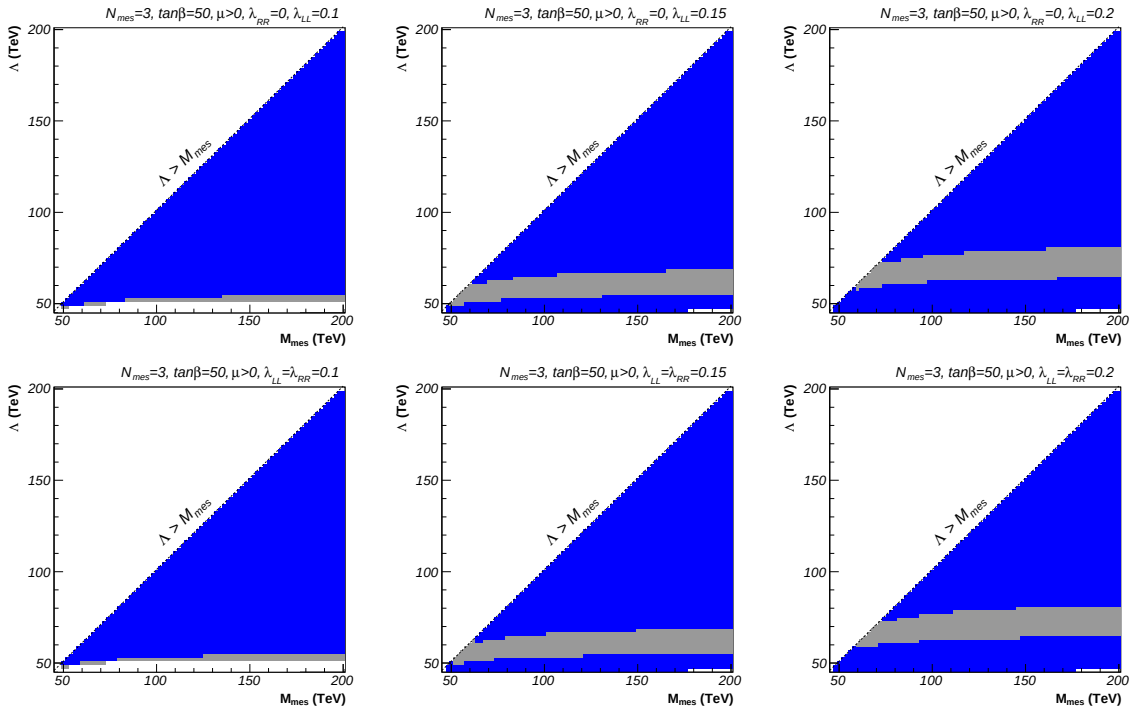

Figure 2.15: Same as Fig. 2.10 for $N_{\rm mes} = 3$, $\tan\beta = 50$, and $\mu > 0$.

	Λ	$M_{\rm mes}$	$N_{\rm mes}$	$\tan\beta$	sgn(μ)	$\lambda_{\rm LL}$	NLSP	SPS
E	65 TeV	90 TeV	1	15	+	[0.14, 0.20]	$\tilde{\chi}_1^0$	8
F	30 TeV	80 TeV	3	15	+	[0.12, 0.18]	$\tilde{\tau}_1$	7
G	100 TeV	110 TeV	1	30	+	[0.14, 0.20]	$\tilde{\tau}_1$	–
H	45 TeV	100 TeV	3	30	+	[0.12, 0.18]	$\tilde{\tau}_1$	–
I	130 TeV	140 TeV	1	50	+	[0.14, 0.20]	$\tilde{\tau}_1$	–
J	60 TeV	100 TeV	3	50	+	[0.14, 0.20]	$\tilde{\tau}_1$	–

Table 2.4: GMSB benchmark points allowing for non-minimal flavour violation. We also indicate the allowed range for the NMFV-parameter $\lambda_{\rm LL}$, the nature of the NLSP, and the closest SPS benchmark point.

Starting with $\tan\beta = 15$ and $N_{\rm mes} = 1$ (see Fig. 2.10), we choose our benchmark point E in the region favoured by the electroweak precision constraints corresponding to rather light SUSY particles. As for any GMSB scenario, the gravitino is the lightest SUSY particle (LSP). The next-to-lightest SUSY particle (NLSP) is the lightest neutralino with $m_{\tilde{\chi}_1^0} = 95.4$ GeV, but the three lightest charged sleptons are very close with similar masses around 100 GeV. The other sleptons, sneutrinos, and gauginos have moderate masses of about 150 – 300 GeV, while the squarks and gluino are quite heavy with masses lying in the range of 700 – 800 GeV. They are much lighter than those corresponding to SPS 8 with its large values of Λ and $M_{\rm mes}$, but well above the experimental limits obtained from direct searches assuming cMFV (see Tab. 1.1), and are experimentally accessible at the LHC.

The point F (see Fig. 2.11) differs only very little from the point SPS 7, with the Supersymmetry-breaking scale Λ shifted from 40 TeV to 30 TeV, so that it is no longer excluded by the most recent experimental values of BR($b \to s\gamma$). As for SPS 7, the three lightest sleptons have masses around 100 GeV, the lightest of them being the stau with $m_{\tilde{\tau}_1} = 90.7$ GeV. The other sleptons, sneutrinos, and gauginos are a bit heavier (120 – 200 GeV), and the squarks and gluino are rather heavy (600 – 700 GeV). The points G, H, I, and J (see Figs. 2.12 – 2.15) all have a stau NLSP with a mass between 99 and 160 GeV. The main difference in their spectra is the number and nature of the particles that are closest in mass to the NLSP. For the point G these are two sleptons and the lightest neutralino, whereas for the point H these are only two sleptons. The points I and J do not have any particles close to the NLSP in mass. For the four points G, H, I, and J, the other sleptons and gauginos are rather light (200 – 600 GeV), while the squarks and gluino are very heavy (1 – 1.5 TeV).

2.4.4 Dependence of Observables and Mass Eigenvalues on Flavour Violation

We now study in detail the constraints of the electroweak precision and low-energy observables on, as well as the mass spectra of the points E, F, G, H, I, and J. In the upper and lower left panels of Figs. 2.16 – 2.21 we show the branching ratio BR($b \to s\gamma$) and the observable $\Delta\rho$ as a function of the flavour mixing parameter $\lambda_{\rm LL}$ and including both flavour violation scenarios. As already mentioned, the leptonic observable a_μ depends very weakly (at the two-loop level only) on the squarks. In consequence, we find values of a_μ independent of $\lambda_{\rm LL}$ for our six benchmark scenarios, which are $a_\mu^{\rm SUSY} = 37.7 \cdot 10^{-10}$, $41.3 \cdot 10^{-10}$, $31.4 \cdot 10^{-10}$, $36.6 \cdot 10^{-10}$, $31.8 \cdot 10^{-10}$, and $34.2 \cdot 10^{-10}$ for the points E, F, G, H, I, and J, respectively.

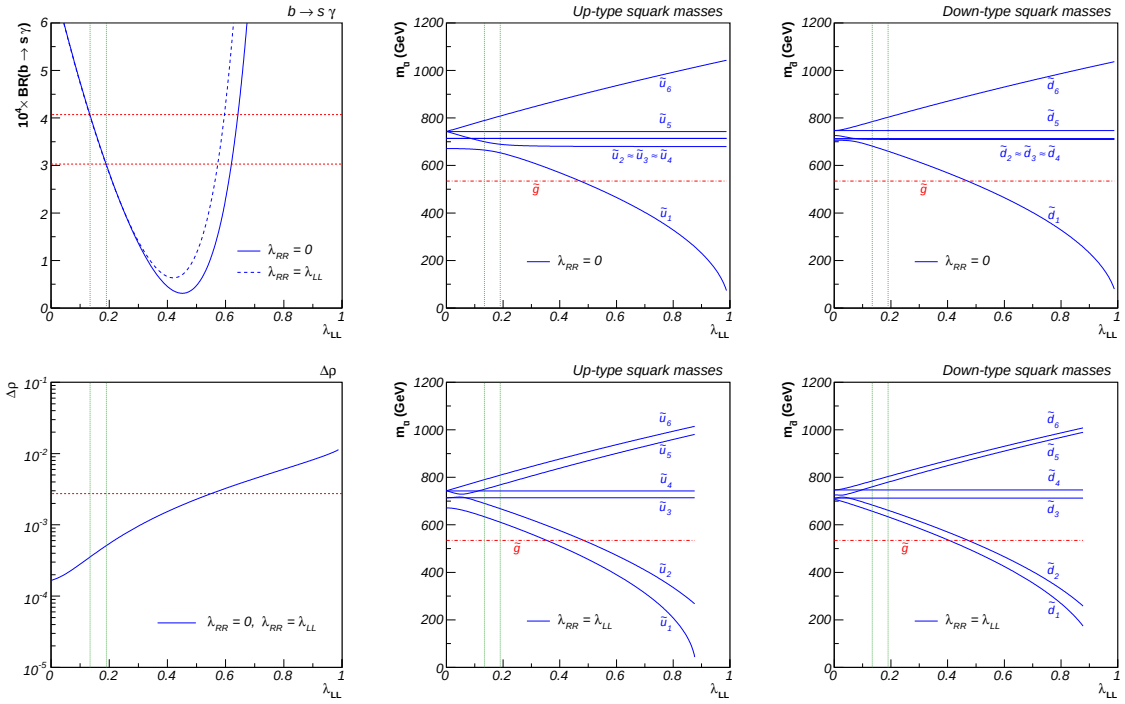

Figure 2.16: Dependence of the precision variables BR($b \to s\gamma$) and $\Delta\rho$, as well as the up- and down-type squark masses on the NMFV-parameter $\lambda_{\rm LL}$ for flavour mixing in the left-left ($\lambda_{\rm RR} = 0$, full) or both in the left-left and right-right ($\lambda_{\rm RR} = \lambda_{\rm LL}$, dashed) chiral squark sectors for our benchmark scenario E. The red dashed bands indicate the experimentally favoured regions at 2σ, and the vertical red dashed lines correspond to the allowed range for $\lambda_{\rm LL}$ with respect to the most stringent $b \to s\gamma$ constraint.

These values lie well within 2σ of the experimentally favoured range of Eq. (2.5), and even within 1σ for the points E, G, H, I, and J. For the inclusive branching ratio BR($b \to s\gamma$), the experimentally allowed range within 2σ is indicated by two horizontal dashed lines. The good agreement between the measurements and the two-loop SM prediction in combination with the strong dependence of the SUSY contribution on squark flavour mixing only leave two allowed narrow intervals for our flavour violation parameter, one being at relatively low values $\lambda_{\rm LL} \sim 0.15$, the second one at higher values of $\lambda_{\rm LL} \sim 0.5 - 0.7$. The latter is, as also in the mSUGRA case, disfavoured by $b \to s\mu^+\mu^-$ data [96]. The remaining interval is indicated by vertical dotted lines. Note that the difference between the two scenarios is small for the relevant values of $\lambda_{\rm LL} \lesssim 0.2$. Concerning the observable $\Delta\rho$, the difference between the two considered flavour mixing scenarios is not visible, so that only one curve is shown. Again, the horizontal line indicates the favoured range within 2σ, where only the upper limit is visible on our logarithmic scale. In contrast to BR($b \to s\gamma$), here the relatively large experimental errors allow for values of $\lambda_{\rm LL} \lesssim 0.3 - 0.6$, depending on the benchmark point. The vertical dashed lines indicate the allowed range for $\lambda_{\rm LL}$ with respect to the more stringent constraint coming from $b \to s\gamma$.

The difference between the two flavour violation scenarios becomes more obvious when we study the squark mass eigenvalues. The up- and down-type squark masses are shown as a function of the flavour mixing parameter $\lambda_{\rm LL}$ in the centre and right upper panels of

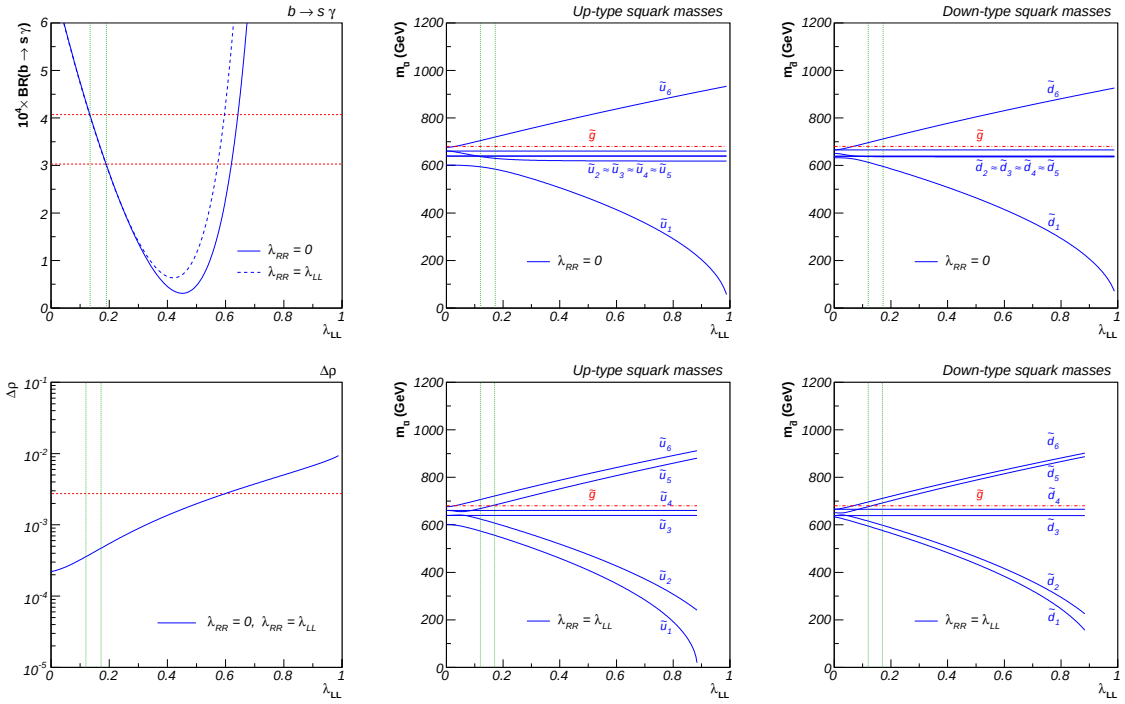

Figure 2.17: Same as Fig. 2.16 for our benchmark scenario F.

Figs. 2.16 – 2.21 for mixing with fundamental messengers ($\lambda_{\rm RR} = 0$) and in the centre and right lower panels for antisymmetric messengers ($\lambda_{\rm RR} = \lambda_{\rm LL}$). We observe here the same level reordering phenomenon between neighbouring states as already in the case of minimal supergravity, discussed in Sec. 2.3.2. With increasing flavour violation the mass splitting between the lightest and heaviest mass eigenstates becomes larger, while the intermediate squark masses are practically unchanged. At the points, where two levels should cross, we observe again the so-called "avoided crossings" already discussed for mSUGRA. Unfortunately, many "avoided crossings" lie below, but some also within the allowed ranges of the flavour violating parameter $\lambda_{\rm LL}$, indicated by green vertical lines for each of the six benchmark scenarios. The level reordering phenomenon is of similar importance for up-type and down-type squarks. Concerning the difference between our two implementations of flavour violation in the squark matrices, we observe an important splitting for only the lightest and heaviest eigenstates in the case of flavour mixing only in the left-left chiral sector. In contrast, for flavour violation in both the left-left and right-right chiral squark sectors, the two lightest and two heaviest mass eigenvalues give rise to important splitting, while only the remaining two masses are practically independent of $\lambda_{\rm LL}$. This is a direct consequence of the fact that we have introduced additional flavour mixing in two distinct sectors of the squark mass matrices and will influence the squark and gaugino production cross sections presented in Chap. 5. Note also that in the case of flavour mixing in only the left-left chiral sector, "avoided" level crossings occur among the $\tilde{q}_{1,2}$, $\tilde{q}_{3,4}$, and $\tilde{q}_{5,6}$ mass eigenstates, whereas in the case of flavour mixing in both the left-left and right-right chiral squark sectors, we rather observe the mass flips among the $\tilde{q}_{2,3}$ and $\tilde{q}_{4,5}$ mass eigenstates, respectively.

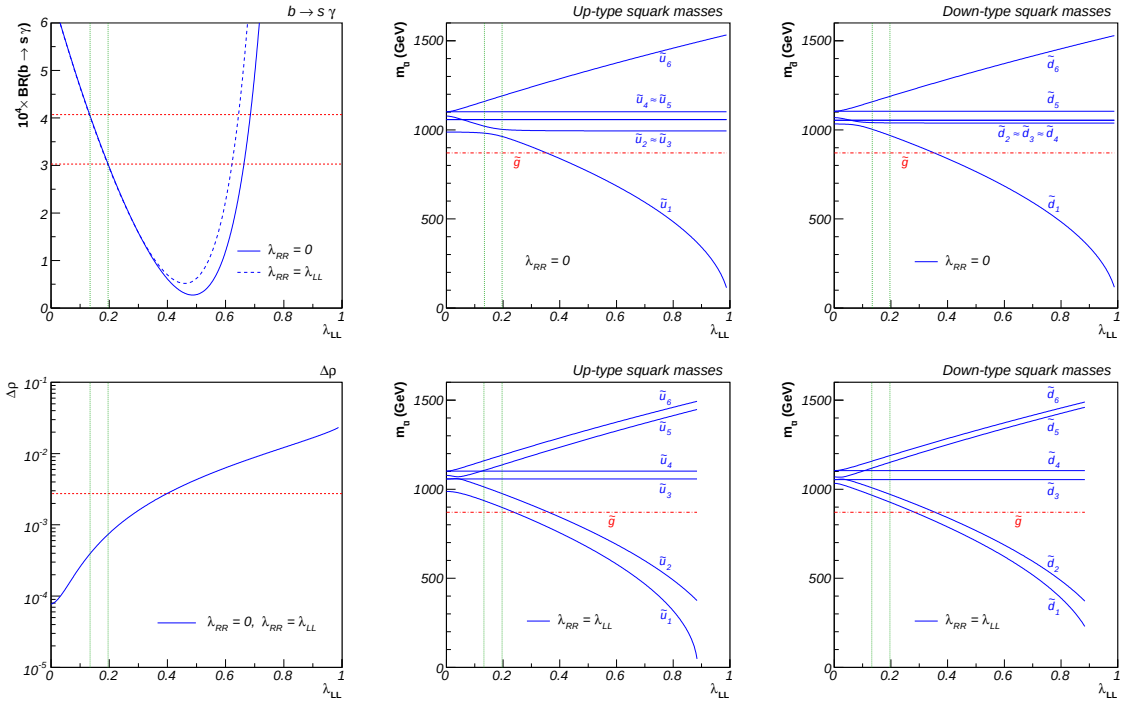

Figure 2.18: Same as Fig. 2.16 for our benchmark scenario G.

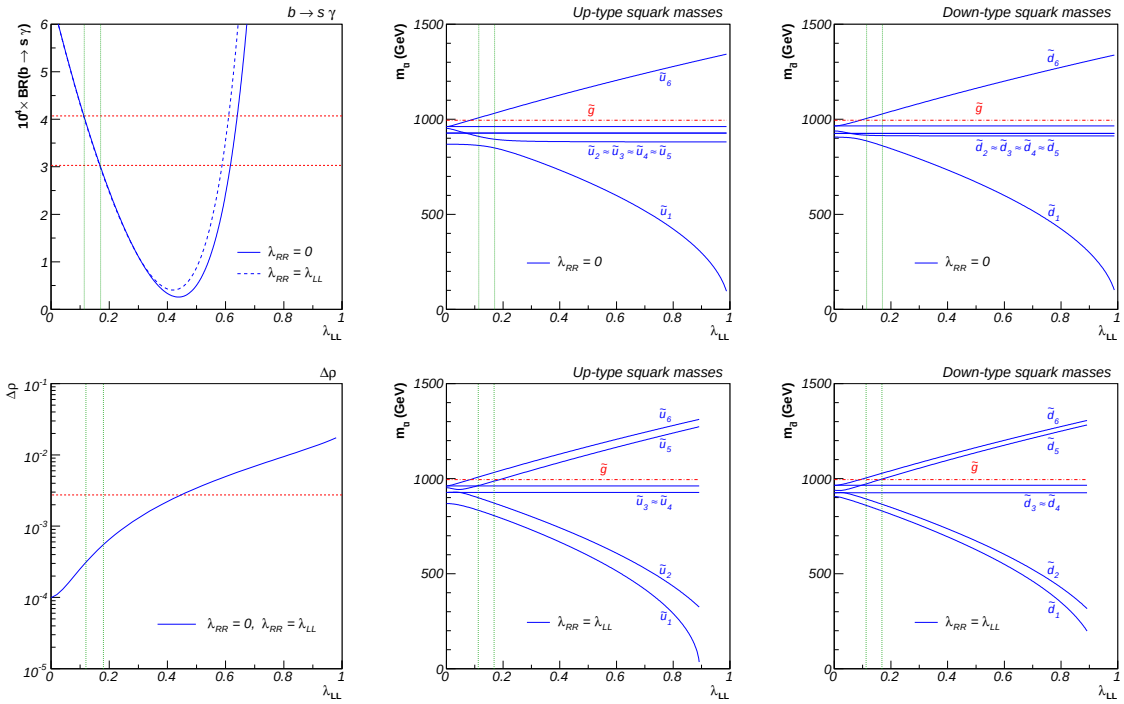

Figure 2.19: Same as Fig. 2.16 for our benchmark scenario H.

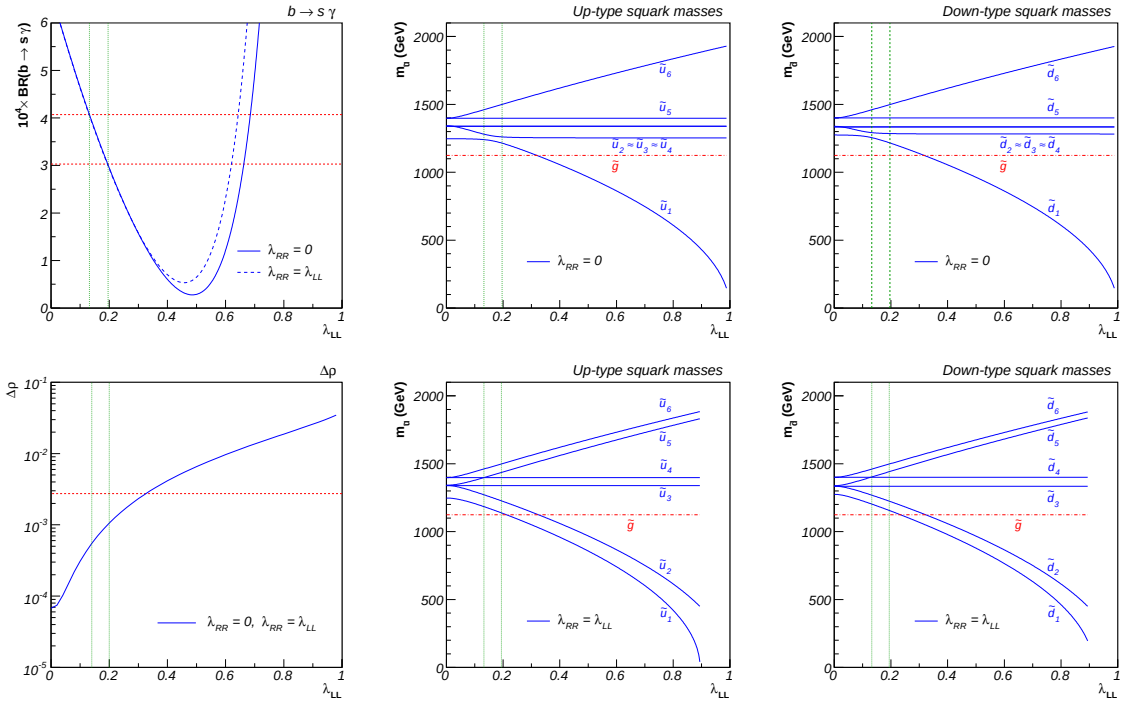

Figure 2.20: Same as Fig. 2.16 for our benchmark scenario I.

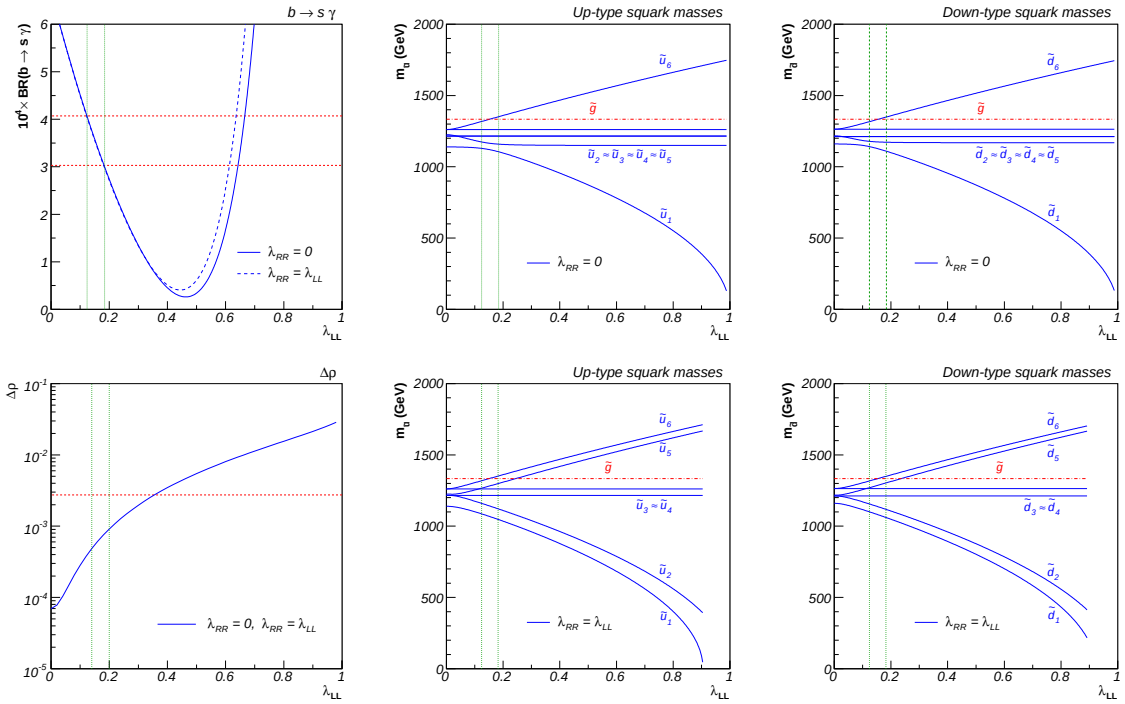

Figure 2.21: Same as Fig. 2.16 for our benchmark scenario J.

2.4.5 Cosmological Limits on the Gravitino Mass

To make sure that the chosen benchmark points do not lead to cosmologically disfavoured configurations, we determine the allowed regions for the gravitino mass $m_{\tilde{G}}$ with respect to the limits imposed by the relic abundance of cold dark matter in our Universe, the lifetime of the next-to-lightest SUSY particle (NLSP) before decaying into the gravitino, as well as the constraints on the reheating temperature T_{R} due to leptogenesis. We therefore compute the gravitino energy density $\Omega_{\tilde{G}}h^2$ in our Universe as described in Sec. 2.2.2, taking into account the contributions from thermal production in the early Universe and from NLSP decay. For each benchmark point, the relic density of the NLSP has been obtained with the public code `micrOMEGAs`. In Fig. 2.22 we compare the gravitino relic density computed in this way with the 2σ range of Eq. (2.7) as a function of the gravitino mass $m_{\tilde{G}}$ and the reheating temperature T_{R}. For each scenario, we also indicate the upper limit on the gravitino mass coming from the constraint on the NLSP lifetime, the cosmologically favoured range for the reheating temperature $T_{\mathrm{R}} \gtrsim 10^9$ GeV, the point where the gravitino mass would become heavier than the NLSP mass, the limit between warm (WDM) and cold (CDM) dark matter, as well as the gluino and NLSP masses entering the calculation.

Note that the contribution to $\Omega_{\tilde{G}}h^2$ from NLSP decay is only relevant for our point E with its neutralino NLSP and $\Omega^{\mathrm{th}}_{\mathrm{NLSP}}h^2 = 0.1275$. The fact that this value already lies within the WMAP favoured interval, opens an allowed band around $m_{\tilde{G}} \approx m_{\tilde{\chi}^0_1} = 95.4$ GeV, as can be seen in the first panel of Fig. 2.22. For the other points, the annihilation cross section of the stau NLSP is more important, so that the resulting relic NLSP density is quite low ($\Omega^{\mathrm{th}}_{\mathrm{NLSP}}h^2 \sim 0.003 - 0.012$) and its values lie well below the lower limit 0.094 of the WMAP 2σ range.

From the graphs in Fig. 2.22 it becomes clear that for the chosen "collider-friendly" benchmark points, we cannot simultaneously fulfill all the three more or less strict cosmological constraints. For instance, for a scenario featuring leptogenesis, i.e. having $T_{\mathrm{R}} > 10^9$ GeV, the lifetime of the next-to-lightest Supersymmetric particle (NLSP) would be too long for not spoiling the light element abundances. We therefore relax the less stringent constraint coming from leptogenesis and allow for a reheating temperature $T_{\mathrm{R}} < 10^9$ GeV. If we then impose the constraint due to the lifetime of the NLSP, our six benchmark scenarios all lead to an upper limit on the gravitino mass of $m_{\tilde{G}} \lesssim 10^{-1} - 1$ GeV. For simplicity, we propose the same value $m_{\tilde{G}} = 10^{-1}$ GeV for all points. This choice respects the limit due to the NLSP lifetime, allows for a relic gravitino density agreeing with current WMAP data, and this in combination with relatively high values of $T_{\mathrm{R}} \sim 10^7$ GeV for the reheating temperature.

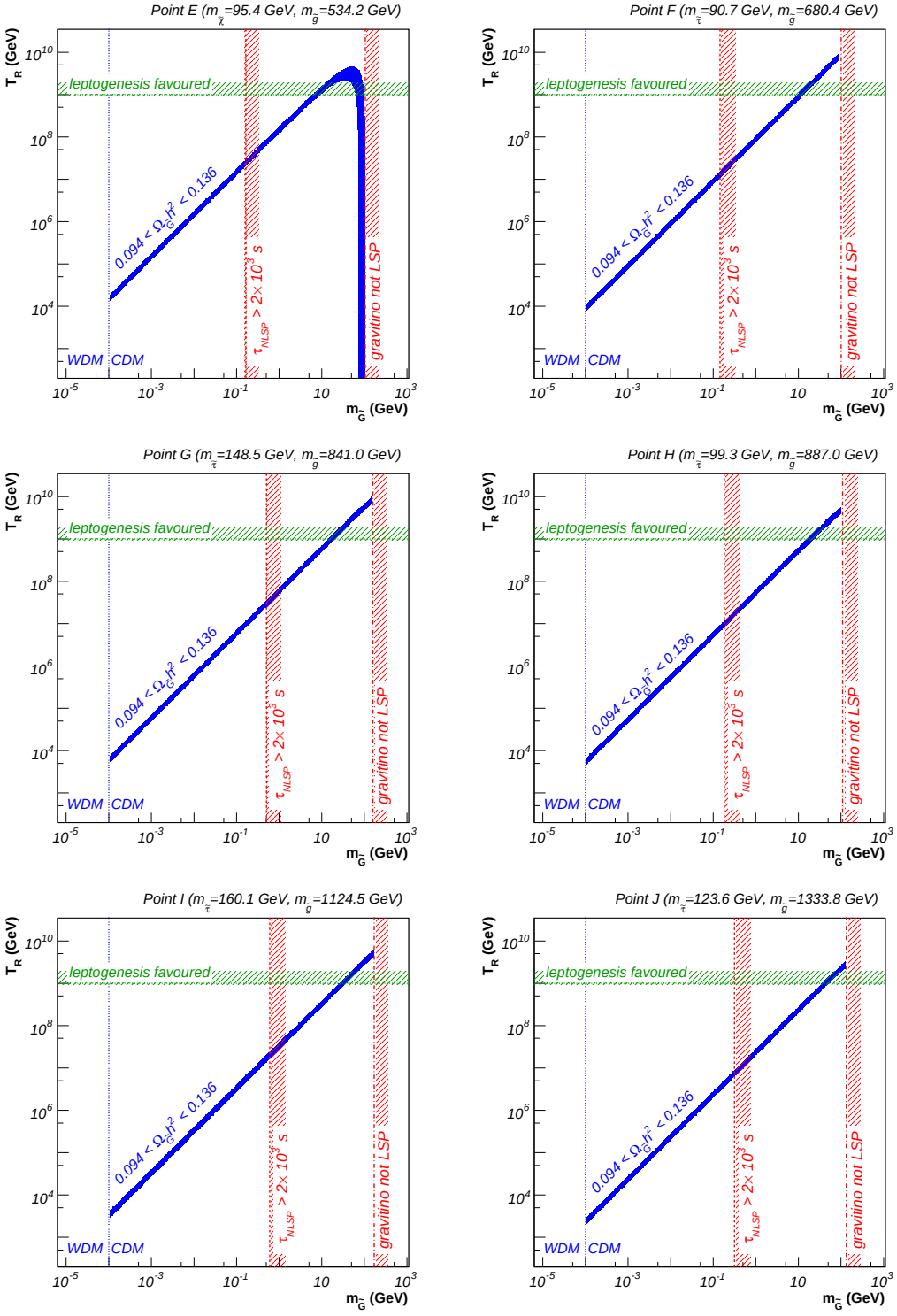

Figure 2.22: The cosmologically favoured regions in the $m_{\tilde{G}}$-T_{R} plane for our benchmark scenarios E, F, G, H, I, and J with respect to WMAP data (blue), the NLSP lifetime (vertical red line), and leptogenesis (horizontal green line).

Chapter 3

SUSY-QCD Corrections to Dark Matter Annihilation in the Higgs-Funnel

From a theoretical point of view, due to the large magnitude of the strong coupling constant, QCD and SUSY-QCD corrections are bound to affect the dark matter annihilation cross section into quarks in a significant way. They may even be enhanced logarithmically by kinematics or in certain regions of the parameter space. On the experimental side, new cosmological precision missions are to be launched in the near future. The `Planck` mission will improve the present measurements of the CMB anisotropies by the `COBE` and `WMAP` missions significantly and, in consequence, the cold dark matter relic density will be constrained to a narrower interval. We therefore also need more accurate theoretical predictions, which makes it necessary to include radiative corrections into the calculation of the annihilation cross section.

In this Chapter, we present the calculation of these corrections for neutralino pair annihilation into a bottom quark-antiquark pair through the s-channel exchange of a pseudoscalar Higgs boson A^0 [100]. This process dominates in the so-called "A-funnel" region of the minimal supergravity (mSUGRA) parameter space at large values of $\tan\beta$, which is theoretically favoured by the unification of Yukawa couplings in Grand Unified Theories (GUTs) suggesting that $\tan\beta$ should be of the order of the ratio between the top and bottom quark masses [101], $\tan\beta \simeq \frac{m_t}{m_b} \sim 40-45$. Supposing a WIMP mass of 50 – 70 GeV, this process has been claimed to be compatible with the gamma-ray excess observed in all sky directions by the `EGRET` satellite [102–104]. However, the corresponding scenarios may lead to antiproton overproduction, so that they would not be compatible with the observed antiproton flux [105].

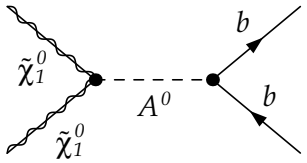

Figure 3.1: The leading order Feynman diagram of the neutralino annihilation process $\tilde{\chi}\tilde{\chi} \to A^0 \to b\bar{b}$.

3.1 Leading Order Cross Section

The Feynman diagram corresponding to the process of our interest is shown in Fig. 3.1. Denoting the neutralino and bottom quark velocities by

$$\beta_{\tilde{\chi}} \;=\; \frac{v}{2} \;=\; \sqrt{1-\frac{4m_{\tilde{\chi}}^2}{s}} \qquad \text{and} \qquad \beta_b \;=\; \sqrt{1-\frac{4m_b^2}{s}} \tag{3.1}$$

and the squared total center-of-momentum energy by s, the properly anti-symmetrized neutralino annihilation cross section can be written at leading order (LO) of perturbation theory as

$$\sigma_{\mathrm{LO}} v \;=\; \frac{1}{2}\frac{\beta_b}{8\pi s}\frac{N_C g^2 T_{A11}^2 h_{Abb}^2 s^2}{|s-m_A^2+im_A\Gamma_A|^2}. \tag{3.2}$$

It is proportional to the inverse of the flux factor sv, the integrated two-particle phase space $s\beta_b/(8\pi s)$, the number of quark colours $N_C = 3$ and the squares of the weak coupling constant g, a neutralino mixing factor

$$T_{Aij} \;=\; \frac{1}{2}\Big(\mathcal{N}_{2j} - \tan\theta_W \mathcal{N}_{1j}\Big)\Big(\mathcal{N}_{4i}\cos\beta - \mathcal{N}_{3i}\sin\beta\Big) + \{i \leftrightarrow j\}, \tag{3.3}$$

the bottom quark mass m_b and $\tan\beta$ through the Yukawa coupling

$$h_{Abb} \;=\; -\frac{g m_b \tan\beta}{2m_W}, \tag{3.4}$$

and the Higgs boson propagator.

As the neutralinos are supposed to be highly non-relativistic, it is common to express the annihilation cross section in terms of the relative neutralino velocity v. This can be done by expanding the squared center-of-momentum energy s in powers of v,

$$s \;\doteq\; 4m_{\tilde{\chi}}^2\left(1+\frac{v^2}{4}\right) + \mathcal{O}(v^4). \tag{3.5}$$

Inserting this result in the expression for the cross section, Eq. (3.2), we obtain its non-relativistic expansion

$$\sigma_{\mathrm{LO}} v \;\doteq\; a_{\mathrm{LO}} + b_{\mathrm{LO}} v^2 + \mathcal{O}(v^4) \tag{3.6}$$

with the coefficients

$$a_{\mathrm{LO}} \;=\; 2b_{\mathrm{LO}} \;=\; \frac{N_C g^2 T_{A11}^2 h_{Abb}^2}{4\pi m_{\tilde{\chi}}^2\left|4-\frac{m_A^2}{m_{\tilde{\chi}}^2}+\frac{im_A\Gamma_A}{m_{\tilde{\chi}}^2}\right|^2}\sqrt{1-\frac{m_b^2}{m_{\tilde{\chi}}^2}} \tag{3.7}$$

in agreement with the result given in Ref. [82].

In Fig. 3.2 we show the leading order cross section σ_{LO} for two typical minimal supergravity (mSUGRA) scenarios that lead to a dark matter relic density within the experimentally favoured range of Eq. (2.7). We have chosen the parameters $m_0 = 1200$ GeV, $m_{1/2} = 900$ GeV, $A_0 = 0$, and $\tan\beta = 44.5$ for $\mu < 0$, as well as $m_0 = 1200$ GeV, $m_{1/2} = 800$ GeV, $A_0 = 0$, and $\tan\beta = 54$ for $\mu > 0$. The annihilation cross section is presented as a function of the center-of-momentum energy $\sqrt{s}$. For reference, we also show the value for the lower values of $\tan\beta = 10$

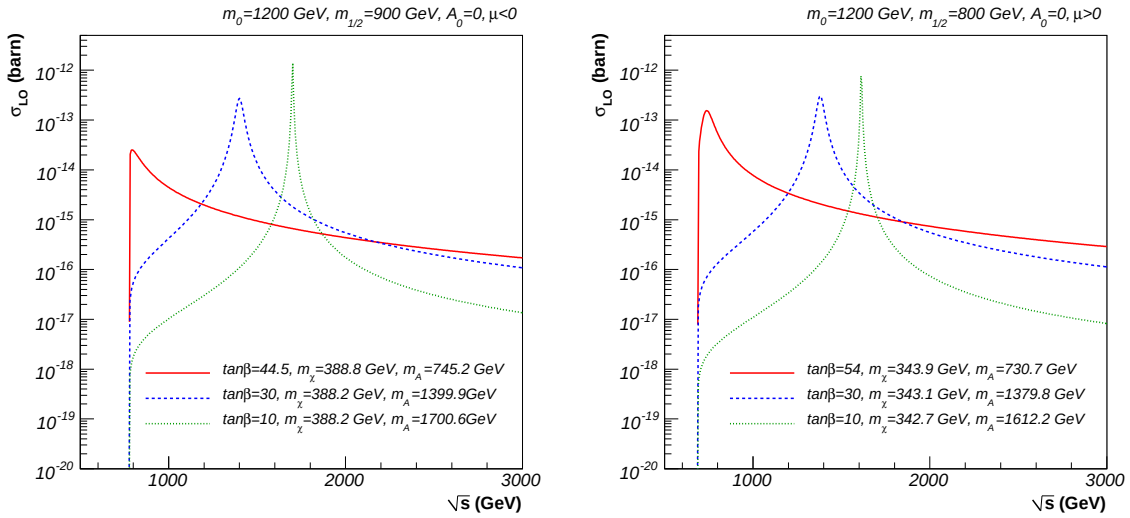

Figure 3.2: The leading order (LO) cross section of the neutralino annihilation process $\tilde{\chi}\tilde{\chi} \to A^0 \to b\bar{b}$ as a function of the center-of-momentum energy $\sqrt{s}$. The two scenarios lead at the respectively largest indicated value of $\tan\beta$ to a dark matter relic density agreeing with the experimental limits. The neutralino and pseudoscalar Higgs boson masses are indicated in GeV.

and 30. It is obvious that the decay width increases with $\tan\beta$. Due to the decreasing Higgs boson mass, the peak in the cross section approaches the threshold at $2m^2_{\tilde{\chi}^0_1} = m_{A^0}$ for higher values of $\tan\beta$. Note that, in the case of dark matter annihilation, only the region close to the threshold is relevant, higher energies being Boltzmann suppressed. Near the threshold, the annihilation cross section acquires values of the order of $\sigma_{\mathrm{LO}} \sim 10^{-13}$ barn.

3.2 QCD Corrections

The neutralino pair annihilation process $\tilde{\chi}\tilde{\chi} \to A^0 \to b\bar{b}$ receives $\mathcal{O}(\alpha_s)$ QCD corrections from the self-energy, vertex correction, and real gluon emission diagrams shown in Fig. 3.3. We apply dimensional regularization and on-shell renormalization for the virtual corrections, which cancels the ultraviolet (UV) singularities. The remaining infrared (IR) poles vanish by combining the virtual and the real emission contributions, which is done by applying the dipole subtraction method [106]. For a discussion of technical details see App. C. Using these standard methods, we obtain the $\mathcal{O}(\alpha_s)$ correction in the on-shell scheme

$$\begin{aligned}\Delta^{(1)}_{\mathrm{QCD}} \;=\; & \frac{\alpha_s(s)}{\pi} C_F \left[\frac{1+\beta_b^2}{\beta_b} \left(4\mathrm{Li}_2 \frac{1-\beta_b}{1+\beta_b} + 2\mathrm{Li}_2 \frac{\beta_b - 1}{1+\beta_b} - 3\log\frac{2}{1+\beta_b}\log\frac{1+\beta_b}{1-\beta_b} \right.\right. \\ & \left.\left. -2\log\beta_b \log\frac{1+\beta_b}{1-\beta_b} \right) - 3\log\frac{4}{1-\beta_b^2} - 4\log\beta_b \right. \\ & \left. + \frac{3}{8}(7-\beta_b^2) + \frac{1}{16\beta_b}(19 + 2\beta_b^2 + 3\beta_b^4)\log\frac{1+\beta_b}{1-\beta_b} \right], \end{aligned} \tag{3.8}$$

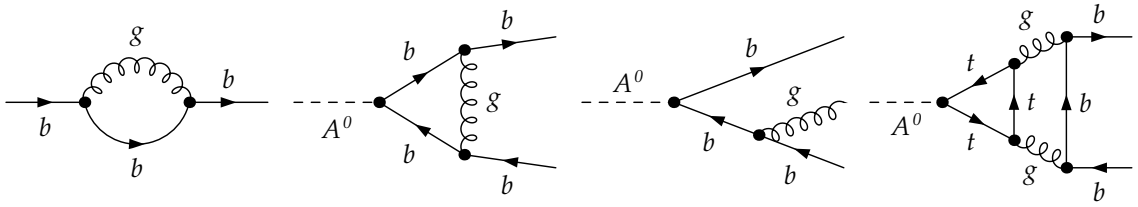

Figure 3.3: Diagrams for one-loop self-energy, vertex, and real QCD corrections contributing to the process $\tilde{\chi}\tilde{\chi} \to A^0 \to b\bar{b}$. We also show the top quark induced correction contributing at the two-loop level.

which agrees with the known result for pseudoscalar Higgs boson decays [107]. Writing $\Delta_{\rm QCD} = \sum_i \Delta^{(i)}_{\rm QCD}$, where the index i refers to the contribution of $\mathcal{O}(\alpha_s^i)$, Eq. (3.8) contributes to the total correction of the annihilation cross section

$$\sigma \;=\; \sigma_{\rm LO}\Big[1 + \Delta_{\rm QCD} + \Delta_{\rm top} + \Delta_{\rm SUSY}\Big] \tag{3.9}$$

and equivalently for the Higgs decay width

$$\Gamma_{A\to b\bar{b}} \;=\; \Gamma^{\rm LO}_{A\to b\bar{b}}\Big[1 + \Delta_{\rm QCD} + \Delta_{\rm top} + \Delta_{\rm SUSY}\Big], \tag{3.10}$$

which is valid in particular for low energies (LE). The contributions $\Delta^{(i)}_{\rm QCD}$ for $i \geq 2$, $\Delta_{\rm top}$ and $\Delta_{\rm SUSY}$ are discussed later in this and the next Section, respectively.

In the "high-energy" limit $\beta_b \to 1$, i.e. for $m_b^2 \ll s$, the correction in Eq. (3.8) develops a logarithmic mass singularity

$$\Delta^{(1)}_{\rm QCD} \;\simeq\; \frac{\alpha_s(s)}{\pi} C_F\bigg[-\frac{3}{2}\log\frac{s}{m_b^2} + \frac{9}{4}\bigg] \;\equiv\; \Delta^{\rm (HE)}_{\rm QCD}, \tag{3.11}$$

which has been introduced by the renormalization procedure and can be resummed to all orders of perturbation theory using the renormalization group. This mass resummation is based on the leading-logarithm approximation in QCD and is equivalent to replacing the bottom quark mass m_b with the running quark mass $\overline{m}_b(s)$ in the Yukawa coupling h_{Abb} [108],

$$h_{Abb} \;=\; -\frac{g m_b \tan\beta}{2m_W} \quad\longrightarrow\quad -\frac{g\overline{m}_b(s)\tan\beta}{2m_W}. \tag{3.12}$$

For lower energies, the limit in Eq. (3.11) is not valid, and there is thus no need for a resummation procedure. In order to connect the high and low energy domains, we use the simple matching scheme

$$\sigma_{\rm QCD} \;=\; \Big[1-\beta_b\Big]\sigma^{\rm (LE)}_{\rm QCD} + \beta_b\sigma^{\rm (HE)}_{\rm QCD}, \tag{3.13}$$

so that we use the resummed expression in the high-energy (HE) domain,

$$\sigma^{\rm (HE)}_{\rm QCD} \;=\; \sigma_{\rm LO}\big(m_b \to \overline{m}_b(s)\big)\bigg[1 + \Delta^{\rm (HE)}_{\rm QCD}\bigg], \tag{3.14}$$

and the valid result from Eq. (3.8) without using the running quark mass in the low-energy (LE) case. The matching introduced in Eq. (3.13) allows for a smooth interpolation between the two limits.

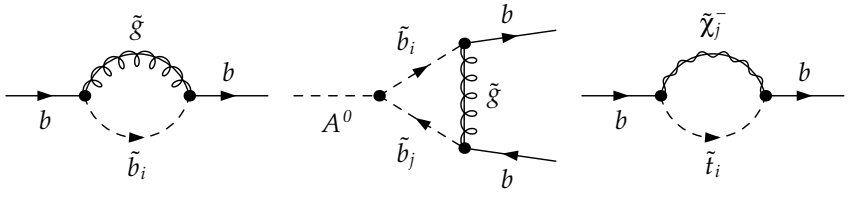

Figure 3.4: Diagrams for one-loop self-energy and vertex SUSY-QCD corrections to the process $\tilde{\chi}\tilde{\chi} \to A^0 \to b\bar{b}$. We also show the electroweak stop-chargino contribution to the bottom mass renormalization.

The remaining finite QCD-corrections in the $\overline{\text{MS}}$-scheme are known up to $\mathcal{O}(\alpha_s^4)$ and are numerically important at scales of the order of a few GeV. In parametrized form they can be written as [109, 110]

$$\begin{aligned}\Delta_{\text{QCD}} &= \frac{\alpha_s(s)}{\pi} C_F \frac{17}{4} + \frac{\alpha_s^2(s)}{\pi^2}\Big[35.94 - 1.359 n_f\Big] + \frac{\alpha_s^3(s)}{\pi^3}\Big[164.14 - 25.77 n_f + 0.259 n_f^2\Big] \\ &\quad + \frac{\alpha_s^4(s)}{\pi^4}\Big[39.34 - 220.9 n_f + 9.685 n_f^2 - 0.0205 n_f^3\Big], \end{aligned} \tag{3.15}$$

with $n_f = 5$ denoting the number of flavours. The corrections of $\mathcal{O}(\alpha_s^3)$ and $\mathcal{O}(\alpha_s^4)$ have been obtained for scalar Higgs bosons, but since the quarks are taken to be massless in the calculation, the results also apply in the pseudoscalar case.

A separately gauge-independent correction of $\mathcal{O}(\alpha_s^2)$ is induced by the top quark loop diagram shown on the right panel of Fig. 3.3. Its contribution [111]

$$\Delta_{\text{top}} = \frac{1}{\tan^2\beta}\frac{\alpha_s^2(s)}{\pi^2}\left[\frac{23}{6} - \log\frac{s}{m_t^2} + \frac{1}{6}\log^2\frac{\overline{m}_b^2(s)}{s}\right] \tag{3.16}$$

can be important at small values of $\tan\beta$, but is largely suppressed in the Higgs funnel region considered here.

3.3 SUSY-QCD Corrections

In Supersymmetry, additional corrections arise through the sbottom-gluino exchanges shown in Fig. 3.4. Note that there is no real emission contribution at this order due to R-parity conservation. Working again in the on-shell renormalization scheme, they lead to the mass renormalization

$$\begin{aligned}\left(\frac{\Delta m_b}{m_b}\right)_{\tilde{g}\tilde{b}} &= \frac{\alpha_s(s)}{\pi} C_F \Big[B_0(m_b^2; m_{\tilde{b}_1}^2, m_{\tilde{g}}^2) - B_0(m_b^2; m_{\tilde{b}_2}^2, m_{\tilde{g}}^2)\Big] \sin 2\theta_{\tilde{b}} \\ &\quad + \frac{\alpha_s(s)}{\pi}\frac{C_F}{m_b^2}\sum_{i=1,2}\Big[A_0(m_{\tilde{g}}^2) - A_0(m_{\tilde{b}_i}^2) + \big(m_{\tilde{b}_i}^2 - m_{\tilde{g}}^2 - m_b^2\big) B_0(m_b^2; m_{\tilde{g}}^2, m_{\tilde{b}_i}^2)\Big]. \end{aligned} \tag{3.17}$$

In the limit of large SUSY masses ($m_b \ll m_{\tilde{b}_i}, m_{\tilde{g}}$) only the first line of Eq. (3.17) survives and the remaining two-point functions can be rewritten as a three-point function with zero external momentum, so that the mass renormalization becomes

$$\left(\frac{\Delta m_b}{m_b}\right)_{\tilde{g}\tilde{b}} = \frac{\alpha_s(s)}{\pi} C_F \frac{m_{\tilde{g}}}{2}\Big(A_b - \mu\tan\beta\Big) I(m_{\tilde{b}_1}^2, m_{\tilde{b}_2}^2, m_{\tilde{g}}^2), \tag{3.18}$$

which is proportional to

$$\sin 2\theta_{\tilde{b}} \;=\; \frac{2m_b\big(A_b - \mu\tan\beta\big)}{m^2_{\tilde{b}_1} - m^2_{\tilde{b}_2}}, \tag{3.19}$$

i.e. the off-diagonal component of the sbottom mass matrix, and the three-point function at zero external momentum

$$I(m_a^2, m_b^2, m_c^2) \;=\; C_0(0,0,0; m_a^2, m_b^2, m_c^2) \;=\; \frac{m_a^2 m_b^2 \log\frac{m_a^2}{m_b^2} + m_b^2 m_c^2 \log\frac{m_b^2}{m_c^2} + m_c^2 m_a^2 \log\frac{m_c^2}{m_a^2}}{(m_a^2 - m_b^2)(m_b^2 - m_c^2)(m_c^2 - m_a^2)}. \tag{3.20}$$

In the above limit ($m_b \ll m_{\tilde{b}_i}, m_{\tilde{g}}$) where we now also neglect $s \ll m^2_{\tilde{b}_i}, m^2_{\tilde{g}}$ and A_b with respect to the $\tan\beta$-enhanced μ, the vertex correction equals the mass renormalization in Eq. (3.18) up to a factor $1/\tan^2\beta$, so that the total SUSY correction becomes in this low energy (LE) limit

$$\Delta^{(\mathrm{LE})}_{\mathrm{SUSY}} \;=\; \frac{\alpha_s(s)}{\pi} C_F \Big[1 + \frac{1}{\tan^2\beta}\Big] m_{\tilde{g}} \mu \tan\beta \; I(m^2_{\tilde{b}_1}, m^2_{\tilde{b}_2}, m^2_{\tilde{g}}). \tag{3.21}$$

It has long been known that for large $\tan\beta$, the mass renormalization Δm_b can be significant and must be resummed by replacing

$$m_b \;\longrightarrow\; \frac{m_b}{1 + \lim_{A_b\to 0} \frac{\Delta m_b}{m_b}} \tag{3.22}$$

in the Yukawa coupling h_{Abb} [112]. More recently, it has been observed that A_b may be of similar size as $\mu\tan\beta$, for example in no-mixing scenarios, so that its contribution must also be resummed. This is done by the replacement [113]

$$\lim_{A_b\to 0} \frac{\Delta m_b}{m_b} \;\longrightarrow\; \frac{\lim_{A_b\to 0} \frac{\Delta m_b}{m_b}}{1 + \lim_{\mu\tan\beta\to 0} \frac{\Delta m_b}{m_b}}, \tag{3.23}$$

which is, at $\mathcal{O}(\alpha_s)$, equivalent to resumming the whole low-energy expression for Δm_b, i.e. replacing

$$\overline{m}_b \;\longrightarrow\; \frac{\overline{m}_b}{1 + \frac{\Delta m_b}{m_b}} \tag{3.24}$$

in the Yukawa coupling h_{Abb}.

The remaining finite contribution Δ_{SUSY} to the cross section in Eq. (3.9) is finally given by the difference between the full SUSY-QCD contribution and its resummed low-energy limit that has been absorbed into the Yukawa coupling,

$$\Delta_{\mathrm{SUSY}} \;=\; \frac{\alpha_s(s)}{\pi} C_F \frac{1+\tan^2\beta}{\tan\beta} \Big[C_0(m_b^2, s, m_b^2; m^2_{\tilde{b}_1}, m^2_{\tilde{b}_2}, m^2_{\tilde{g}}) - C_0(0,0,0; m^2_{\tilde{b}_1}, m^2_{\tilde{b}_2}, m^2_{\tilde{g}})\Big]. \tag{3.25}$$

An additional contribution to the quark mass renormalization, that can have an effect of the same order of magnitude as Δ_{SUSY}, arises from the stop-chargino loops shown in Fig. 3.4. Its dominant contribution is given by [112]

$$\left(\frac{\Delta m_b}{m_b}\right)_{\tilde{t}\tilde{\chi}^\pm} \;=\; -\frac{\lambda_t^2}{16\pi^2}\Big[A_t \mu \tan\beta - \mu^2\Big] I(\mu^2, m^2_{\tilde{t}_1}, m^2_{\tilde{t}_2}), \tag{3.26}$$

where $\lambda_t = \sqrt{2} m_t / \big(\sqrt{v_u^2 + v_d^2}\sin\beta\big)$ denotes the top Yukawa coupling. Again the bottom quark mass has been neglected with respect to the larger SUSY masses.

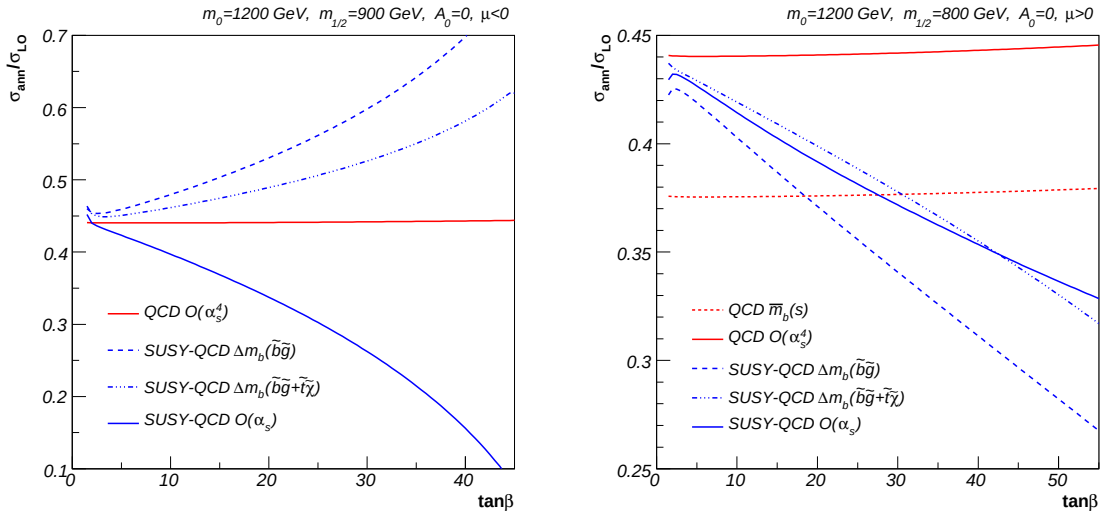

Figure 3.5: Annihilation cross section including the different QCD and SUSY-QCD corrections normalized to the leading order cross section. We show the QCD corrected cross section including only the mass resummation (red dotted) and also the finite terms up to $\mathcal{O}(\alpha_s^4)$ (red line), as well as the SUSY-QCD corrected cross section including mass resummation effects due to the sbottom-gluino (blue dashed) and the stop-chargino (blue dash-dotted) contributions, and finally also the finite terms (blue line).

3.4 Impact on the Annihilation Cross Section

For the numerical evaluation of the presented results, we place ourselves in minimal supergravity (mSUGRA) scenarios with $A_0 = 0$ and large $\tan\beta$, namely $\tan\beta = 44.5$ for $\mu < 0$ and $\tan\beta = 54$ for $\mu > 0$. These choices correspond to an important contribution of the annihilation process $\tilde{\chi}\tilde{\chi} \to A^0 \to b\bar{b}$ and still allow for electroweak symmetry breaking (EWSB) in a large region of the m_0-$m_{1/2}$ plane.

Starting from the mSUGRA parameters at the high scale, the weak-scale parameters are determined through renormalization group running with `SPheno` [90], which includes two-loop renormalization group equations (RGEs), the complete one-loop formulas for the soft SUSY breaking masses supplemented by two-loop contributions in the case of the neutral Higgs bosons and the μ parameter, and resummed $\lim_{A_b \to 0} \Delta m_b$ corrections. We then diagonalize the mass matrices obtained in this way with `FeynHiggs` [91] to determine the physical Higgs and SUSY masses. For the Standard Model input parameters, i.e. particle masses and coupling constants, see App. B. In particular, we use the values $\overline{m}_b^{\overline{\text{MS}}}(m_b) = 4.2$ GeV and $m_t^{\text{pole}} = 174.2$ GeV for the bottom and top quark masses, as well as $\alpha_s(m_Z) = 0.1176$ for the strong coupling constant.

In Fig. 3.5 we show the annihilation cross section of the process $\tilde{\chi}\tilde{\chi} \to A^0 \to b\bar{b}$ normalized to the leading order cross section σ_{LO}, including the different QCD and SUSY-QCD corrections. Since the dependence on the centre-of-momentum energy $\sqrt{s}$ is weak, the ratio is shown as a function of $\tan\beta$ for fixed m_0, $m_{1/2}$, A_0, and $\text{sgn}(\mu)$. The two scenarios for $\mu > 0$ and $\mu < 0$ are the same as for the leading order cross section in Fig. 3.2.

The QCD correction, including finite terms up to $\mathcal{O}(\alpha_s^4)$, decreases the annihilation cross section by more than a factor of two. The main effect, however, is due to the performed mass

resummation, the running squared quark mass $\overline{m}_b^2(s)$ being lower than the bare squared mass m_b^2 in the leading order cross section by approximately the same factor. The finite terms $\Delta_{\rm QCD}$ are less important, as can be seen in the right panel of Fig. 3.5. The slight increase of the QCD correction is explained by the fact that we have fixed the squared centre-of-momentum energy s at a constant and small distance the threshold. As the mass spectrum is influenced by the increasing $\tan\beta$, the threshold, together with the neutralino mass, is shifted to higher energies. The top quark loop correction $\Delta_{\rm top}$ is also independent of the other supersymmetric parameters. At very low values of $\tan\beta$, its contribution accounts for a few percent of the QCD correction, while it accounts for less than 0.01% for $\tan\beta \geq 40$ in the case of the "A-funnel" region in mSUGRA.

In addition to the QCD contributions discussed above, the annihilation cross section is further reduced by the SUSY-QCD corrections. In the case of $\mu > 0$, the effect is enhanced by about 10% with respect to the leading order cross section, while in the case of $\mu < 0$ the SUSY-QCD correction accounts for up to another 40% of decrease at large $\tan\beta$. To disentangle the effects of the different contributions, we show the annihilation cross section including first only the sbottom-gluino mass renormalization, then include also the stop-chargino loop contribution, and finally the full SUSY-QCD correction including also the finite remainder of Eq. (3.25). For positive μ, the resummation effects are more important than the finite terms $\Delta_{\rm SUSY}$, that account only for about one percent of the annihilation cross section. The electroweak stop-chargino loop contribution is not negligible with respect to the QCD terms. The situation changes for the case of negative μ, where the mass resummation has opposite sign and increases the annihilation cross section. In contrast, the finite terms are here more important and decrease the annihilation cross section to as little as ten percent of the leading order cross section.

3.5 Impact on the Neutralino Relic Density

The cold dark matter relic density is calculated with the public tool `DarkSUSY` [83], which includes the QCD corrections up to $\mathcal{O}(\alpha_s^2)$, i.e. Eq. (3.8), the $\mathcal{O}(\alpha_s^2)$ term of Eq. (3.15), and the top quark loop correction Eq. (3.16). We have added the $\mathcal{O}(\alpha_s^3)$ and $\mathcal{O}(\alpha_s^4)$ QCD as well as our $\mathcal{O}(\alpha_s)$ SUSY-QCD corrections described above. We also include their dependence on the center-of-momentum energy $\sqrt{s}$, which is absent in `DarkSUSY` where the corrections are always evaluated at the scale $Q^2 = m_A^2$ for the Higgs decay width and at $Q^2 = 4m_{\tilde{\chi}}^2$ for the annihilation cross section.

We first determine the allowed regions in the m_0-$m_{1/2}$ plane shown in Fig. 3.6. The Higgs funnel contribution to $\sigma_{\rm eff}$ rises from 40% for low values of $m_{1/2}$ (or m_0 for $\mu < 0$) to more than 95%, when $m_{1/2}$ (and m_0) is (are) large. It is obvious that the leading order (LO) allowed regions are dramatically changed by the $\mathcal{O}(\alpha_s^2)$, $\mathcal{O}(\alpha_s^3)$, and $\mathcal{O}(\alpha_s^4)$ QCD and $\mathcal{O}(\alpha_s)$ SUSY-QCD corrections, which reduce the annihilation cross section $\sigma_{\rm eff}$ by more than a factor of two in this region. The increase in $\Omega_{\rm CDM}h^2$ must therefore be compensated by smaller masses, which results in a shift of the favoured contour towards smaller values of m_0 and $m_{1/2}$. As expected, the effect is negligible in the focus point (very low values of $m_{1/2}$) and co-annihilation (very low m_0) regions as well as for small and intermediate values of $\tan\beta$.

In Fig. 3.7 we plot the dark matter relic density as a function of $m_{1/2}$ for fixed $m_0 =$ 1200 GeV, corresponding to the cuts indicated by the horizontal dashed lines in the two panels of Fig. 3.6. The effect of the $\mathcal{O}(\alpha_s^2)$ QCD corrections already included in `DarkSUSY` is

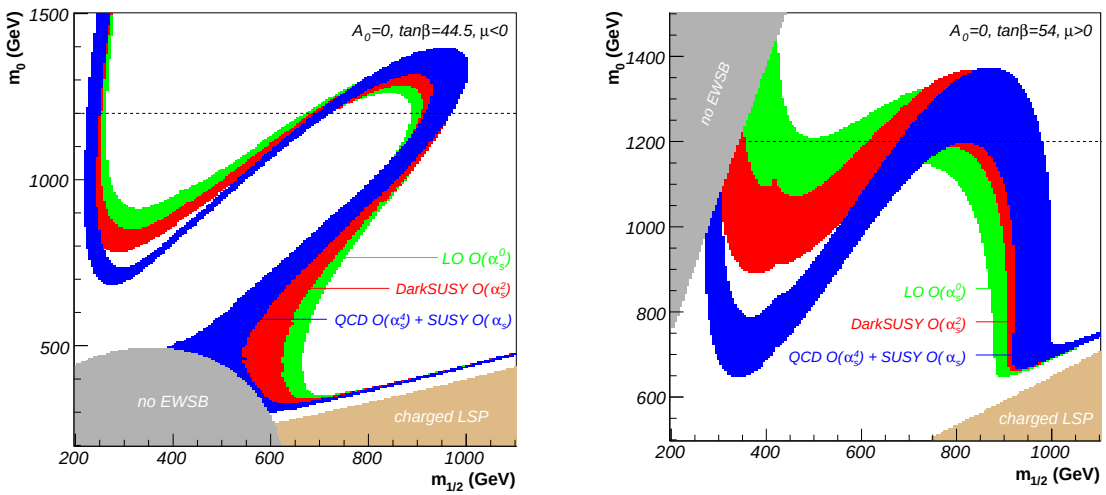

Figure 3.6: Regions in the m_0-$m_{1/2}$ plane forbidden by a charged LSP (beige) or by no electroweak symmetry breaking (grey) and favoured by the observed dark matter relic density $\Omega_{\mathrm{CDM}}h^2$ for large $\tan\beta = 44.5$ at $\mu < 0$ (left) and $\tan\beta = 54$ at $\mu > 0$ (right). The green contour corresponds to the pure $\mathcal{O}(\alpha_s^0)$ leading order calculation of the process $\tilde{\chi}\tilde{\chi} \to A^0 \to b\bar{b}$, the red contour is computed with `DarkSUSY` including QCD corrections up to $\mathcal{O}(\alpha_s^2)$, and the blue contour includes the full $\mathcal{O}(\alpha_s^4)$ QCD and the $\mathcal{O}(\alpha_s)$ SUSY-QCD corrections.

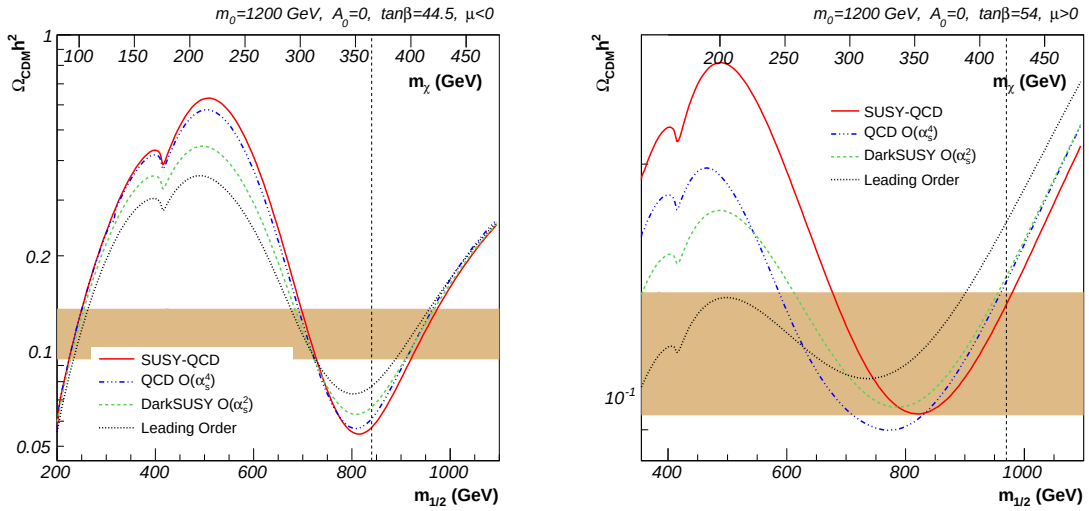

Figure 3.7: Leading order (black dotted), $\mathcal{O}(\alpha_s^2)$ (green dashed) and $\mathcal{O}(\alpha_s^4)$ (blue dot-dashed) QCD, and $\mathcal{O}(\alpha_s)$ SUSY-QCD corrected predictions for the cold dark matter relic density $\Omega_{\mathrm{CDM}}h^2$ as a function of $m_{1/2}$ for fixed $m_0 = 1200$ GeV, $A_0 = 0$, and for $\tan\beta = 44.5$ at $\mu < 0$ (left) and for $\tan\beta = 54$ at $\mu > 0$ (right). The coloured band shows the experimentally favoured range. The Higgs pole is indicated by a vertical dashed line.

considerably enhanced by the $\mathcal{O}(\alpha_s^3)$ and $\mathcal{O}(\alpha_s^4)$ QCD and the $\mathcal{O}(\alpha_s)$ SUSY-QCD corrections, while the top quark loop contributes less than 0.01% for the large values of $\tan\beta$ under consideration here. However, the difference between the $\mathcal{O}(\alpha_s^3)$ and $\mathcal{O}(\alpha_s^4)$ terms is not visible on our logarithmic scale. Note that a local minimum of the relic density at $m_{1/2} = 420$ GeV occurs when $m_{\tilde{\chi}} = m_t$, where the $t\bar{t}$ annihilation channel is opened [114].

Due to our corrections the Higgs decay width Γ_A is reduced by approximately the same amount as the cross section. In consequence, on the Higgs pole, where Γ_A is of particular importance, the effect is reversed. Since the Higgs width Γ_A increases with $m_{1/2}$, in particular for $\mu > 0$, the annihilation cross section σ_{eff} reaches its maximum, corresponding to the minimum of the relic density $\Omega_{\text{CDM}}h^2$, at some distance from the pole. Further away, the QCD and SUSY-QCD corrections decrease σ_{eff}, and thus increase $\Omega_{\text{CDM}}h^2$, as expected. Closer to the pole, indicated in Fig. 3.7 by a vertical dashed line, the reduced width becomes important, so that the maximum of σ_{eff}, and thus the minimum of $\Omega_{\text{CDM}}h^2$, approaches the pole.

3.6 Theoretical Uncertainties

An important uncertainty is coming from the choice of the renormalization scale, that vanishes when taking into account all orders of perturbation theory. Since the leading order cross section involves only electroweak couplings, this dependence is important for the QCD and SUSY-QCD loops at $\mathcal{O}(\alpha_s)$. Typical variations $\frac{\mu_R}{2} \leq Q \leq 2\mu_R$ of the renormalization scale lead in our case to a variation of up to four percent for the prediction of the neutralino relic density.

Another non-negligible uncertainty is introduced by the choice of the Supersymmetry spectrum generator. It is well known that, for the same input parameters at high scale, different spectrum generators deliver different spectra at low scale, depending on the numerical and theoretical accuracy in the renormalization group running [115], i.e. numerical methods and the implemented level of loops, respectively. It is also known that these differences in the spectrum may influence the prediction of the cold dark matter relic density [116].

Due to the fact that the top quark loop correction is negligible in the case of large $\tan\beta$, the numerical value of the top quark mass has no direct influence on our QCD and SUSY-QCD corrections. However, variations of the top quark mass induce variations in the SUSY particle spectrum through the renormalization group running. In consequence, for example, the pseudoscalar Higgs mass increases with the top quark mass, so that the cosmologically favoured "A-funnel" region lies at higher values of m_χ and thus of $m_{1/2}$. Note that, independently of the spectrum generator and the value of the top quark mass, the impact of our QCD and SUSY-QCD corrections remains the same as discussed in the Secs. 3.4 and 3.5.

Most neutralino dark matter studies in minimal supergravity (mSUGRA) assume a vanishing trilinear coupling A_0. However, it has recently been shown that a non-vanishing A_0, that varies in a range of ± 4 TeV, leads to new allowed regions in the m_0-$m_{1/2}$ plane of the mSUGRA parameter space that are consistent with the cosmologically favoured region [117]. Concerning our analysis, variations of A_0 might be interesting, as they may lead to important variations of the coupling A_b at the electroweak scale. However, we have focused here on $A_0 = 0$ and leave the case of a non-vanishing trilinear coupling to further studies.

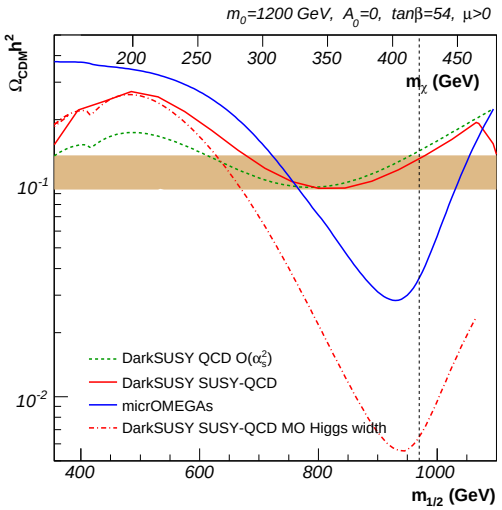

Figure 3.8: The predictions for the neutralino relic density obtained with the public codes `DarkSUSY` and `micrOMEGAs` as a function of the gaugino mass parameter $m_{1/2}$. The coloured band corresponds to the WMAP 2σ favoured interval.

3.7 Comparison with `micrOMEGAs`

We finally compare the results obtained with our modified version of `DarkSUSY` to the predictions given by the public tool `micrOMEGAs` [84]. It is well known that the two codes agree well in wide regions of the mSUGRA parameter space. However, there are also regions with disagreement, in particular in the "A-funnel" region studied in this Chapter. In `micrOMEGAs`, the presented mass resummation approximations in QCD and SUSY-QCD are implemented, based on the results given in Ref. [113]. They also include the finite QCD terms up to $\mathcal{O}(\alpha_s^3)$ and the stop-chargino loop contributing to the bottom mass resummation. However, the finite SUSY-QCD contribution of Eq. (3.25) is not implemented in `micrOMEGAs`.

In Fig. 3.8 we show the neutralino relic density computed with `micrOMEGAs` compared to the one obtained with `DarkSUSY` including the same corrections as are included in `micrOMEGAs`, i.e. the $\mathcal{O}(\alpha_s^3)$ QCD corrections and the SUSY-QCD bottom mass resummation. The mass spectrum for both dark matter codes has been computed with our combination of `SPheno` and `FeynHiggs` as described in Section 3.4.

Around the Higgs pole, indicated by the vertical dashed line, the predictions given by `DarkSUSY` (green dashed line) and `micrOMEGAs` (blue line) show important differences. In particular, the distance between the pole and the minimum of the relic density differs as do the minimal values of $\Omega_{\rm CDM}h^2$. When we include in `DarkSUSY` the same QCD and SUSY-QCD (red line) corrections as are included in `micrOMEGAs`, important differences remain. These are in particular due to different values of the Higgs decay with, Γ_A. The red dash-dotted line shows the prediction of the relic density obtained with `DarkSUSY` including QCD and SUSY-QCD corrections, but with the Higgs decay width calculated and used by `micrOMEGAs`. As expected, the minima in the relic density lie now at the same value of $m_{1/2}$. However, the relic density in this point still differs by one order of magnitude, which might be explained by different implementations of the QCD running in the two codes. A detailed investigation of the exact implementation of the running masses and coupling constants will therefore be

necessary.

Note that the difference in the relic density at lower values of $m_{1/2}$ is due to the fact that `micrOMEGAs` includes also the SUSY-QCD corrections to the couplings of the CP-even Higgs bosons, which are absent in `DarkSUSY`. In consequence, the annihilation cross section in the relevant region at lower $m_{1/2}$ is overestimated by `DarkSUSY`, leading to an underestimation of $\Omega_{\mathrm{CDM}}h^2$.

Chapter 4

SUSY-QCD Corrections to Neutralino Pair Annihilation $\tilde{\chi}\tilde{\chi} \to q\bar{q}$

Besides the annihilation through a pseudoscalar Higgs exchange presented in the previous Chapter, further neutralino pair annihilation processes receive QCD and SUSY-QCD corrections. These are the annihilation into quark-antiquark pairs through Z^0-boson, CP-even Higgs-boson and squark exchange, and also neutralino-stop coannihilation. For the latter, QCD and SUSY-QCD corrections have recently been published [118]. In this Chapter, we present the corrections for the remaining channels, i.e. for neutralino pair annihilation into quark-antiquark pairs through the exchange of a Z^0-boson, a squark, or a neutral Higgs-boson [119].

4.1 Contribution of Quark-Antiquark Final States

Neutralino pair annihilation into a quark-antiquark pair can proceed through the exchange of a Z-boson or a neutral Higgs boson ($\phi^0 = h^0, H^0, A^0$) in the s-channel, as well as through squark ($\tilde{q}_i$ with $i, j = 1, 2$) exchange in the t- or u-channel, as shown in Fig. 4.1. As a first step, it is interesting to study the relative contributions of the different quark-antiquark final states to the effective total annihilation cross section $\langle \sigma_{\rm ann} v \rangle$, that in turn determines the relic abundance of dark matter. To this end, we have performed detailed scans over the $m_0 - m_{1/2}$ planes of the minimal supergravity (mSUGRA) parameter space for fixed values $\tan\beta$, A_0, and

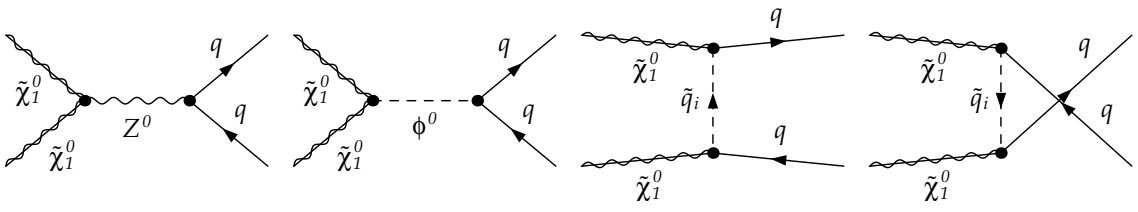

Figure 4.1: The leading-order diagrams for neutralino pair annihilation into quark pairs through Z-boson, neutral Higgs boson ($\phi^0 = h^0,\ H^0,\ A^0$), or squark ($\tilde{q}_i$ with $i, j = 1, 2$) exchange.

sgn(μ). Starting from these high-scale parameters, the renormalization group equations have been solved and the physical supersymmetric mass spectrum at the electroweak scale has been obtained with the computer programme `SPheno 2.2.3` [90]. For each point, the neutralino relic density $\Omega_{\rm CDM}h^2$ and the contributions of the six quark-antiquark production channels, $u\bar{u}$, $d\bar{d}$, $s\bar{s}$, $c\bar{c}$, $b\bar{b}$, and $t\bar{t}$ have then been computed using the public code `micrOMEGAs 2.1` [84]. For the Standard Model input parameters such as particle masses and coupling constants we have again used the numerical values given in App. B, except for the top quark pole mass, which has now been set to the more recent value $m_t^{\rm pole} = 171.4$ GeV [120].

The results of this analysis are shown in Figs. 4.2 and 4.3 for $\mu > 0$, $\tan\beta = 10$, and $A_0 = 0$ and $A_0 = -1500$ GeV, respectively. In Figs. 4.4 and 4.5, we then show the parameter space scans for $\mu > 0$, $A_0 = 0$, and $\tan\beta = 30$ and 50. We indicate the relative contributions to $\sigma_{\rm ann}v$ for all quark final states ($q\bar{q}$), the sum of the four "light" quarks ($u\bar{u}$, $d\bar{d}$, $s\bar{s}$, and $c\bar{c}$), as well as bottom ($b\bar{b}$) and top ($t\bar{t}$) quark-antiquark final states. In each graph we also show in blue the favoured region of the m_0-$m_{1/2}$ plane with respect to measurements of the cold dark matter relic density of Eq. (2.7). Grey shaded regions are excluded due to a charged LSP (high $m_{1/2}$ and small m_0), current SUSY particle mass limits (small $m_{1/2}$), the stringent constraint from the measurements of the inclusive branching ratio BR($b \to s\gamma$) (small m_0 and $m_{1/2}$), or unphysical solutions to the renormalization group equations (high m_0). Note that measurements of the electroweak ρ-parameter only exclude regions of higher masses lying beyond the limits of our graphs in Figs. 4.2 – 4.5.

In the first panels of Figs. 4.2 – 4.5 we see that neutralino annihilation into quarks is generally dominant over wide ranges of the m_0-$m_{1/2}$ plane. Focusing on regions that lead to a neutralino relic density agreeing with the cosmological limits, the only exceptions at $\tan\beta = 10$ are the coannihilation region at small m_0 and high $m_{1/2}$ and in the region $m_0 \gtrsim 1000$ GeV and $m_{1/2} \sim 300 - 400$ GeV, where gauge and Higgs boson final states dominate. With increasing $\tan\beta$ the former is shifted to higher gaugino masses, while the latter looses its importance. Both of these observations can be traced to the fact that the Yukawa couplings of the Higgs bosons to down-type quarks become numerically larger, enhancing the corresponding quark final states.

Let us now turn to the individual contributions of the different quark flavours. From the upper right panels of Figs. 4.2 – 4.5, it becomes obvious that the "light" first and second generation quarks only play a non-negligible role in the case of light neutralinos, namely for values of $m_{1/2} \lesssim 300$ GeV for the gaugino mass parameter. These regions, however, do either not coincide with the WMAP favoured band of the neutralino relic density or are excluded by the direct mass limits or the $b \to s\gamma$ branching ratio. We will therefore focus in this analysis on the third generation "heavy" quark final states. For a future analysis of scenarios with important contributions of the four "light" flavours, it might be interesting to consider a more general MSSM instead of minimal supergravity.

The contribution of bottom-antibottom final states to the total annihilation cross section is shown in the lower left panels of Figs. 4.2 – 4.5. At $\tan\beta = 10$, this annihilation channel dominates close to the pole of the CP-even Higgs boson, where $2m_{\tilde{\chi}_1^0} = m_{h^0}$. The resonance occurs at a constant value of $m_{1/2}$. The corresponding part of the WMAP favoured band, however, is for $A_0 = 0$ excluded by the current mass limits. In particular, the lightest chargino is here too light to satisfy the limits obtained from the LEP experiments. This situation changes when we consider a non-vanishing trilinear coupling, since new loop contributions then alter the particle masses. In Fig. 4.3, we show the case of $A_0 = -1500$ GeV, where the WMAP favoured region and also the Higgs pole now lie outside the zone excluded by direct

mass limits.

As already stated, the Yukawa coupling of the pseudoscalar Higgs boson to bottom quarks becomes more important for higher values of $\tan\beta$. In consequence, the region where neutralinos annihilate into bottom quarks grows (see Fig. 4.4 for $\tan\beta = 30$) and the "A-funnel" region already discussed in Chap. 3 makes its appearance at $\tan\beta \simeq 50$, as can be seen in Fig. 4.5.

The annihilation of a neutralino pair into a top quark-antiquark pair is kinematically allowed if the neutralino mass is larger than the top quark mass, $m_{\tilde{\chi}_1^0} \geq m_t$. Since the neutralino mass is at the tree level proportional to the gaugino mass parameter $m_{1/2}$, the corresponding annihilation channels open only beyond a certain threshold in $m_{1/2}$. This is well observed in the lower right panels of Figs. 4.2 – 4.5, where we show the relative contribution of top quark-antiquark final states to the annihilation cross section $\langle\sigma_{\text{ann}}v\rangle$. It is interesting to note that the contribution is very similar for low and intermediate values of $\tan\beta$. It only decreases at large $\tan\beta$ in favour of the now dominant bottom quark final states. Due to the large magnitude of the top quark mass and the resulting numerical importance of the top Yukawa coupling, the relative contribution of the top quark final states is rather important, if it is kinematically allowed. This is well visible in the four corresponding graphs, where an important gradient between the region of too low neutralino masses and the one of high $t\bar{t}$ contributions is observed. The WMAP favoured band coincides in the focus point region with top quark contributions of more than 60 percent.

As already mentioned in Chap. 3, the prediction of the neutralino relic density strongly depends on the involved numerical programmes. On the one hand, there are differences between the two public codes `DarkSUSY 4.2` and `micrOMEGAs 2.1`, mainly due to the different implementations of the corrections to the bottom mass and the related Yukawa couplings to the Higgs bosons. On the other hand, since all particle masses are involved in the calculation, the choice of the spectrum generator also implies important uncertainties. This can be illustrated with the help of Fig. 4.6, where we show the same scan as in Fig. 4.2 of the $m_0 - m_{1/2}$ plane for $\tan\beta = 10$, $A_0 = 0$, and $\mu > 0$, but the renormalization group equations have now been solved and the physical mass spectrum has been obtained using the public code `SuSpect 2.34` instead of `SPheno 2.2.3`. Comparing the two scans, minor differences appear in the form and place of the different contours, due to the high sensitivity of the prediction of the neutralino relic density on small differences in the SUSY masses. The main difference, however, concerns the region which is close to the sector where no physical solutions to the renormalization group equations leading to electroweak symmetry breaking can be achieved. The scans shown in Fig. 4.6 reveal a relatively wide zone where `SuSpect 2.34` already outputs warnings indicating that the numerical solution does not proceed in a stable manner, whereas `SPheno 2.2.3` treats them without incidents. An analogous behaviour also appears for higher values of $\tan\beta$. Differences between SUSY spectrum generators and their implications on the dark matter relic density are discussed in Refs. [115, 116]. Since it provides more viable solutions and since the WMAP favoured band follows these particular regions, we shall continue to work with `SPheno 2.2.3` in the following.

Inspecting again Figs. 4.2 – 4.5, interesting regions that agree with the observed dark matter relic density of Eq. (2.7) and that involve at the same time important cross sections for the annihilation of neutralinos into "heavy" quark-antiquark pairs can be found either in the focus point region or around the Higgs resonances. At small $\tan\beta = 10$ and $A_0 = -1500$ GeV, the latter is found at $m_{1/2} \approx 132$ GeV, where annihilation into $b\bar{b}$ final states through exchange of a light Higgs boson is important. At high $\tan\beta = 50$, this region is excluded by

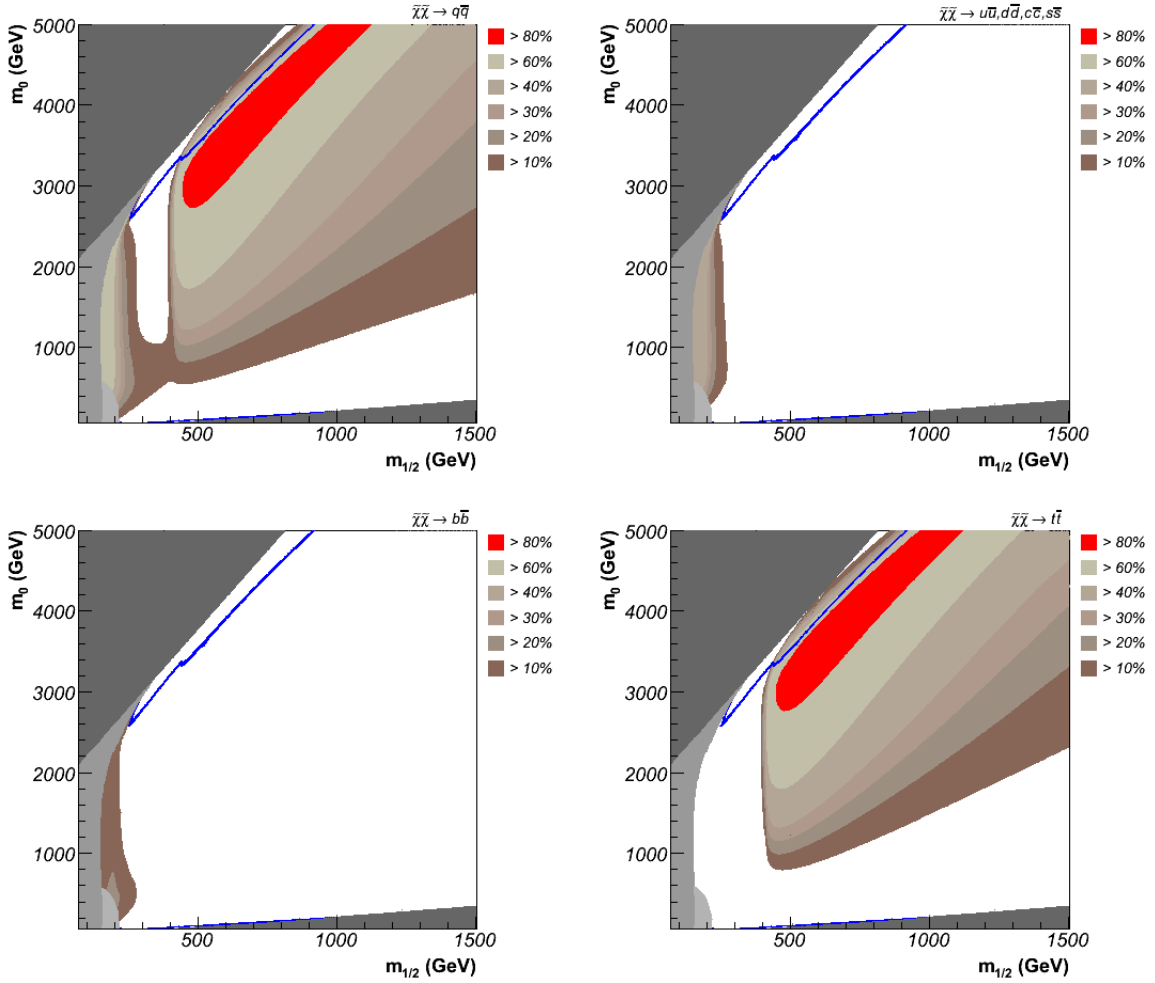

Figure 4.2: The m_0-$m_{1/2}$ plane of the mSUGRA parameter space for $\tan\beta = 10$, $A_0 = 0$, and $\mu > 0$ showing the relative contributions of all (top left), light (top right), bottom (bottom left), and top (bottom right) quark final states to the total annihilation cross section $\sigma_{\text{eff}} v$, as well as the points favoured with respect to WMAP data (blue), and those excluded by a charged LSP (dark grey, high $m_{1/2}$), mass limits on superpartners (intermediate grey), the measurement of BR($b \to s\gamma$) (light grey), or no electroweak symmetry breaking (dark grey, high m_0). The SUSY mass spectrum has been obtained from the parameters at the high scale through renormalization group running with `SPheno 2.2.3`.

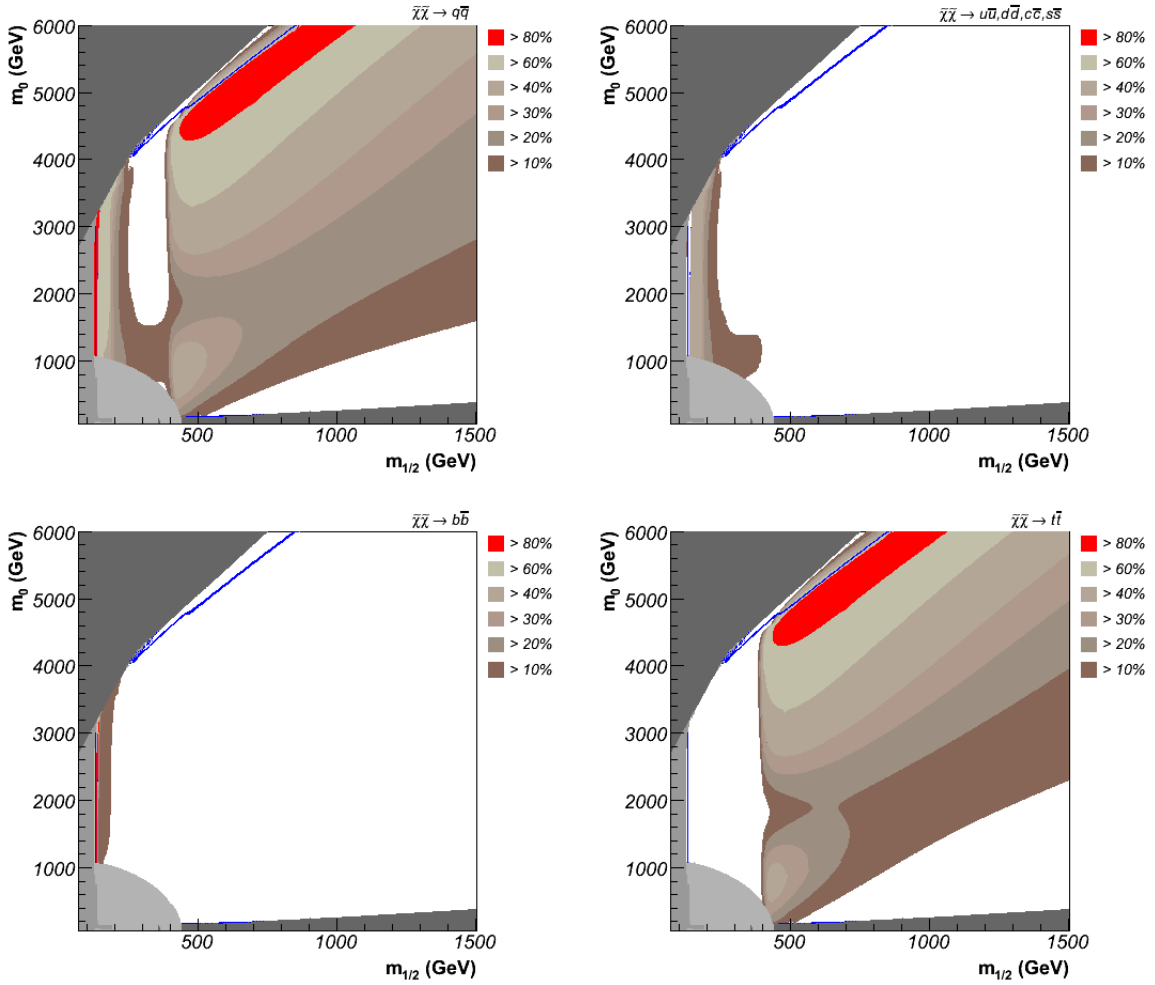

Figure 4.3: Same as Fig. 4.2 for $\tan\beta = 10$ and $A_0 = -1500$ GeV.

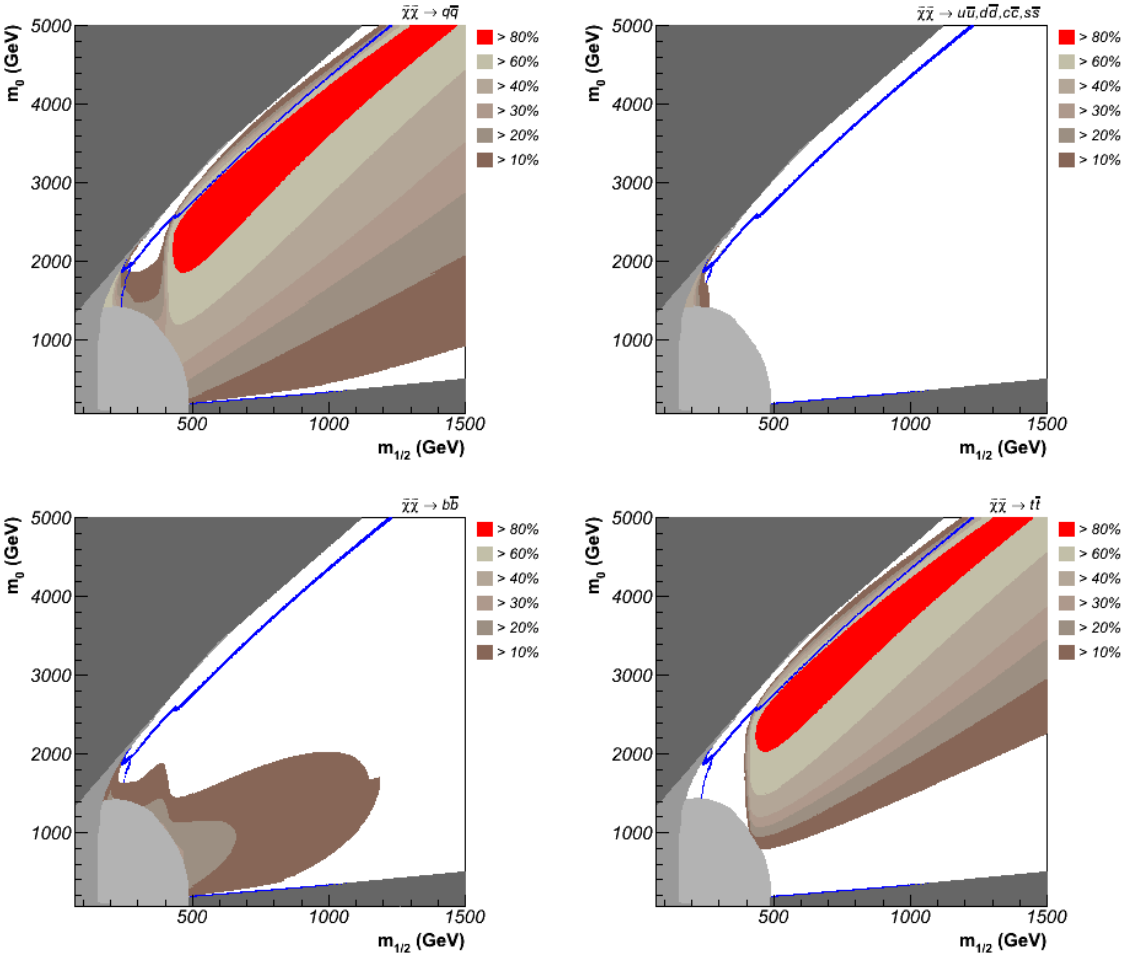

Figure 4.4: Same as Fig. 4.2 for $\tan\beta = 30$ and $A_0 = 0$.

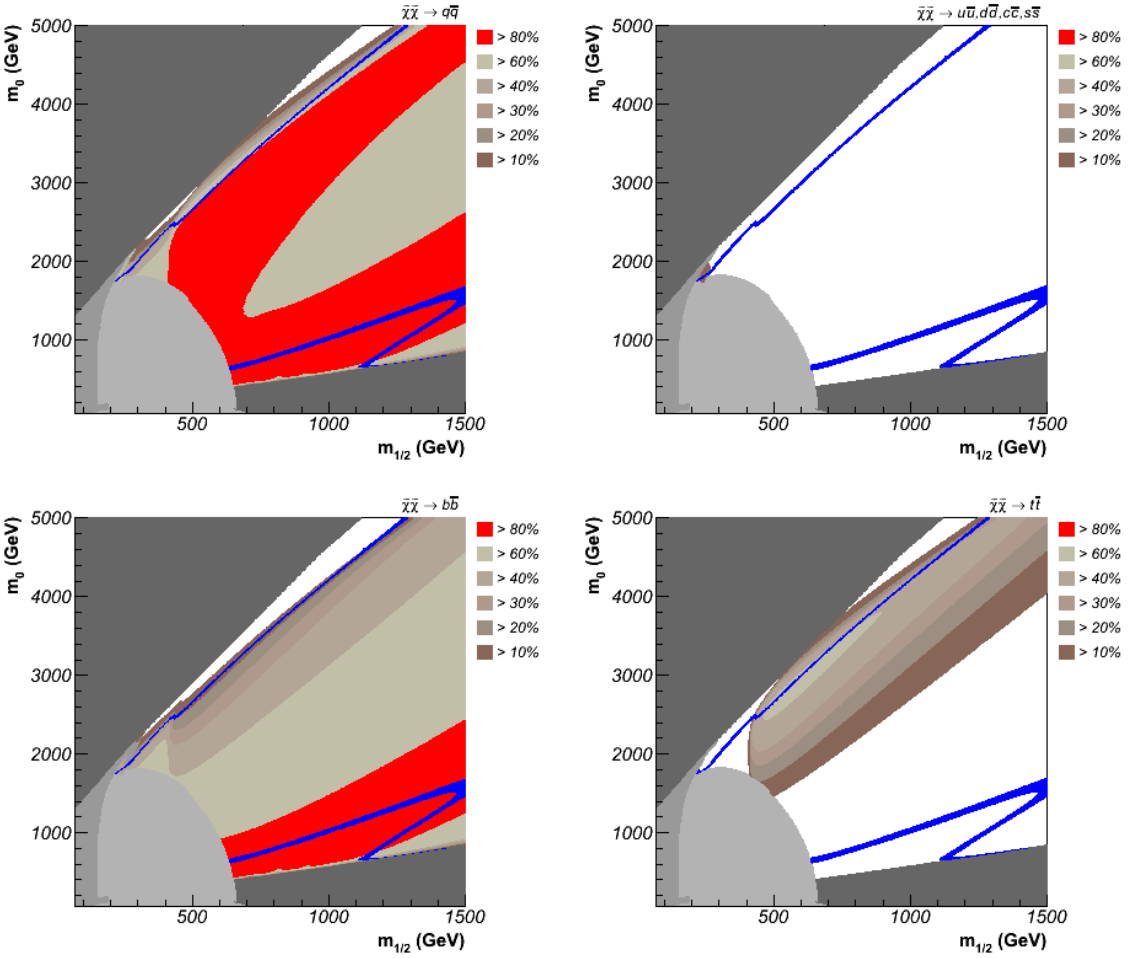

Figure 4.5: Same as Fig. 4.2 for $\tan\beta = 50$ and $A_0 = 0$.

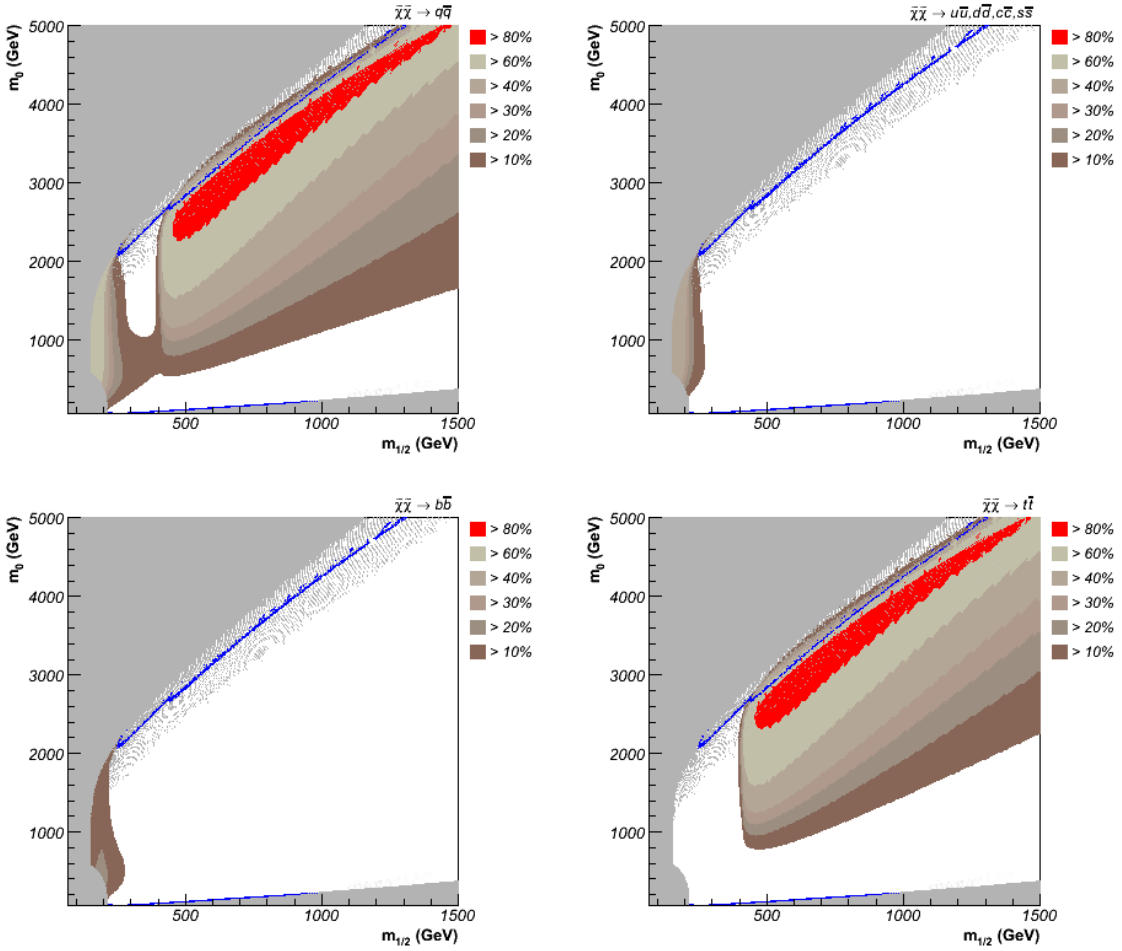

Figure 4.6: Same as Fig. 4.2 for $\tan\beta = 10$ and $A_0 = 0$, where the SUSY mass spectrum has now been calculated with `SuSpect 2.34`. Grey shaded regions are excluded due to a charged LSP, no electroweak symmetry breaking, current LEP mass limits, or $b \to s\gamma$ measurements.

the constraint from $b \to s\gamma$, so that only the "A-funnel" region around the resonance of the pseudoscalar Higgs boson survives. In the focus point region at high values of m_0 neutralinos annihilate dominantly into top quark-antiquark pairs. Note that at high $\tan\beta$ this proceeds mainly through the exchange of a CP-even heavy Higgs boson, due to its enhanced Yukawa coupling in this sector of the parameter space. For lower values of $\tan\beta$, not only the Higgs exchange, but also the Z-boson and squark exchanges play a significant role.

4.2 QCD and SUSY-QCD Corrections

Corrections of $\mathcal{O}(\alpha_s)$ to the neutralino pair annihilation processes shown in Fig. 4.1 arise through the quark and squark self-energies shown in Fig. 4.7, the gluon and gluino vertex corrections shown in Fig. 4.8, the gluon and gluino box diagrams shown in Fig. 4.9, and the real gluon emission diagrams shown in Fig. 4.10. Note that for each t-channel diagram, a u-channel diagram is obtained through crossing (not shown).

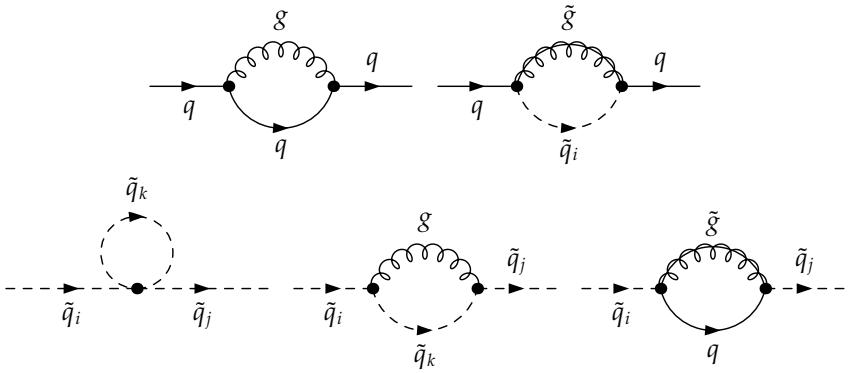

Figure 4.7: Quark (top) and squark (bottom) self-energy diagrams contributing at $\mathcal{O}(\alpha_s)$ to the annihilation cross section.

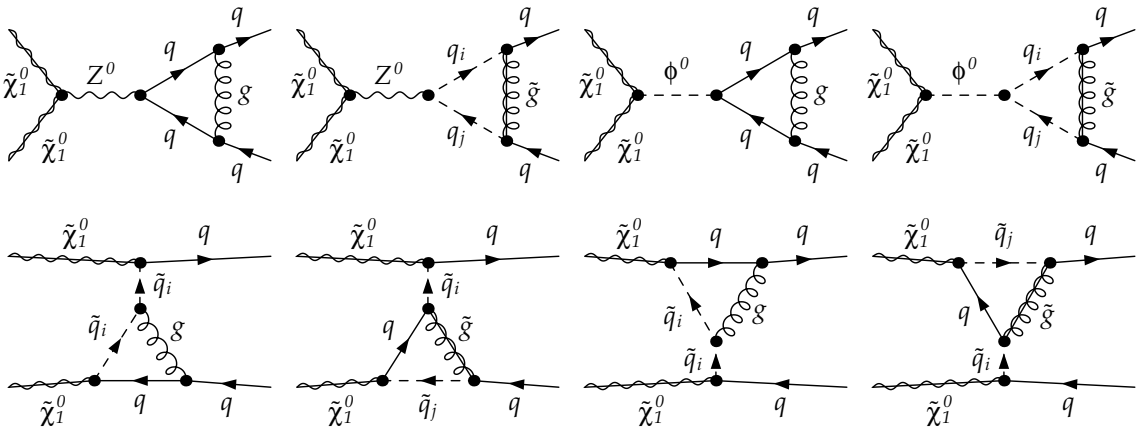

Figure 4.8: Vertex correction diagrams to the s-channel Z- and Higgs-boson exchange (top) and to the t-channel squark exchange (bottom) contributing at $\mathcal{O}(\alpha_s)$ to the annihilation cross section. The corresponding u-channel squark- exchange diagrams are not shown.

Starting with the virtual corrections, the quark and squark self-energies, the gluon and gluino vertex corrections, as well as the gluon and gluino box diagrams have been calculated, partly using the symbolic manipulation programme `FORM 3.1` [121]. We have also numerically compared our results for the squared matrix elements of all relevant squared matrix elements and interference terms with those obtained using the combination of `FeynArts 3.3` [122,123] and `FormCalc 5.0` [124,125]. The arising tensor integrals have been expressed in terms of the scalar integrals A_0, B_0, C_0, and D_0 by applying the common reduction methods described e.g. in Refs. [126, 127].

For the "heavy" third generation quarks, the squark propagators, and the Yukawa couplings the involved ultraviolet (UV) singularities are treated in the on-shell renormalization scheme, where the counterterms to the quark and squark masses, wave functions, and mixing matrices cancel the poles in $\epsilon = \big(4-D\big)/2$. Here, $D = 4-2\epsilon$ denotes the number of space-time dimensions. For a detailed calculation of the involved self-energies, vertex corrections, and box amplitudes see App. C.

After the renormalization procedure, only infrared (IR) singularities remain, which include

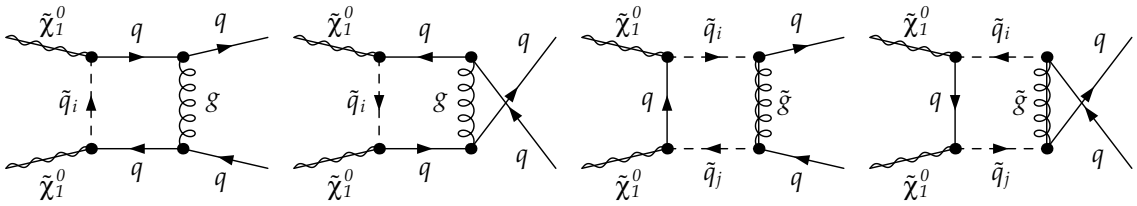

Figure 4.9: Box diagrams contributing at $\mathcal{O}(\alpha_s)$ to the annihilation cross section.

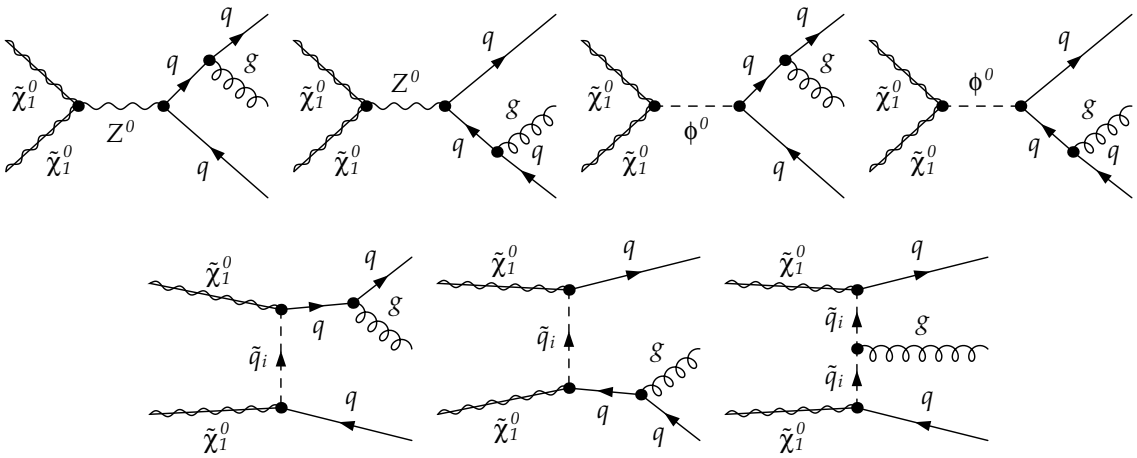

Figure 4.10: Real gluon emission diagrams contributing at $\mathcal{O}(\alpha_s)$ to the annihilation cross section. The corresponding u-channel squark exchange diagrams are not shown.

soft radiation and collinear divergences. These are canceled when taking into account the real gluon emission corrections shown in Fig. 4.10. Here, crossing leads again to u-channel diagrams that are not shown. The connection between the virtual and real emission parts of the cross sections has been implemented using the dipole subtraction method for massive partons proposed in Refs. [106, 128], based on the construction of an unphysical auxiliary cross section $\sigma_{\rm aux}$. By definition, the latter contains the same infrared singularities as also the virtual and real contributions. It is subtracted from the real part and added to the virtual part in order to cancel the remaining infrared poles in both contributions, that can then be integrated numerically separately. A more detailed presentation and discussion of the dipole subtraction method is given in App. D.

A careful treatment is required for the bottom-quark mass appearing in the Yukawa couplings, since it receives important corrections from QCD and SUSY-QCD loops, as already discussed in Chap. 3. We start from the running quark mass in the $\overline{\rm MS}$ scheme at the scale m_b as input parameter, $m_b^{\overline{\rm MS}}(m_b) = 4.2$ GeV, from which we obtain in a first step the $\overline{\rm MS}$ mass at the scale $Q^2 = s$ by applying three-loop renormalization group running [129],

$$m_b^{\overline{\rm MS}}(Q) \;=\; m_b^{\overline{\rm MS}}(m_b)\frac{F_b(Q)}{F_b(m_b)}, \tag{4.1}$$

where the function F_b is given by

$$F_b(Q) \;=\; \left[\frac{23}{6}\frac{\alpha_s(Q)}{\pi}\right]^{12/23}\left[1+\frac{3731}{3174}\frac{\alpha_s(Q)}{\pi}+1.500706\frac{\alpha_s^2(Q)}{\pi^2}\right]. \tag{4.2}$$

This intermediate result is then transformed at the two-loop level into the $\overline{\rm DR}$ scheme using the relation [129, 130]

$$m_b^{\overline{\rm DR}}(Q) \;=\; m_b^{\overline{\rm MS}}(Q)\left[1-\frac{1}{3}\frac{\alpha_s(Q)}{\pi}-\frac{29}{72}\frac{\alpha_s^2(Q)}{\pi^2}\right]. \tag{4.3}$$

We finally include one-loop threshold corrections at the scale $Q^2 = s$ in order to obtain the MSSM running mass in the $\overline{\rm DR}$ scheme [131],

$$m_b^{\overline{\rm DR}}(Q)_{\rm MSSM} \;=\; m_b^{\overline{\rm DR}}(Q)_{\rm SM}+\delta m_b^{\rm threshold}, \tag{4.4}$$

where the term $\delta m_b^{\rm threshold}$ includes the gluino-sbottom and stop-chargino loop contributions to the bottom-quark self-energy. The resulting value of $m_b^{\overline{\rm DR}}(Q)_{\rm MSSM}$ is then implemented in the Yukawa couplings. Note that the typical scale of a neutralino annihilation process is of the order of $Q \sim 100$ GeV, so that using the threshold corrections instead of the full MSSM renormalization group equations is a reasonable approximation [131]. Based on the value obtained in this way for the running bottom mass, we then resum the numerically important SUSY-QCD corrections coming from the sbottom-gluino and stop-chargino loops and take into account the finite remainders for the corresponding vertices as discussed in Sec. 3.3. We should note again that the mass resummation is already implemented at this order in the public version of `micrOMEGAs`, while `DarkSUSY` includes only the QCD running mass and finite corrections at $\mathcal{O}(\alpha_s^2)$, but no SUSY-QCD corrections.

The bottom quark pole mass $m_b^{\rm pole}$, which is used in the kinematics, is obtained from the input value $m_b^{\overline{\rm MS}}(m_b)$ through the two-loop relation [129]

$$\begin{aligned}\frac{m_b^{\overline{\rm MS}}(Q)}{m_b^{\rm pole}} \;&=\; 1+\frac{\alpha_s(Q)}{\pi}\left[\ln\frac{m_b^2(Q)}{Q^2}-\frac{4}{3}\right]+\frac{\alpha_s^2(Q)}{\pi^2}\left[-\frac{11}{3}\ln^2\frac{m_b^2(Q)}{Q^2}\right.\\ &\left.+\frac{197}{72}\ln\frac{m_b^2(Q)}{Q^2}-\frac{187}{32}+\frac{\zeta(3)}{6}+\frac{\pi^2}{9}\big(1+\ln 2\big)+\Delta\right],\end{aligned} \tag{4.5}$$

where ζ denotes the Riemann zeta-function and the correction effects due to the four light quarks are contained in the term

$$\Delta \;=\; \sum_{q=u,d,s,c}\frac{\pi^2}{6}\frac{m_q}{m_b}\left(1+\frac{m_q^2}{m_b^2}\right)-\frac{m_q^2}{m_b^2}. \tag{4.6}$$

The latter is, due to the involved mass ratios, however, numerically important only for the charm-quark mass, and negligible for the bottom quark considered here. Note that `micrOMEGAs` does not follow the same calculation prescription as the one discussed above. In particular, they use the same effective quark mass in the Yukawa coupling and in the kinematics. Thus, small differences in the cross section, and in consequence in the prediction of the relic density, may occur due to the different treatment of the bottom quark mass.

	m_0 (GeV)	$m_{1/2}$ (GeV)	A_0 (GeV)	$\tan\beta$	sgn(μ)	$\Omega_{\rm CDM}h^2$	$b\bar{b}$	$t\bar{t}$
1	1500	130	-1500	10	+	0.116	86%	–
2	1500	1500	0	50	+	0.112	83%	–
3	3800	570	0	10	+	0.108	–	72%
4	5300	625	-1500	10	+	0.110	–	72%
5	3000	600	0	50	+	0.110	15%	64%

Table 4.1: Scenarios in minimal supergravity (mSUGRA) that lead to a neutralino relic density agreeing with the current limits of Eq. (2.7), satisfy the current SUSY-particle mass limits, and present important contributions of neutralino annihilation into bottom or top quark-antiquark pairs. We indicate the mSUGRA parameters at the high scale, the relic density obtained with `micrOMEGAs 2.1`, and the contributions of the different quark final states to the annihilation cross section $\sigma_{\rm ann}v$.

For the top quark mass, we have as input parameter the pole mass $m_t^{\rm pole} = 171.4$ GeV, which can directly be used in the kinematics. Contrary to the bottom mass, we also implement the pole mass in the Yukawa couplings of the tree-level calculation, while we take into account all higher order effects in the calculation of the corresponding loop diagrams. Note that the top quark Yukawa couplings implemented in `micrOMEGAs 2.1` include already the calculation of an effective mass, which is also used in the kinematics instead of the pole mass in our calculation.

4.3 Impact on the Annihilation Cross Section

We now turn to the numerical impact of the QCD and SUSY-QCD corrections presented in Sec. 4.2 on the neutralino annihilation cross section. Based on the analysis of Sec. 4.1 we have chosen five scenarios in the minimal supergravity (mSUGRA) parameter space, shown in Tab. 4.1, that lead to a cold dark matter relic density in agreement with the limits of Eq. (2.7) and which are characterized by important contributions of top and/or bottom final states. For each set of parameters, we indicate the neutralino relic density obtained with `micrOMEGAs 2.1` as well as the relative contributions of bottom and top quark final states to the total annihilation cross section $\langle\sigma_{\rm ann}v\rangle$. Our scenario 1 is situated in the neighbourhood of the resonance of the light CP-even Higgs boson, while scenario 2 lies in the "A-funnel" region. Both are dominated by $b\bar{b}$ final states. Our scenarios 3, 4, and 5 all lie in the focus point region and have dominant contributions from annihilation into top quarks. Note that scenario 5 receives also a sizeable contributions from $b\bar{b}$ final states due to the important bottom Yukawa coupling at high $\tan\beta$. Note also that scenarios agreeing with the LEP mass limits and featuring an important contribution of light Higgs boson exchange can only be found for non-vanishing A_0. Regions with a top-quark contribution of more than 80 percent can be found for negative values of the Higgs mass parameter μ. We do, however, not consider those points in our analysis, since negative values of μ are disfavoured by the supersymmetric contributions to the anomalous magnetic moment a_μ, see Eq. (2.6).

In Figs. 4.11 – 4.13, we show the annihilation cross section $\sigma_{\rm ann}v$ of a neutralino pair into bottom or top quark-antiquark pairs for our scenarios 1 to 5 as a function of the relative

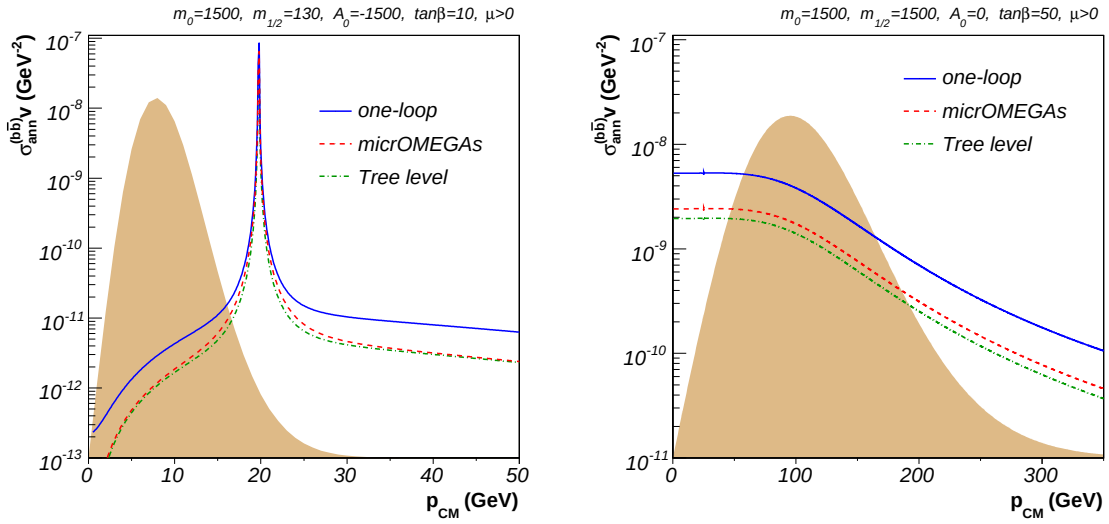

Figure 4.11: The annihilation cross section $\sigma_{\text{ann}}^{(b\bar{b})}v$ of a neutralino pair into a bottom quark-antiquark pair multiplied with the relative neutralino velocity v for our scenarios 1 (left) and 2 (right). We show our tree-level result (green dash-dotted), the cross section implemented in `micrOMEGAs 2.1` (red dashed), and the cross section including the full QCD and SUSY-QCD corrections (blue solid). The coloured area indicates, on a linear scale and in arbitrary units, the s-dependence of the Boltzmann velocity distribution involved in the calculation of the thermal averaged cross section.

momentum p_{cm} in the centre-of-momentum frame, related to the energy $\sqrt{s}$ through

$$s \;=\; 4\big(p_{\text{cm}}^2 + m_{\tilde{\chi}_1^0}^2\big). \tag{4.7}$$

The threshold at $p_{\text{cm}} = 0$ corresponds to $s = 4m_{\tilde{\chi}}^2$. For each scenario we show the cross sections calculated by `micrOMEGAs 2.1` (red dashed), our calculation at the tree-level (green dash-dotted), and our calculation including the full QCD and SUSY-QCD corrections (blue solid) discussed in Sec. 4.2. The coloured areas show the Boltzmann velocity distribution function $f_v(s)$ that governs the integral in the calculation of the thermal average $\langle\sigma_{\text{ann}}v\rangle$, see Eq. (2.11) and the discussion in Sec. 2.2. Since we are only interested in the relative distribution we omit all normalization factors, such as $m_{\tilde{\chi}}$ or T, that are constant with respect to the energy, and the s-dependent part of the distribution is shown in arbitrary units. For the temperature we insert the freeze-out temperature obtained through $T_f = m_{\tilde{\chi}_1^0}/x_f$, where x_f is the freeze-out parameter determined by `micrOMEGAs 2.1` in the calculation of the dark matter relic density.

For our scenario 1, shown in the left panel of Fig. 4.11, the resonance of the light Higgs boson h^0 is well visible around $p_{\text{cm}} \approx 20$ GeV. The Higgs and neutralino masses in this point are $m_{h^0} = 114.5$ GeV and $m_{\tilde{\chi}_1^0} = 53.7$ GeV, respectively, and the freeze-out parameter is $x_f = 24.35$ leading to $T_f = 2.21$ GeV. The width of the CP-even Higgs-boson is numerically small, $\Gamma_{h^0} = 3 \cdot 10^{-3}$ GeV, which results in a rather high and narrow peak of the annihilation cross section. Our tree-level cross section (green dash-dotted) agrees well with the one computed by `CalcHEP` in the `micrOMEGAs` package. The small but well visible difference can be traced to the different treatments of the bottom mass in the two calculations. First, `micrOMEGAs`

`2.1` calculates the bottom Yukawa coupling with the running mass in the $\overline{\text{MS}}$-scheme instead of $\overline{\text{DR}}$ in our calculation, see Sec. 4.2 for details. Second, in `micrOMEGAs 2.1`, the running bottom mass is also used in the kinematics, whereas in our calculation the kinematics is calculated using the on-shell mass as described in Sec. 4.2. Note, however, that the bottom mass is small compared to the centre-of-momentum energy $\sqrt{s} \geq 2m_{\tilde{\chi}_1^0} \approx 107.4$ GeV, so that the major part of the difference is due to the different masses in the calculation of the Yukawa couplings.

It is interesting to note that the peak of the velocity distribution, $p_{\text{cm}} \approx 8$ GeV, does not coincide with the peak of the annihilation cross section, $p_{\text{cm}} \approx 20$ GeV. This is connected to the fact that the favoured band with respect to WMAP data does not exactly lie on the resonance of the light Higgs boson, see Fig. 4.2. If the peaks were at the same value of p_{cm}, the resulting thermal averaged annihilation cross section would be too high to allow for a relic density agreeing with current cosmological data. The increase in the cross section when taking into account the full QCD and SUSY-QCD corrections, i.e. adding the finite terms and box contributions to the tree-level result containing already the bottom mass resummation, is numerically more important around the peak of the velocity distribution than around the Higgs resonance. For the latter, the dominating corrections are already contained in the QCD and SUSY-QCD bottom mass resummation. However, farther away from the pole, the finite contributions increase the annihilation cross section significantly. Let us recall that bottom quark final states account for 86 percent of the total annihilation cross section $\langle \sigma_{\text{ann}} v \rangle$.

For our scenario 2, situated in the "A-funnel" region of the mSUGRA parameter space, the neutralino mass is with $m_{\tilde{\chi}_1^0} = 655.7$ GeV too large to give rise to a resonance with the light Higgs boson ($m_{h^0} = 122.0$ GeV). However, the mass and width of the pseudoscalar Higgs boson are in this point $m_A = 1312.5$ GeV and $\Gamma_A = 43.0$ GeV, respectively, so that already the point $p_{\text{cm}} = 0$ is situated in the resonance of the pseudoscalar Higgs boson. The decrease of the cross section for larger values of p_{cm} is due to moving away from the pole. Again, we observe a noticeable difference between the predictions based on the effective tree-level calculations, which is explained by the same arguments as for scenario 1, i.e. the different treatments of the bottom quark mass. Taking into account the QCD and SUSY-QCD corrections leads to an increase of about 25 percent in the annihilation cross section, that is practically independent of the energy p_{cm}.

For the top quark dominated scenarios, the annihilation cross section $\sigma_{\text{ann}}^{(t\bar{t})} v$ of a neutralino pair into a top quark-antiquark pair is shown in Fig. 4.12 for our scenarios 3 and 4, lying both in the focus point region at $\tan\beta$ and $A_0 = 0$ and $A_0 = -1500$ GeV, respectively. We show again the cross sections obtained with the effective tree-level calculation, with `micrOMEGAs 2.1`, and including the full one-loop cross section. Due to the large top quark mass, the resonance of the light Higgs boson ($m_{h^0} = 120.5$ GeV) can not be encountered in these scenarios. Since the resonances of the heavy and pseudoscalar Higgs bosons occur at $p_{\text{cm}} \approx 1900$ GeV, the dependence of the cross sections on the energy is weak in the region of our interest. Note that the light scalar Higgs masses are with $m_{h^0} = 120.5$ GeV and $m_{h^0} = 120.8$ GeV practically independent from the rather important variation of the trilinear coupling A_0. The difference between the cross sections obtained with the `micrOMEGAs` calculation and our tree-level calculation are explained, as in the case of bottom quarks, by the different treatment of the top quark mass in the Yukawa couplings. `micrOMEGAs` uses an effective mass, while our calculation includes the value of the pole mass for the top quark, as discussed in Sec. 4.2. Numerically important contributions arise then from the QCD and SUSY-QCD corrections,

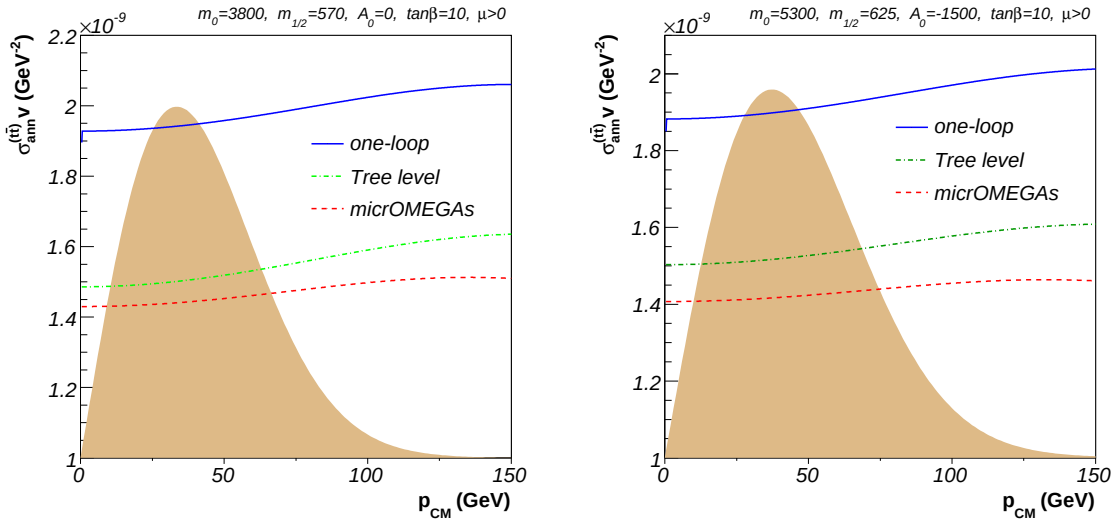

Figure 4.12: The annihilation cross section $\sigma_{\text{ann}}^{(t\bar{t})}v$ of a neutralino pair into a top quark-antiquark pair multiplied with the relative neutralino velocity v for our scenarios 3 (left) and 4 (right). We show our tree-level result (green dash-dotted), the cross section implemented in `micrOMEGAs 2.1` (red dashed), and the cross section including the full QCD and SUSY-QCD corrections (blue solid). The coloured area indicates, in arbitrary units, the s-dependence of the Boltzmann velocity distribution involved in the calculation of the thermal averaged cross section.

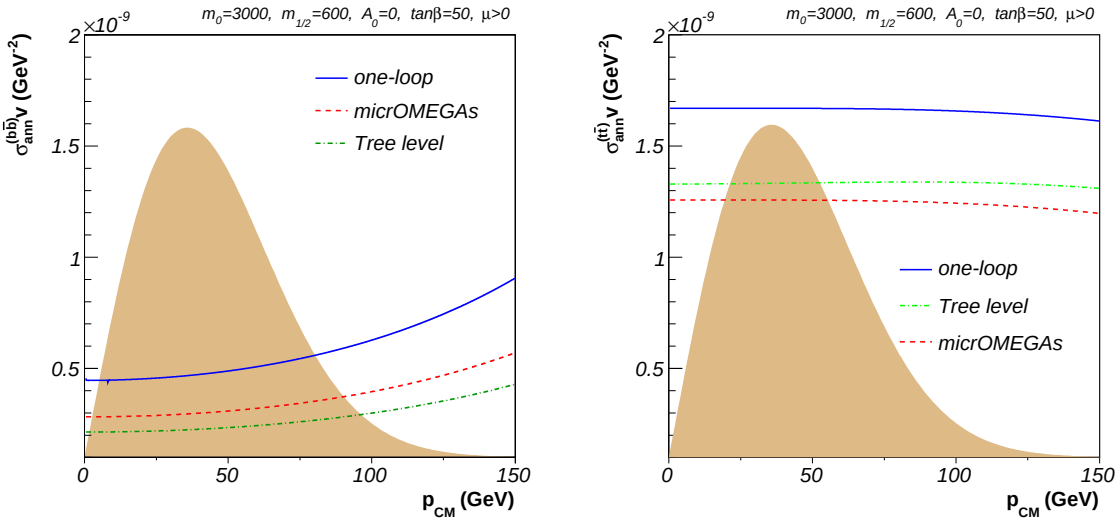

Figure 4.13: The annihilation cross sections $\sigma_{\text{ann}}^{(b\bar{b})}v$ (left) and $\sigma_{\text{ann}}^{(t\bar{t})}v$ of a neutralino pair into a bottom or top quark-antiquark pair multiplied with the relative neutralino velocity v for our scenarios 5. We show our tree-level result (green dash-dotted), the cross section implemented in `micrOMEGAs 2.1` (red dashed), and the cross section including the full QCD and SUSY-QCD corrections (blue solid). The coloured area indicates, in arbitrary units, the s-dependence of the Boltzmann velocity distribution involved in the calculation of the thermal averaged cross section.

that increase the annihilation cross section by up to 50 percent of the tree-level value in both scenarios.

Finally, let us discuss the neutralino pair annihilation cross section into bottom and top quark pairs for scenario 5 shown in Fig. 4.13. This parameter point is located in the focus point region at large $\tan\beta = 50$. Bottom quarks contribute here already to 15 percent of the total annihilation cross section, while top quarks are still dominant with 64 percent. This is due to the fact that the cross section for top quarks is about five times larger than the one for bottom quarks, as can be seen in Fig. 4.13. The neutralino mass is here $m_{\tilde{\chi}_1^0} = 245.5$ GeV, so that again no Higgs resonance is visible in the interesting range with $p_{\rm cm} \leq 150$ GeV. The tree-level calculation compared to `micrOMEGAs` shows the differences already discussed for the other parameter points. The corrections due to one-loop QCD and SUSY-QCD diagrams increase the cross section by about 50 percent for bottom and 20 percent for top quark final states, which corresponds to their numerical impact for the other scenarios.

4.4 Impact on the Neutralino Relic Density

We now study the effects of the QCD and SUSY-QCD corrections to neutralino annihilation into top and bottom quark-antiquark pairs on the prediction of the neutralino relic density. To this aim, the cross section including the corrections has been implemented into the public code `micrOMEGAs 2.1`. In this way, the relic density can be calculated either using the tree-level calculation for the processes shown in Fig. 4.1 or taking into account the new corrections presented in Sec. 4.2 for top- and/or bottom-quark final states.

In Fig. 4.14 we show the predictions for the relic density as a function $m_{1/2}$ and fixed $m_0 = 1500$ GeV, i.e. for a slope in the vicinity of our scenario 1. Since both the Higgs pole and the WMAP favoured band are independent from m_0 in this region (see Fig. 4.3), we do not study here a variation of m_0. We show the relic density obtained with `micrOMEGAs 2.1` using the originally implemented cross section (red dashed), our calculation of the tree-level (green dash-dotted), as well as our calculation including the full QCD and SUSY-QCD corrections (blue solid). The current limits of Eq. (2.7) obtained from WMAP, supernovae, and BAO data are represented as a coloured band. The Higgs pole is situated at $m_{1/2} = 138.5$ GeV, where the relic density is too low due to the enhanced annihilation cross section. To both sides of the pole, the cross section falls rapidly (see Fig. 4.11), so that the relic density increases. In consequence, two allowed intervals for $m_{1/2}$ are observed, the first being rather large at $m_{1/2} \approx 128.5 - 130.0$ GeV, the second very narrow around $m_{1/2} \approx 138.3$ GeV. Note that the latter is invisible on the scans of Fig. 4.3 due to the insufficient resolution. At lower values of $m_{1/2}$, the relic density is with $\Omega_{\rm CDM}h^2 \approx 0.17$ again rather low, but does not reach the WMAP favoured band. This behaviour is explained by the resonance of the Z^0-boson, situated at $m_{1/2} = 110.8$ GeV and enhancing again the annihilation cross section. However, the region where $m_{1/2} \lesssim 126$ GeV, indicated by a vertical dashed line, is already excluded by the LEP mass limits on the chargino, that becomes too light at such low values of the gaugino mass parameter $m_{1/2}$.

The differences between the tree-level calculations due to the treatment of the bottom quark mass and discussed in Sec. 4.3 propagate into the prediction of the relic density presented here. Since the annihilation through Z^0-boson exchange does not involve a quark Yukawa coupling, this difference is absent in the region around the Z^0-pole, where our tree-level prediction agrees well with the `micrOMEGAs` calculation. Taking into account the full

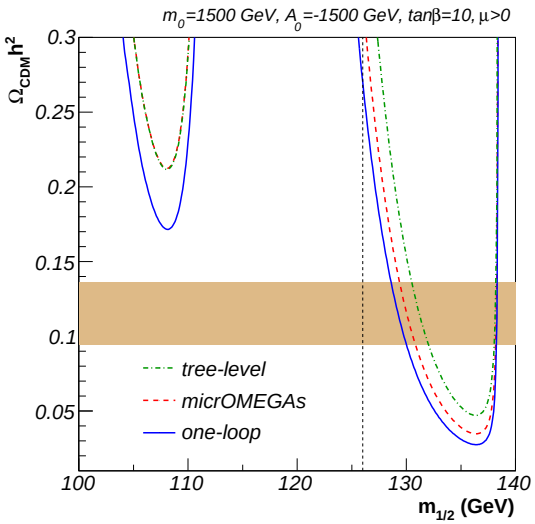

Figure 4.14: Prediction for the neutralino relic density $\Omega_{\mathrm{CDM}}h^2$ as a function of the gaugino mass parameter $m_{1/2}$ for our scenario 1. The coloured band indicates the cosmologically favoured region at 2σ, while the vertical dashed line separates the excluded (left) from the allowed (right) regions due to the LEP chargino-mass limit.

one-loop QCD and SUSY-QCD corrections, the relic density decreases. This is coherent with the increase of the cross section observed in Fig. 4.11. Since the numerically most important contribution, the bottom quark mass resummation, is already included as an effective coupling in the tree-level calculation, the decrease in the relic density around the Higgs pole is rather small. It is even smaller than the difference between the two predictions including the effective tree-level annihilation cross section. Note that, in order to compensate the larger annihilation cross section, the cosmologically preferred region is shifted away from the Higgs pole to smaller gaugino masses $m_{1/2}$, i.e. it approaches the exclusion limit on the chargino mass. Concerning the exchange of a Z^0-boson, no corrections are included in the tree-level calculation, so that the impact of the QCD and SUSY-QCD corrections is numerically more important around the Z^0-resonance.

In Fig. 4.15, we show the prediction for the neutralino relic density for our scenario 2. We here analyze its dependence on the scalar mass parameter m_0 and the gaugino mass parameter $m_{1/2}$. This scenario is situated at high $\tan\beta$ in the Higgs funnel region of the parameter space, and bottom quark final states contribute 83 percent of the total annihilation cross section. Again, a difference between the results obtained using the effective cross section at the tree-level is observed in both graphs. When implementing the one-loop corrections, the cross section is increased and the predicted relic density is significantly lower, resulting in a deformation of the cosmologically favoured contour in the parameter space. In particular, the allowed intervals for m_0 and $m_{1/2}$ based on the tree-level calculation are split into two ranges for the mass parameters, respectively. This is well visible in both panels of Fig. 4.15 and underlines again the importance of the non-resummable QCD and SUSY-QCD contributions to the annihilation cross section in this region of the mSUGRA parameter space.

Let us now turn to the scenarios that are dominated by top quark final states. In Fig. 4.16 we show the prediction of the neutralino relic density for scenario 3 in the focus point region,

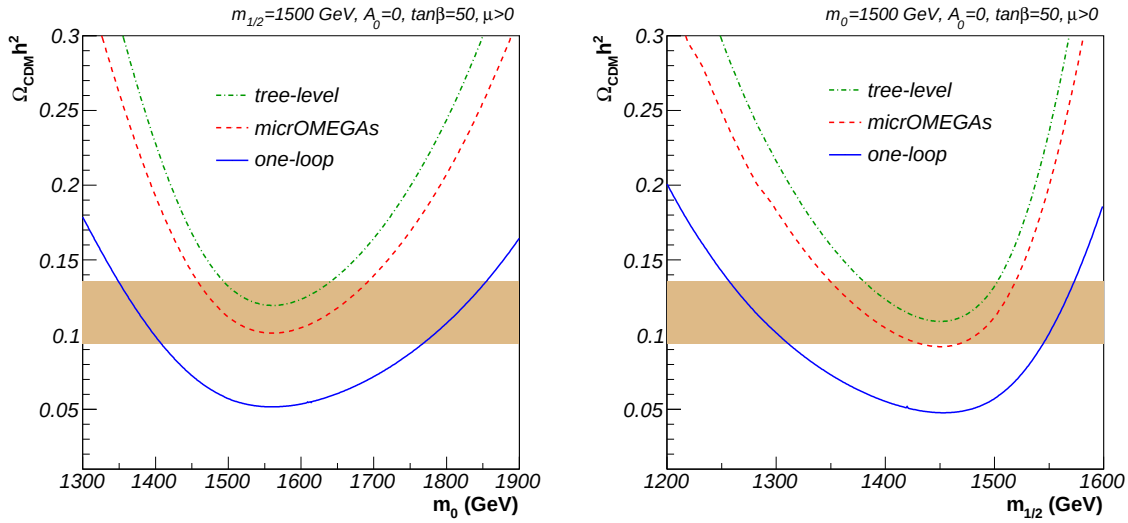

Figure 4.15: The prediction for the neutralino relic density $\Omega_{\mathrm{CDM}}h^2$ as a function of the scalar mass parameter m_0 (left) and the gaugino mass parameter $m_{1/2}$ (right) for our scenario 2 obtained with `micrOMEGAs 2.1` including their cross section calculation (red dashed), our tree-level calculation (greed dash-dotted), and our full one-loop QCD and SUSY-QCD cross section (blue solid) of the annihilation into $b\bar{b}$ and $t\bar{t}$ final states. The coloured band indicates the cosmologically favoured region at 2σ.

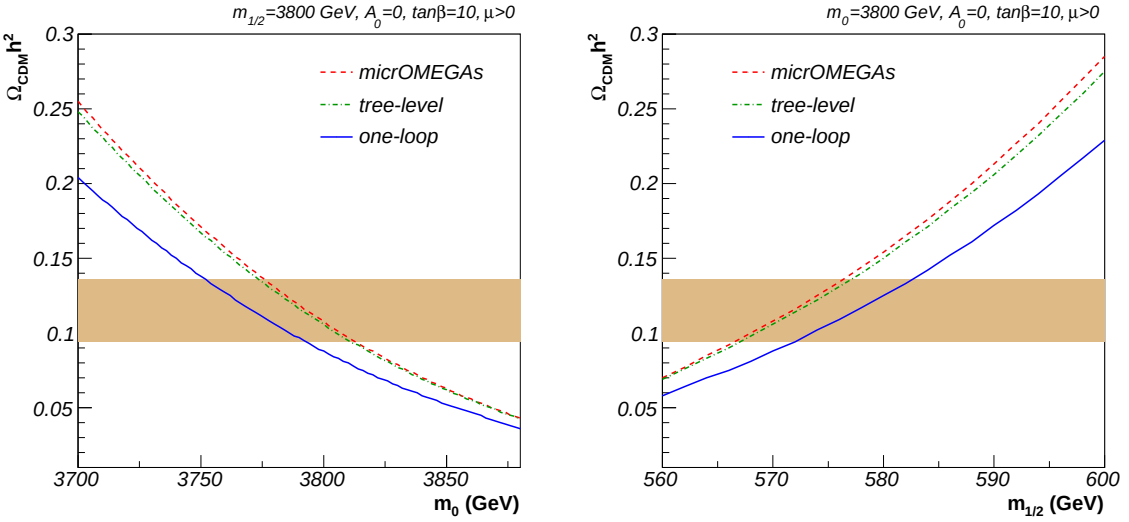

Figure 4.16: Same as Fig. 4.15 for our scenario 3.

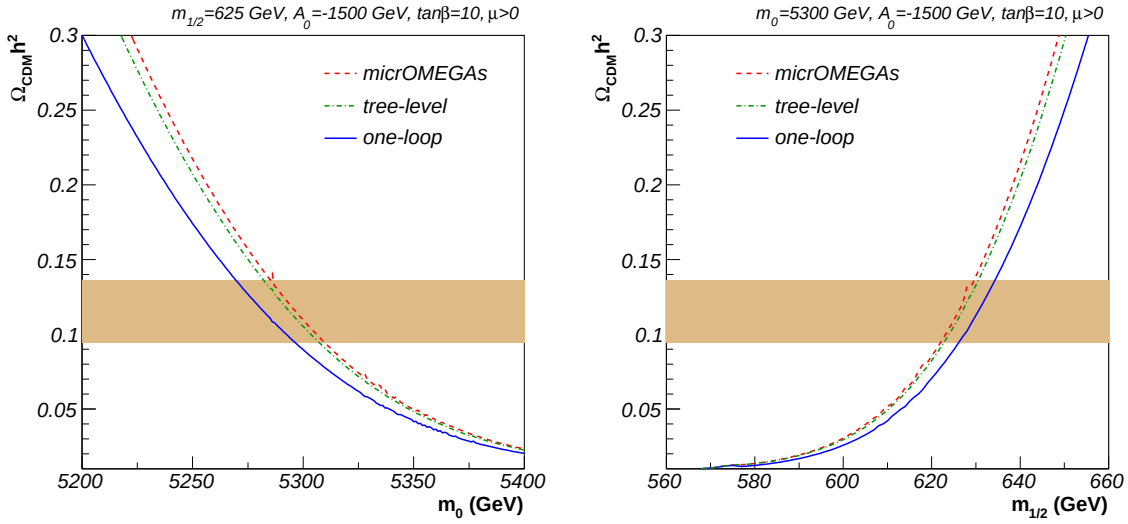

Figure 4.17: Same as Fig. 4.15 for our scenario 4.

where top final states contribute 72 percent to the thermally averaged annihilation cross section $\langle \sigma_{\rm ann} v \rangle$. Again, we analyze variations of m_0 and $m_{1/2}$ around the original parameter point. Here, the predictions based on the effective tree-level are in good agreement. As for the bottom quark final states, the one-loop QCD and SUSY-QCD corrections then increase the annihilation cross section, resulting in a decrease of about 20 percent in the neutralino relic density. In order to compensate this decrease, the WMAP-favoured regions are shifted to smaller scalar masses m_0, but larger gaugino masses $m_{1/2}$. This deformation gives rise to shifts of up to 50 GeV in m_0 and up to 30 GeV in $m_{1/2}$ and is therefore rather important. Note also that due to the implemented corrections, the WMAP favoured band becomes slightly larger, as can be seen in Fig. 4.15.

Scenario 4 is also situated in the focus point region at small $\tan\beta = 10$, but features a non-vanishing trilinear coupling $A_0 = -1500$ GeV. The corresponding predictions for the neutralino relic density obtained with `micrOMEGAs 2.1` are shown in Fig. 4.17. The situation is very similar to the one of the previous parameter point. We have rather good agreement between our tree-level calculation and the one implemented in `micrOMEGAs 2.1`, while the new one-loop corrections lead to a decrease of the order of 15 percent in the neutralino relic density. The preferred intervals are shifted smaller values of m_0 and to larger $m_{1/2}$, respectively.

Our scenario 5, lying in the focus point region at high $\tan\beta = 50$, presents an interesting configuration, since it receives sizeable annihilation contributions both from bottom (15%) and top (64%) quark final states. In the analysis of the impact of the one-loop corrections on the prediction of the neutralino relic density, shown in Fig. 4.18, we take into account not only the effective cross section at the tree-level and the full one-loop corrected cross section, but also the cross section taking into account only the one-loop corrections to the bottom quark final state while including only the effective tree-level for the top quarks. The latter is shown as an additional black dotted curve in the two panels of Fig. 4.18. It is interesting to note that the one-loop corrections to annihilation into bottom quarks contribute as much as about 50 percent of the total correction, while the total contribution of bottom quark final states is

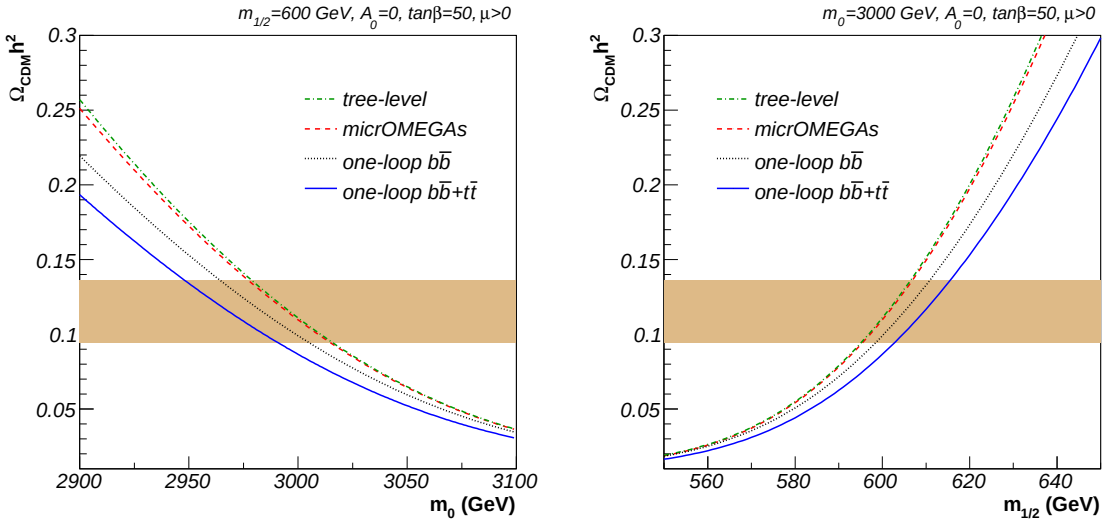

Figure 4.18: Same as Fig. 4.15 for our scenario 5. We here show in addition the neutralino relic density obtained implementing only the corrections to bottom quark final states (black dotted).

only of 15 percent in this region of the parameter space. This is explained by the fact that the annihilation cross section for $b\bar{b}$ final states receives numerically more important corrections that the one for $t\bar{t}$, as can be seen in Fig. 4.15. As in the other focus point scenarios, the WMAP favoured contour is shifted to smaller values of m_0 and higher values of $m_{1/2}$. The total shift is here of about 25 GeV in m_0 and 10 GeV in $m_{1/2}$. Note that the two independent contributions to the correction deform the contour in the same direction.

Chapter 5

Supersymmetric Particle Production at the LHC

As already seen in Chap. 2, non-minimal flavour violation (NMFV) may lead to interesting phenomenological aspects, in particular due to the avoided crossings of mass eigenvalues. This also holds for the production of supersymmetric particles at hadron colliders, which is discussed for the case of gauge-mediated Supersymmetry breaking (GMSB) in this Chapter. A similar study has been presented for mSUGRA scenarios within Ref. [65], that is, however, beyond the scope of this Thesis.

Total unpolarized hadronic cross sections

$$\sigma \;=\; \int_{4m^2/s}^{1} \mathrm{d}\tau \int_{-1/2\ln\tau}^{1/2\ln\tau} \mathrm{d}y \int_{t_{\min}}^{t_{\max}} \mathrm{d}t \; f_{a/A}(x_a, M_a^2)\; f_{b/B}(x_b, M_b^2)\; \frac{\mathrm{d}\hat{\sigma}}{\mathrm{d}t} \tag{5.1}$$

are obtained through convolving the relevant partonic cross section $\mathrm{d}\hat{\sigma}/\mathrm{d}t$ with universal parton densities $f_{a/A}$ and $f_{b/B}$ of partons a, b in the hadrons A, B, which depend on the longitudinal momentum fractions of the two partons $x_{a,b} = \sqrt{\tau}e^{\pm y}$ and on the unphysical factorization scales $M_{a,b}$. Unpolarized cross sections, averaged over initial spins, can be derived from the expression

$$\mathrm{d}\hat{\sigma} \;=\; \frac{1}{4}\Big[\mathrm{d}\hat{\sigma}_{1,1} + \mathrm{d}\hat{\sigma}_{1,-1} + \mathrm{d}\hat{\sigma}_{-1,1} + \mathrm{d}\hat{\sigma}_{-1,-1}\Big], \tag{5.2}$$

while single- and double-polarized cross sections, including the same average factor for initial spins, are given by

$$\mathrm{d}\Delta\hat{\sigma}_{\mathrm{L}} \;=\; \frac{1}{4}\Big[\mathrm{d}\hat{\sigma}_{1,1} + \mathrm{d}\hat{\sigma}_{1,-1} - \mathrm{d}\hat{\sigma}_{-1,1} - \mathrm{d}\hat{\sigma}_{-1,-1}\Big], \tag{5.3}$$

$$\mathrm{d}\Delta\hat{\sigma}_{\mathrm{LL}} \;=\; \frac{1}{4}\Big[\mathrm{d}\hat{\sigma}_{1,1} - \mathrm{d}\hat{\sigma}_{1,-1} - \mathrm{d}\hat{\sigma}_{-1,1} + \mathrm{d}\hat{\sigma}_{-1,-1}\Big]. \tag{5.4}$$

We first give analytical expressions for the helicity-depending partonic production cross sections $\mathrm{d}\hat{\sigma}_{h_a,h_b}$ of squarks, gluinos, gauginos, and gravitinos in non-minimal flavour violating Supersymmetry. We also include analytical results for decay widths that involve gravitinos. We finally present numerical predictions for the relevant production channels at the CERN Large Hadron Collider (LHC) for the benchmark points E to J presented in Chap. 2 [66].

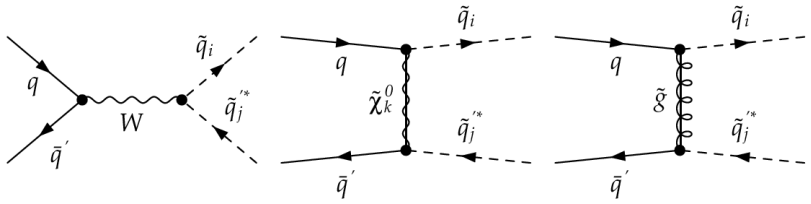

Figure 5.1: Tree-level Feynman diagrams for the production of charged squark-antisquark pairs in quark-antiquark collisions.

5.1 Squark and Gaugino Production

For definite helicities h_a, h_b of the initial state partons $a, b = q, \bar{q}, g$ the cross sections are expressed in terms of the squark, chargino, neutralino, and gluino masses $m_{\tilde{q}_k}$, $m_{\tilde{\chi}_k^\pm}$, $m_{\tilde{\chi}_k^0}$, and $m_{\tilde{g}}$, the conventional Mandelstam variables

$$s \;=\; \big(p_a + p_b\big)^2, \quad t \;=\; \big(p_a - p_1\big)^2, \quad \text{and} \quad u \;=\; \big(p_a - p_2\big)^2, \tag{5.5}$$

and the masses of the neutral and charged electroweak gauge bosons m_Z and m_W. Propagators appear as mass-subtracted Mandelstam variables

$$s_\xi \;=\; s - m_\xi^2, \quad t_\xi \;=\; t - m_\xi^2, \quad \text{and} \quad u_\xi \;=\; u - m_\xi^2, \tag{5.6}$$

for $\xi = Z,\ W,\ \tilde{q}_i,\ \tilde{g},\ \tilde{\chi}_k^\pm,\ \tilde{\chi}_k^0$. The generalized coupling strengths in non-minimal flavour violating Supersymmetry are denoted L_{abc}, R_{abc}, or for simplicity

$$\big\{\mathcal{C}^1_{abc},\ \mathcal{C}^2_{abc}\big\} \;=\; \big\{L_{abc},\ R_{abc}\big\}. \tag{5.7}$$

Also involved are several form factors, which are, together with all generalized couplings and charges, listed in App. A. Note that the definition slightly differs from the one of Ref. [65] in order to have a single notation for chargino and neutralino production and decays.

Let us start with the production of charged squark-antisquark pairs proceeding from an equally charged quark-antiquark initial state through the Feynman diagrams shown in Fig. 5.1. The corresponding cross section can be written in a compact way as

$$\begin{aligned}
\frac{\mathrm{d}\hat{\sigma}^{q\bar{q}'}_{h_a,h_b}}{\mathrm{d}t} \;=\;& \big(1-h_a\big)\big(1+h_b\big)\left[\frac{\mathcal{W}}{s_W^2} + \left(\sum_{k,l=1}^{4} \frac{\mathcal{N}^{kl}_{11}}{t_{\tilde{\chi}_k^0} t_{\tilde{\chi}_l^0}}\right) + \frac{\mathcal{G}_{11}}{t_{\tilde{g}}^2} + \left(\sum_{k=1}^{4} \frac{\big[\mathcal{N}\mathcal{W}\big]^k}{t_{\tilde{\chi}_k^0} s_W}\right) + \frac{\big[\mathcal{G}\mathcal{W}\big]}{t_{\tilde{g}}^2}\right] \\
&+ \big(1-h_a\big)\big(1-h_b\big)\left[\left(\sum_{k,l=1}^{4} \frac{\mathcal{N}^{kl}_{12}}{t_{\tilde{\chi}_k^0} t_{\tilde{\chi}_l^0}}\right) + \frac{\mathcal{G}_{12}}{t_{\tilde{g}}^2}\right] \\
&+ \big(1+h_a\big)\big(1+h_b\big)\left[\left(\sum_{k,l=1}^{4} \frac{\mathcal{N}^{kl}_{21}}{t_{\tilde{\chi}_k^0} t_{\tilde{\chi}_l^0}}\right) + \frac{\mathcal{G}_{21}}{t_{\tilde{g}}^2}\right] \\
&+ \big(1+h_a\big)\big(1-h_b\big)\left[\left(\sum_{k,l=1}^{4} \frac{\mathcal{N}^{kl}_{22}}{t_{\tilde{\chi}_k^0} t_{\tilde{\chi}_l^0}}\right) + \frac{\mathcal{G}_{22}}{t_{\tilde{g}}^2}\right],
\end{aligned} \tag{5.8}$$

where coupling constants and Dirac traces are contained in the form factors. In constrained minimal flavour violation (cMFV), superpartners of heavy flavours can only be produced

through the purely left-handed s-channel W-boson exchange, since the t-channel diagrams are suppressed by the small bottom and negligible top quark densities in the proton, and one recovers the result of Ref. [132]. In non-minimal flavour violation (NMFV), t-channel exchanges can, however, contribute to heavy-flavour final state production from light-flavour initial states and even become dominant, due to the strong gluino coupling.

Neutral squark-antisquark pairs are produced either from equally neutral quark-antiquark initial states through different gauge-boson or gaugino exchanges or from gluon fusion through purely strong couplings. The corresponding Feynman diagrams are shown in Fig. 5.2. The differential cross section for quark-antiquark scattering is given by

$$\begin{aligned}
\frac{\mathrm{d}\hat{\sigma}^{q\bar{q}'}_{h_a,h_b}}{\mathrm{d}t} &= \big(1-h_a\big)\big(1+h_b\big)\Bigg[\frac{\mathcal{Y}}{s^2}+\frac{\mathcal{Z}_1}{s_Z^2}+\frac{\mathcal{G}}{s^2}+\frac{\tilde{\mathcal{G}}_{11}}{t_{\tilde{g}}^2}+\frac{\big[\mathcal{Y}\mathcal{Z}\big]_1}{ss_Z}+\frac{\big[\tilde{\mathcal{G}}\mathcal{Y}\big]_1}{t_{\tilde{g}}s}+\frac{\big[\tilde{\mathcal{G}}Z\big]_1}{t_{\tilde{g}}s_Z} \\
&\quad+\frac{\big[\tilde{\mathcal{G}}\mathcal{G}\big]_1}{t_{\tilde{g}}s}+\Bigg(\sum_{k,l=1}^{4}\frac{\mathcal{N}_{11}^{kl}}{t_{\tilde{\chi}_k^0}t_{\tilde{\chi}_l^0}}\Bigg)+\sum_{k=1}^{4}\Bigg(\frac{\big[\mathcal{N}\mathcal{Y}\big]_1^k}{t_{\tilde{\chi}_k^0}s}+\frac{\big[\mathcal{N}\mathcal{Z}\big]_1^k}{t_{\tilde{\chi}_k^0}s_Z}+\frac{\big[\mathcal{N}\mathcal{G}\big]_1^k}{t_{\tilde{\chi}_k^0}s}\Bigg) \\
&\quad+\Bigg(\sum_{k,l=1}^{2}\frac{\mathcal{C}_{11}^{kl}}{t_{\tilde{\chi}_k^\pm}t_{\tilde{\chi}_l^\pm}}\Bigg)+\sum_{k=1}^{2}\Bigg(\frac{\big[\mathcal{C}\mathcal{Y}\big]_1^k}{t_{\tilde{\chi}_k^0}s}+\frac{\big[\mathcal{C}\mathcal{Z}\big]_1^k}{t_{\tilde{\chi}_k^\pm}s_Z}+\frac{\big[\mathcal{C}\mathcal{G}\big]_1^k}{t_{\tilde{\chi}_k^\pm}s}\Bigg)\Bigg] \\
&\quad+\big(1+h_a\big)\big(1-h_b\big)\Bigg[\frac{\mathcal{Y}}{s^2}+\frac{\mathcal{Z}_2}{s_Z^2}+\frac{\mathcal{G}}{s^2}+\frac{\tilde{\mathcal{G}}_{22}}{t_{\tilde{g}}^2}+\frac{\big[\mathcal{Y}\mathcal{Z}\big]_2}{ss_Z}+\frac{\big[\tilde{\mathcal{G}}\mathcal{Y}\big]_2}{t_{\tilde{g}}s}+\frac{\big[\tilde{\mathcal{G}}Z\big]_2}{t_{\tilde{g}}s_Z} \\
&\quad+\frac{\big[\tilde{\mathcal{G}}\mathcal{G}\big]_2}{t_{\tilde{g}}s}+\Bigg(\sum_{k,l=1}^{4}\frac{\mathcal{N}_{22}^{kl}}{t_{\tilde{\chi}_k^0}t_{\tilde{\chi}_l^0}}\Bigg)+\sum_{k=1}^{4}\Bigg(\frac{\big[\mathcal{N}\mathcal{Y}\big]_2^k}{t_{\tilde{\chi}_k^0}s}+\frac{\big[\mathcal{N}\mathcal{Z}\big]_2^k}{t_{\tilde{\chi}_k^0}s_Z}+\frac{\big[\mathcal{N}\mathcal{G}\big]_2^k}{t_{\tilde{\chi}_k^0}s}\Bigg) \\
&\quad+\Bigg(\sum_{k,l=1}^{2}\frac{\mathcal{C}_{22}^{kl}}{t_{\tilde{\chi}_k^\pm}t_{\tilde{\chi}_l^\pm}}\Bigg)+\sum_{k=1}^{2}\Bigg(\frac{\big[\mathcal{C}\mathcal{Y}\big]_2^k}{t_{\tilde{\chi}_k^0}s}+\frac{\big[\mathcal{C}\mathcal{Z}\big]_2^k}{t_{\tilde{\chi}_k^\pm}s_Z}+\frac{\big[\mathcal{C}\mathcal{G}\big]_2^k}{t_{\tilde{\chi}_k^\pm}s}\Bigg)\Bigg] \\
&\quad+\big(1-h_a\big)\big(1-h_b\big)\Bigg[\frac{\tilde{\mathcal{G}}_{12}}{t_{\tilde{g}}^2}+\Bigg(\sum_{k,l=1}^{4}\frac{\mathcal{N}_{12}^{kl}}{t_{\tilde{\chi}_k^0}t_{\tilde{\chi}_l^0}}\Bigg)+\Bigg(\sum_{k,l=1}^{2}\frac{\mathcal{C}_{12}^{kl}}{t_{\tilde{\chi}_k^\pm}t_{\tilde{\chi}_l^\pm}}\Bigg)\Bigg] \\
&\quad+\big(1+h_a\big)\big(1+h_b\big)\Bigg[\frac{\tilde{\mathcal{G}}_{21}}{t_{\tilde{g}}^2}+\Bigg(\sum_{k,l=1}^{4}\frac{\mathcal{N}_{21}^{kl}}{t_{\tilde{\chi}_k^0}t_{\tilde{\chi}_l^0}}\Bigg)+\Bigg(\sum_{k,l=1}^{2}\frac{\mathcal{C}_{21}^{kl}}{t_{\tilde{\chi}_k^\pm}t_{\tilde{\chi}_l^\pm}}\Bigg)\Bigg], \qquad (5.9)
\end{aligned}$$

where only very few interferences are eliminated due to colour conservation. The gluon-initiated cross section reads

$$\frac{\mathrm{d}\hat{\sigma}^{gg}_{h_a,h_b}}{\mathrm{d}t} = \frac{\pi\alpha_s}{6s^2}\Bigg[1-\frac{9t_{\tilde{q}_i}u_{\tilde{q}_i}}{4s^2}\Bigg]\Bigg[\big(1-h_ah_b\big)-\frac{2sm_{\tilde{q}_i}^2}{t_{\tilde{q}_i}u_{\tilde{q}_i}}\Bigg(\big(1-h_ah_b\big)-\frac{sm_{\tilde{q}_i}^2}{t_{\tilde{q}_i}u_{\tilde{q}_i}}\Bigg)\Bigg], \qquad (5.10)$$

involving only the strong coupling constant and being therefore more compact. In the limit of constrained minimal flavour violation (cMFV), but diagonal or non-diagonal squark helicity, these results agree with those of Ref. [132]. Diagonal production of identical squark-antisquark mass eigenstates is, of course, dominated by the strong quark-antiquark and gluon-gluon channels. Their relative importance depends on the partonic luminosity and thus on the type and energy of the hadron collider under consideration. Non-diagonal production of squarks of different helicity or flavour involves only electroweak and gluino-mediated quark-antiquark scattering, and the relative importance of these processes depends largely on the gluino mass.

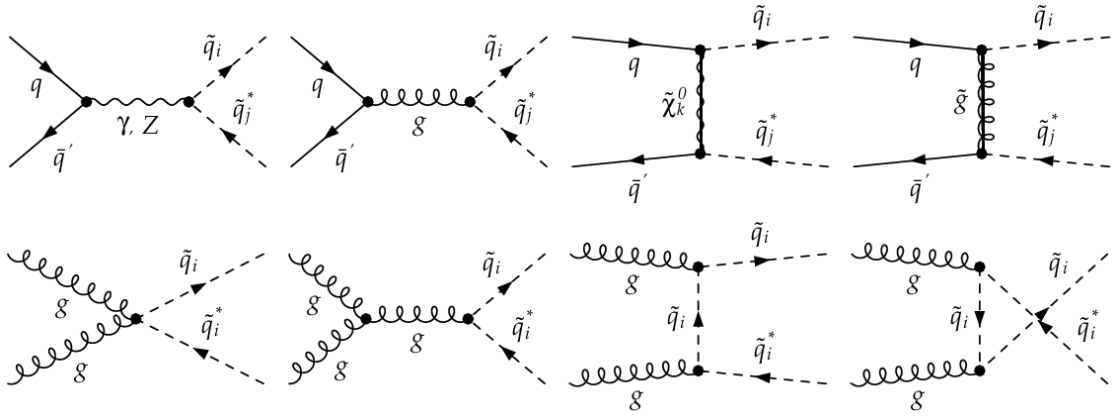

Figure 5.2: Tree-level Feynman diagrams for the production of neutral squark-antisquark pairs.

While squark-antisquark pairs are readily produced in $p\bar{p}$ collisions, e.g. at the Tevatron, from valence quarks and antiquarks, pp colliders have a larger quark-quark luminosity and will thus more easily lead to squark pair production. The production of one down-type and one up-type squark in the collision of an up-type and a down-type quark proceeds through the t-channel chargino or u-channel neutralino and gluino exchanges shown in Fig. 5.3. The corresponding cross section is given by

$$
\begin{aligned}
\frac{\mathrm{d}\hat{\sigma}^{qq'}_{h_a,h_b}}{\mathrm{d}t} \;=\; & \big(1-h_a\big)\big(1-h_b\big)\left[\frac{\mathcal{G}_{11}}{u^2_{\tilde{g}}}+\left(\sum_{k,l=1}^{2}\frac{\mathcal{C}^{kl}_{11}}{t_{\tilde{\chi}_k}t_{\tilde{\chi}_l}}\right)+\left(\sum_{k,l=1}^{4}\frac{\mathcal{N}^{kl}_{11}}{u_{\tilde{\chi}^0_k}u_{\tilde{\chi}^0_l}}\right)\right.\\
& \left.+\left(\sum_{k=1}^{2}\sum_{l=1}^{4}\frac{\big[\mathcal{CN}\big]^{kl}_{11}}{t_{\tilde{\chi}_k}u_{\tilde{\chi}^0_l}}\right)+\left(\sum_{k=1}^{2}\frac{\big[\mathcal{CG}\big]^{k}_{11}}{t_{\tilde{\chi}_k}u_{\tilde{g}}}\right)\right]\\
& +\big(1+h_a\big)\big(1+h_b\big)\left[\frac{\mathcal{G}_{22}}{u^2_{\tilde{g}}}+\left(\sum_{k,l=1}^{2}\frac{\mathcal{C}^{kl}_{22}}{t_{\tilde{\chi}_k}t_{\tilde{\chi}_l}}\right)+\left(\sum_{k,l=1}^{4}\frac{\mathcal{N}^{kl}_{22}}{u_{\tilde{\chi}^0_k}u_{\tilde{\chi}^0_l}}\right)\right.\\
& \left.+\left(\sum_{k=1}^{2}\sum_{l=1}^{4}\frac{\big[\mathcal{CN}\big]^{kl}_{22}}{t_{\tilde{\chi}_k}u_{\tilde{\chi}^0_l}}\right)+\left(\sum_{k=1}^{2}\frac{\big[\mathcal{CG}\big]^{k}_{22}}{t_{\tilde{\chi}_k}u_{\tilde{g}}}\right)\right]\\
& +\big(1-h_a\big)\big(1+h_b\big)\left[\frac{\mathcal{G}_{12}}{u^2_{\tilde{g}}}+\left(\sum_{k,l=1}^{2}\frac{\mathcal{C}^{kl}_{12}}{t_{\tilde{\chi}_k}t_{\tilde{\chi}_l}}\right)+\left(\sum_{k,l=1}^{4}\frac{\mathcal{N}^{kl}_{12}}{u_{\tilde{\chi}^0_k}u_{\tilde{\chi}^0_l}}\right)\right.\\
& \left.+\left(\sum_{k=1}^{2}\sum_{l=1}^{4}\frac{\big[\mathcal{CN}\big]^{kl}_{12}}{t_{\tilde{\chi}_k}u_{\tilde{\chi}^0_l}}\right)+\left(\sum_{k=1}^{2}\frac{\big[\mathcal{CG}\big]^{k}_{12}}{t_{\tilde{\chi}_k}u_{\tilde{g}}}\right)\right]\\
& +\big(1+h_a\big)\big(1-h_b\big)\left[\frac{\mathcal{G}_{21}}{u^2_{\tilde{g}}}+\left(\sum_{k,l=1}^{2}\frac{\mathcal{C}^{kl}_{21}}{t_{\tilde{\chi}_k}t_{\tilde{\chi}_l}}\right)+\left(\sum_{k,l=1}^{4}\frac{\mathcal{N}^{kl}_{21}}{u_{\tilde{\chi}^0_k}u_{\tilde{\chi}^0_l}}\right)\right.\\
& \left.+\left(\sum_{k=1}^{2}\sum_{l=1}^{4}\frac{\big[\mathcal{CN}\big]^{kl}_{21}}{t_{\tilde{\chi}_k}u_{\tilde{\chi}^0_l}}\right)+\left(\sum_{k=1}^{2}\frac{\big[\mathcal{CG}\big]^{k}_{21}}{t_{\tilde{\chi}_k}u_{\tilde{g}}}\right)\right]. \qquad (5.11)
\end{aligned}
$$

Note the absence of a neutralino-gluino interference term due to colour conservation. The

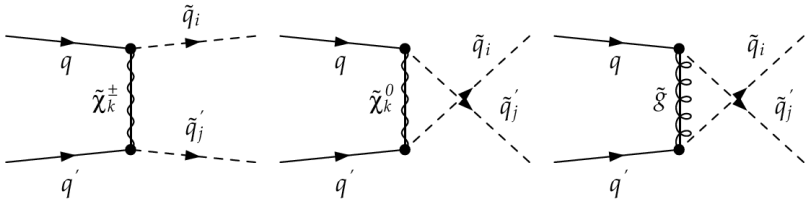

Figure 5.3: Tree-level Feynman diagrams for the production of an up-type and a down-type squark in the collision of an up-type and a down-type quark.

cross section for the charge-conjugated production of antisquarks from antiquarks can be obtained from the equations above by replacing $h_{a,b} \to -h_{a,b}$. Heavy flavour final states are completely absent in constrained minimal flavour violation (cMFV) due to the negligible top quark and small bottom quark densities in the proton and can thus only be obtained in non-minimal flavour violation.

In Fig. 5.4, we show the Feynman diagrams for the production of a pair of up-type or down-type squarks. Taking into account non-minimal flavour violation, neutralino and gluino exchanges can lead to identical squark flavours for different quark initial states, so that both t- and u-channels contribute and may interfere. In the cross section

$$
\begin{aligned}
\frac{\mathrm{d}\hat{\sigma}^{qg}_{h_a,h_b}}{\mathrm{d}t} \;=\; & \frac{(1-h_a)(1-h_b)}{1+\delta_{ij}}\left[\sum_{k,l=1}^{4}\left(\frac{[\mathcal{NT}]^{kl}_{11}}{t_{\tilde{\chi}^0_k}t_{\tilde{\chi}^0_l}}+\frac{[\mathcal{NU}]^{kl}_{11}}{u_{\tilde{\chi}^0_k}u_{\tilde{\chi}^0_l}}+\frac{[\mathcal{NTU}]^{kl}_{11}}{t_{\tilde{\chi}^0_k}u_{\tilde{\chi}^0_l}}\right)+\frac{[\mathcal{GT}]^{kl}_{11}}{t^2_{\tilde{g}}}\right.\\
& \left.+\frac{[\mathcal{GU}]^{kl}_{11}}{u^2_{\tilde{g}}}+\frac{[\mathcal{GTU}]^{kl}_{11}}{t_{\tilde{g}}u_{\tilde{g}}}+\sum_{k=1}^{4}\left(\frac{[\mathcal{NGA}]^{k}_{11}}{t_{\tilde{\chi}^0_k}u_{\tilde{g}}}+\frac{[\mathcal{NGB}]^{k}_{11}}{u_{\tilde{\chi}^0_k}t_{\tilde{g}}}\right)\right]\\
& +\frac{(1+h_a)(1+h_b)}{1+\delta_{ij}}\left[\sum_{k,l=1}^{4}\left(\frac{[\mathcal{NT}]^{kl}_{22}}{t_{\tilde{\chi}^0_k}t_{\tilde{\chi}^0_l}}+\frac{[\mathcal{NU}]^{kl}_{22}}{u_{\tilde{\chi}^0_k}u_{\tilde{\chi}^0_l}}+\frac{[\mathcal{NTU}]^{kl}_{22}}{t_{\tilde{\chi}^0_k}u_{\tilde{\chi}^0_l}}\right)+\frac{[\mathcal{GT}]^{kl}_{22}}{t^2_{\tilde{g}}}\right.\\
& \left.+\frac{[\mathcal{GU}]^{kl}_{22}}{u^2_{\tilde{g}}}+\frac{[\mathcal{GTU}]^{kl}_{22}}{t_{\tilde{g}}u_{\tilde{g}}}+\sum_{k=1}^{4}\left(\frac{[\mathcal{NGA}]^{k}_{22}}{t_{\tilde{\chi}^0_k}u_{\tilde{g}}}+\frac{[\mathcal{NGB}]^{k}_{22}}{u_{\tilde{\chi}^0_k}t_{\tilde{g}}}\right)\right]\\
& +\frac{(1-h_a)(1+h_b)}{1+\delta_{ij}}\left[\sum_{k,l=1}^{4}\left(\frac{[\mathcal{NT}]^{kl}_{12}}{t_{\tilde{\chi}^0_k}t_{\tilde{\chi}^0_l}}+\frac{[\mathcal{NU}]^{kl}_{12}}{u_{\tilde{\chi}^0_k}u_{\tilde{\chi}^0_l}}+\frac{[\mathcal{NTU}]^{kl}_{12}}{t_{\tilde{\chi}^0_k}u_{\tilde{\chi}^0_l}}\right)+\frac{[\mathcal{GT}]^{kl}_{12}}{t^2_{\tilde{g}}}\right.\\
& \left.+\frac{[\mathcal{GU}]^{kl}_{12}}{u^2_{\tilde{g}}}+\frac{[\mathcal{GTU}]^{kl}_{12}}{t_{\tilde{g}}u_{\tilde{g}}}+\sum_{k=1}^{4}\left(\frac{[\mathcal{NGA}]^{k}_{12}}{t_{\tilde{\chi}^0_k}u_{\tilde{g}}}+\frac{[\mathcal{NGB}]^{k}_{12}}{u_{\tilde{\chi}^0_k}t_{\tilde{g}}}\right)\right]\\
& +\frac{(1+h_a)(1-h_b)}{1+\delta_{ij}}\left[\sum_{k,l=1}^{4}\left(\frac{[\mathcal{NT}]^{kl}_{21}}{t_{\tilde{\chi}^0_k}t_{\tilde{\chi}^0_l}}+\frac{[\mathcal{NU}]^{kl}_{21}}{u_{\tilde{\chi}^0_k}u_{\tilde{\chi}^0_l}}+\frac{[\mathcal{NTU}]^{kl}_{21}}{t_{\tilde{\chi}^0_k}u_{\tilde{\chi}^0_l}}\right)+\frac{[\mathcal{GT}]^{kl}_{21}}{t^2_{\tilde{g}}}\right.\\
& \left.+\frac{[\mathcal{GU}]^{kl}_{21}}{u^2_{\tilde{g}}}+\frac{[\mathcal{GTU}]^{kl}_{21}}{t_{\tilde{g}}u_{\tilde{g}}}+\sum_{k=1}^{4}\left(\frac{[\mathcal{NGA}]^{k}_{21}}{t_{\tilde{\chi}^0_k}u_{\tilde{g}}}+\frac{[\mathcal{NGB}]^{k}_{21}}{u_{\tilde{\chi}^0_k}t_{\tilde{g}}}\right)\right]
\end{aligned}
\tag{5.12}
$$

gluinos dominate over neutralino exchanges due to their strong coupling, and the two only interfere in the mixed t- and u-channels due to colour conservation. At the LHC, up-type squark pair production should dominate over mixed up-/down-type squark production and down-type squark pair production, since the proton contains two valence up-quarks and only

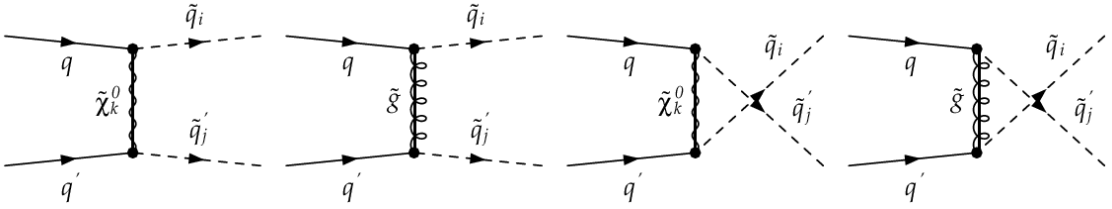

Figure 5.4: Tree-level Feynman diagrams for the production of two up-type or down-type squarks.

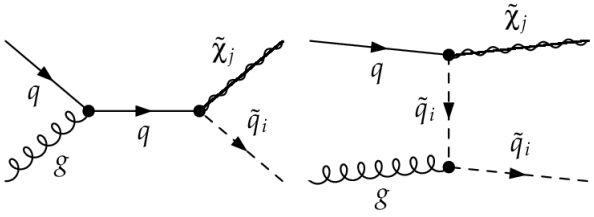

Figure 5.5: Tree-level Feynman diagrams for the associated production of a squark and a gaugino.

one valence down-quark. As before, the charge conjugate production of antisquark pairs is obtained by making the replacement $h_{a,b} \to -h_{a,b}$. If we neglect electroweak contributions as well as squark flavour and helicity mixing and sum over left- and right-handed squark states, we recover the results from Ref. [133].

The associated production of squarks and neutralinos or charginos is a semi-weak process originating from quark-gluon initial states. The s-channel quark and the t-channel squark contributions are shown in Fig. 5.5. Flavour violation is involved through the quark-squark-gaugino vertex. The corresponding differential cross section can be written without form factors as

$$\begin{aligned}
\frac{\mathrm{d}\hat{\sigma}^{qg}_{h_a,h_b}}{\mathrm{d}t} &= \frac{\pi\alpha\alpha_s}{n_{\tilde{\chi}} s^2}\Bigg[-\frac{u_{\tilde{\chi}_j}}{s}\Big[\big(1-h_a\big)\big(1-h_b\big)\big|L_{\tilde{q}_i q\tilde{\chi}_j}\big|^2+\big(1+h_a\big)\big(1+h_b\big)\big|R_{\tilde{q}_i q\tilde{\chi}_j}\big|^2\Big] \\
&\quad+\frac{t_{\tilde{\chi}_j}\big(t+m^2_{\tilde{q}_i}\big)}{t^2_{\tilde{q}_i}}\Big[\big(1-h_a\big)\big|L_{\tilde{q}_i q\tilde{\chi}_j}\big|^2+\big(1+h_a\big)\big|R_{\tilde{q}_i q\tilde{\chi}_j}\big|^2\Big] \\
&\quad+\frac{2\big(ut-m^2_{\tilde{q}_i}m^2_{\tilde{\chi}_j}\big)}{st_{\tilde{q}_i}}\Big[\big(1-h_a\big)\big(1-h_b\big)\big|L_{\tilde{q}_i q\tilde{\chi}_j}\big|^2+\big(1+h_a\big)\big(1+h_b\big)\big|R_{\tilde{q}_i q\tilde{\chi}_j}\big|^2\Big] \\
&\quad+\frac{t_{\tilde{\chi}_j}\big(t_{\tilde{\chi}_j}-u_{\tilde{q}_i}\big)}{st_{\tilde{q}_i}}\Big[\big(1-h_a\big)\big|L_{\tilde{q}_i q\tilde{\chi}_j}\big|^2+\big(1+h_a\big)\big|R_{\tilde{q}_i q\tilde{\chi}_j}\big|^2\Big]\Bigg],
\end{aligned} \tag{5.13}$$

where $n_{\tilde{\chi}} = 6\sin^2\theta_W\big(1-\sin^2\theta_W\big)$ for neutralinos and $n_{\tilde{\chi}} = 12\sin^2\theta_W$ for charginos. The t-channel diagram involves the coupling of the gluon to scalars and does thus not depend on its helicity h_b. The cross section of the charge-conjugate process can be obtained by taking $h_a \to -h_a$. Third generation squarks can, again, only be produced in non-minimal flavour violation (NMFV), preferably through a light (valence) quark in the s-channel. For non-mixing squarks and gauginos, we agree again with the results of Ref. [133].

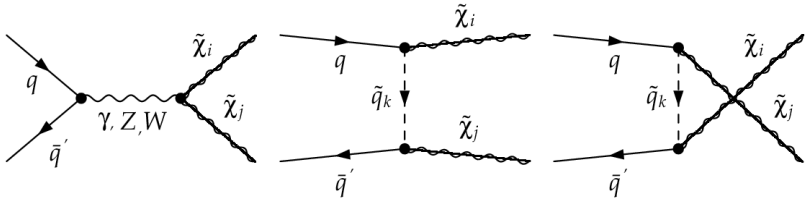

Figure 5.6: Tree-level Feynman diagrams for gaugino pair production.

We finally consider the purely electroweak production of gaugino pairs from quark-anti-quark initial states, shown in Fig. 5.6. Flavour violation can here occur via the quark-squark-gaugino vertices in the t- and u-channels. However, since the summation over complete squark multiplet exchanges makes these channels insensitive to the exchanged squark flavour, the only dependence on flavour violation is due to the different parton density weights in the proton. Furthermore, there are no final state squarks that could be experimentally tagged. The cross section

$$\begin{aligned}
\frac{\mathrm{d}\hat{\sigma}^{q\bar{q}'}_{h_a,h_b}}{\mathrm{d}t} &= \frac{\pi\alpha^2}{3s^2}(1-h_a)(1+h_b)\Big[\big|Q^u_{LL}\big|^2 u_{\tilde{\chi}_i}u_{\tilde{\chi}_j} + \big|Q^t_{LL}\big|^2 t_{\tilde{\chi}_i}t_{\tilde{\chi}_j} \\
&\quad +2\Re\big\{Q^{u*}_{LL}Q^t_{LL}\big\}m_{\tilde{\chi}_i}m_{\tilde{\chi}_j}s\Big] \\
&\quad +\frac{\pi\alpha^2}{3s^2}(1+h_a)(1-h_b)\Big[\big|Q^u_{RR}\big|^2 u_{\tilde{\chi}_i}u_{\tilde{\chi}_j} + \big|Q^t_{RR}\big|^2 t_{\tilde{\chi}_i}t_{\tilde{\chi}_j} \\
&\quad +2\Re\big\{Q^{u*}_{RR}Q^t_{RR}\big\}m_{\tilde{\chi}_i}m_{\tilde{\chi}_j}s\Big] \\
&\quad +\frac{\pi\alpha^2}{3s^2}(1+h_a)(1+h_b)\Big[\big|Q^u_{RL}\big|^2 u_{\tilde{\chi}_i}u_{\tilde{\chi}_j} + \big|Q^t_{RL}\big|^2 t_{\tilde{\chi}_i}t_{\tilde{\chi}_j} \\
&\quad +2\Re\big\{Q^{u*}_{RL}Q^t_{RL}\big\}\big(ut-m^2_{\tilde{\chi}_i}m^2_{\tilde{\chi}_j}\big)\Big] \\
&\quad +\frac{\pi\alpha^2}{3s^2}(1-h_a)(1-h_b)\Big[\big|Q^u_{LR}\big|^2 u_{\tilde{\chi}_i}u_{\tilde{\chi}_j} + \big|Q^t_{LR}\big|^2 t_{\tilde{\chi}_i}t_{\tilde{\chi}_j} \\
&\quad +2\Re\big\{Q^{u*}_{LR}Q^t_{LR}\big\}\big(ut-m^2_{\tilde{\chi}_i}m^2_{\tilde{\chi}_j}\big)\Big]
\end{aligned} \tag{5.14}$$

can be expressed in terms of the generalized charges given in App. A. The charge-conjugate process is again obtained by replacing $h_{a,b} \to -h_{a,b}$. The cross section for chargino pair production in e^+e^- collisions can be deduced by setting $e_q \to e_l = -1$, $L_{qq'Z} \to L_{eeZ} = \big(2T^3_l - 2e_l \sin^2\theta_W\big)$ and $R_{qq'Z} \to R_{eeZ} = -2e_l \sin^2\theta_W$. Neglecting all Yukawa couplings, our cross section then agrees with the results of Ref. [134]. We also agree with the results of Ref. [135] for chargino pair production in the case of non-mixing squarks. For the associated production of a chargino and a neutralino, we recover the results of Ref. [136], provided we correct a sign in their Eq. (2) as described in Ref. [137].

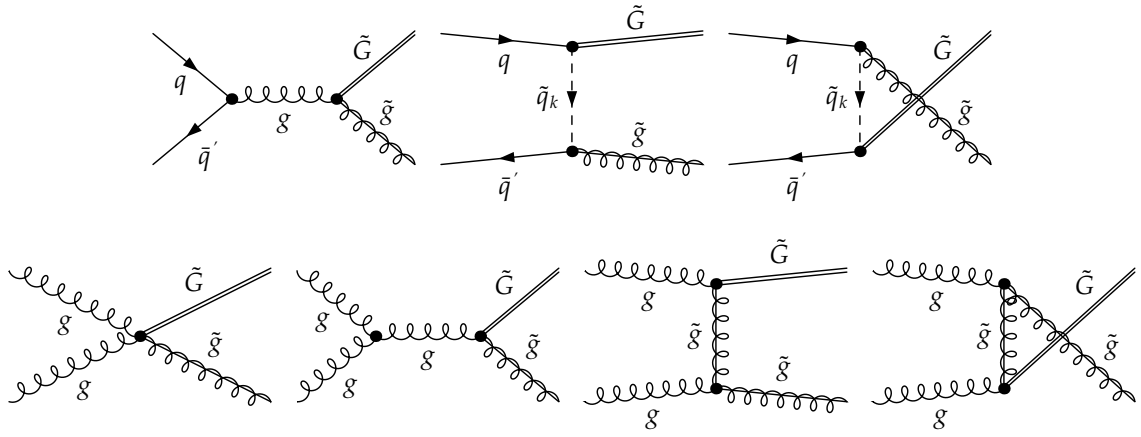

Figure 5.7: Leading order Feynman diagrams for the associated production of a gravitino and a gluino.

5.2 Production Cross Sections and Decays involving Gravitinos

If the gravitino is light, as it can be the case e.g. in scenarios with gauge-mediated Supersymmetry breaking, it is also interesting to study its production at current hadron colliders. In this Section, we present analytical expressions in non-minimal flavour violating Supersymmetry for the production cross section of gravitinos in association with squarks, gluinos, charginos, or neutralinos at hadron colliders, as well as for the decay widths of supersymmetric particles involving gravitinos.

We refer to the effective Lagrangian for light gravitinos and the corresponding couplings of goldstinos with quarks, squarks, gluons, and gluinos discussed e.g. in Ref. [67]. All vertices are proportional to the Supersymmetry-breaking mass terms $m_{\tilde{q}}^2 - m_q^2$ and $m_{\tilde{g}}^2$. The Yukawa coupling of the goldstino to quarks and squarks can be obtained from the gluino-quark-squark vertex by the replacement [138]

$$g_s T^a_{ij} \;\rightarrow\; \frac{m^2_{\tilde{q}_i} - m^2_q}{\sqrt{6} M_{\rm P} m_{\tilde{G}}} \tag{5.15}$$

while the goldstino-gluon-gluino vertex can be obtained from the gluino-gluino-gluon coupling by the replacement

$$-\, g_s f^{abc} \gamma^\mu \;\rightarrow\; i \frac{m^2_{\tilde{g}}}{2\sqrt{6} M_{\rm P} m_{\tilde{G}}} \left[\not{p}, \gamma^\mu\right] \delta_{ab}, \tag{5.16}$$

p denoting the incoming momentum of the gluon. For a summary of couplings in non-minimal flavour violating Supersymmetry, in particular for the gluino, see App. A. In all expressions, we neglect the small gravitino mass $m_{\tilde{G}}$ with respect to the other particle masses, except for the above couplings.

The associated production of a gravitino and a gluino originates either from a neutral quark-antiquark pair or from a gluon pair initial state, as it is shown in Fig. 5.7. The quark-antiquark annihilation subprocess contains s-channel gluon and t- and u-channel squark

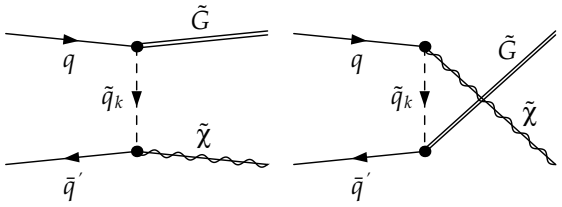

Figure 5.8: Leading order Feynman diagrams for the associated production of a gravitino and a neutralino or chargino.

exchange contributions. The corresponding differential cross section is

$$\begin{aligned}\frac{\mathrm{d}\hat{\sigma}^{q\bar{q}'}_{h_a,h_b}}{\mathrm{d}t} &= \frac{\alpha_s}{27 s^2 M_P^2 m^2_{\tilde{G}}} \sum_{I,J=1}^{2} \big(1+(-1)^I h_a\big)\big(1+(-1)^I h_b\big) \\ &\times \Bigg[m^2_{\tilde{g}} \Bigg[\frac{2ut - m^2_{\tilde{g}}(t+u)}{2s} - \sum_{k=1}^{6} \Big(\frac{t}{t_{\tilde{q}_k}} + \frac{u}{u_{\tilde{q}_k}}\Big)\Big(m^2_{\tilde{q}_k} \Re\big\{ \mathcal{C}^{I}_{\tilde{q}_k q \tilde{g}} \mathcal{C}^{J*}_{\tilde{q}_k q' \tilde{g}} \big\}\Big) \Bigg] \delta_{qq'}\delta_{IJ} \\ &+ \sum_{k,l=1}^{6} m^2_{\tilde{q}_k} m^2_{\tilde{q}_l} \mathcal{C}^{I}_{\tilde{q}_k q \tilde{g}} \mathcal{C}^{J*}_{\tilde{q}_k q' \tilde{g}} \mathcal{C}^{I*}_{\tilde{q}_l q \tilde{g}} \mathcal{C}^{J}_{\tilde{q}_l q' \tilde{g}} \Big(\frac{t_{\tilde{g}} t}{2 t_{\tilde{q}_k} t_{\tilde{q}_l}} + \frac{u_{\tilde{g}} u}{2 u_{\tilde{q}_k} u_{\tilde{q}_l}} - \frac{tu(1-\delta_{IJ})}{t_{\tilde{q}_k} t_{\tilde{u}_l}} \Big) \Bigg], \end{aligned} \tag{5.17}$$

where we use again the generic notation of Eq. (5.7) for the coupling strengths $\mathcal{C}^{\{I,J\}}_{abc}$. Flavour violation can be involved through the squark-quark-gluino and squark-quark-gravitino vertices. However, the summation over the complete squark multiplet reduces these effects, the small remaining sensitivity coming from the different parton density weights, as it is the case for gaugino-pair production. The gluon fusion subprocess involves a quartic coupling and a gluon and a two gluino exchange diagrams, yielding the cross section

$$\begin{aligned}\frac{\mathrm{d}\hat{\sigma}^{gg}_{h_a,h_b}}{\mathrm{d}t} &= \frac{\alpha_s m^2_{\tilde{g}}}{32 s^3 M_P^2 m^2_{\tilde{G}}} \Bigg[\big(1+h_a h_b\big) \Bigg(\frac{t^3 - m^2_{\tilde{g}}\big(3t^2+3tu+u^2\big) m^4_{\tilde{g}}\big(3t+2u\big) - m^6_{\tilde{g}}}{t^2_{\tilde{g}}} \\ &+ \frac{\big(t-u\big)^2 + m^2_{\tilde{g}}\big(2t+u\big) - m^4_{\tilde{g}}}{2} t + 2t \frac{t\big(u-t\big) + m^2_{\tilde{g}}\big(2t+u\big) - m^4_{\tilde{g}}}{t_{\tilde{g}}} \\ &- \frac{tu + m^2_{\tilde{g}}\big(t+u\big) - m^4_{\tilde{g}}}{t_{\tilde{g}} u_{\tilde{g}}} tu \Bigg) + \big(1-h_a h_b\big) \frac{t^2 u u_{\tilde{g}}}{t^2_{\tilde{g}}} \Bigg] + \big\{ t \leftrightarrow u \big\}. \end{aligned} \tag{5.18}$$

Note that this cross section is not affected by flavour violation and the expression is therefore rather compact.

The associated production of a gravitino and a chargino or neutralino proceeds through the diagrams shown in Fig. 5.8, i.e. from the collision of a quark-antiquark pair and through t- or u-channel squark exchanges. It can involve flavour violation effects through the squark-quark-gravitino and the squark-quark-gaugino vertices, but these are again reduced when we sum over all squarks in a given supermultiplet. The differential cross section can be obtained from Eq. (5.17) by removing the s-channel contribution and its interferences and replacing

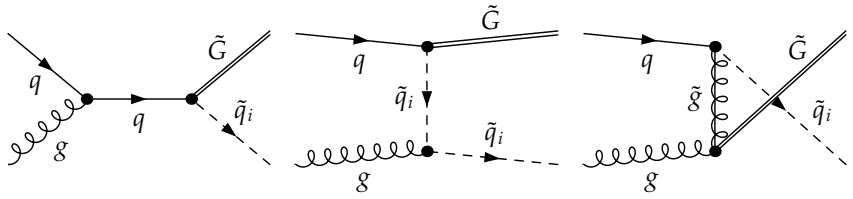

Figure 5.9: Leading order Feynman diagrams for the associated production of a gravitino and a squark.

the gluino-squark-quark coupling by the chargino-squark-quark ones,

$$\begin{aligned}\frac{\mathrm{d}\sigma^{q\bar{q}'}_{h_a,h_b}}{\mathrm{d}t} &= \frac{\alpha}{36 s^2 M_{\mathrm{P}}^2 m_{\tilde{G}}^2 \sin^2\theta_W} \sum_{I,J=1}^{2} \sum_{k,l=1}^{6} \big(1+(-1)^I h_a\big)\big(1-(-1)^J h_b\big) m_{\tilde{q}_k}^2 m_{\tilde{q}_l}^2 \\ &\quad \times \Bigg[\frac{\mathcal{C}^I_{\tilde{q}_k q \tilde{g}} \mathcal{C}^J_{\tilde{q}_k q' g\tilde{\chi}_i} \mathcal{C}^{I*}_{\tilde{q}_l q \tilde{g}} \mathcal{C}^{J*}_{\tilde{q}_l q' g\tilde{\chi}_i} t_{\tilde{\chi}_i} t}{t_{\tilde{q}_k} t_{\tilde{q}_l}} + \frac{\mathcal{C}^{J*}_{\tilde{q}_k q' \tilde{g}} \mathcal{C}^{I*}_{\tilde{q}_k q g\tilde{\chi}_i} \mathcal{C}^{J}_{\tilde{q}_l q' \tilde{g}} \mathcal{C}^{I}_{\tilde{q}_l q g\tilde{\chi}_i} u_{\tilde{\chi}_i} u}{u_{\tilde{q}'_k} u_{\tilde{q}'_l}} \\ &\quad + \big(1-\delta_{IJ}\big) \frac{\mathcal{C}^I_{\tilde{q}_k q \tilde{g}} \mathcal{C}^J_{\tilde{q}_k q' g\tilde{\chi}_i} \mathcal{C}^J_{\tilde{q}_l q' \tilde{g}} \mathcal{C}^I_{\tilde{q}_l q g\tilde{\chi}_i} ut}{t_{\tilde{q}_k} u_{\tilde{q}'_l}} \Bigg]. \end{aligned} \tag{5.19}$$

Finally, gravitinos can also be produced in association with squarks, as shown in Fig. 5.9. Originating from a quark-gluon initial state and proceeding through s-channel quark, t-channel squark, or u-channel gluino exchange, flavour violation effects can occur here as before due to the squark-quark-gluino and squark-quark-gravitino vertices. The associated cross section is given by

$$\begin{aligned}\frac{\mathrm{d}\sigma^{qg}_{h_a,h_b}}{\mathrm{d}t} &= \frac{\alpha_s}{144 s^2 M_{\mathrm{P}}^2 m_{\tilde{G}}^2} \Bigg[\Bigg(-\frac{m^4_{\tilde{q}_i} u}{s} + \frac{2 m^4_{\tilde{q}_i} ut}{s t_{\tilde{q}_i}} - \frac{m^4_{\tilde{q}_i} us}{u^2_{\tilde{g}}} - \frac{2 m^2_{\tilde{g}} m^2_{\tilde{q}_i} t^2 u}{s t^2_{\tilde{q}_i}} \Bigg) \\ &\qquad \times \Big[\big(1-h_a\big)\big(1-h_b\big) \big|L_{\tilde{q}_i q \tilde{g}}\big|^2 + \big(1+h_a\big)\big(1+h_b\big) \big|R_{\tilde{q}_i q \tilde{g}}\big|^2 \Big] \\ &\quad - \frac{m^4_{\tilde{q}_i} t^2 u}{s t^2_{\tilde{q}_i}} \Big[\big(1-h_a\big) \big|L_{\tilde{q}_i q \tilde{g}}\big|^2 + \big(1+h_a\big) \big|R_{\tilde{q}_i q \tilde{g}}\big|^2 \Big] \\ &\quad - \frac{m^2_{\tilde{g}} t u^2}{u^2_{\tilde{g}}} \Big[\big(1-h_a\big)\big(1+h_b\big) \big|L_{\tilde{q}_i q \tilde{g}}\big|^2 + \big(1+h_a\big)\big(1-+h_b\big) \big|R_{\tilde{q}_i q \tilde{g}}\big|^2 \Big] \Bigg]. \end{aligned} \tag{5.20}$$

Note that the expressions in Eqs. (5.17) - (5.20) agree in the limit of constrained minimal flavour violation and non-mixing mass-degenerate squarks with the results of Ref. [67].

We now turn from the production to the two-body decay processes of supersymmetric particles. As for the cross sections, we express them in terms of the masses of the involved particles, the electroweak gauge boson masses, m_Z and m_W, and the reduced Planck mass M_P. Analytical expressions for decay widths of squarks, gluons, and gauginos in non-minimal flavour violation Supersymmetry can be found in Ref. [65], but without taking into account final states with a gravitinos. We here extend this work and focus on the decays that involve gravitinos shown in Fig. 5.10, i.e. decays of a supersymmetric particle into its Standard Model partner and a gravitino.

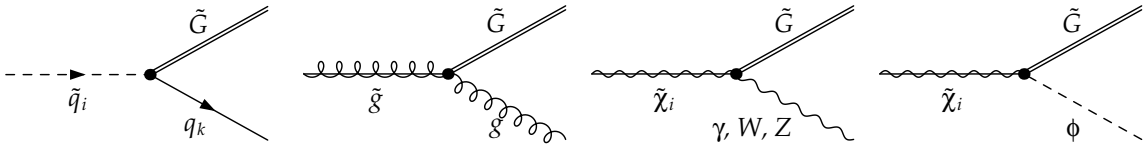

Figure 5.10: Leading order Feynman diagrams for the decay of a squark, a gluino, or a gaugino into its Standard Model partner and a gravitino.

Flavour violation is involved here only in the squark decay through the squark-quark-gravitino coupling. The corresponding decay width is given by

$$\Gamma_{\tilde{q}_i\to q_k\tilde{G}} \;=\; \frac{\left(m^2_{\tilde{q}_i}-m^2_{q_k}\right)^2}{48\pi m^3_{\tilde{q}_i}M_P^2 m^2_{\tilde{G}}}\Big(\big|L_{\tilde{q}_i q_k\tilde{G}}\big|^2+\big|L_{\tilde{q}_i q_k\tilde{G}}\big|^2\Big), \tag{5.21}$$

where we have again neglected the gravitino mass everywhere except in the coupling constant. The corresponding slepton decay width can easily be deduced from the previous result by replacing consistently the couplings and masses. Note that there is no need to adapt colour factors, since they are equal to unity for each decay mode except for the gluino which is not relevant for slepton decay. In the limit of constrained minimal flavour violation (cMFV) we recover the result for the decay width of Ref. [67]. For completeness, we recall the expressions of gluino, chargino, and neutralino decays involving gravitinos but no flavour violation [139],

$$\begin{aligned}
\Gamma_{\tilde{g}\to g\tilde{G}} &= \frac{m^5_{\tilde{g}}}{48\pi M_P^2 m^2_{\tilde{G}}},\\
\Gamma_{\tilde{\chi}^0_i\to\gamma\tilde{G}} &= \frac{m^5_{\tilde{\chi}^0_i}}{48\pi M_P^2 m^2_{\tilde{G}}}\Big|\mathcal{N}_{i1}\cos\theta_W+\mathcal{N}_{i2}\sin\theta_W\Big|^2,\\
\Gamma_{\tilde{\chi}^0_i\to Z\tilde{G}} &= \frac{\left(m_{\tilde{\chi}^0_i}-m_Z^2\right)^4}{48\pi m^3_{\tilde{\chi}^0_i}M_P^2 m^2_{\tilde{G}}}\left(\Big|\mathcal{N}_{i1}s_W+\mathcal{N}_{i2}c_W\Big|^2+\frac{1}{2}\Big|\mathcal{N}_{i3}\cos\beta+\mathcal{N}_{i4}\sin\beta\Big|^2\right),\\
\Gamma_{\tilde{\chi}^0_i\to h^0\tilde{G}} &= \frac{\left(m_{\tilde{\chi}^0_i}-m_{h^0}^2\right)^4}{96\pi m^3_{\tilde{\chi}^0_i}M_P^2 m^2_{\tilde{G}}}\Big|\mathcal{N}_{i3}\sin\alpha+\mathcal{N}_{i4}\cos\alpha\Big|^2,\\
\Gamma_{\tilde{\chi}^0_i\to H^0\tilde{G}} &= \frac{\left(m_{\tilde{\chi}^0_i}-m_{H^0}^2\right)^4}{96\pi m^3_{\tilde{\chi}^0_i}M_P^2 m^2_{\tilde{G}}}\Big|\mathcal{N}_{i3}\cos\alpha+\mathcal{N}_{i4}\sin\alpha\Big|^2,\\
\Gamma_{\tilde{\chi}^0_i\to A^0\tilde{G}} &= \frac{\left(m_{\tilde{\chi}^0_i}-m_{A^0}^2\right)^4}{96\pi m^3_{\tilde{\chi}^0_i}M_P^2 m^2_{\tilde{G}}}\Big|\mathcal{N}_{i3}\sin\beta+\mathcal{N}_{i4}\cos\beta\Big|^2,\\
\Gamma_{\tilde{\chi}^\pm_i\to W^\pm\tilde{G}} &= \frac{\left(m_{\tilde{\chi}^\pm_i}-m_W^2\right)^4}{96\pi m^3_{\tilde{\chi}^\pm_i}M_P^2 m^2_{\tilde{G}}}\Big(\big|\mathcal{V}_{i1}\big|^2+\big|\mathcal{U}_{i1}\big|^2+\big|\mathcal{V}_{i2}\big|^2\sin^2\beta+\big|\mathcal{U}_{i2}\big|^2\cos^2\beta\Big),\\
\Gamma_{\tilde{\chi}^\pm_i\to H^\pm\tilde{G}} &= \frac{\left(m_{\tilde{\chi}^\pm_i}-m_{H^\pm}^2\right)^4}{96\pi m^3_{\tilde{\chi}^\pm_i}M_P^2 m^2_{\tilde{G}}}\Big(\big|\mathcal{V}_{i2}\big|^2\cos^2\beta+\big|\mathcal{U}_{i2}\big|^2\sin^2\beta\Big).
\end{aligned} \tag{5.22}$$

5.3 Numerical Predictions for the LHC

In this Section, we present numerical predictions for the production cross sections in non-minimal flavour violating Supersymmetry at the CERN Large Hadron Collider (LHC), i.e. for pp-collisions at $\sqrt{s} = 14$ TeV centre-of-momentum energy [66]. For consistency with our leading order (LO) QCD calculation in the collinear approximation, where all quark masses but the top mass are neglected with respect to the centre-of-momentum energy $\sqrt{s}$, we employ the LO set of the latest `CTEQ6` global parton density fit [140], which includes $n_f = 5$ "light" quark flavours and the gluon, but no top-quark density. Whenever it occurs, i.e. for gluon initial states and gluon and gluino exchanges, the strong coupling constant $\alpha_s(\mu_R)$ is calculated with the corresponding LO value of $\Lambda_{\rm LO}^{n_f=5} = 165$ MeV. We identify the renormalization scale μ_R with the factorization scales $M_a = M_b$ and set the scales to the average mass of the produced supersymmetric particles.

In Figs. 5.11 – 5.22, we show examples of the obtained numerical cross sections for charged squark-antisquark and squark-squark production, neutral up- and down-type squark-antisquark and squark-squark pair production, associated production of squarks with charginos and neutralinos, and gaugino pair production for our benchmark points E, F, G, H, I, and J, and for both of the two considered implementations of non-minimal flavour violation in the GMSB model discussed in Sec. 2.4.2. We recall that the first is based on mixing between matter and fundamental messengers, leading to flavour mixing only in the left-left chiral squark sector and implemented at the electroweak scale through the parameter $\lambda_{\rm LL}$ while $\lambda_{\rm RR}$ is set to zero. The second scenario involves mixing with antisymmetric messengers, giving rise to flavour violation in both the left-left and right-right chiral squark sectors governed by the parameter $\lambda_{\rm LL} = \lambda_{\rm RR}$. For the sake of better readability, we show only the numerically most important curves as well as a selection of those that involve visible flavour violating effects.

The magnitudes of the cross sections vary from the barely visible level of 10^{-2} fb for weak production of heavy final states over the semi-strong production of average squarks and gauginos and quark-gluon initial states to large cross sections of 10^2 to 10^3 fb for the strong production of diagonal squark-squark and squark-antisquark pairs or weak production of very light gaugino pairs. Unfortunately, the processes whose cross sections are largest are mostly insensitive to the parameter $\lambda_{\rm LL}$ in both flavour violation scenarios, as the strong gauge interaction is insensitive to quark flavours and gaugino pair production cross sections are summed over exchanged squark flavours.

Some of the subleading, non-diagonal cross sections show, however, sharp transitions in particular squark production channels. These transitions are directly related to the "avoided crossings" of the mass eigenvalues discussed in Sec. 2.4.3. At the point, where two levels should cross, the involved squarks change character and are subject to an exchange of their flavour contents. Rather than the mass dependence on $\lambda_{\rm LL}$, these exchanges then lead together with the different parton densities in the proton to more or less sharp transitions in the production cross sections, where the corresponding squarks are involved. This phenomenon is analogously observed in the case of squark and gaugino hadroproduction in minimal supergravity [65].

As an example, let us discuss in detail the production of quarks and gauginos for our benchmark point E. The cross sections in the flavour violation scenario based on fundamental messengers are shown in Fig. 5.11. "Avoided crossing" of mass eigenvalues occur here, e.g., for down-type squarks at a value of $\lambda_{\rm LL} \approx 0.145$ between the squarks $\tilde{d}_3$ and $\tilde{d}_4$, see also Fig. 2.16. Before this point, $\tilde{d}_3$ is characterized by a dominant sdown content, while $\tilde{d}_4$ has first a dominant sbottom and then sstrange content. For $\lambda_{\rm LL} \gtrsim 0.145$, these contents are

exchanged, i.e. $\tilde{d}_3$ is then a strange-squark and $\tilde{d}_4$ becomes sdown-like. As a consequence, the cross sections involving the two mass eigenstates exchange their values, since the production of first generation squarks is preferred due to the more important parton density of up- and down-quarks in the proton. This can be seen in our example for the production of down-type squark-squark and squark-antisquark pairs, mixed up- and down-type squark-squark and squark-antisquark pair production, as well as for the associated production of down-type squarks and charginos or neutralinos.

For up-type squarks, the level-reordering phenomenon occurs at values of $\lambda_{\rm LL} \simeq 0.09$ in the range excluded by the constraint from the inclusive branching ratio BR($b \to s\gamma$) (left of the vertical green dashed line) and is therefore not shown here. However, another effect becomes visible in the case of production cross sections that involve final states with up-type squarks. Some of the mass eigenstates do not present sharp transitions, but rather a continuous change in their flavour content. This is, e.g., the case for the lightest mass eigenstate $\tilde{u}_1$. The corresponding production cross sections increase smoothly with the flavour violation parameter $\lambda_{\rm LL}$, which is explained by the fact that at lower values of $\lambda_{\rm LL}$ the lightest up-squark $\tilde{u}_1$ is mostly stop-like, but receives sizeable contributions of the light flavours for higher $\lambda_{\rm LL}$. Together with the more important parton densities, this results in an increase of the corresponding production cross sections. In the same way, we also observe cross sections that decrease with $\lambda_{\rm LL}$, due to a decrease of the light flavour content of the involved squarks.

The same phenomena are observed in the case of our second flavour violation scenario with antisymmetric messengers, see Fig. 5.12 for the benchmark point E. Note that here also "avoided crossings" between up-type squark mass eigenstates are observed, e.g. between $\tilde{u}_4$ and $\tilde{u}_5$ at $\lambda_{\rm LL} \sim 0.11$, which lies, however, already in the range excluded by BR($b \to s\gamma$). In this example, the $\tilde{u}_5$ loses its important up-squark content to the scharm-dominated $\tilde{u}_4$. The latter becomes then purely sup-like, enhancing its production cross section due to the parton density in the proton, while the cross sections involving $\tilde{u}_5$ become less important.

For the benchmark points H with fundamental (see Fig. 5.17) and I (Fig. 5.20) and J (Fig. 5.22) with antisymmetric messengers, we observe a third effect at $\lambda_{\rm LL} = 0.158,\ 0.132,$ and 0.114, respectively. Here, the pair production of up-type squark pairs ($\tilde{u}_3\tilde{u}_4$ for fundamental and $\tilde{u}_4\tilde{u}_5$ for antisymmetric messengers) exhibits an interesting resonance-like behaviour. It is generated by the fact that these squark mass eigenstates exchange their up and charm flavour contents (and also their chiralities in the case of antisymmetric messengers) at the critical values of $\lambda_{\rm LL}$ in a rather smooth way, so that both squark mass eigenstates receive significant up-quark contributions to their production cross sections in the vicinity.

Let us recall that in the case of flavour mixing only in the left-left chiral sector, "avoided crossings" occur among the $\tilde{q}_{1,2}$, $\tilde{q}_{3,4}$, and $\tilde{q}_{5,6}$ mass eigenstates, whereas in the case of flavour mixing in both the left-left and right-right chiral sectors, we rather observe the mass flips among the $\tilde{q}_{2,3}$ and $\tilde{q}_{4,5}$ mass eigenstates, respectively. Note also that the difference between the two flavour violation scenarios is invisible for the gaugino pair production in the bottom right panels of Figs. 5.11 – 5.22, respectively, that are practically insensitive to flavour violation in the squark sector.

Concerning the production of gravitinos, the cross sections corresponding to the channels presented in Sec. 5.2 achieve sizeable orders of magnitude only in the case of a rather light gravitino, see e.g. Ref. [67]. Contrary, if the latter is too heavy, its couplings are too small to yield discoverable cross sections, since they are proportional to the inverse of the gravitino mass squared. In particular, this is the case for our scenarios with gravitino cold dark matter discussed in Sec. 2.4.5, where we have found a value of the order of $m_{\tilde{G}} \sim 10^{-1}$ GeV in order to

fulfill the different cosmological constraints. Note that, in order to have a very light gravitino and in consequence sizeable production cross sections, one could consider a GMSB scenario with gravitino hot dark matter ($m_{\tilde{G}} \lesssim 1$ keV) and additional cold dark matter from stable messenger particles [141–144]. In scenarios with a mixing between messenger and matter fields, however, the stability of the lightest messenger might be lost. We therefore do not consider the production of light gravitinos in our GMSB scenarios with additional flavour violation in the squark sector.

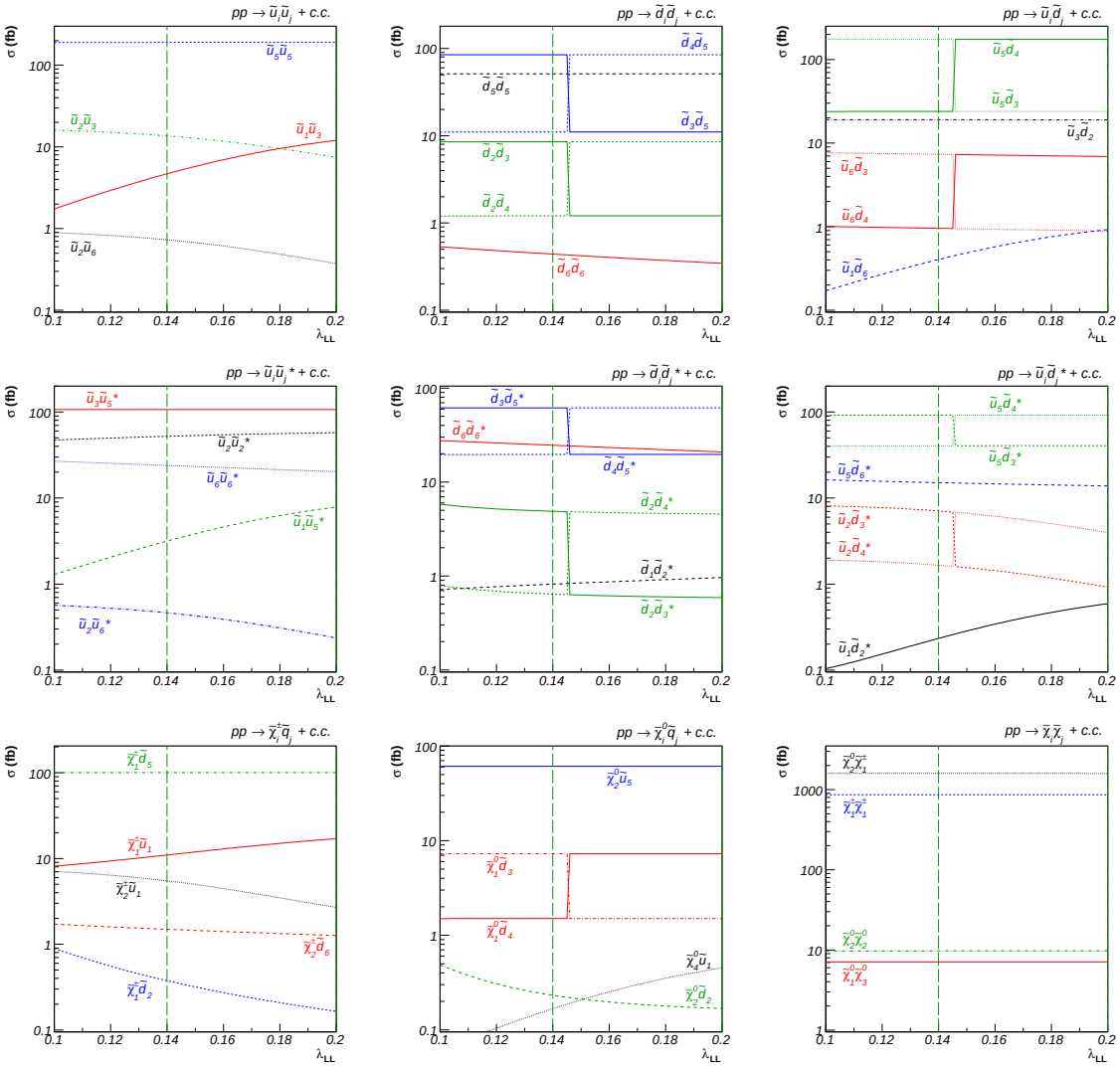

Figure 5.11: Examples of cross sections for charged squark-antisquark and squark-squark production, neutral up- and down-type squark-antisquark and squark-squark pair production, associated production of squarks with charginos and neutralinos, and gaugino pair production at the LHC in our benchmark scenario E with flavour violation in the left-left chiral squark sector ($\lambda_{\mathrm{RR}} = 0$). The allowed range for the flavour violation parameter λ_{LL} is indicated by vertical green dashed lines.

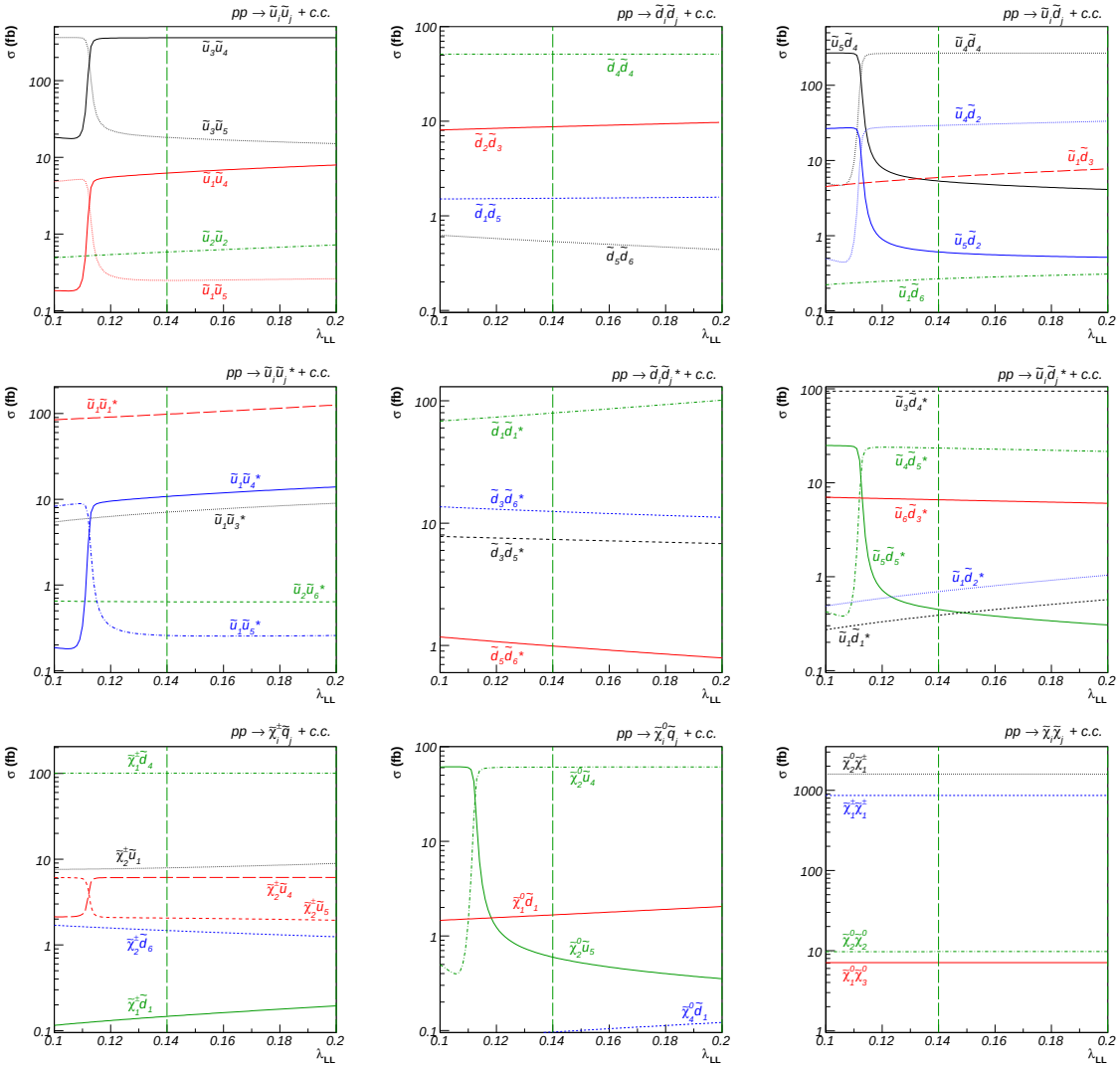

Figure 5.12: Same as Fig. 5.11 for our benchmark scenario E with flavour violation in the left-left and right-right chiral squark sectors ($\lambda_{\rm RR} = \lambda_{\rm LL}$).

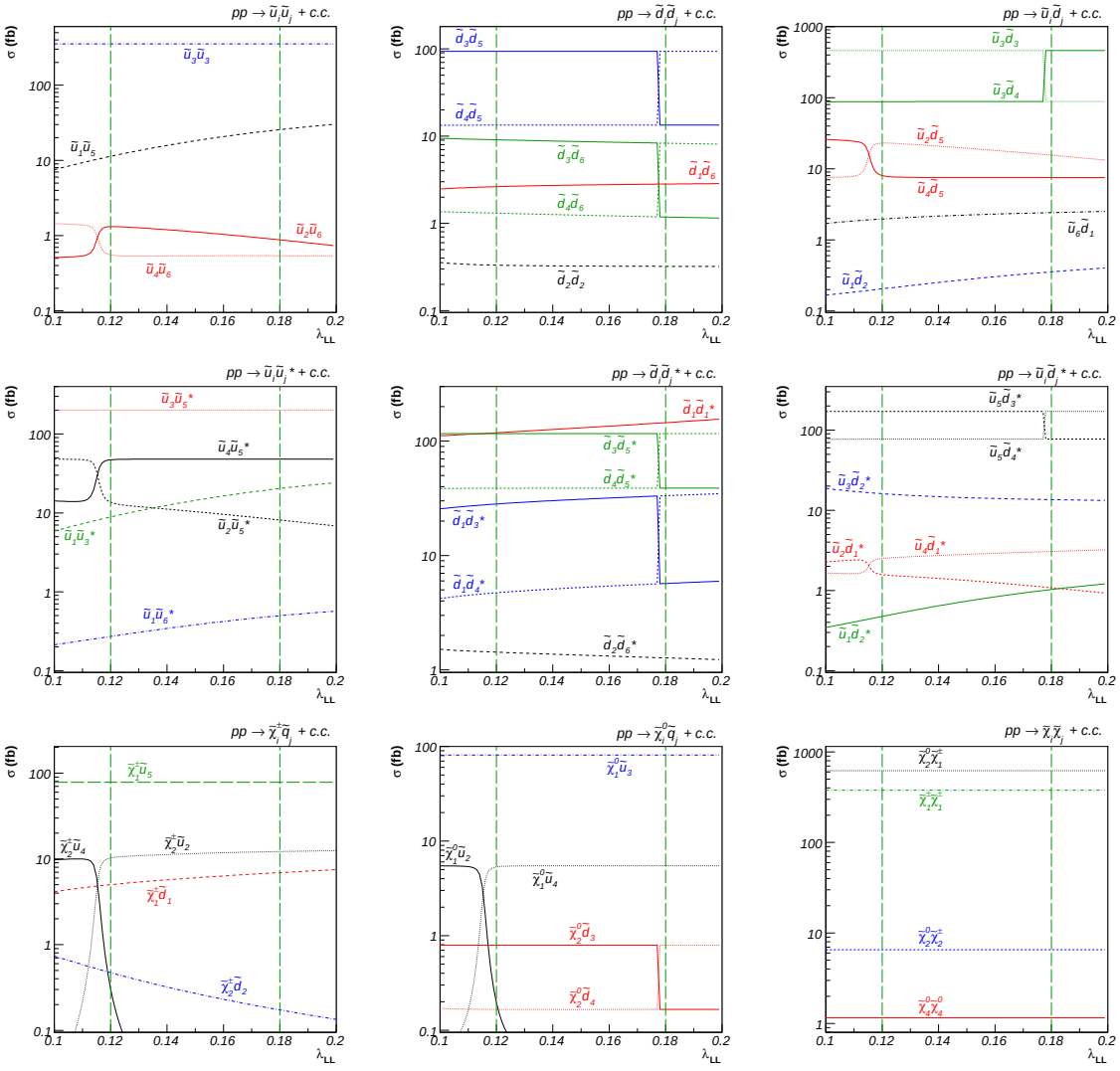

Figure 5.13: Same as Fig. 5.11 for our benchmark scenario F.

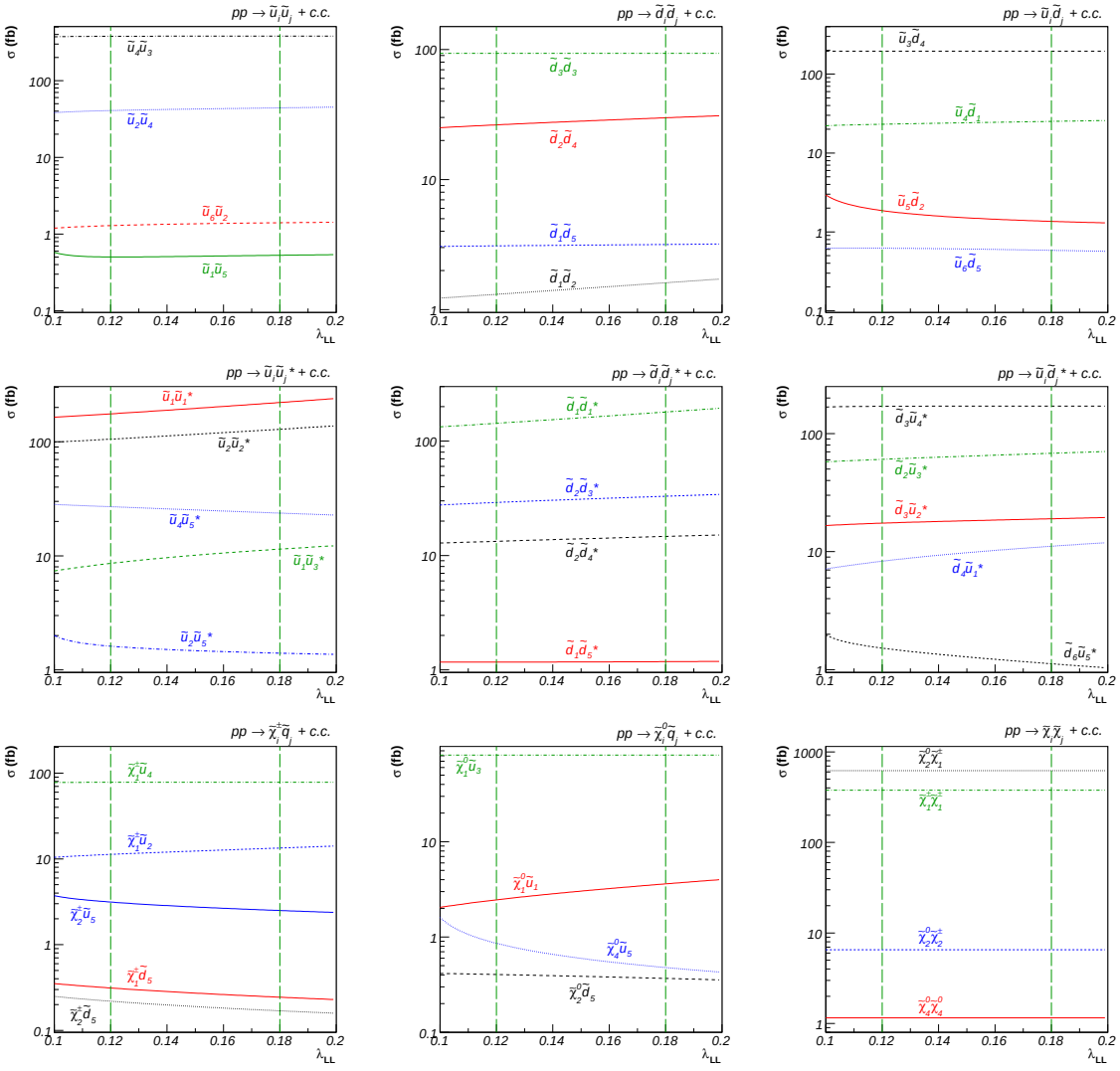

Figure 5.14: Same as Fig. 5.12 for our benchmark scenario F.

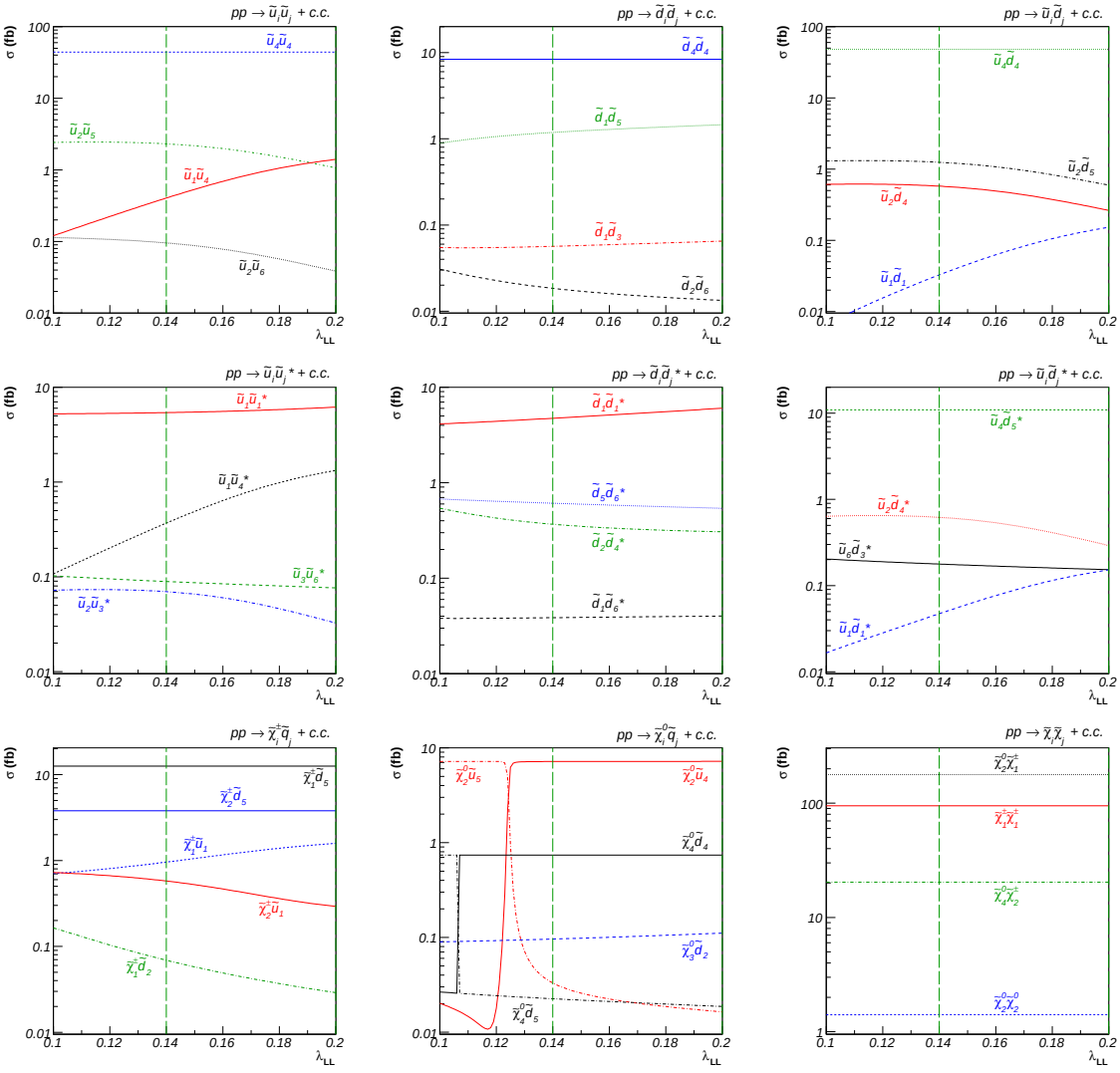

Figure 5.15: Same as Fig. 5.11 for our benchmark scenario G.

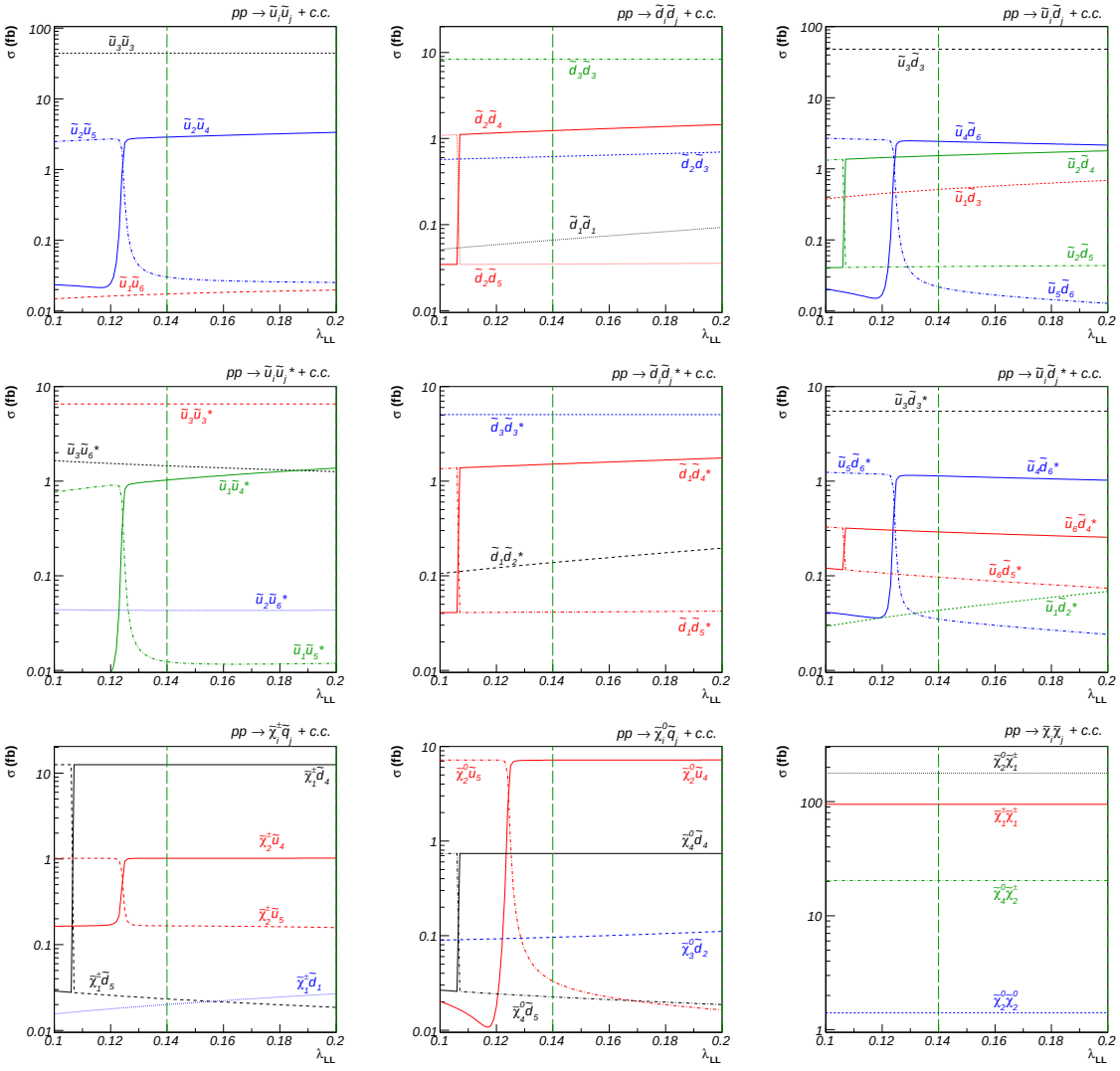

Figure 5.16: Same as Fig. 5.12 for our benchmark scenario G.

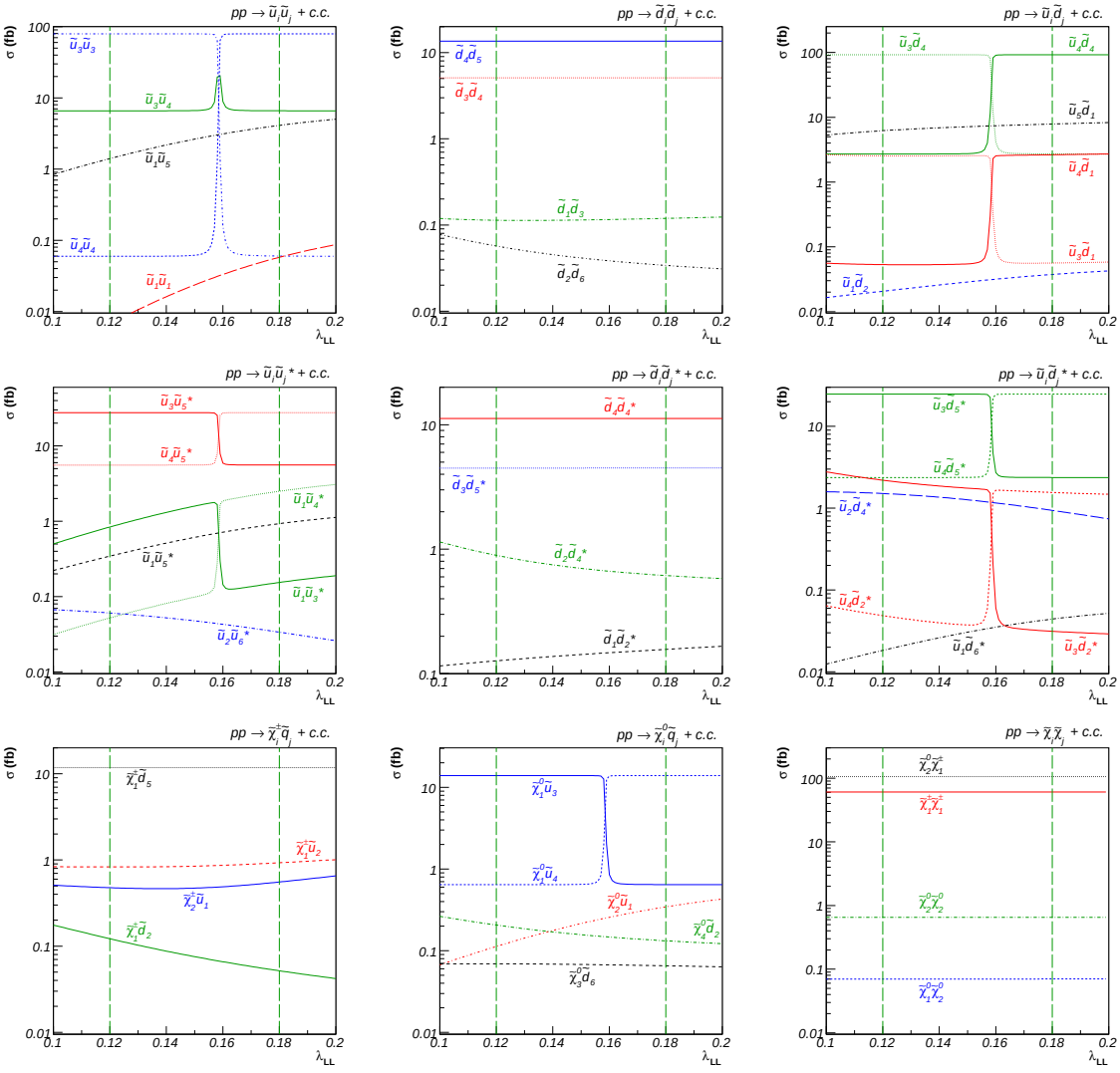

Figure 5.17: Same as Fig. 5.11 for our benchmark scenario H.

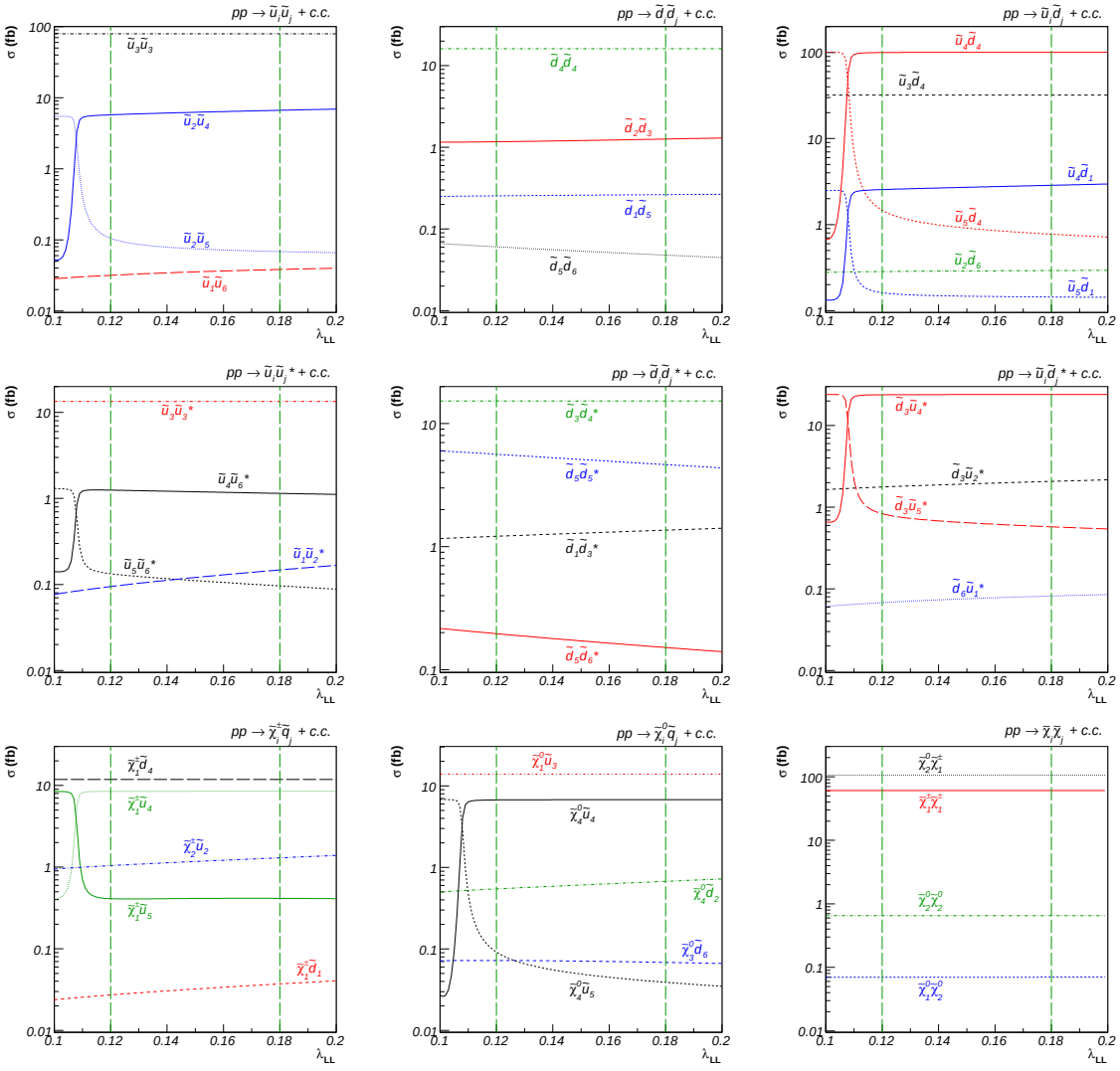

Figure 5.18: Same as Fig. 5.12 for our benchmark scenario H.

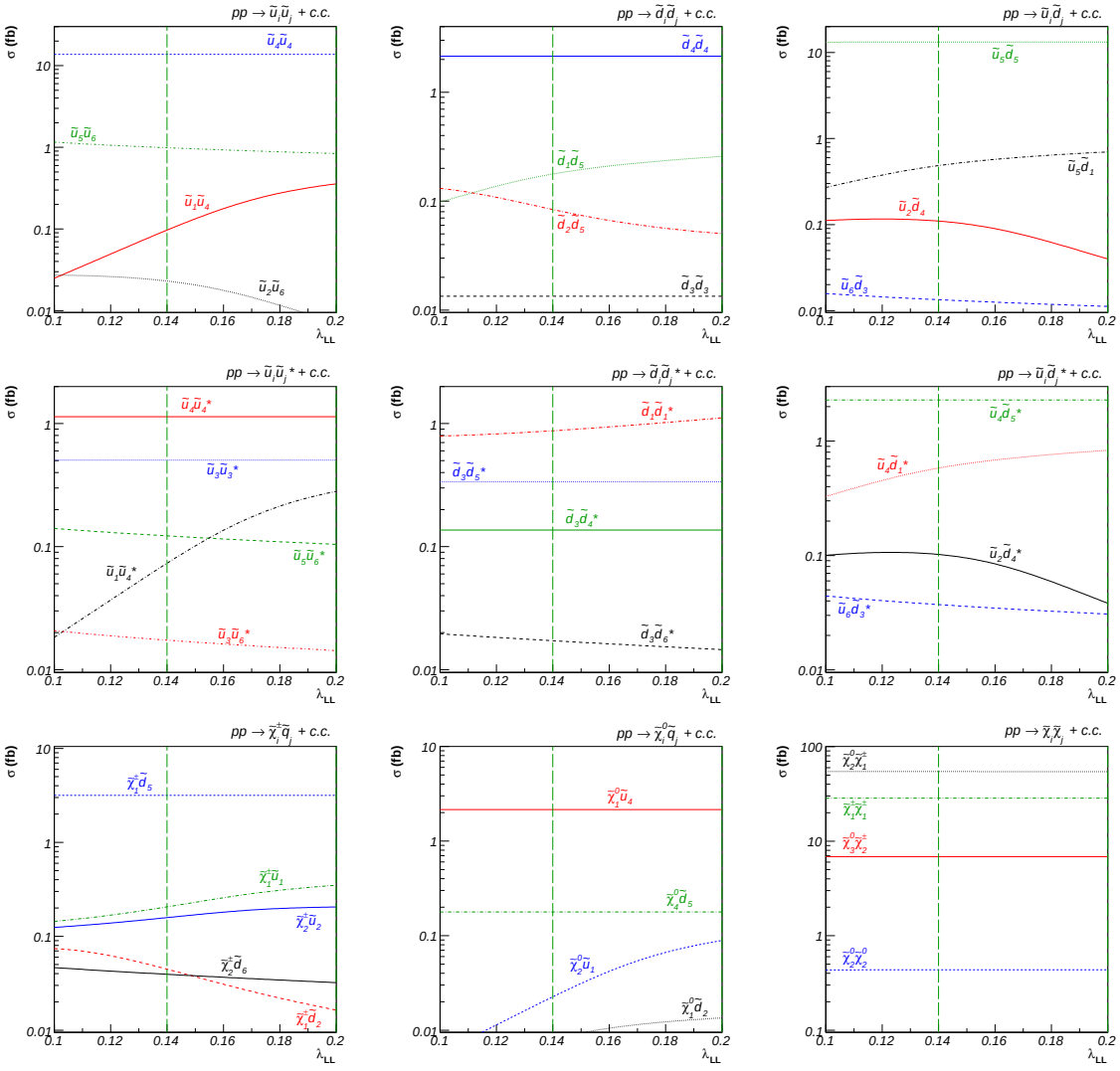

Figure 5.19: Same as Fig. 5.11 for our benchmark scenario I.

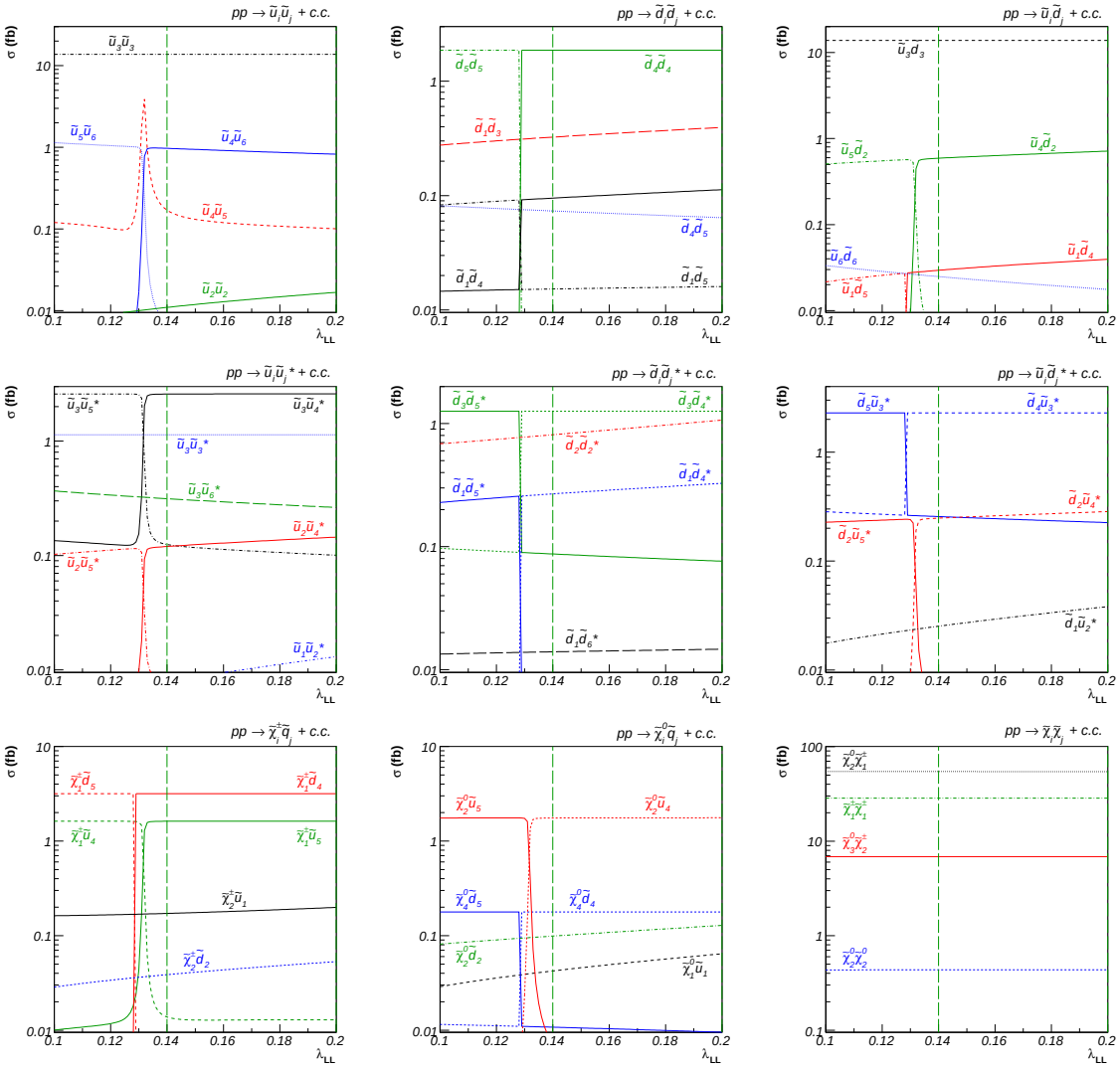

Figure 5.20: Same as Fig. 5.12 for our benchmark scenario I.

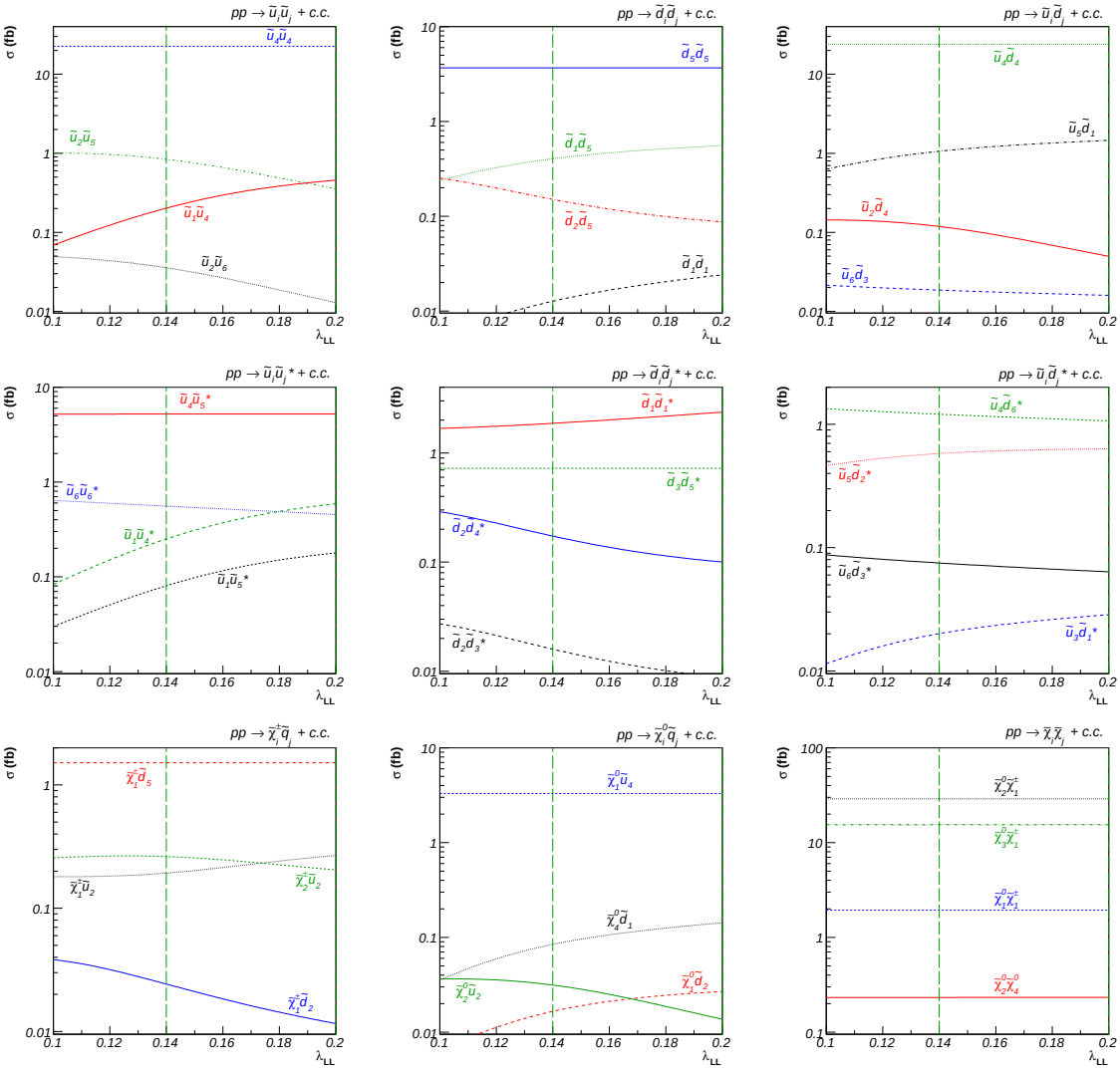

Figure 5.21: Same as Fig. 5.11 for our benchmark scenario J.

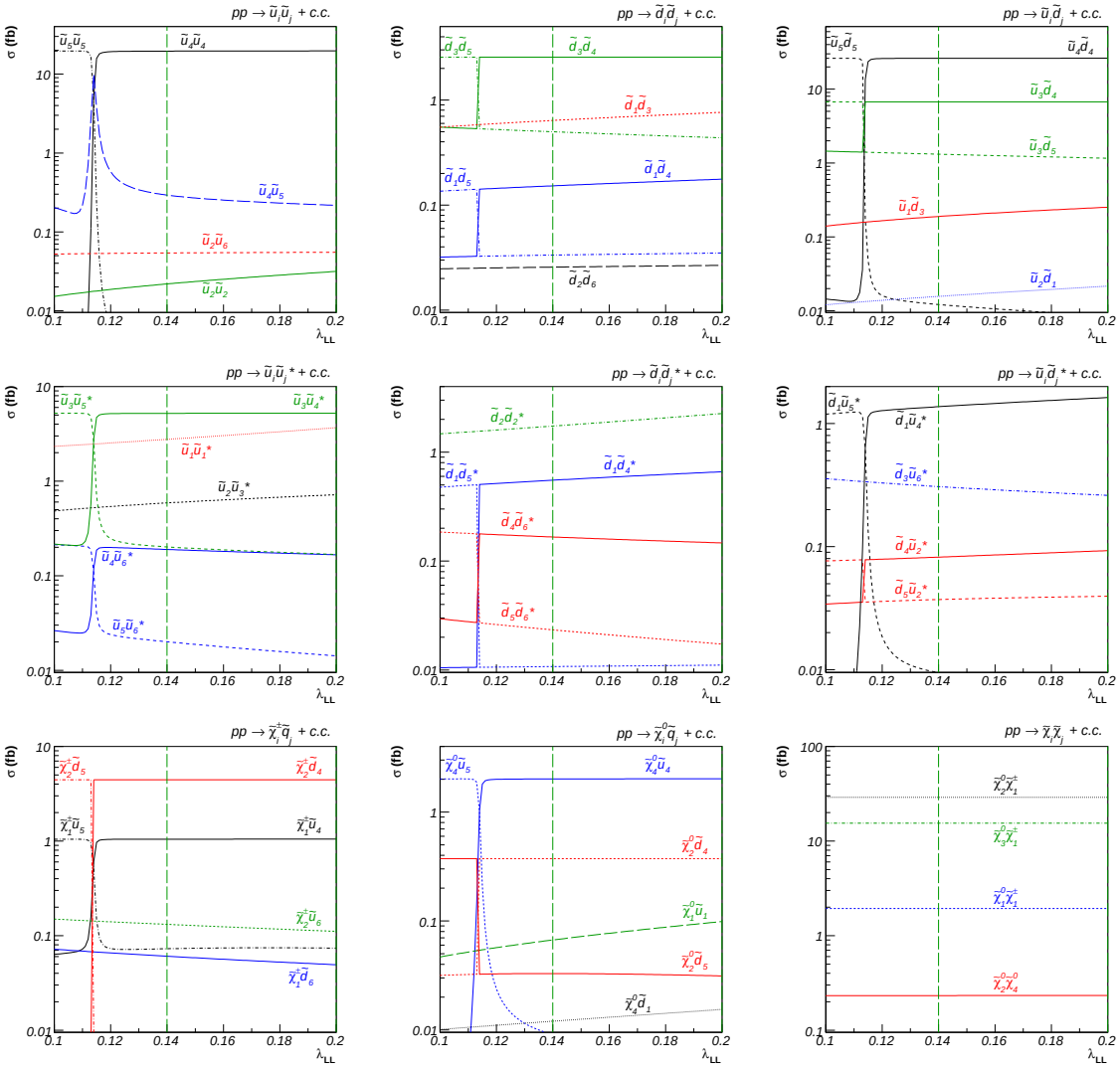

Figure 5.22: Same as Fig. 5.12 for our benchmark scenario J.

Chapter 6

Conclusions and Perspectives

Supersymmetry is an attractive framework postulating a symmetry between bosonic and fermionic degrees of freedom and thus predicting superpartners for the Standard Model particles. It cures the hierarchy problem between the electroweak and the Planck scale, leads to gauge coupling unification, and provides promising candidates for the cold dark matter in our Universe. However, since no superpartners have been observed so far, Supersymmetry has to be broken. The exact mechanism of Supersymmetry-breaking is thus of particular interest, in particular since there is no consensus on how it should proceed. Different scenarios are accepted by the community, based on different ways of mediation of Supersymmetry-breaking to the observable sector and leading to different phenomenologies. It is therefore essential to constrain the parameter space within the different models, both at the electroweak and the Supersymmetry-breaking scale.

In the first part of this Thesis, we have investigated in detail the different constraints that can be imposed on the MSSM parameter space. Apart from direct mass limits from collider experiments, these are in particular due to electroweak precision and low-energy observables, such as the inclusive branching ratio BR($b \to s\gamma$), the electroweak parameter $\Delta\rho$, and the anomalous magnetic moment of the muon a_μ. Further strong constraints come from cosmology, requiring that a supersymmetric model should include a viable candidate for cold dark matter and lead to a relic density agreeing with recent observational data. We have analyzed these constraints for minimal supergravity (mSUGRA) and gauge-mediated Supersymmetry breaking (GMSB) scenarios, where we have taken into account the possibility of non-minimal flavour violation in the squark sector, implemented through two real parameters $\lambda_{\rm LL}$ and $\lambda_{\rm RR}$ corresponding to the left-left and right-right chiral sectors, respectively. For the case of minimal supergravity, allowed regions of the parameter space remain for up to reasonably important values of the off-diagonal elements of the squark mass matrices. For gauge-mediated Supersymmetry-breaking, it turns out that the minimal model without additional sources of flavour violation suffers from the constraints, in particular from the recent measurements of the inclusive branching ration BR($b \to s\gamma$). We have reintroduced flavour violation into GMSB models by considering mixing between messenger and matter fields, that leads to flavour mixing either only in the left-left or both in the left-left and right-right chiral squark sectors. In both scenarios, this introduction of squark flavour violation opens windows in the parameter space that are preferred by electroweak precision data with respect to the minimal GMSB model. Based on our analysis, we have defined ten benchmark scenarios, that lie in the experimentally favoured regions of the parameter space, that are "collider-friendly", i.e. do

not involve to high masses of the superpartners, and allow for non-minimal flavour violation in a considerable range of the flavour mixing parameters $\lambda_{\rm LL}$ and $\lambda_{\rm RR}$. For these points, a detailed study has revealed that the phenomenology of non-minimal flavour violation Supersymmetry is strongly influenced by "avoided crossings" of squark mass eigenvalues. These lead to exchanges of the flavour content between neighbouring up- or down-type squarks and show in the numerical predictions for squark production cross sections.

We have also investigated in detail the cosmological implications on the benchmark scenarios. For mSUGRA, the neutralino relic density has been computed using the public code `DarkSUSY`, which has been adapted to include squark flavour violation entries in the squark rotation matrices. The four benchmark points in mSUGRA all lead to dark matter relic density in agreement with current `WMAP` limits. For the scenarios with GMSB, where the dark matter candidate is the gravitino, further constraints related to leptogenesis and big bang nucleosynthesis have to be taken into account. It has been shown that for the six benchmark points, these can be well fulfilled by adjusting the gravitino mass. The only exception concerns the preferred interval of the reheating temperature of the Universe, which enters in conflict with the constraints preserving the abundances of light elements.

One important part of this Thesis deals with radiative corrections to the neutralino pair annihilation cross section. The latter plays an important role in the prediction of the relic dark matter density for a given supersymmetric model. Due to the large strong coupling constant, corrections of $\mathcal{O}(\alpha_s)$ can have a numerically important impact on the annihilation cross section, and in consequence on the relic density and the cosmologically favoured regions in the MSSM parameter space. As a first step, we have calculated the radiative corrections of $\mathcal{O}(\alpha_s)$ to neutralino pair annihilation into a bottom quark-antiquark pair through the exchange of a pseudoscalar Higgs boson. This process dominates in the so-called "A-funnel" region of the mSUGRA parameter space at large $\tan\beta$. Including the corrections into the public code `DarkSUSY`, we have demonstrated that they have an important impact on the annihilation cross section and, in consequence, on the prediction of the neutralino relic density. Taking into account the corrections, the preferred region in the parameter space is shifted to smaller sparticle masses. We have also discussed the effects of the simultaneously corrected width of the Higgs boson, which plays an important role near the Higgs pole.

The work concerning only the "A-funnel" region has then been extended by calculating the complete QCD and SUSY-QCD corrections to neutralino pair annihilation into quark-antiquark pairs at the one-loop level. A detailed analysis of the minimal supergravity parameter space has helped to identify the regions in the parameter space, where the different quark-antiquark final states contribute significantly. As a first result, it has been revealed that the first and second generation quarks only play important roles in regions that do either not agree with the current WMAP limits or that are excluded by mass limits or the branching ratio BR($b \to s\gamma$). In consequence, we have focused on the "heavy" third generation quarks. The complete one-loop corrections of $\mathcal{O}(\alpha_s)$ have been implemented in a numerical programme which has been used in combination with the public code `micrOMEGAs`. This has allowed to study their impact on the neutralino pair annihilation cross section and the resulting neutralino relic density. We have shown that taking into account the corrections leads to a modification of the cosmologically favoured regions in the mSUGRA parameter space. In particular, we have revealed the effects of the contributions that are not yet implemented in the public version of `micrOMEGAs`.

We finally have studied the production of squark and gauginos at the CERN Large Hadron Collider (LHC) within gauge-mediated Supersymmetry-breaking models including

non-minimal flavour violation. We have pointed out the novel effects of flavour breaking entries in the squark mass matrices, mainly due to the "avoided crossings" of squark mass eigenvalues, on the production cross sections.

As perspectives, the obtained results on non-minimal flavour violation (NMFV) in minimal supergravity and gauge-mediated Supersymmetry-breaking encourage to investigate further in this sector. It will be interesting to perform a similar analysis of the electroweak precision, low-energy, and cosmological constraints for scenarios with anomaly-mediated Supersymmetry-breaking (AMSB). Since in those models, Supersymmetry-breaking is mediated by gravity as in mSUGRA, flavour violation naturally appears at the electroweak scale. It would also be interesting to study numerically the gravitino production cross sections presented in Chap. 5. However, a scenario with a light gravitino, agreeing with the experimental constraints, and providing a viable candidate for the cold dark matter has to be found. This might also lead the analysis of non-minimal flavour violation beyond mSUGRA and GMSB. Of course, for better theoretical accuracy it would be necessary to include higher order corrections to the production cross sections and decay widths.

Concerning dark matter annihilation, scenarios with important contributions of light quark final states to the annihilation cross section have not yet been studied. However, it has been shown that in mSUGRA models these scenarios are already excluded by current mass limits and measurements of the $b \to s\gamma$ branching ratio. We therefore should choose a scenario beyond minimal supergravity with a neutralino LSP. Finally it would be interesting to perform a study combining dark matter annihilation and non-minimal flavour violation. This might be done for scenarios where coannihilations play an important role. The lightest neutralino can then annihilate with a light stau or stop into Standard Model particles, which may open space for flavour violation effects.

Appendix A

Couplings and Form Factors in Non-Minimal Flavour Violating Supersymmetry

In this Appendix, we give detailed analytical expressions for generalized coupling strength, charges, and form factors entering the squark and gaugino production cross section presented in Chap. 5.

A.1 Generalized Strong and Electroweak Couplings

Considering the strong interaction first, the interaction of quarks, squarks, and gluinos, whose coupling is normally just given by $g_s = \sqrt{4\pi\alpha_s}$, can in general lead to flavour violation in the left- and right-handed chiral sectors through non-diagonal entries in the 6×6 squark rotation matrices $\mathcal{R}^{\tilde{q}}$ defined in Eqs. (1.54) and (1.55) for up-type and down-type squarks, respectively. The generalized left- and right-handed quark-squark-gluino couplings are then given by [65]

$$\left\{L_{\tilde{q}_j q_k \tilde{g}}, R_{\tilde{q}_j q_k \tilde{g}}\right\} \;=\; \left\{\mathcal{R}^q_{jk}, -\mathcal{R}^q_{j(k+3)}\right\}, \tag{A.1}$$

where, since the gluino is electrically neutral, the involved quark and squark both have to be up- or down-type.

For the electroweak interaction, the square of the weak coupling $g_W^2 = e^2/\sin^2\theta_W$ is defined in terms of the electromagnetic fine structure constant $\alpha = e^2/(4\pi)$ and the squared sine of the electroweak mixing angle $\sin^2\theta_W = 1 - \cos^2\theta_W$. Following the standard notation, the $W^\pm - \tilde{\chi}_i^0 - \tilde{\chi}_j^\pm$, $Z^0 - \tilde{\chi}_i^+ - \tilde{\chi}_j^-$, and $Z^0 - \tilde{\chi}_i^0 - \tilde{\chi}_j^0$ interaction vertexes are proportional to

$$\begin{aligned}
O_{ij}^L &= -\frac{1}{\sqrt{2}}\mathcal{N}_{i4}\mathcal{V}_{j2}^* + \mathcal{N}_{i2}\mathcal{V}_{j1}^*, \\
O_{ij}^{\prime L} &= -\mathcal{V}_{i1}\mathcal{V}_{j1}^* - \frac{1}{2}\mathcal{V}_{i2}\mathcal{V}_{j2}^* + \delta_{ij}\sin^2\theta_W, \\
O_{ij}^{\prime\prime L} &= -\frac{1}{2}\mathcal{N}_{i3}\mathcal{N}_{j3}^* + \frac{1}{2}\mathcal{N}_{i4}\mathcal{N}_{j4}^*
\end{aligned} \tag{A.2}$$

and

$$\begin{aligned} O_{ij}^{R} &= -\frac{1}{\sqrt{2}}\mathcal{N}_{i3}^{*}\mathcal{U}_{j2} + \mathcal{N}_{i2}^{*}\mathcal{U}_{j1}, \\ O_{ij}^{\prime R} &= -\mathcal{U}_{i1}^{*}\mathcal{U}_{j1} - \frac{1}{2}\mathcal{U}_{i2}^{*}\mathcal{U}_{j2} + \delta_{ij}\sin^2\theta_W, \\ O_{ij}^{\prime\prime R} &= -O_{ij}^{\prime\prime L}, \end{aligned} \tag{A.3}$$

where the matrices $\mathcal{N}$, $\mathcal{V}$, and $\mathcal{V}$ relate to neutralino and chargino mixing as discussed in Sec. 1.5.2.

In non-minimal flavour violating Supersymmetry, the coupling strengths of left- and right-handed quark and squarks to the electroweak gauge bosons are given by [65]

$$\begin{aligned} L_{qq'Z} &= \left(2T_q^3 - 2e_q\sin^2\theta_W\right)\delta_{qq'}, \\ L_{\tilde{q}_i\tilde{q}_jZ} &= \left(2T_{\tilde{q}}^3 - 2e_{\tilde{q}}\sin^2\theta_W\right)\sum_{k=1}^{3}\mathcal{R}_{ik}^{\tilde{q}}\mathcal{R}_{jk}^{\tilde{q}*}, \\ L_{qq'W} &= \sqrt{2}\cos\theta_W V_{qq'}, \\ L_{\tilde{u}_i\tilde{d}_jW} &= \sqrt{2}\cos\theta_W\sum_{k,l=1}^{3}V_{u_kd_l}\mathcal{R}_{ik}^{\tilde{u}}\mathcal{R}_{jl}^{\tilde{d}*}, \end{aligned} \tag{A.4}$$

and

$$\begin{aligned} R_{qq'Z} &= \left(2T_q^3 - 2e_q\sin^2\theta_W\right)\delta_{qq'}, \\ R_{\tilde{q}_i\tilde{q}_jZ} &= \left(2T_{\tilde{q}}^3 - 2e_{\tilde{q}}\sin^2\theta_W\right)\sum_{k=1}^{3}\mathcal{R}_{i(k+3)}^{\tilde{q}}\mathcal{R}_{j(k+3)}^{\tilde{q}*}, \end{aligned} \tag{A.5}$$

respectively. The right-handed couplings to W-bosons are, of course, zero. Here, the weak isospin quantum numbers are $T_{q,\tilde{q}}^3 = \pm 1/2$ for left-handed and $T_{q,\tilde{q}}^3 = 0$ for right-handed quarks and squarks, their fractional electromagnetic charges are denoted by $e_{q,\tilde{q}}$ and V_{kl} are the elements of the CKM-matrix, defined through

$$V = V_L^u V_L^{d\dagger} = \begin{pmatrix} V_{ud} & V_{us} & V_{ub} \\ V_{cd} & V_{cs} & V_{cb} \\ V_{td} & V_{ts} & V_{tb} \end{pmatrix} \tag{A.6}$$

with the matrices V^u and V^d that rotate the up- and down-type quark interaction eigenstates to the basis of physical mass eigenstates. To simplify the notation, we have introduced the flavour indices $d_1 = d$, $d_2 = s$, $d_3 = b$, $u_1 = u$, $u_2 = c$, and $u_3 = t$.

The supersymmetric counterparts of the above vertices correspond to the quark-squark-gaugino couplings, whose left- and right-handed contributions are given by [65]

$$\begin{aligned} L_{\tilde{d}_jd_k\tilde{\chi}_i^0} &= \left[\left(e_q - T_q^3\right)\sin\theta_W\mathcal{N}_{i1} + T_q^3\cos\theta_W\mathcal{N}_{i2}\right]\mathcal{R}_{jk}^{d*} + \frac{m_{d_k}\cos\theta_W}{2m_W\cos\beta}\mathcal{N}_{i3}\mathcal{R}_{j(k+3)}^{d*}, \\ L_{\tilde{u}_ju_k\tilde{\chi}_i^0} &= \left[\left(e_q - T_q^3\right)\sin\theta_W\mathcal{N}_{i1} + T_q^3\cos\theta_W\mathcal{N}_{i2}\right]\mathcal{R}_{jk}^{u*} + \frac{m_{u_k}\cos\theta_W}{2m_W\sin\beta}\mathcal{N}_{i4}\mathcal{R}_{j(k+3)}^{u*}, \end{aligned}$$

$$
\begin{aligned}
L_{\tilde{d}_j u_l \tilde{\chi}_k^\pm} &= \sum_{k=1}^{3} \left[\mathcal{U}_{i1} \mathcal{R}^{d*}_{jk} - \frac{m_{d_k}}{\sqrt{2} m_W \cos\beta} \mathcal{U}_{i2} \mathcal{R}^{d*}_{j(k+3)} \right] V_{u_l d_k}, \\
L_{\tilde{u}_j d_l \tilde{\chi}_k^\pm} &= \sum_{k=1}^{3} \left[\mathcal{V}^*_{i1} \mathcal{R}^{u}_{jk} - \frac{m_{u_k}}{\sqrt{2} m_W \sin\beta} \mathcal{V}^*_{i2} \mathcal{R}^{u}_{j(k+3)} \right] V_{u_k d_l},
\end{aligned} \tag{A.7}
$$

and

$$
\begin{aligned}
-R^*_{\tilde{d}_j d_k \tilde{\chi}_i^0} &= e_q \sin\theta_W \mathcal{N}_{i1} \mathcal{R}^{d}_{j(k+3)} - \frac{m_{d_k} \cos\theta_W}{2 m_W \cos\beta} \mathcal{N}_{i3} \mathcal{R}^{d*}_{jk}, \\
-R^*_{\tilde{u}_j u_k \tilde{\chi}_i^0} &= e_q \sin\theta_W \mathcal{N}_{i1} \mathcal{R}^{u}_{j(k+3)} + \frac{m_{u_k} \cos\theta_W}{2 m_W \sin\beta} \mathcal{N}_{i4} \mathcal{R}^{u}_{jk}, \\
-R^*_{\tilde{d}_j u_l \tilde{\chi}_k^\pm} &= \sum_{k=1}^{3} \frac{m_{u_l}}{\sqrt{2} m_W \sin\beta} V^*_{u_l d_k} \mathcal{V}_{i2} \mathcal{R}^{d}_{jk}, \\
-R^*_{\tilde{u}_j d_l \tilde{\chi}_k^\pm} &= \sum_{k=1}^{3} \frac{m_{d_l}}{\sqrt{2} m_W \cos\beta} V^*_{u_k d_l} \mathcal{U}^*_{i2} \mathcal{R}^{u*}_{jk},
\end{aligned} \tag{A.8}
$$

respectively. All other couplings vanish due to electromagnetic charge conservation. Note that the corresponding couplings for (s)leptons and (s)neutrinos can be deduced by taking the proper limits, i.e. removing the up-type quark masses and set the CKM-matrix to unity.

A.2 Form Factors for Squark Production

In this Section, we give a summary of all form factors appearing in the cross sections of squark-(anti)squark production, Eqs. (5.8), (5.9), (5.11), and (5.12). The form factors are given by [65]

$$
\begin{aligned}
\mathcal{W} &= \frac{\pi \alpha^2}{16 \sin^4\theta_W \cos^4\theta_W s^2} \left| L^*_{qq'W} L_{\tilde{u}_i \tilde{d}_j W} \right|^2 \left(u\,t - m^2_{\tilde{u}_i} m^2_{\tilde{d}_j} \right), \\
\mathcal{Y} &= \frac{\pi \alpha^2 e_q^2 e_{\tilde{q}}^2 \delta_{ij} \delta_{qq'}}{s^2} \left(u\,t - m^2_{\tilde{q}_i} m^2_{\tilde{q}'_j} \right), \\
\mathcal{Z}_m &= \frac{\pi \alpha^2}{16 s^2 \sin^4\theta_W \cos^4\theta_W} \left| L_{\tilde{q}_i \tilde{q}_j Z} + R_{\tilde{q}_i \tilde{q}_j Z} \right|^2 \left(\mathcal{C}^m_{qq'Z} \right)^2 \left(u\,t - m^2_{\tilde{q}_i} m^2_{\tilde{q}'_j} \right), \\
&\quad \times \left[\left(u\,t - m^2_{\tilde{u}_i} m^2_{\tilde{d}_j} \right) \delta_{mn} + \left(m_{\tilde{\chi}^0_k} m_{\tilde{\chi}^0_l} s \right) (1 - \delta_{mn}) \right], \\
\mathcal{G} &= \frac{2 \pi \alpha_s^2 \delta_{ij} \delta_{qq'}}{9 s^2} \left(u\,t - m^2_{\tilde{q}_i} m^2_{\tilde{q}'_j} \right), \\
\mathcal{G}_{mn} &= \frac{2 \pi \alpha_s^2}{9 s^2} \left| \mathcal{C}^{n*}_{\tilde{d}_j q' \tilde{g}} \mathcal{C}^m_{\tilde{u}_i q \tilde{g}} \right|^2 \left[\left(u\,t - m^2_{\tilde{u}_i} m^2_{\tilde{d}_j} \right) \delta_{mn} + \left(m^2_{\tilde{g}} s \right) (1 - \delta_{mn}) \right], \\
\widetilde{\mathcal{G}}_{mn} &= \frac{2 \pi \alpha_s^2}{9 s^2} \left| \mathcal{C}^m_{\tilde{q}_i q \tilde{g}} \mathcal{C}^{n*}_{\tilde{q}_j q' \tilde{g}} \right|^2 \left[\left(u\,t - m^2_{\tilde{q}_i} m^2_{\tilde{q}_j} \right) \delta_{mn} + \left(m^2_{\tilde{g}} s \right) (1 - \delta_{mn}) \right],
\end{aligned}
$$

$$
\begin{aligned}
\mathcal{C}^{kl}_{mn} &= \frac{\pi\,\alpha^2}{4\,\sin^4\theta_W\,s^2}\mathcal{C}^{n}_{\tilde{u}_j q' \tilde{\chi}^{\pm}_k}\,\mathcal{C}^{m*}_{\tilde{d}_i q \tilde{\chi}^{\pm}_k}\,\mathcal{C}^{n*}_{\tilde{u}_j q' \tilde{\chi}^{\pm}_l}\,\mathcal{C}^{m}_{\tilde{d}_i q \tilde{\chi}^{\pm}_l} \\
&\quad \times\left[\left(u\,t - m^2_{\tilde{d}_i}\,m^2_{\tilde{u}_j}\right)(1-\delta_{mn}) + m_{\tilde{\chi}^{\pm}_k}\,m_{\tilde{\chi}^{\pm}_l}\,s\,\delta_{mn}\right], \\
\mathcal{N}^{kl}_{mn} &= \frac{\pi\,\alpha^2}{\sin^4\theta_W\,\cos^4\theta_W\,s^2}\mathcal{C}^{n}_{\tilde{d}_j q' \tilde{\chi}^{0}_k}\,\mathcal{C}^{m*}_{\tilde{u}_i q \tilde{\chi}^{0}_k}\,\mathcal{C}^{n*}_{\tilde{d}_j q' \tilde{\chi}^{0}_l}\,\mathcal{C}^{m}_{\tilde{u}_i q \tilde{\chi}^{0}_l} \\
[\mathcal{NW}]^k &= \frac{\pi\,\alpha^2}{6\,\sin^4\theta_W\,\cos^4\theta_W\,s^2}\,\Re\left\{L^*_{qq'W}\,L_{\tilde{u}_i\tilde{d}_j W}\,L_{\tilde{u}_i q\tilde{\chi}^0_k}\,L^*_{\tilde{q}_j q'\tilde{\chi}^0_k}\right\}\left(u\,t - m^2_{\tilde{u}_i}\,m^2_{\tilde{d}_j}\right), \\
[\mathcal{GW}] &= \frac{4\,\pi\,\alpha_s\,\alpha}{18\,\sin^2\theta_W\,\cos^2\theta_W\,s^2}\,\Re\left\{L^*_{\tilde{u}_i q\tilde{g}}\,L_{\tilde{d}_j q'\tilde{g}}\,L^*_{qq'W}\,L_{\tilde{u}_i\tilde{d}_j W}\right\}\left(u\,t - m^2_{\tilde{u}_i}\,m^2_{\tilde{d}_j}\right), \\
[\mathcal{YZ}]_m &= \frac{\pi\,\alpha^2\,e_q\,e_{\tilde{q}}\,\delta_{ij}\,\delta_{qq'}}{2\,s^2\,\sin^2\theta_W\cos^2\theta_W}\,\Re\left\{L_{\tilde{q}_i\tilde{q}_j Z} + R_{\tilde{q}_i\tilde{q}_j Z}\right\}\,\mathcal{C}^{m}_{qq'Z}\left(u\,t - m^2_{\tilde{q}_i}\,m^2_{\tilde{q}'_j}\right), \\
[\mathcal{NY}]^k_m &= \frac{2\,\pi\,\alpha^2\,e_q\,e_{\tilde{q}}\,\delta_{ij}\,\delta_{qq'}}{3\,\sin^2\theta_W\,\cos^2\theta_W\,s^2}\,\Re\left\{\mathcal{C}^{m}_{\tilde{q}_i q\tilde{\chi}^0_k}\,\mathcal{C}^{m*}_{\tilde{q}_j q'\tilde{\chi}^0_k}\right\}\left(u\,t - m^2_{\tilde{q}_i}\,m^2_{\tilde{q}_j}\right), \\
[\mathcal{NZ}]^k_m &= \frac{\pi\,\alpha^2}{6\,\sin^4\theta_W\,\cos^4\theta_W\,s^2}\,\Re\left\{\mathcal{C}^{m}_{\tilde{q}_i q\tilde{\chi}^0_k}\,\mathcal{C}^{m*}_{\tilde{q}_j q'\tilde{\chi}^0_k}\left(L_{\tilde{q}_i\tilde{q}_j Z} + R_{\tilde{q}_i\tilde{q}_j Z}\right)\right\}\,\mathcal{C}^{m}_{qq'Z}\left(u\,t - m^2_{\tilde{q}_i}\,m^2_{\tilde{q}_j}\right), \\
[\mathcal{NG}]^k_m &= \frac{8\,\pi\,\alpha\,\alpha_s\,\delta_{ij}\,\delta_{qq'}}{9\,\sin^2\theta_W\,\cos^2\theta_W\,s^2}\,\Re\left\{\mathcal{C}^{m}_{\tilde{q}_i q\tilde{\chi}^0_k}\,\mathcal{C}^{m*}_{\tilde{q}_j q'\tilde{\chi}^0_k}\right\}\left(u\,t - m^2_{\tilde{q}_i}\,m^2_{\tilde{q}_j}\right), \\
[\mathcal{CY}]^k_m &= \frac{2\,\pi\,\alpha^2\,e_q\,e_{\tilde{q}}\,\delta_{ij}\,\delta_{qq'}}{3\,\sin^2\theta_W\,s^2}\,\Re\left\{\mathcal{C}^{m}_{\tilde{q}_i q\tilde{\chi}^{\pm}_k}\,\mathcal{C}^{m*}_{\tilde{q}_j q'\tilde{\chi}^{\pm}_k}\right\}\left(u\,t - m^2_{\tilde{q}_i}\,m^2_{\tilde{q}_j}\right), \\
[\mathcal{CZ}]^k_m &= \frac{\pi\,\alpha^2}{6\,\sin^4\theta_W\,\cos^4\theta_W\,s^2}\,\Re\left\{\mathcal{C}^{m}_{\tilde{q}_i q\tilde{\chi}^{\pm}_k}\,\mathcal{C}^{m*}_{\tilde{q}_j q'\tilde{\chi}^{\pm}_k}\left(L_{\tilde{q}_i\tilde{q}_j Z} + R_{\tilde{q}_i\tilde{q}_j Z}\right)\right\}\,\mathcal{C}^{m}_{qq'Z}\left(u\,t - m^2_{\tilde{q}_i}\,m^2_{\tilde{q}_j}\right), \\
[\mathcal{CG}]^k_m &= \frac{8\,\pi\,\alpha\,\alpha_s\,\delta_{ij}\,\delta_{qq'}}{9\,\sin^2\theta_W\,s^2}\,\Re\left\{\mathcal{C}^{m}_{\tilde{q}_i q\tilde{\chi}^{\pm}_k}\,\mathcal{C}^{m*}_{\tilde{q}_j q'\tilde{\chi}^{\pm}_k}\right\}\left(u\,t - m^2_{\tilde{q}_i}\,m^2_{\tilde{q}_j}\right), \\
\left[\widetilde{\mathcal{GG}}\right]_m &= -\frac{4\,\pi\,\alpha_s^2\,\delta_{ij}\,\delta_{qq'}}{27\,s^2}\,\Re\left\{\mathcal{C}^{m*}_{\tilde{q}_i q\tilde{g}}\,\mathcal{C}^{m}_{\tilde{q}_j q'\tilde{g}}\right\}\left(u\,t - m^2_{\tilde{q}_i}\,m^2_{\tilde{q}_j}\right), \\
[\widetilde{\mathcal{GY}}]_m &= \frac{8\,\pi\,\alpha\,\alpha_s\,e_q\,e_{\tilde{q}}\,\delta_{ij}\,\delta_{qq'}}{9\,s^2}\,\Re\left\{\mathcal{C}^{m*}_{\tilde{q}_i q\tilde{g}}\,\mathcal{C}^{m}_{\tilde{q}_j q'\tilde{g}}\right\}\left(u\,t - m^2_{\tilde{q}_i}\,m^2_{\tilde{q}_j}\right), \\
[\widetilde{\mathcal{GZ}}]_m &= \frac{2\,\pi\,\alpha\,\alpha_s}{9\,\sin^2\theta_W\,\cos^2\theta_W\,s^2}\,\Re\left\{\mathcal{C}^{m*}_{\tilde{q}_i q\tilde{g}}\,\mathcal{C}^{m}_{\tilde{q}_j q'\tilde{g}}\left(L_{\tilde{q}_i\tilde{q}_j Z} + R_{\tilde{q}_i\tilde{q}_j Z}\right)\right\}\,\mathcal{C}^{m}_{qq'Z}\left(u\,t - m^2_{\tilde{q}_i}\,m^2_{\tilde{q}_j}\right), \\
[\mathcal{CN}]^{kl}_{mn} &= \frac{\pi\,\alpha^2}{3\,\sin^4\theta_W\,\cos^2\theta_W\,s^2}\Re\left\{\mathcal{C}^{n}_{\tilde{u}_j q'\tilde{\chi}^{\pm}_k}\,\mathcal{C}^{m*}_{\tilde{d}_i q\tilde{\chi}^{\pm}_k}\,\mathcal{C}^{m}_{\tilde{u}_j q\tilde{\chi}^{0}_l}\,\mathcal{C}^{n}_{\tilde{d}_i q'\tilde{\chi}^{0}_l}\right\} \\
&\quad \times\left[\left(u\,t - m^2_{\tilde{d}_i}\,m^2_{\tilde{u}_j}\right)(\delta_{mn}-1) + m_{\tilde{\chi}^{\pm}_k}\,m_{\tilde{\chi}^{0}_l}\,s\,\delta_{mn}\right], \\
[\mathcal{CG}]^k_{mn} &= \frac{4\,\pi\,\alpha\,\alpha_s}{9\,s^2\,\sin^2\theta_W}\Re\left\{\mathcal{C}^{n}_{\tilde{u}_j q'\tilde{\chi}^{\pm}_k}\,\mathcal{C}^{m*}_{\tilde{d}_i q\tilde{\chi}^{\pm}_k}\,\mathcal{C}^{m*}_{\tilde{u}_j q\tilde{g}}\,\mathcal{C}^{n*}_{\tilde{d}_i q'\tilde{g}}\right\} \\
&\quad \times\left[\left(u\,t - m^2_{\tilde{d}_i}\,m^2_{\tilde{u}_j}\right)(\delta_{mn}-1) + m_{\tilde{\chi}^{\pm}_k}\,m_{\tilde{g}}\,s\,\delta_{mn}\right], \\
[\mathcal{NT}]^{kl}_{mn} &= \frac{\pi\,\alpha^2}{\sin^4\theta_W\,\cos^4\theta_W\,s^2}\mathcal{C}^{n*}_{\tilde{q}_j q'\tilde{\chi}^{0}_k}\,\mathcal{C}^{m*}_{\tilde{q}_i q\tilde{\chi}^{0}_k}\,\mathcal{C}^{n}_{\tilde{q}_j q'\tilde{\chi}^{0}_l}\,\mathcal{C}^{m}_{\tilde{q}_i q\tilde{\chi}^{0}_l} \\
&\quad \times\left[\left(u\,t - m^2_{\tilde{q}_i}\,m^2_{\tilde{q}_j}\right)(1-\delta_{mn}) + m_{\tilde{\chi}^{0}_k}\,m_{\tilde{\chi}^{0}_l}\,s\,\delta_{mn}\right],
\end{aligned}
$$

$$
\begin{aligned}
[\mathcal{NU}]^{kl}_{mn} &= \frac{\pi\,\alpha^2}{\sin^4\theta_W\,\cos^4\theta_W\,s^2}\mathcal{C}^{n*}_{\tilde{q}_i q'\tilde{\chi}^0_k}\,\mathcal{C}^{m*}_{\tilde{q}_j q\tilde{\chi}^0_k}\,\mathcal{C}^{n}_{\tilde{q}_i q'\tilde{\chi}^0_l}\,\mathcal{C}^{m}_{\tilde{q}_j q\tilde{\chi}^0_l} \\
&\quad\times\left[\left(u\,t-m^2_{\tilde{q}_i}\,m^2_{\tilde{q}_j}\right)(1-\delta_{mn})+m_{\tilde{\chi}^0_k}\,m_{\tilde{\chi}^0_l}\,s\,\delta_{mn}\right], \\
[\mathcal{NTU}]^{kl}_{mn} &= \frac{2\,\pi\,\alpha^2}{3\,\sin^4\theta_W\,\cos^4\theta_W\,s^2}\Re\left\{\mathcal{C}^{m*}_{\tilde{q}_i q\tilde{\chi}^0_k}\,\mathcal{C}^{n*}_{\tilde{q}_j q'\tilde{\chi}^0_k}\,\mathcal{C}^{n}_{\tilde{q}_i q'\tilde{\chi}^0_l}\,\mathcal{C}^{m}_{\tilde{q}_j q\tilde{\chi}^0_l}\right\} \\
&\quad\times\left[\left(u\,t-m^2_{\tilde{q}_i}\,m^2_{\tilde{q}_j}\right)(\delta_{mn}-1)+m_{\tilde{\chi}^0_k}\,m_{\tilde{\chi}^0_l}\,s\,\delta_{mn}\right], \\
[\mathcal{GT}]_{mn} &= \frac{2\,\pi\,\alpha_s^2}{9\,s^2}\left|\mathcal{C}^{n}_{\tilde{q}_j q'\tilde{g}}\,\mathcal{C}^{m}_{\tilde{q}_i q\tilde{g}}\right|^2\left[\left(u\,t-m^2_{\tilde{q}_i}\,m^2_{\tilde{q}_j}\right)(1-\delta_{mn})+m^2_{\tilde{g}}\,s\,\delta_{mn}\right], \\
[\mathcal{GU}]_{mn} &= \frac{2\,\pi\,\alpha_s^2}{9\,s^2}\left|\mathcal{C}^{n}_{\tilde{q}_i q'\tilde{g}}\,\mathcal{C}^{m}_{\tilde{q}_j q\tilde{g}}\right|^2\left[\left(u\,t-m^2_{\tilde{q}_i}\,m^2_{\tilde{q}_j}\right)(1-\delta_{mn})+m^2_{\tilde{g}}\,s\,\delta_{mn}\right], \\
[\mathcal{GTU}]_{mn} &= \frac{4\,\pi\,\alpha_s^2}{27\,s^2}\Re\left\{\mathcal{C}^{m}_{\tilde{q}_i q\tilde{g}}\,\mathcal{C}^{n}_{\tilde{q}_j q'\tilde{g}}\mathcal{C}^{m*}_{\tilde{q}_i q'\tilde{g}}\,\mathcal{C}^{n*}_{\tilde{q}_j q\tilde{g}}\right\} \\
&\quad\times\left[\left(u\,t-m^2_{\tilde{q}_i}\,m^2_{\tilde{q}_j}\right)(1-\delta_{mn})-m^2_{\tilde{g}}\,s\,\delta_{mn}\right], \\
[\mathcal{NGA}]^{k}_{mn} &= \frac{8\,\pi\,\alpha\alpha_s}{9\,s^2\,\sin^2\theta_W\,\cos^2\theta_W}\Re\left\{\mathcal{C}^{n*}_{\tilde{q}_j q'\tilde{\chi}^0_k}\,\mathcal{C}^{m*}_{\tilde{q}_i q\tilde{\chi}^0_k}\,\mathcal{C}^{m*}_{\tilde{q}_i q'\tilde{g}}\,\mathcal{C}^{n*}_{\tilde{q}_j q\tilde{g}}\right\} \\
&\quad\times\left[\left(u\,t-m^2_{\tilde{q}_i}\,m^2_{\tilde{q}_j}\right)(\delta_{mn}-1)+m_{\tilde{\chi}^0_k}\,m_{\tilde{g}}\,s\,\delta_{mn}\right], \\
[\mathcal{NGB}]^{k}_{mn} &= \frac{8\,\pi\,\alpha\alpha_s}{9\,s^2\,\sin^2\theta_W\,\cos^2\theta_W}\Re\left\{\mathcal{C}^{n*}_{\tilde{q}_i q'\tilde{\chi}^0_k}\,\mathcal{C}^{m*}_{\tilde{q}_j q\tilde{\chi}^0_k}\,\mathcal{C}^{n*}_{\tilde{q}_j q'\tilde{g}}\,\mathcal{C}^{m*}_{\tilde{q}_i q\tilde{g}}\right\} \\
&\quad\times\left[\left(u\,t-m^2_{\tilde{q}_i}\,m^2_{\tilde{q}_j}\right)(\delta_{mn}-1)+m_{\tilde{\chi}^0_k}\,m_{\tilde{g}}\,s\,\delta_{mn}\right]. \qquad \text{(A.9)}
\end{aligned}
$$

A.3 Generalized Charges for Gaugino Production

The generalized charges for chargino pair production appearing in Eq. (5.14) are given by [65]

$$
\begin{aligned}
Q^{u-+}_{LL} &= \frac{e_q\delta_{ij}\delta_{qq'}}{s}-\frac{L_{qq'Z}O'^{R*}_{ij}}{2\sin^2\theta_W\cos^2\theta_W s_Z}+\sum_{k=1}^{6}\frac{L_{\tilde{d}_k q'\tilde{\chi}^\pm_i}L^*_{\tilde{d}_k q\tilde{\chi}^\pm_j}}{2\sin^2\theta_W u_{\tilde{d}_k}}, \\
Q^{t-+}_{LL} &= \frac{e_q\delta_{ij}\delta_{qq'}}{s}-\frac{L_{qq'Z}O'^{L*}_{ij}}{2\sin^2\theta_W\cos^2\theta_W s_Z}+\sum_{k=1}^{6}\frac{L^*_{\tilde{d}_k q'\tilde{\chi}^\pm_i}L_{\tilde{d}_k q\tilde{\chi}^\pm_j}}{2\sin^2\theta_W t_{\tilde{d}_k}}, \\
Q^{u-+}_{RR} &= \frac{e_q\delta_{ij}\delta_{qq'}}{s}-\frac{R_{qq'Z}O'^{L*}_{ij}}{2\sin^2\theta_W\cos^2\theta_W s_Z}+\sum_{k=1}^{6}\frac{R_{\tilde{d}_k q'\tilde{\chi}^\pm_i}R^*_{\tilde{d}_k q\tilde{\chi}^\pm_j}}{2\sin^2\theta_W u_{\tilde{d}_k}}, \\
Q^{t-+}_{RR} &= \frac{e_q\delta_{ij}\delta_{qq'}}{s}-\frac{R_{qq'Z}O'^{R*}_{ij}}{2\sin^2\theta_W\cos^2\theta_W s_Z}+\sum_{k=1}^{6}\frac{R^*_{\tilde{d}_k q'\tilde{\chi}^\pm_i}R_{\tilde{d}_k q\tilde{\chi}^\pm_j}}{2\sin^2\theta_W t_{\tilde{d}_k}},
\end{aligned}
$$

$$
\begin{aligned}
Q_{LR}^{u-+} &= \sum_{k=1}^{6} \frac{R_{\tilde{d}_k q\ \tilde{\chi}_i^\pm} L^*_{\tilde{d}_k q\ \tilde{\chi}_j^\pm}}{2\sin^2\theta_W u_{\tilde{d}_k}}, \\
Q_{LR}^{t-+} &= \sum_{k=1}^{6} \frac{R^*_{\tilde{d}_k q\ \tilde{\chi}_i^\pm} L_{\tilde{d}_k q\ \tilde{\chi}_j^\pm}}{2\sin^2\theta_W t_{\tilde{d}_k}}, \\
Q_{RL}^{u-+} &= \sum_{k=1}^{6} \frac{L_{\tilde{d}_k q\ \tilde{\chi}_i^\pm} R^*_{\tilde{d}_k q\ \tilde{\chi}_j^\pm}}{2\sin^2\theta_W u_{\tilde{d}_k}}, \\
Q_{RL}^{t-+} &= \sum_{k=1}^{6} \frac{L^*_{\tilde{d}_k q\ \tilde{\chi}_i^\pm} R_{\tilde{d}_k q\ \tilde{\chi}_j^\pm}}{2\sin^2\theta_W t_{\tilde{d}_k}}.
\end{aligned} \tag{A.10}
$$

For the associated production of charginos and neutralinos the charges are

$$
\begin{aligned}
Q_{LL}^{u+0} &= \frac{1}{\sqrt{2}\cos\theta_W \sin^2\theta_W}\left[\frac{O_{ji}^{L*} L^*_{qq'W}}{\sqrt{2}s_W} + \sum_{k=1}^{6} \frac{L^*_{\tilde{u}_k q'\tilde{\chi}_i^\pm} L^*_{\tilde{u}_k q\tilde{\chi}_j^0}}{u_{\tilde{u}_k}}\right], \\
Q_{LL}^{t+0} &= \frac{1}{\sqrt{2}\cos\theta_W \sin^2\theta_W}\left[\frac{O_{ji}^{R*} L^*_{qq'W}}{\sqrt{2}s_W} - \sum_{k=1}^{6} \frac{L^*_{\tilde{d}_k q\tilde{\chi}_i^\pm} L_{\tilde{d}_k q'\tilde{\chi}_j^0}}{t_{\tilde{d}_k}}\right], \\
Q_{RR}^{u+0} &= \frac{1}{\sqrt{2}\cos\theta_W \sin^2\theta_W} \sum_{k=1}^{6} \frac{R^*_{\tilde{u}_k q'\tilde{\chi}_i^\pm} R^*_{\tilde{u}_k q\tilde{\chi}_j^0}}{u_{\tilde{u}_k}}, \\
Q_{RR}^{t+0} &= \frac{1}{\sqrt{2}\cos\theta_W \sin^2\theta_W} \sum_{k=1}^{6} \frac{R^*_{\tilde{d}_k q\tilde{\chi}_i^\pm} R_{\tilde{d}_k q'\tilde{\chi}_j^0}}{t_{\tilde{d}_k}}, \\
Q_{LR}^{u+0} &= \frac{1}{\sqrt{2}\cos\theta_W \sin^2\theta_W} \sum_{k=1}^{6} \frac{R^*_{\tilde{u}_k q'\tilde{\chi}_i^\pm} L^*_{\tilde{u}_k q\tilde{\chi}_j^0}}{u_{\tilde{u}_k}}, \\
Q_{LR}^{t+0} &= \frac{1}{\sqrt{2}\cos\theta_W \sin^2\theta_W} \sum_{k=1}^{6} \frac{L^*_{\tilde{d}_k q\tilde{\chi}_i^\pm} R_{\tilde{d}_k q'\tilde{\chi}_j^0}}{t_{\tilde{d}_k}}, \\
Q_{RL}^{u+0} &= \frac{1}{\sqrt{2}\cos\theta_W \sin^2\theta_W} \sum_{k=1}^{6} \frac{L^*_{\tilde{u}_k q'\tilde{\chi}_i^\pm} R^*_{\tilde{u}_k q\tilde{\chi}_j^0}}{u_{\tilde{u}_k}}, \\
Q_{RL}^{t+0} &= \frac{1}{\sqrt{2}\cos\theta_W \sin^2\theta_W} \sum_{k=1}^{6} \frac{R^*_{\tilde{d}_k q\tilde{\chi}_i^\pm} L_{\tilde{d}_k q'\tilde{\chi}_j^0}}{t_{\tilde{d}_k}}.
\end{aligned} \tag{A.11}
$$

Finally, the charges for neutralino pair production are given by

$$
\begin{aligned}
Q_{LL}^{u00} &= \frac{1}{\sin^2\theta_W \cos^2\theta_W \sqrt{1+\delta_{ij}}}\left[\frac{L_{qq'Z} O''^{L}_{ij}}{2s_Z} + \sum_{k=1}^{6} \frac{L_{\tilde{q}_k q'\tilde{\chi}_i^0} L^*_{\tilde{q}_k q\tilde{\chi}_j^0}}{u_{\tilde{q}_k}}\right], \\
Q_{LL}^{t00} &= \frac{1}{\sin^2\theta_W \cos^2\theta_W \sqrt{1+\delta_{ij}}}\left[\frac{L_{qq'Z} O''^{R}_{ij}}{2s_Z} - \sum_{k=1}^{6} \frac{L^*_{\tilde{q}_k q\tilde{\chi}_i^0} L_{\tilde{q}_k q'\tilde{\chi}_j^0}}{t_{\tilde{q}_k}}\right],
\end{aligned}
$$

$$
\begin{aligned}
Q_{RR}^{u00} &= \frac{1}{\sin^2\theta_W \cos^2\theta_W \sqrt{1+\delta_{ij}}} \left[\frac{R_{qq'Z} O''^{R}_{ij}}{2 s_Z} + \sum_{k=1}^{6} \frac{R_{\tilde{q}_k q' \tilde{\chi}_i^0} R^*_{\tilde{q}_k q \tilde{\chi}_j^0}}{u_{\tilde{q}_k}} \right], \\
Q_{RR}^{t00} &= \frac{1}{\sin^2\theta_W \cos^2\theta_W \sqrt{1+\delta_{ij}}} \left[\frac{R_{qq'Z} O''^{L}_{ij}}{2 s_Z} - \sum_{k=1}^{6} \frac{R^*_{\tilde{q}_k q \tilde{\chi}_i^0} R_{\tilde{q}_k q' \tilde{\chi}_j^0}}{t_{\tilde{q}_k}} \right], \\
Q_{LR}^{u00} &= \frac{1}{\sin^2\theta_W \cos^2\theta_W \sqrt{1+\delta_{ij}}} \sum_{k=1}^{6} \frac{R_{\tilde{q}_k q' \tilde{\chi}_i^0} L^*_{\tilde{q}_k q \tilde{\chi}_j^0}}{u_{\tilde{q}_k}}, \\
Q_{LR}^{t00} &= \frac{1}{\sin^2\theta_W \cos^2\theta_W \sqrt{1+\delta_{ij}}} \sum_{k=1}^{6} \frac{L^*_{\tilde{q}_k q \tilde{\chi}_i^0} R_{\tilde{q}_k q' \tilde{\chi}_j^0}}{t_{\tilde{q}_k}}, \\
Q_{RL}^{u00} &= \frac{1}{\sin^2\theta_W \cos^2\theta_W \sqrt{1+\delta_{ij}}} \sum_{k=1}^{6} \frac{L_{\tilde{q}_k q' \tilde{\chi}_i^0} R^*_{\tilde{q}_k q \tilde{\chi}_j^0}}{u_{\tilde{q}_k}}, \\
Q_{RL}^{t00} &= \frac{1}{\sin^2\theta_W \cos^2\theta_W \sqrt{1+\delta_{ij}}} \sum_{k=1}^{6} \frac{R^*_{\tilde{q}_k q \tilde{\chi}_i^0} L_{\tilde{q}_k q' \tilde{\chi}_j^0}}{t_{\tilde{q}_k}}.
\end{aligned}
\tag{A.12}
$$

Appendix B

Numerical Values

This Appendix consists of a compilation of the parameter values that have been used for all numerical calculations throughout this work. We have used the following values for the masses of the Standard Model fermions [64]:

Top quark pole mass	m_t^{pole}	$=$	174.2 GeV
Bottom quark mass	$m_b^{\overline{\text{MS}}}(m_b)$	$=$	4.2 GeV
Charm quark mass	$m_c^{\overline{\text{MS}}}(m_c)$	$=$	1.25 GeV
Light quark masses	$m_s^{\overline{\text{MS}}}(m_s)$	$=$	0.095 GeV
	$m_d^{\overline{\text{MS}}}(2\text{ GeV})$	$=$	0.007 GeV
	$m_u^{\overline{\text{MS}}}(2\text{ GeV})$	$=$	0.003 GeV
Tau lepton mass	m_τ	$=$	1.777 GeV
Muon mass	m_μ	$=$	0.106 GeV
Electron mass	m_e	$=$	$0.511 \cdot 10^{-3}$ GeV

Note, however, that we have neglected the quark masses except the top mass in the calculation of production cross sections at the LHC. In Chap. 4, we have used the more recent value of $m_t^{\text{pole}} = 171.4$ GeV [120] for the top pole mass.

The coupling constants of the strong, electroweak, and gravitational interactions are [64]:

Strong coupling constant	$\alpha_s(m_Z)$	$=$	0.1176
Fine structure constant	$\alpha^{-1}(0)$	$=$	137.0359998
	$\alpha^{-1}(m_Z)$	$=$	127.906
Fermi's coupling constant	G_{F}	$=$	$1.16637 \cdot 10^{-5}$ GeV^{-2}
Gravitational constant	G_{N}	$=$	$6.7087 \cdot 10^{-39}$ GeV^{-2}
Reduced Planck mass	M_{P}	$=$	$\sqrt{1/8\pi G_{\text{N}}}$

The masses and widths of the electroweak gauge bosons and the squared sine of the weak mixing angle are given by [64]:

Z-boson mass	m_Z	=	91.1876 GeV
Z-boson width	Γ_Z	=	2.4952 GeV
W-boson mass	m_W	=	80.403 GeV
W-boson width	Γ_W	=	2.141 GeV
Weak mixing angle	$\sin^2\theta_W$	=	0.23122

The CKM-matrix is parametrized in the standard way, see Eq. (A.6), using the following values for the mixing angles and the CP-violating phase [64]:

Mixing angles	$\sin\theta_{12}$	=	0.2243
	$\sin\theta_{13}$	=	0.0037
	$\sin\theta_{23}$	=	0.0413
CP-violating phase	δ_{13}	=	1.05

Appendix C

Virtual One-Loop Calculations

In this Appendix, we present detailed calculations of the one-loop diagrams appearing in this work.

C.1 Heavy Quark Self-Energy and Renormalization

The quark self-energy has QCD and SUSY-QCD contributions, that arise from the gluon-quark and gluino-squark loops shown in Fig. C.1. For a quark having mass m_q and four-momentum p_q, the self-energy can generally be split into its scalar and vector parts according to

$$\Sigma_q(p_q^2) \;=\; m_q\Sigma_S(p_q^2) + \not{p}_q\Big[\Sigma_L(p_q^2)P_L + \Sigma_R(p_q^2)P_R\Big]. \tag{C.1}$$

In the on-shell renormalization scheme, the mass and wavefunction renormalization constants are then obtained through

$$\delta Z_m \;=\; \frac{\Delta m_q}{m_q} \;=\; \Sigma_S(m_q^2) + \frac{1}{2}\Big[\Sigma_L(m_q^2) + \Sigma_R(m_q^2)\Big], \tag{C.2}$$

$$\begin{aligned}\delta Z_\psi \;=\;& -\frac{1}{2}\Big[\Sigma_L(m_q^2) + \Sigma_R(m_q^2)\Big] \\ & -m_q^2\Big[\Sigma'_L(m_q^2) + \Sigma'_R(m_q^2)\Big] - 2m_q^2\Sigma'_S(m_q^2),\end{aligned} \tag{C.3}$$

where $\Sigma'_{S,L,R}(p^2)$ denotes the derivative of $\Sigma_{S,L,R}(p^2)$ with respect to p^2.

In the case of the quark-gluon loop, the scalar and vector contributions of the quark

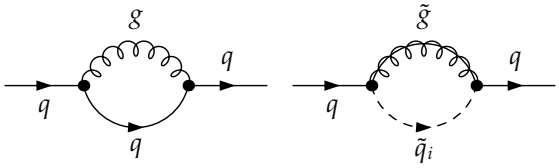

Figure C.1: Gluon-quark and gluino-squark contributions to the quark self-energy at $\mathcal{O}(\alpha_s)$.

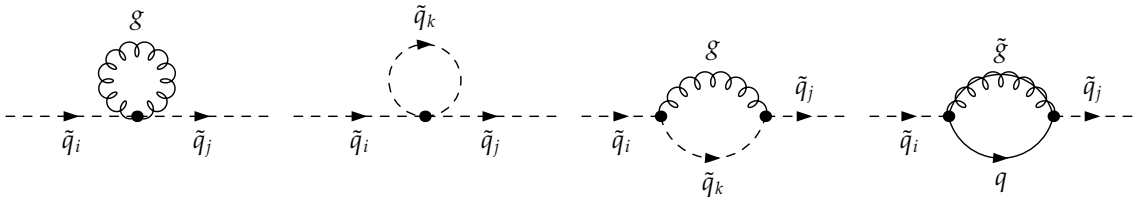

Figure C.2: Contributions to the squark self-energy at $\mathcal{O}(\alpha_s)$.

self-energy are given by

$$\Sigma_S^{(g)} = -\frac{\alpha_s C_F}{4\pi}(4-2\epsilon)B_0(p_q^2; m_q^2, 0) \tag{C.4}$$

$$\Sigma_{L,R}^{(g)} = -\frac{\alpha_s C_F}{4\pi}(2-2\epsilon)\Big[B_0(p_q^2; m_q^2, 0) + B_1(p_q^2; m_q^2, 0)\Big]. \tag{C.5}$$

For the squark-gluino loop, we obtain explicitly $(i = 1, 2)$

$$\Sigma_S^{(\tilde{q}_i\tilde{g})} = (-1)^i \frac{\alpha_s C_F}{4\pi}\frac{m_{\tilde{g}}}{m_q}B_0(p_q^2; m_{\tilde{g}}^2, m_{\tilde{q}_i}^2)\sin 2\theta_{\tilde{q}}, \tag{C.6}$$

$$\Sigma_R^{(\tilde{q}_1\tilde{g})} = -\frac{\alpha_s C_F}{4\pi}\Big[A_0(m_{\tilde{g}}^2) - A_0(m_{\tilde{q}_1}^2) - \big(m_{\tilde{g}}^2 - m_{\tilde{q}_1}^2 + p_q^2\big)B_0(p_q^2; m_{\tilde{g}}^2, m_{\tilde{q}_1}^2)\Big]\frac{\sin^2\theta_{\tilde{q}}}{p_q^2}, \tag{C.7}$$

while the remaining vectors parts can be derived using the relations

$$\Sigma_R^{(\tilde{q}_i\tilde{g})} = \Sigma_L^{(\tilde{q}_i\tilde{g})}(\sin\theta_{\tilde{q}} \leftrightarrow \cos\theta_{\tilde{q}}), \tag{C.8}$$

$$\Sigma_{R,L}^{(\tilde{q}_2\tilde{g})} = \Sigma_{R,L}^{(\tilde{q}_1\tilde{g})}(1 \leftrightarrow 2, \sin\theta_{\tilde{q}} \leftrightarrow \cos\theta_{\tilde{q}}). \tag{C.9}$$

C.2 Squark Self-Energy and Renormalization

The squark mass receives corrections through the one-point and two-point loop diagrams shown in Fig. C.2. The one-point contributions originating from the squark bubble are given by $(i \neq j)$

$$\Sigma_{\tilde{q}_i\tilde{q}_i}^{(\tilde{q}_i)} = \frac{\alpha_s C_F}{4\pi}A_0(m_{\tilde{q}_i}^2)\cos^2 2\theta_{\tilde{q}}, \tag{C.10}$$

$$\Sigma_{\tilde{q}_i\tilde{q}_i}^{(\tilde{q}_j)} = \frac{\alpha_s C_F}{4\pi}A_0(m_{\tilde{q}_j}^2)\sin^2 2\theta_{\tilde{q}}, \tag{C.11}$$

$$\Sigma_{\tilde{q}_i\tilde{q}_j}^{(\tilde{q}_i)} = \frac{\alpha_s C_F}{8\pi}A_0(m_{\tilde{q}_i}^2)\sin 4\theta_{\tilde{q}}, \tag{C.12}$$

$$\Sigma_{\tilde{q}_i\tilde{q}_j}^{(\tilde{q}_j)} = -\frac{\alpha_s C_F}{8\pi}A_0(m_{\tilde{q}_j}^2)\sin 4\theta_{\tilde{q}}, \tag{C.13}$$

while all other contributions are zero. The gluon bubble contribution also vanishes due to the massless gluon in the loop. The two-point contributions originating from the squark-gluon

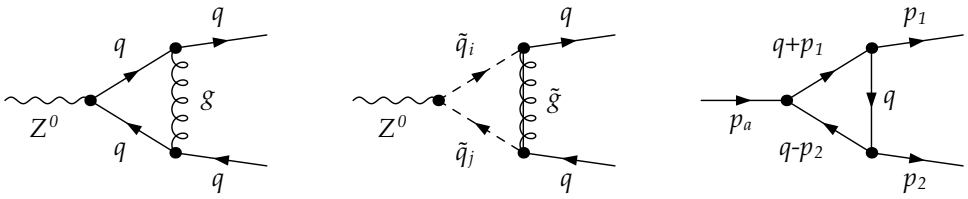

Figure C.3: Feynman diagrams for the gluon (left) and gluino (centre) correction to the Z-quark-quark vertex and generic diagram (right) indicating the notation for masses and momenta.

and quark-gluino loops read

$$\Sigma^{(g\tilde{q}_i)}_{\tilde{q}_i\tilde{q}_i} = -\frac{\alpha_s C_F}{2\pi} m^2_{\tilde{q}_i}\Big[2B_0(p^2_{\tilde{q}_i};0,m^2_{\tilde{q}_i}) + B_1(p^2_{\tilde{q}_i};0,m^2_{\tilde{q}_i})\Big], \tag{C.14}$$

$$\begin{aligned}\Sigma^{(\tilde{g}q)}_{\tilde{q}_i\tilde{q}_i} &= -\frac{\alpha_s C_F}{\pi}\Big[A_0(m^2_q) + B_1(p^2_{\tilde{q}_i};m^2_{\tilde{g}},m^2_q) \\ &\quad + \Big(m^2_{\tilde{g}} + (-1)^i m_{\tilde{g}} m_q \sin 2\theta_{\tilde{q}}\Big) B_0(p^2_{\tilde{q}_i};m^2_{\tilde{g}},m^2_q)\Big],\end{aligned} \tag{C.15}$$

$$\Sigma^{(\tilde{g}q)}_{\tilde{q}_i\tilde{q}_j} = \frac{\alpha_s C_F}{\pi} m_{\tilde{g}} m_q \sin 2\theta_{\tilde{q}} B_0(p^2_{\tilde{q}_i};m^2_{\tilde{g}},m^2_q), \tag{C.16}$$

respectively. In the on-shell scheme, the squark mass and wave function renormalization constants are given by

$$\delta Z_{m_{\tilde{q}_i}} = \Re\big\{\Sigma^{(g)}_{\tilde{q}_i\tilde{q}_i} + \Sigma^{(\tilde{g})}_{\tilde{q}_i\tilde{q}_i} + \Sigma^{(\tilde{q}_1)}_{\tilde{q}_i\tilde{q}_i} + \Sigma^{(\tilde{q}_2)}_{\tilde{q}_i\tilde{q}_i}\big\}, \tag{C.17}$$

$$\delta Z_{\psi_{\tilde{q}_i}} = -\Re\big\{\dot{\Sigma}_{\tilde{q}_i\tilde{q}_i}(m^2_{\tilde{q}_i})\big\}. \tag{C.18}$$

C.3 Vertex Corrections

In the calculation of our radiative corrections to neutralino pair annihilation into quark-antiquark pairs, contributions at $\mathcal{O}(\alpha_s)$ arise from the gluon and gluino exchange between quark and antiquark in the s-channel diagrams or between (anti)quark and squark in the t- and u-channel diagrams. We here present analytical expressions for the corresponding diagrams, that then have to be combined with the different diagrams at the tree-level in order to obtain the squared matrix elements.

The quark-quark-vector coupling receives corrections of $\mathcal{O}(\alpha_s)$ through the gluon and gluino exchanges shown in Fig. C.3. The leading order left- and right-handed coupling strengths L_{qqZ} and R_{qqZ} are then corrected according to

$$L_{qqZ} \;\to\; L_{qqZ}\big(1+\delta L_{qqZ}\big) \qquad \text{and} \qquad R_{qqZ} \;\to\; R_{qqZ}\big(1+\delta R_{qqZ}\big). \tag{C.19}$$

For the gluon correction, the corrections δL_{qqZ} and δR_{qqZ} can be expressed in terms of the tree-level coupling strengths,

$$\delta L_{qqZ} = \frac{\alpha_s C_F}{4\pi}\big(\mathcal{F}^{\mathrm{LL}}_{qqZ} L_{qqZ} + \mathcal{F}^{\mathrm{LR}}_{qqZ} R_{qqZ}\big), \tag{C.20}$$

$$\delta R_{qqZ} = \frac{\alpha_s C_F}{4\pi}\big(\mathcal{F}^{\mathrm{RL}}_{qqZ} L_{qqZ} + \mathcal{F}^{\mathrm{RR}}_{qqZ} R_{qqZ}\big). \tag{C.21}$$

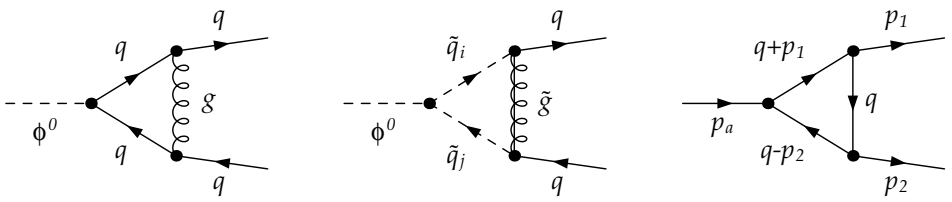

Figure C.4: Feynman diagrams for the gluon (left) and gluino (centre) correction to the Higgs-quark-quark vertex and generic diagram (right) indicating the notation for masses and momenta.

Denoting the external particle momenta p_a, p_1, and p_2, the corresponding masses m_a, m_1, and m_2, and the internal loop masses M_0, M_1, and M_2 as indicated in the generic diagram on the right-hand side of Fig. C.3, the form factors appearing in Eqs. C.21 can be written as

$$\begin{aligned}
\mathcal{F}^{\mathrm{LL}}_{qqZ} \;=\; \mathcal{F}^{\mathrm{RR}}_{qqZ} \;&=\; 2\big(m_1m_2 - M_1M_2\big)\gamma^\mu C_0 + 4\big(m_1 - M_1\big)p_2^\mu C_0 \\
&\quad +2m_1m_2\gamma^\mu\big(C_1 + C_2\big) - 4m_1\big(p_1^\mu C_1 - p_2^\mu C_2\big) \\
&\quad -4m_1\big(p_1^\mu C_{11} - p_2^\mu C_{12}\big), \qquad \text{(C.22)} \\
\mathcal{F}^{\mathrm{RL}}_{qqZ} \;=\; \mathcal{F}^{\mathrm{LR}}_{qqZ} \;&=\; \gamma^\mu B_0 + 4\big(M_2 - m_2\big)p_1^\mu C_0 - 2\big(s - m_1^2 - m_2^2\big)\gamma^\mu C_0 \\
&\quad +4\big(M_1 + M_2 - m_2\big)\big(p_1^\mu C_1 - p_2^\mu C_2\big) + 4m_1p_2^\mu C_1 - 4m_2p_1^\mu C_2 \\
&\quad -2\big(s - m_1^2 - m_2^2\big)\gamma^\mu\big(C_1 + C_2\big) + 2m_1^2\gamma^\mu C_1 + 2m_2^2\gamma^\mu C_2 \\
&\quad -4\gamma^\mu C_{00} - 4m_2\big(p_1^\mu C_{12} - p_2^\mu C_{22}\big). \qquad \text{(C.23)}
\end{aligned}$$

where we have already set the $M_0 = 0$ for the gluon mass and the coefficient integrals are given by

$$C_\alpha \;=\; C_\alpha\big(p_1^2, s, p_2^2; 0, M_1^2, M_2^2\big) \qquad \text{and} \qquad B_0 \;=\; B_0\big(s; m_1^2, m_2^2\big). \qquad \text{(C.24)}$$

with $s = (p_1 + p_2)^2$.

Adopting the same notation for the gluon correction to the quark-quark-Higgs coupling shown in Fig. C.4, the tree-level left- and right-handed coupling strengths receive corrections

$$L_{qq\phi} \;\to\; L_{qq\phi}\big(1 + \delta L_{qq\phi}\big) \qquad \text{and} \qquad R_{qq\phi} \;\to\; R_{qq\phi}\big(1 + \delta R_{qq\phi}\big). \qquad \text{(C.25)}$$

for $\phi = h^0, H^0, A^0$. The corrections are again expressed in terms of the tree-level couplings,

$$\begin{aligned}
\delta L_{qqZ} \;&=\; \frac{\alpha_s C_F}{4\pi}\big(\mathcal{F}^{\mathrm{LL}}_{qq\phi}L_{qq\phi} + \mathcal{F}^{\mathrm{LR}}_{qq\phi}R_{qq\phi}\big), \qquad \text{(C.26)} \\
\delta R_{qqZ} \;&=\; \frac{\alpha_s C_F}{4\pi}\big(\mathcal{F}^{\mathrm{RL}}_{qq\phi}L_{qq\phi} + \mathcal{F}^{\mathrm{RR}}_{qq\phi}R_{qq\phi}\big) \qquad \text{(C.27)}
\end{aligned}$$

and the corresponding form factors, defined as in Eqs. (C.20) and (C.21), are here given by

$$\begin{aligned}
\mathcal{F}^{\mathrm{LL}}_{qq\phi} \;=\; \mathcal{F}^{\mathrm{RR}}_{qq\phi} \;&=\; B_0 - 2\big(s - m_1^2 - m_2^2\big)\big(C_0 + C_1\big) \\
&\quad -2m_1M_1C_1 - 2m_2M_2C_2 + 4m_2^2C_2, \qquad \text{(C.28)} \\
\mathcal{F}^{\mathrm{RL}}_{qq\phi} \;=\; \mathcal{F}^{\mathrm{LR}}_{qq\phi} \;&=\; \big(4M_1M_2 - 2m_2M_1 - 2m_1M_2\big)C_0 - 2\big(s - m_1^2 - m_2^2\big)C_2 \\
&\quad -2m_1M_2C_1 - 2m_2M_1C_2 + 4m_1^2C_1, \qquad \text{(C.29)}
\end{aligned}$$

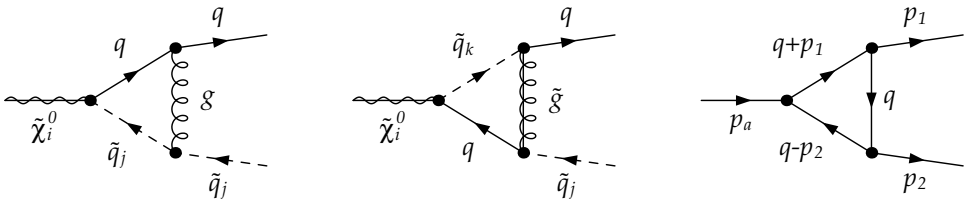

Figure C.5: Feynman diagrams for gluon (left) and gluino (centre) correction to the neutralino-squark-quark vertex and generic diagram (right) indicating the notation for masses and momenta.

with the same coefficient integrals as in Eq. (C.24).

The gluon loop diagram shown in Fig. C.5, implies the corrections

$$L_{\tilde{\chi}_i\tilde{q}_jq} \;\to\; L_{\tilde{\chi}_i\tilde{q}_jq}\big(1+\delta L_{\tilde{\chi}_i\tilde{q}_jq}\big) \qquad \text{and} \qquad R_{\tilde{\chi}_i\tilde{q}_jq} \;\to\; R_{\tilde{\chi}_i\tilde{q}_jq}\big(1+\delta R_{\tilde{\chi}_i\tilde{q}_jq}\big) \tag{C.30}$$

to the neutralino-squark-squark vertex, leading to the one-loop contributions

$$\delta L_{\tilde{\chi}_i\tilde{q}_jq} \;=\; \frac{\alpha_s C_F}{4\pi}\Big[\mathcal{F}^{\rm LL}_{\tilde{\chi}_i\tilde{q}_jq}L_{\tilde{\chi}_i\tilde{q}_jq}+\mathcal{F}^{\rm LR}_{\tilde{\chi}_i\tilde{q}_jq}R_{\tilde{\chi}_i\tilde{q}_jq}\Big], \tag{C.31}$$

$$\delta R_{\tilde{\chi}_i\tilde{q}_jq} \;=\; \frac{\alpha_s C_F}{4\pi}\Big[\mathcal{F}^{\rm RL}_{\tilde{\chi}_i\tilde{q}_jq}L_{\tilde{\chi}_i\tilde{q}_jq}+\mathcal{F}^{\rm RR}_{\tilde{\chi}_i\tilde{q}_jq}R_{\tilde{\chi}_i\tilde{q}_jq}\Big], \tag{C.32}$$

to the tree-level left- and right-handed coupling strenghts $L_{\tilde{\chi}_i\tilde{q}_jq}$ and $R_{\tilde{\chi}_i\tilde{q}_jq}$. Here, the form factors can be written as

$$\mathcal{F}^{\rm LL}_{\tilde{\chi}_i\tilde{q}_jq} \;=\; \mathcal{F}^{\rm RR}_{\tilde{\chi}_i\tilde{q}_jq} \;=\; B_0+\big(3m_1^2+m_2^2-m_a^2\big)\big(C_0+C_2\big)+2\big(m_1^2+m_2^2\big)C_1, \tag{C.33}$$

$$\mathcal{F}^{\rm RL}_{\tilde{\chi}_i\tilde{q}_jq} \;=\; \mathcal{F}^{\rm LR}_{\tilde{\chi}_i\tilde{q}_jq} \;=\; 2m_1m_aC_2. \tag{C.34}$$

The appearing integrals are

$$C_\alpha \;=\; C_\alpha\big(p_a^2,t,p_1^2;M_0^2,M_1^2,M_2^2\big) \qquad \text{and} \qquad B_0 \;=\; B_0(t;M_1^2,M_2^2). \tag{C.35}$$

In contrast to the gluonic one-loop corrections discussed above, the corrections to the quark-quark-vector and quark-quark-Higgs couplings arising from gluino loops shown in the centre panels of Figs. C.3 and C.5 cannot be directly factorized. The tree-level quark-quark vector coupling is rather replaced by the expression

$$\begin{aligned} L_{qqZ}P_L+R_{qqZ}P_R \;\to\; & C_{\tilde{q}_i\tilde{q}_jZ}\frac{\alpha_s C_F}{4\pi}\Big[L_{\tilde{q}_iq\tilde{g}}L_{\tilde{q}_jq\tilde{g}}\tilde{\mathcal{F}}^{\rm LL}_{qqZ}+L_{\tilde{q}_iq\tilde{g}}R_{\tilde{q}_jq\tilde{g}}\tilde{\mathcal{F}}^{\rm LR}_{qqZ} \\ & +R_{\tilde{q}_iq\tilde{g}}L_{\tilde{q}_jq\tilde{g}}\tilde{\mathcal{F}}^{\rm RL}_{qqZ}+R_{\tilde{q}_iq\tilde{g}}R_{\tilde{q}_jq\tilde{g}}\tilde{\mathcal{F}}^{\rm RR}_{qqZ}\Big], \end{aligned} \tag{C.36}$$

where we note $C_{\tilde{q}_i\tilde{q}_jZ}=L_{\tilde{q}_i\tilde{q}_jZ}=R_{\tilde{q}_i\tilde{q}_jZ}$ the squark-squark-vector coupling and $L_{\tilde{q}_iq\tilde{g}}$, $R_{\tilde{q}_jq\tilde{g}}$ the left- and right-handed coupling strength of the squark-quark-gluino interaction. The form factors appearing in Eq. (C.36) are given by

$$\tilde{\mathcal{F}}^{\rm LL}_{qqZ} \;=\; \tilde{\mathcal{F}}^{\rm RR}_{qqZ} \;=\; M_0(p_1-p_2)^\mu C_0+2M_0\big(p_1^\mu C_1-p_2^\mu C_2\big)+2\gamma^\mu C_{00}, \tag{C.37}$$

$$\begin{aligned} \tilde{\mathcal{F}}^{\rm LR}_{qqZ} \;=\; \tilde{\mathcal{F}}^{\rm RL}_{qqZ} \;=\; & \big(m_1C_1+m_2C_2\big)(p_1-p_2)^\mu+2m_1\big(p_1^\mu C_{11}-p_2^\mu C_{12}\big) \\ & +2m_2\big(p_1^\mu C_{12}-p_2^\mu C_{22}\big), \end{aligned} \tag{C.38}$$

with the integrals

$$C_\alpha \;=\; C_\alpha\big(p_1^2, s, p_2^2; M_0^2, M_1^2, M_2^2\big). \tag{C.39}$$

In the same way, the tree-level quark-quark-Higgs coupling is replaced according to

$$\begin{aligned} L_{qq\phi}P_L + R_{qq\phi}P_R \;\;\rightarrow\;\; & C_{\tilde{q}_i\tilde{q}_j\phi}\frac{\alpha_s C_F}{4\pi}\Big[L_{\tilde{q}_i q\tilde{g}}L_{\tilde{q}_j q\tilde{g}}\tilde{\mathcal{F}}^{\mathrm{LL}}_{qq\phi} + L_{\tilde{q}_i q\tilde{g}}R_{\tilde{q}_j q\tilde{g}}\tilde{\mathcal{F}}^{\mathrm{LR}}_{qq\phi} \\ & + R_{\tilde{q}_i q\tilde{g}}L_{\tilde{q}_j q\tilde{g}}\tilde{\mathcal{F}}^{\mathrm{RL}}_{qq\phi} + R_{\tilde{q}_i q\tilde{g}}R_{\tilde{q}_j q\tilde{g}}\tilde{\mathcal{F}}^{\mathrm{RR}}_{qq\phi}\Big], \end{aligned} \tag{C.40}$$

where $C_{\tilde{q}_i\tilde{q}_j\phi} = L_{\tilde{q}_i\tilde{q}_j\phi} = R_{\tilde{q}_i\tilde{q}_j\phi}$ denotes the squark-squark-Higgs coupling. Due to the fact that there are no vector couplings, the form factors

$$\tilde{\mathcal{F}}^{\mathrm{LL}}_{qq\phi} \;=\; \tilde{\mathcal{F}}^{\mathrm{RR}}_{qq\phi} \;=\; M_0 C_0, \tag{C.41}$$

$$\tilde{\mathcal{F}}^{\mathrm{LR}}_{qq\phi} \;=\; \tilde{\mathcal{F}}^{\mathrm{RL}}_{qq\phi} \;=\; m_1 C_1 + m_2 C_2, \tag{C.42}$$

are rather simple and compact with the same integrals C_0, C_1, and C_2 as in Eq. (C.39).

Finally, the gluonic correction to the neutralino-squark-quark vertex, shown in the centre panel of Fig. C.5, leads to a correction

$$\delta L_{\tilde{\chi}_i\tilde{q}_j q} \;=\; \frac{\alpha_s C_F}{4\pi}\big(\mathcal{F}^{\mathrm{LL}}_{\tilde{\chi}_i\tilde{q}_j q}L_{\tilde{\chi}_i\tilde{q}_j q} + \mathcal{F}^{\mathrm{LR}}_{\tilde{\chi}_i\tilde{q}_j q}R_{\tilde{\chi}_i\tilde{q}_j q}\big), \tag{C.43}$$

$$\delta R_{\tilde{\chi}_i\tilde{q}_j q} \;=\; \frac{\alpha_s C_F}{4\pi}\big(\mathcal{F}^{\mathrm{RL}}_{\tilde{\chi}_i\tilde{q}_j q}L_{\tilde{\chi}_i\tilde{q}_j q} + \mathcal{F}^{\mathrm{RR}}_{\tilde{\chi}_i\tilde{q}_j q}R_{\tilde{\chi}_i\tilde{q}_j q}\big), \tag{C.44}$$

of the tree-level coupling strengths $L_{\tilde{\chi}_i\tilde{q}_j q}$ and $R_{\tilde{\chi}_i\tilde{q}_j q}$. The form factors can be written as

$$\tilde{\mathcal{F}}^{\mathrm{LL}}_{\tilde{\chi}_i\tilde{q}_j q} \;=\; \tilde{\mathcal{F}}^{\mathrm{RR}}_{\tilde{\chi}_i\tilde{q}_j q} \;=\; -M_0\mathcal{V}_1\mathcal{V}_2\big(\not{p}_1 - \not{p}_a\big) - \mathcal{V}_1\mathcal{V}_2\big(\not{p}_1 - \not{p}_a\big)\big(\not{p}_1 C_1 + \not{p}_2 C_2\big), \tag{C.45}$$

$$\begin{aligned} \tilde{\mathcal{F}}^{\mathrm{LR}}_{\tilde{\chi}_i\tilde{q}_j q} \;=\; \tilde{\mathcal{F}}^{\mathrm{RL}}_{\tilde{\chi}_i\tilde{q}_j q} \;=\; & M_0 M_2 \mathcal{V}_1\mathcal{V}_2 - M_2\mathcal{V}_1\mathcal{V}_2\big(\not{p}_1 C_1 + \not{p}_2 C_2\big) \\ & - \mathcal{V}_1\mathcal{V}_2\big(4C_{00} + p_1^2 C_{11} + p_2^2 C_{22} + 2p_1\cdot p_2 C_{12}\big), \end{aligned} \tag{C.46}$$

where $\mathcal{V}_1$ and $\mathcal{V}_2$ correspond to the expressions of the squark-quark-gluino vertices indicated in Fig. C.5.

C.4 Box Contributions

The neutralino pair annihilation into quark-antiquark pairs receives corrections through the box diagrams shown in Fig. C.6. In the following we present analytical results for the corresponding amplitudes $\mathcal{M}_g$ and $\mathcal{M}_{\tilde{g}}$. The amplitudes corresponding to the crossed final states can be obtained by the replacement $t \leftrightarrow u$. In order to express the box amplitudes in a rather generic way, we label the momenta and masses of the external particles by p_i and m_i, while the internal particle masses are named M_i, for $i = 1, \ldots, 4$, respectively, as indicated in the generic diagrams of Fig. C.6. Regardless of their respective tensor structure, we denote the four vertices generically $\mathcal{V}_k$ for $k = 1, \ldots, 4$. Furthermore we introduce the notation $\mathcal{V}'_k = \mathcal{V}_k(P_R \leftrightarrow P_L)$ originating from the exchange of the two chirality projectors in the original vertex expression.

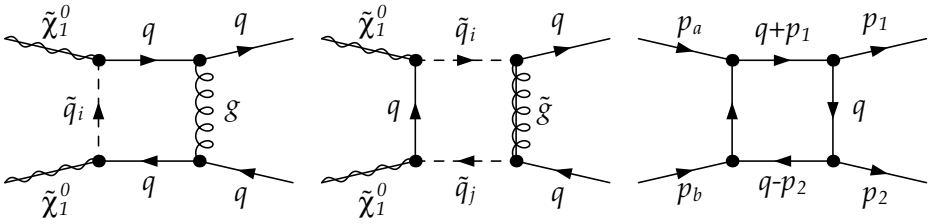

Figure C.6: Feynman diagram for the gluon (left) and gluino (centre) box contributions at $\mathcal{O}(\alpha_s)$ to neutralino pair annihilation into quark-antiquark pairs and generic diagram (right) indicating masses and momenta.

Expressed in terms of four-point integrals, the amplitude of the gluino ("s-channel") box diagram is then given by

$$\begin{aligned} i\mathcal{M} &= \bar{v}(p_2)\mathcal{F}_0^1 u(p_1)\bar{u}(k_1)\mathcal{F}_0^2 v(k_2) D_0 + \sum_{i=1}^{3}\sum_{j=1}^{2} \bar{v}(p_2)\mathcal{F}_i^{2j-1} u(p_1)\bar{u}(k_1)\mathcal{F}_i^{2j} v(k_2) D_i \\ &\quad + \bar{v}(p_2)\mathcal{F}_{00}^1 u(p_1)\bar{u}(k_1)\mathcal{F}_{00}^2 v(k_2) D_{00} + \sum_{i,j=1}^{3} \bar{v}(p_2)\mathcal{F}_{ij}^1 u(p_1)\bar{u}(k_1)\mathcal{F}_{ij}^2 v(k_2) D_{ij} \end{aligned} \tag{C.47}$$

with the form factors

$$\begin{aligned}
\mathcal{F}_0^1 &= m_4\mathcal{V}_2\mathcal{V}_1 + M_2\mathcal{V}_2'\mathcal{V}_1 & \mathcal{F}_0^2 &= m_2\mathcal{V}_3\mathcal{V}_4 + M_3\mathcal{V}_3'\mathcal{V}_4 \\
\mathcal{F}_1^1 &= \mathcal{V}_2\not{k}_1\mathcal{V}_1 & \mathcal{F}_1^2 &= M_3\mathcal{V}_3'\mathcal{V}_4 + m_2\mathcal{V}_3\mathcal{V}_4 \\
\mathcal{F}_1^3 &= M_2\mathcal{V}_2'\mathcal{V}_1 + m_4\mathcal{V}_2\mathcal{V}_1 & \mathcal{F}_1^4 &= M_3\mathcal{V}_3'\mathcal{V}_4 \\
\mathcal{F}_2^1 &= M_2\mathcal{V}_2'\mathcal{V}_1 - M_1\mathcal{V}_2\mathcal{V}_1' & \mathcal{F}_2^2 &= M_3\mathcal{V}_3'\mathcal{V}_4 + m_2\mathcal{V}_3\mathcal{V}_4 \\
\mathcal{F}_2^3 &= M_2\mathcal{V}_2'\mathcal{V}_1 + m_4\mathcal{V}_2\mathcal{V}_1 & \mathcal{F}_2^4 &= M_3\mathcal{V}_3'\mathcal{V}_4 - M_4\mathcal{V}_3\mathcal{V}_4' \\
\mathcal{F}_3^1 &= M_2\mathcal{V}_2'\mathcal{V}_1 & \mathcal{F}_3^2 &= M_3\mathcal{V}_3'\mathcal{V}_4 + m_2\mathcal{V}_3\mathcal{V}_4 \\
\mathcal{F}_3^3 &= M_2\mathcal{V}_2'\mathcal{V}_1 + m_4\mathcal{V}_2\mathcal{V}_1 & \mathcal{F}_3^4 &= -\mathcal{V}_3\not{p}_2\mathcal{V}_4 \\
\mathcal{F}_{00}^1 &= -\mathcal{V}_2\gamma^\mu\mathcal{V}_1 & \mathcal{F}_{00}^2 &= \mathcal{V}_3\gamma_\mu\mathcal{V}_4 \\
\mathcal{F}_{11}^1 &= -\mathcal{V}_2\not{k}_1\mathcal{V}_1 & \mathcal{F}_{11}^2 &= M_3\mathcal{V}_3'\mathcal{V}_4 \\
\mathcal{F}_{12}^1 &= -\mathcal{V}_2\not{k}_1\mathcal{V}_1 & \mathcal{F}_{12}^2 &= M_3\mathcal{V}_3'\mathcal{V}_4 - M_4\mathcal{V}_3\mathcal{V}_4' \\
\mathcal{F}_{13}^1 &= -\mathcal{V}_2\not{k}_1\mathcal{V}_1 & \mathcal{F}_{13}^2 &= \mathcal{V}_3\not{p}_2\mathcal{V}_4 \\
\mathcal{F}_{21}^1 &= M_2\mathcal{V}_2'\mathcal{V}_1 - M_1\mathcal{V}_2\mathcal{V}_1' & \mathcal{F}_{21}^2 &= M_3\mathcal{V}_3'\mathcal{V}_4 \\
\mathcal{F}_{22}^1 &= M_2\mathcal{V}_2'\mathcal{V}_1 - M_1\mathcal{V}_2\mathcal{V}_1' & \mathcal{F}_{22}^2 &= M_3\mathcal{V}_3'\mathcal{V}_4 - M_4\mathcal{V}_3\mathcal{V}_4' \\
\mathcal{F}_{23}^1 &= M_2\mathcal{V}_2'\mathcal{V}_1 - M_1\mathcal{V}_2\mathcal{V}_1' & \mathcal{F}_{23}^2 &= \mathcal{V}_3\not{p}_2\mathcal{V}_4 \\
\mathcal{F}_{31}^1 &= M_2\mathcal{V}_2'\mathcal{V}_1 & \mathcal{F}_{31}^2 &= M_3\mathcal{V}_3'\mathcal{V}_4 \\
\mathcal{F}_{32}^1 &= M_2\mathcal{V}_2'\mathcal{V}_1 & \mathcal{F}_{32}^2 &= M_3\mathcal{V}_3'\mathcal{V}_4 - M_4\mathcal{V}_3\mathcal{V}_4 \\
\mathcal{F}_{33}^1 &= M_2\mathcal{V}_2'\mathcal{V}_1 & \mathcal{F}_{33}^2 &= \mathcal{V}_3\not{p}_2\mathcal{V}_4
\end{aligned} \tag{C.48}$$

and the integrals ($i, j = 0, \ldots, 4$)

$$D_{\{i,ij\}} = D_{\{i,ij\}}(-p_3, -(p_1+p_2), -p_2; m_1, m_2, m_3, m_4). \tag{C.49}$$

Accordingly, the amplitude corresponding to the gluon ("t-channel") box diagram shown in the centre panel of Fig. C.6 reads

$$\begin{aligned} i\mathcal{M} &= -\bar{u}(k_1)\tilde{\mathcal{F}}_0^1 u(p_2)\bar{v}(p_1)\tilde{\mathcal{F}}_0^2 v(k_2) D_0 - \sum_{i=1}^{3}\sum_{j=1}^{2} \bar{u}(k_1)\tilde{\mathcal{F}}_i^{2j-1} u(p_2)\bar{v}(p_1)\tilde{\mathcal{F}}_i^{2j} v(k_2) D_i \\ &\quad -\bar{u}(k_1)\tilde{\mathcal{F}}_{00}^1 u(k_1)\bar{v}(p_1)\tilde{\mathcal{F}}_{00}^2 v(k_2) D_{00} - \sum_{i,j=1}^{3} \bar{u}(k_1)\tilde{\mathcal{F}}_{ij}^1 u(k_1)\bar{v}(p_1)\tilde{\mathcal{F}}_{ij}^2 v(k_2) D_{ij} \end{aligned} \quad \text{(C.50)}$$

with the form factors

$$\begin{aligned}
\tilde{\mathcal{F}}_0^1 &= m_1\gamma^\mu\mathcal{V}_3\mathcal{V}_2 & \tilde{\mathcal{F}}_0^2 &= m_3\mathcal{V}_1\gamma_\mu\mathcal{V}_4 + M_1\mathcal{V}_1'\gamma_\mu\mathcal{V}_4 - \not{p}_2\mathcal{V}_1'\gamma_\mu\mathcal{V}_4 \\
\tilde{\mathcal{F}}_1^1 &= M_3\gamma^\mu\mathcal{V}_3'\mathcal{V}_2 - 2k_1^\mu\mathcal{V}_3'\mathcal{V}_2 & \tilde{\mathcal{F}}_1^2 &= m_3\mathcal{V}_1\gamma_\mu\mathcal{V}_4 + M_1\mathcal{V}_1'\gamma_\mu\mathcal{V}_4 - \not{p}_2\mathcal{V}_1'\gamma_\mu\mathcal{V}_4 \\
\tilde{\mathcal{F}}_1^3 &= -m_1\gamma^\mu\mathcal{V}_3\mathcal{V}_2 & \tilde{\mathcal{F}}_1^4 &= \not{k}_1\mathcal{V}_1'\gamma_\mu\mathcal{V}_4 \\
\tilde{\mathcal{F}}_2^1 &= -\gamma^\mu\not{p}_1\mathcal{V}_3'\mathcal{V}_2 - M_2\gamma^\mu\mathcal{V}_3\mathcal{V}_2' & \tilde{\mathcal{F}}_2^2 &= m_3\mathcal{V}_1\gamma_\mu\mathcal{V}_4 + M_1\mathcal{V}_1'\gamma_\mu\mathcal{V}_4 - \not{p}_2\mathcal{V}_1'\gamma_\mu\mathcal{V}_4 \\
\tilde{\mathcal{F}}_2^3 &= m_1\gamma^\mu\mathcal{V}_3\mathcal{V}_2 & \tilde{\mathcal{F}}_2^4 &= M_1\mathcal{V}_1'\gamma_\mu\mathcal{V}_4 - \not{p}_2\mathcal{V}_1'\gamma_\mu\mathcal{V}_4 \\
\tilde{\mathcal{F}}_3^1 &= -M_2\gamma^\mu\mathcal{V}_3\mathcal{V}_2' & \tilde{\mathcal{F}}_3^2 &= m_3\mathcal{V}_1\gamma_\mu\mathcal{V}_4 + M_1\mathcal{V}_1'\gamma_\mu\mathcal{V}_4 - \not{p}_2\mathcal{V}_1'\gamma_\mu\mathcal{V}_4 \\
\tilde{\mathcal{F}}_3^3 &= m_1\gamma^\mu\mathcal{V}_3\mathcal{V}_2 & \tilde{\mathcal{F}}_3^4 &= \not{p}_2\mathcal{V}_1'\gamma_\mu\mathcal{V}_4 \\
\tilde{\mathcal{F}}_{00}^1 &= \gamma^\mu\mathcal{V}_3\gamma^\nu\mathcal{V}_2 & \tilde{\mathcal{F}}_{00}^2 &= \mathcal{V}_1\gamma_\nu\gamma_\mu\mathcal{V}_4 \\
\tilde{\mathcal{F}}_{11}^1 &= 2k_1^\mu\mathcal{V}_3'\mathcal{V}_2 - M_3\gamma^\mu\mathcal{V}_3'\mathcal{V}_2 & \tilde{\mathcal{F}}_{11}^2 &= \not{k}_1\mathcal{V}_1'\gamma_\mu\mathcal{V}_4 \\
\tilde{\mathcal{F}}_{12}^1 &= 2k_1^\mu\mathcal{V}_3'\mathcal{V}_2 - M_3\gamma^\mu\mathcal{V}_3'\mathcal{V}_2 & \tilde{\mathcal{F}}_{12}^2 &= -M_1\mathcal{V}_1'\gamma_\mu\mathcal{V}_4 + \not{p}_2\mathcal{V}_1'\gamma_\mu\mathcal{V}_4 \\
\tilde{\mathcal{F}}_{13}^1 &= 2k_1^\mu\mathcal{V}_3'\mathcal{V}_2 - M_3\gamma^\mu\mathcal{V}_3'\mathcal{V}_2 & \tilde{\mathcal{F}}_{13}^2 &= \not{p}_2\mathcal{V}_1'\gamma_\mu\mathcal{V}_4 \\
\tilde{\mathcal{F}}_{21}^1 &= \gamma^\mu\not{p}_1\mathcal{V}_3'\mathcal{V}_2 + M_2\gamma^\mu\mathcal{V}_3\mathcal{V}_2' & \tilde{\mathcal{F}}_{21}^2 &= \not{k}_1\mathcal{V}_1'\gamma_\mu\mathcal{V}_4 \\
\tilde{\mathcal{F}}_{22}^1 &= \gamma^\mu\not{p}_1\mathcal{V}_3'\mathcal{V}_2 + M_2\gamma^\mu\mathcal{V}_3\mathcal{V}_2' & \tilde{\mathcal{F}}_{22}^2 &= -M_1\mathcal{V}_1'\gamma_\mu\mathcal{V}_4 + \not{p}_2\mathcal{V}_1'\gamma_\mu\mathcal{V}_4 \\
\tilde{\mathcal{F}}_{23}^1 &= \gamma^\mu\not{p}_1\mathcal{V}_3'\mathcal{V}_2 + M_2\gamma^\mu\mathcal{V}_3\mathcal{V}_2' & \tilde{\mathcal{F}}_{23}^2 &= \not{p}_2\mathcal{V}_1'\gamma_\mu\mathcal{V}_4 \\
\tilde{\mathcal{F}}_{31}^1 &= M_2\gamma^\mu\mathcal{V}_3\mathcal{V}_2' & \tilde{\mathcal{F}}_{31}^2 &= \not{k}_1\mathcal{V}_1'\gamma_\mu\mathcal{V}_4 \\
\tilde{\mathcal{F}}_{32}^1 &= M_2\gamma^\mu\mathcal{V}_3\mathcal{V}_2' & \tilde{\mathcal{F}}_{32}^2 &= -M_1\mathcal{V}_1'\gamma_\mu\mathcal{V}_4 + \not{p}_2\mathcal{V}_1'\gamma_\mu\mathcal{V}_4 \\
\tilde{\mathcal{F}}_{33}^1 &= M_2\gamma^\mu\mathcal{V}_3\mathcal{V}_2' & \tilde{\mathcal{F}}_{33}^2 &= \not{p}_2\mathcal{V}_1'\gamma_\mu\mathcal{V}_4
\end{aligned} \quad \text{(C.51)}$$

and the four-point integrals ($i, j = 0, \ldots, 4$)

$$D_{\{i,ij\}} = D_{\{i,ij\}}(-p_3, -(p_1+p_2), -p_2; m_1, 0, m_3, m_4). \quad \text{(C.52)}$$

In the calculation of the matrix elements these amplitudes are multiplied with the different tree-level amplitudes, and we have to sum over the different squark mass eigenstates. The scalar integrals D_i and D_{ij} can be further reduced into combinations of the functions C_0 and D_0. The reduction formulae can be found e.g. in Ref. [126]. However, the resulting expressions are too long to be represented here.

Appendix D

Real Emission Corrections and Dipole Subtraction Formalism

In addition to the virtual corrections discussed in App. C, the neutralino pair annihilation into quark-antiquark pairs discussed in Chaps. 3 and 4 receives corrections through the emission of a real gluon by one of the involved quarks or squarks. The corresponding matrix elements comprise infrared (IR) singularities for soft or collinear gluons. In the total cross section, these will cancel the infrared singularities remaining in the virtual part of the cross section. In our work, the two parts of the cross section have been connected using the dipole subtraction formalism [106,128]. In this Appendix, we present the involved real emission matrix elements and discuss the implementation of the dipole formalism.

D.1 Diagrams and Matrix Elements

Corrections of $\mathcal{O}(\alpha_s)$ arise through the emission of a real gluon from one of the final state quarks in the s-, t-, or u-channels and from the exchanged squark in the t- and u-channels. The corresponding Feynman diagrams are shown in Figs. D.1 and D.2, except for the u-channels which can easily be obtained through crossing. For a given quark-antiquark final state and for the generic notation for Higgs bosons and squarks, the shown diagrams lead to a total of 45 different classes of squared matrix elements. Because of their number and length, they are here, however, not given in detail, except for typical examples for the different classes of singularities.

For topological reasons, each matrix element comprises the same infrared poles as its virtual counterpart. For example, the matrix element constructed from the first diagram of

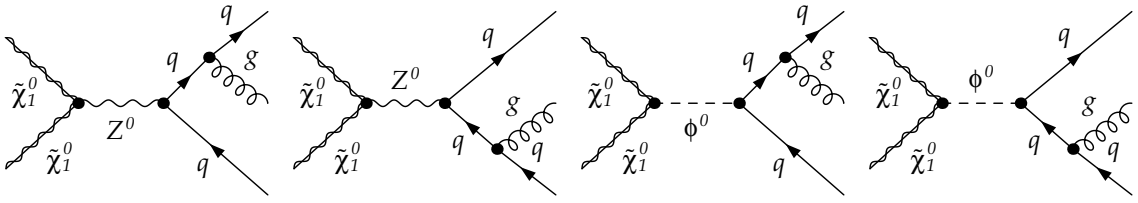

Figure D.1: Feynman diagrams for real gluon emission from a final state quark in the s-channel Z^0- or Higgs-boson ($\phi^0 = h^0, H^0, A^0$) exchange.

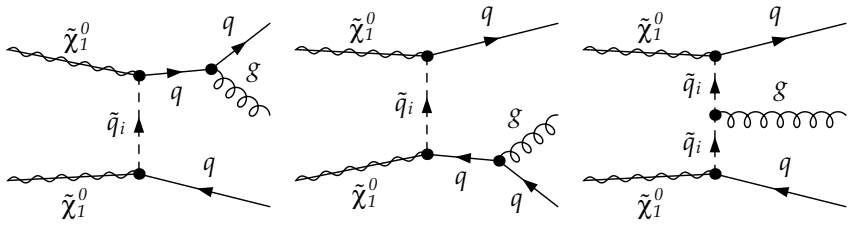

Figure D.2: Feynman diagrams for real gluon emission from a final state quark or the exchanged squark in the t-channel squark ($\tilde{q}_i$ with $i = 1, 2$) exchange.

Fig. D.1 and its conjugated diagram will cancel the infrared singularity of the corresponding self-energy contribution, while the matrix element combining the first and second diagrams of Fig. D.2 involves the same topology as the gluon box multiplied with a tree-level diagram. In contrast to the virtual part, where the singularities show up as poles in ϵ, the real correction matrix elements are expressed in terms of the scaling variables

$$x_i \;=\; \frac{2p_i \cdot p_{tot}}{s} \;=\; \frac{2E_i}{\sqrt{s}}, \tag{D.1}$$

where the index $i = 1, 2, 3$ labels the three final state particles, $i = 3$ being the emitted gluon. E_i is the energy of the corresponding particle and $\sqrt{s}$ the total energy in the centre-of-momentum frame. As a consequence of energy-momentum conservation, only two scaling variables are independent, so that all matrix elements can be expressed in terms of x_1 and x_2. In terms of the scaling variables and without the angular integration, the three-particle phase space can be expressed as [106]

$$\mathrm{dPS}^{(3)} \;=\; \frac{s}{16\pi^2}\mathrm{d}x_1\mathrm{d}x_2\Theta(x_+ - x_2)\Theta(x_2 - x_-)\Theta(1 - x_1)\Theta(x_1 - 2\mu_q), \tag{D.2}$$

where the integration limits are given by

$$x_\pm \;=\; \frac{\big(2 - x_1\big)\big(1 - x_1 + 2\mu_q^2\big) \pm \big(1 - x_1\big)\sqrt{x_1^2 - 4\mu_q^2}}{2\big(1 - x_1 + \mu_q^2\big)} \tag{D.3}$$

and $\mu_q = m_q\sqrt{s}$. For a more detailed discussion of the three-particle kinematics and phase space see e.g. Ref. [145].

Soft and collinear singularities arise if $x_1 \to 1$ and/or $x_2 \to 1$. As an example, let us discuss the simplest squared amplitude, involving the Higgs-boson exchange corresponding to the third diagram of Fig. D.1 and its conjugated counterpart. The squared matrix element can be written as

$$\big|\mathcal{M}^{(1)}_{\phi^0}\big|^2 \;=\; -\frac{8\pi\alpha_s C_F}{\big|s - m^2_{\phi^0} + i m_{\phi^0}\Gamma_{\phi^0}\big|^2}\frac{\mathcal{T}_{\tilde{\chi}_1^0\phi^0\tilde{\chi}_1^0}\;\mathcal{T}_{q\phi^0\bar{q}}}{s^2\big(1 - x_1\big)^2}, \tag{D.4}$$

where the traces of the initial and final state fermionic lines are given by

$$\begin{aligned}
\mathcal{T}_{\tilde{\chi}_1^0\phi^0\tilde{\chi}_1^0} \;&=\; \big(s - 2m_{\tilde{\chi}_1^0}\big)\Big[\big|L_{\tilde{\chi}_1^0\tilde{\chi}_1^0\phi^0}\big|^2 + \big|R_{\tilde{\chi}_1^0\tilde{\chi}_1^0\phi^0}\big|^2\Big] - 4m^2_{\tilde{\chi}_1^0}L_{\tilde{\chi}_1^0\tilde{\chi}_1^0\phi^0}R_{\tilde{\chi}_1^0\tilde{\chi}_1^0\phi^0},\\
\mathcal{T}_{q\phi^0\bar{q}} \;&=\; \Big(4m_q^4 - 2m_q^2 s x_2 + s^2(1 - x_1)(1 - x_2)\Big)\Big[\big|L_{q\bar{q}\phi^0}\big|^2 + \big|R_{q\bar{q}\phi^0}\big|^2\Big]\\
&\quad + 4m_q^2\Big(2m_q^2 + s(1 - x_2)\Big)L_{q\bar{q}\phi^0}R_{q\bar{q}\phi^0},
\end{aligned} \tag{D.5}$$

respectively, and m_{ϕ^0} and Γ_{ϕ^0} denote mass and width of the exchanged Higgs-boson. In Eqs. (D.5), we note L_{abc} and R_{abc} the left- and right-handed coupling strengths contained in the Feynman rules of the corresponding vertices. The squared amplitude of the last diagram of Fig. D.1 is obtained by replacing $x_1 \leftrightarrow x_2$, while the interference of the two diagrams involves more complex combinations of the scaling variables. It is easy to check that the expression in Eq. (D.4) is singular for $x_1 \to 1$ and for all values of m_q. Note that in the case of vector boson exchange in the s-channel, the amplitudes become more complicated due to the exchange of spin information between the initial and final state particles.

Since infrared singularities only arise from gluon radiation off a final state quark, the matrix elements involving emission only from squark propagators are infrared-finite. As an example for this class of matrix elements, we show the squared amplitude obtained from the diagram on the right-hand side of Fig. D.2 and its conjugated one. Labeling the incoming momenta p_a, p_b, and the final state quark momenta p_1, p_2, the squared amplitude is given by

$$\left|\mathcal{M}^{(3)}_{\tilde{q}_k}\right|^2 = -\frac{8\pi\alpha_s C_F\left(2m^2_{\tilde{\chi}^0_1} + 2m_q^2 - sx_1 + 2p_a\cdot p_1 - 2p_a\cdot p_2\right)\mathcal{T}^{(1)}_{\tilde{\chi}^0_1\tilde{q}_k q}\,\mathcal{T}^{(2)}_{\tilde{\chi}^0_1\tilde{q}_k q}}{\left|m^2_{\tilde{\chi}} + m_q^2 - m^2_{\tilde{q}_k} - sx_1 + 2p_a\cdot p_1\right|^2\left|m^2_{\tilde{\chi}} + m_q^2 - m^2_{\tilde{q}_k} 2p_a\cdot p_1\right|^2}. \tag{D.6}$$

Here, the involved traces are given by

$$\begin{aligned}
\mathcal{T}^{(1)}_{\tilde{\chi}^0_1\tilde{q}_k q} &= 2\big(L^2_{q\tilde{q}_k\tilde{\chi}^0_1} + R^2_{q\tilde{q}_k\tilde{\chi}^0_1}\big)p_b\cdot p_1 + 4m_{\tilde{\chi}^0_1}m_q L^2_{q\tilde{q}_k\tilde{\chi}^0_1}R^2_{q\tilde{q}_k\tilde{\chi}^0_1},\\
\mathcal{T}^{(2)}_{\tilde{\chi}^0_1\tilde{q}_k q} &= \mathcal{T}^{(1)}_{\tilde{\chi}\tilde{q}q}(1\leftrightarrow 2, a\leftrightarrow b),
\end{aligned} \tag{D.7}$$

where we use the same generic notation as in Eqs. (D.5) for the masses and coupling strengths. The scalar products appearing in the expressions of Eqs. (D.6) and (D.7) are given in terms of the scaling variables by

$$\begin{aligned}
p_a\cdot p_1 &= \frac{s}{4}\Big(x_1 - \sqrt{1-4\mu^2_{\tilde{\chi}^0_1}}\sqrt{x_1^2-4\mu_q^2}\Big)\Big(\cos\theta\cos\xi - \sin\theta\sin\xi\sin\eta\Big),\\
p_a\cdot p_2 &= \frac{s}{4}\Big(x_2 - \cos\theta\sqrt{1-4\mu^2_{\tilde{\chi}^0_1}}\sqrt{x_2^2-4\mu_q^2}\Big),\\
p_b\cdot p_1 &= \frac{s}{2}x_1 - p_a\cdot p_1,\\
p_b\cdot p_2 &= \frac{s}{2}x_2 - p_a\cdot p_2,
\end{aligned} \tag{D.8}$$

where we use again the reduced particle masses $\mu_i = m_i/\sqrt{s}$ for $i = q, \tilde{\chi}^0_1$. For a detailed discussion of the three-particle phase space involving the angles θ, η, and ξ see e.g. Refs. [106, 145]. Again, it is straightforward to check that the expression of the squared amplitude is free of singularities for $x_{1,2} \to 1$.

However, the combination of emission from the squark propagator with emission from a massless final state quark gives rise to a collinear singularity. This can be seen in the amplitude obtained from the interference of the two diagrams separately discussed above. It can be written as

$$\mathcal{M}^{(1)}_{\phi^0}\mathcal{M}^{(3)*}_{\tilde{q}_k} = \frac{2\pi\alpha_s C_F\,\mathcal{T}_{\text{int}}}{s(1-x_1)\big(s - m^2_{\phi^0} + im_{\phi^0}\Gamma_{\phi^0}\big)\big(X - sx_1 + 2p_a\cdot p_1\big)\big(X - 2p_a\cdot p_2\big)}, \tag{D.9}$$

where we use the abbreviation $X = m^2_{\tilde{\chi}^0_1} + m^2_q - m^2_{\tilde{q}_k}$. For massless final state quarks, the only fermionic line in this interference term leads to the trace

$$\begin{aligned}\mathcal{T}_{\text{int}} &= L_{\tilde{\chi}^0_1\tilde{\chi}^0_1\phi^0} R_{\tilde{\chi}^0_1\tilde{\chi}^0_1\phi^0} \Big(L_{q\bar{q}\phi^0} L_{q\tilde{q}_k\tilde{\chi}^0_1} L^*_{q\tilde{q}_k\tilde{\chi}^0_1} + R_{q\bar{q}\phi^0} R_{q\tilde{q}_k\tilde{\chi}^0_1} R^*_{q\tilde{q}_k\tilde{\chi}^0_1} \Big) \\ &\quad \times \Big[s^2(1-x_1)(1-x_1-x_2) - 4sm^2_{\tilde{\chi}^0_1}\big((1-x_1)^2 - (1-2x_1)x_2\big) \\ &\quad + 2(p_a\cdot p_1)\big(4m^2_{\tilde{\chi}^0_1} + s(1-x_1)\big) + 2x_1(p_a\cdot p_2)\big(s(3+x_1) - 4m^2_{\tilde{\chi}^0_1}\big) \\ &\quad - 16(p_a\cdot p_1)(p_a\cdot p_2)\Big] \end{aligned} \tag{D.10}$$

and the scalar products can again be expressed using Eqs. (D.8). Note that the expression in Eq. (D.9) is not singular if $m_q > 0$. Due to its length, the fermionic trace corresponding to the massive case can, however, not be shown here.

D.2 Dipole Contributions to Real Emission Cross Section

A numerically efficient way of computing the total one-loop cross section out of the separate parts containing virtual and real emission correction is the dipole subtraction method [106, 128]. This method is based on the construction of an unphysical auxiliary cross section, σ_{aux}, that contains the same infrared singularities as do separately the real and virtual corrections. It is implemented according to

$$\sigma_{\text{NLO}} = \int_3 \Big[\big(\mathrm{d}\sigma_{\text{R}}\big)_{\epsilon=0} - \big(\mathrm{d}\sigma_{\text{aux}}\big)_{\epsilon=0} \Big] + \int_2 \Big[\mathrm{d}\sigma_{\text{V}} + \int_1 \mathrm{d}\sigma_{\text{aux}} \Big]_{\epsilon=0}, \tag{D.11}$$

so that the two parts of the cross section become separately convergent and can be integrated numerically. The schematic notation in Eq. (D.11) is understood to involve the integration over the three- and two-particle phase space of the real and virtual contributions, respectively, each including the auxiliary cross section. In the latter, the real gluon has to be integrated out for the virtual contribution.

The dipole terms appearing in the construction of the auxiliary cross section σ_{aux} depend only on the final state of the process in question. We therefore can use the expressions given in App. C of Ref. [106] for the case of gluon emission and heavy partons in the final state. The matrix element corresponding to the auxiliary cross section can then be written as

$$\big|\mathcal{M}_{\text{aux}}\big|^2 = \big|\mathcal{M}_{\text{LO}}\big|^2 \Big(\mathcal{D}_{31,2} + \mathcal{D}_{32,1} \Big), \tag{D.12}$$

where $|\mathcal{M}_{\text{LO}}|^2$ denotes the squared amplitude at leading order and the two dipole contributions are in the case of identical final state quarks with mass $m_q = \mu_q\sqrt{s}$ given by $(i, j = 1, 2)$ [106]

$$\mathcal{D}_{3i,j} = \frac{8\pi\alpha_s C_F}{s\big(1-x_j\big)} \left[\frac{2-4\mu_q^2}{2-x_i-x_j} - \sqrt{\frac{1-4\mu_q^2}{x_j^2-4\mu_q^2}} \frac{x_j - 2\mu_q^2}{1-2\mu_q^2} \left(2 + \frac{x_i - 1}{x_j - 2\mu_q^2} + \frac{2\mu_q^2}{1-x_j} \right) \right]. \tag{D.13}$$

When integrating over the three-particle phase space, the subtraction of the expression in Eq. (D.13) renders all of the divergent matrix elements finite, provided that the corresponding leading order matrix element is inserted in the expressions of the dipole contributions. Note

that, in order to match with the real emission contribution, the matrix element at leading order has to be expressed in terms of the "reduced" kinematic for $2 \to 3$ processes which is discussed in App. D.3. The expressions given in Eqs. (D.12) and (D.13) also hold in the case of massless quarks where $\mu_q = 0$.

D.3 Kinematics for Dipole Contributions

In this Appendix, we discuss the "reduced" $2 \to 3$ kinematics, needed to express the squared leading order $2 \to 2$ matrix element in terms of the scaling variables of the three-particle phase space, x_1 and x_2, see Eq. (D.1). In the usual parametrization, the final state momenta are labeled p_1, p_2, p_3, the corresponding masses are m_1, m_2, m_3 with $p_i^2 = m_i^2$ $(i = 1, 2, 3)$, and the total momentum is $p_{\text{tot}} = p_1 + p_2 + p_3$. If we define the parton k to be the "spectator" parton, i.e. the parton that is not involved in the emission of the gluon, the so-called "parent" parton $\widetilde{ij}$ contains the emitting parton and the emitted gluon of the subprocess $\widetilde{ij} \to i + j$. The auxiliary momenta $\tilde{p}_{ij}$ of the emitter and $\tilde{p}_k$ of the spectator can be defined in terms of the original momenta p_i $(i = 1, 2, 3)$ as

$$\begin{aligned} \tilde{p}_k^\mu &= \frac{\kappa^{1/2}(p_{\text{tot}}^2, m_{ij}^2, m_k^2)}{\kappa^{1/2}(p_{\text{tot}}^2, (p_i + p_j)^2, p_k^2)} \left[p_k^\mu - \frac{p_k \cdot p_{\text{tot}}}{p_{\text{tot}}^2} p_{\text{tot}}^\mu \right] + \frac{p_{\text{tot}}^2 + m_k^2 - m_{ij}^2}{2 p_{\text{tot}}^2} p_{\text{tot}}^\mu, \\ \tilde{p}_{ij}^\mu &= p_{\text{tot}}^\mu - \tilde{p}_k^\mu. \end{aligned} \tag{D.14}$$

Here, m_{ij} is the on-shell mass of the emitter $\widetilde{ij}$ and κ denotes the Källén function,

$$\kappa(x, y, z) = (x - y - z)^2 - 4yz. \tag{D.15}$$

Note that the auxiliary momenta obey the mass-shell conditions $\tilde{p}_{ij}^2 = m_{ij}^2$ and $\tilde{p}_k^2 = m_k^2$, and the total momentum conservation $p_{\text{tot}} = \tilde{p}_{ij} + \tilde{p}_k$.

The three-particle phase space $\mathrm{dPS}^{(3)}(p_i, p_j, p_k)$ can then be exactly factorized in terms of the two-particle phase space $\mathrm{dPS}^{(2)}(\tilde{p}_{ij}, \tilde{p}_k)$ and a single-particle phase space factor $\mathrm{d}p_i(\tilde{p}_{ij}, \tilde{p}_k)$ according to [106, 128]

$$\mathrm{dPS}^{(3)}(p_i, p_j, p_k) = \mathrm{dPS}^{(2)}(\tilde{p}_{ij}, \tilde{p}_k)\ \mathrm{d}p_i(\tilde{p}_{ij}, \tilde{p}_k)\ \Theta(1 - \mu_1 - \mu_2 - \mu_3). \tag{D.16}$$

The rather complex expressions of the complete analytical result and corresponding integration limits for the case of massive quarks can be found in Ref. [106]. Note that both factors on the right-hand side of Eq. (D.16) can be expressed in terms of the scaling variables x_1 and x_2.

D.4 Dipole Contributions to Virtual Cross Section

In order to counterbalance the subtraction of the unphysical auxiliary cross section from the real emission cross section and to cancel the remaining infrared singularities in the virtual part, the so-called insertion operator has to be taken into account in the virtual part of the cross section. The insertion operator $\mathcal{I}$ is obtained from the dipole terms discussed in App. D.2 through integration over the single-particle phase space $\mathrm{d}p_i(\tilde{p}_{ij}\tilde{p}_k)$, as schematically

indicated in the last term of Eq. (D.11). In our case of real gluon emission from final state quarks, and in $D = 4 - 2\epsilon$ dimensions, the insertion operator can be written as [106]

$$\mathcal{I} \;=\; \left|\mathcal{M}_{\rm LO}\right|^2 \frac{\alpha_s C_F}{\pi} \frac{(4\pi)^\epsilon}{\Gamma(1-\epsilon)} \left[\left(\frac{\mu^2}{s_{12}}\right)^\epsilon \left(\mathcal{V}_q - \frac{\pi^2}{3}\right) + \Gamma_q + \frac{3}{2}\ln\frac{\mu^2}{s_{12}} + 5 - \frac{\pi^2}{6} \right], \qquad \text{(D.17)}$$

where μ denotes the renormalization scale and $s_{12} = 2p_1 \cdot p_2 = s - 2m_q^2$. The term $\mathcal{V}_q$ contains a singular and a non-singular part [106],

$$\begin{aligned}
\mathcal{V}_q^{(\rm S)} &= \frac{1+\beta_q^2}{2\beta_q} \left[\frac{1}{\epsilon} \ln\frac{1-\beta_q}{1+\beta_q} - \frac{1}{2}\ln^2\frac{1-\beta_q}{1+\beta_q} + \ln\frac{1-\beta_q}{1+\beta_q}\ln\frac{2}{1+\beta_q^2} - \frac{\pi^2}{6} \right], \\
\mathcal{V}_q^{(\rm NS)} &= \frac{1+\beta_q^2}{2\beta_q} \left[2\ln\frac{1-\beta_q}{1+\beta_q}\ln\frac{2(1+\beta_q^2)}{(1+\beta_q)^2} + 2\,\mathrm{Li}_2\frac{(1-\beta_q)^2}{(1+\beta_q)^2} - 2\,\mathrm{Li}_2\frac{2\beta_q}{1+\beta_q} - \frac{\pi^2}{6} \right] \\
&\quad + \frac{3}{2}\ln\frac{1+\beta_q^2}{2} + \ln(1-\mu_q) - 2\ln(1-2\mu_q) - \frac{1-\beta_q^2}{1+\beta_q^2}\ln\frac{\mu_q}{1-\mu_q} \\
&\quad - \frac{\mu_q}{1-\mu_q} + \frac{8\mu_q^2 - 4\mu_q}{1+\beta_q^2} + \frac{\pi^2}{2}, \qquad \text{(D.18)}
\end{aligned}$$

involving the quark velocity $\beta_q = \sqrt{1-4\mu_q^2}$. Note that the non-singular contribution vanishes in the case of massless quarks, where $\beta_q = 1$. The function Γ_q appearing in Eq. (D.17) is here given by [106]

$$\Gamma_q \;=\; \frac{1}{\epsilon} + \frac{1}{2}\ln\frac{m_q^2}{\mu^2} - 2. \qquad \text{(D.19)}$$

The expression in Eq. (D.17) contains the same infrared divergence as do the virtual contributions presented in App. C. Combining the virtual and the dipole contributions as indicated in Eq. (D.11) results therefore in a finite expression for the virtual part of the annihilation cross section.

Bibliography

[1] S. L. Glashow. *Partial symmetries of weak interactions*. Nucl. Phys. 22:579–588, 1961.

[2] S. Weinberg. *A model of leptons*. Phys. Rev. Lett. 19:1264–1266, 1967.

[3] S. L. Glashow, J. Iliopoulos, L. Maiani. *Weak interactions with lepton-hadron symmetry*. Phys. Rev. D2:1285–1292, 1970.

[4] S. Weinberg. *Effects of a neutral intermediate boson in semileptonic processes*. Phys. Rev. D5:1412–1417, 1972.

[5] D. J. Gross, F. Wilczek. *Asymptotically free gauge theories (1)*. Phys. Rev. D8:3633–3652, 1973.

[6] D. J. Gross, F. Wilczek. *Asymptotically free gauge theories (2)*. Phys. Rev. D9:980–993, 1974.

[7] H. D. Politzer. *Asymptotic freedom: An approach to strong interactions*. Phys. Rept. 14:129–180, 1974.

[8] J. Goldstone. *Field theories with superconductor solutions*. Nuovo Cim. 19:154–164, 1961.

[9] J. Goldstone, A. Salam, S. Weinberg. *Broken symmetries*. Phys. Rev. 127:965–970, 1962.

[10] P. W. Higgs. *Broken symmetries, massless particles and gauge fields*. Phys. Lett. 12:132–133, 1964.

[11] F. Englert, R. Brout. *Broken symmetry and the mass of gauge vector mesons*. Phys. Rev. Lett. 13:321–322, 1964.

[12] P. W. Higgs. *Broken symmetries and the masses of gauge bosons*. Phys. Rev. Lett. 13:508–509, 1964.

[13] E. Witten. *Dynamical breaking of Supersymmetry*. Nucl. Phys. B188:513, 1981.

[14] R. K. Kaul. *Supersymmetric solution of gauge hierarchy problem*. Pramana 19:183, 1982.

[15] F. Zwicky. *Die Rotverschiebung von extragalaktischen Nebeln*. Helv. Phys. Acta 6:110–127, 1933.

[16] V. C. Rubin, J. Ford, W. K. *Rotation of the Andromeda Nebula from a spectroscopic survey of emission regions*. Astrophys. J. 159:379–404, 1970.

[17] V. C. Rubin, D. Burstein, J. Ford, W. K., N. Thonnard. *Rotation velocities of 16 SA galaxies and a comparison of Sa, Sb, and SC rotation properties*. Astrophys. J. 289:81, 1985.

[18] W. J. G. de Blok, S. S. McGaugh, A. Bosma, V. C. Rubin. *Mass density profiles of LSB galaxies*. Astrophys. J. 552:L23–l26, 2001. `astro-ph/0103102`.

[19] L. V. E. Koopmans, T. Treu. *The structure and dynamics of luminous and dark matter in the early-type lens galaxy of 0047-281 at z=0.485*. Astrophys. J. 583:606–615, 2003. `astro-ph/0205281`.

[20] H. Hoekstra, H. Yee, M. Gladders. *Current status of weak gravitational lensing*. New Astron. Rev. 46:767–781, 2002. `astro-ph/0205205`.

[21] M. Mateo. *Dwarf galaxies of the local group*. Ann. Rev. Astron. Astrophys. 36:435–506, 1998. `astro-ph/9810070`.

[22] D. Zaritsky, R. Smith, C. Frenk, S. D. M. White. *More satellites of spiral galaxies*. Astrophys. J. 478:39–48, 1997. `astro-ph/9611199`.

[23] D. Clowe *et al.* *A direct empirical proof of the existence of dark matter*. Astrophys. J. 648:L109–L113, 2006. `astro-ph/0608407`.

[24] A. H. Jaffe *et al.* (Boomerang). *Cosmology from Maxima-1, Boomerang and COBE/DMR CMB observations*. Phys. Rev. Lett. 86:3475–3479, 2001. `astro-ph/0007333`.

[25] D. N. Spergel *et al.* (WMAP). *First year Wilkinson Microwave Anisotropy Probe (WMAP) observations: Determination of cosmological parameters*. Astrophys. J. Suppl. 148:175, 2003. `astro-ph/0302209`.

[26] D. N. Spergel *et al.* (WMAP). *Wilkinson Microwave Anisotropy Probe (WMAP) three year results: Implications for cosmology*. Astrophys. J. Suppl. 170:377, 2007. `astro-ph/0603449`.

[27] G. Hinshaw *et al.* (WMAP). *Five-year Wilkinson Microwave Anisotropy Probe (WMAP) observations: Data processing, sky maps, and basic results* , 2008. `arXiv:0803.0732`.

[28] P. Astier *et al.* (The SNLS). *The Supernova Legacy Survey: Measurement of Ω_M, Ω_Λ and w from the first year data set*. Astron. Astrophys. 447:31–48, 2006. `astro-ph/0510447`.

[29] D. J. Eisenstein *et al.* (SDSS). *Detection of the baryon acoustic peak in the large-scale correlation function of SDSS luminous red galaxies*. Astrophys. J. 633:560–574, 2005. `astro-ph/0501171`.

[30] G. R. Blumenthal, S. M. Faber, J. R. Primack, M. J. Rees. *Formation of galaxies and large-scale structure with cold dark matter*. Nature 311:517–525, 1984.

[31] J. Wess, B. Zumino. *A Lagrangian model invariant under supergauge transformations*. Phys. Lett. B49:52, 1974.

[32] J. Wess, B. Zumino. *Supergauge transformations in four dimensions*. Nucl. Phys. B70:39–50, 1974.

[33] H. E. Haber, G. L. Kane. *The search for Supersymmetry: Probing physics beyond the Standard Model*. Phys. Rept. 117:75–263, 1985.

[34] S. P. Martin. *A Supersymmetry primer*, 1997. `hep-ph/9709356`.

[35] I. J. R. Aitchison. *Supersymmetry and the MSSM: An elementary introduction*, 2005. `hep-ph/0505105`.

[36] A. H. Chamseddine, R. Arnowitt, P. Nath. *Locally supersymmetric grand unification*. Phys. Rev. Lett. 49:970, 1982.

[37] R. Barbieri, S. Ferrara, C. A. Savoy. *Gauge models with spontaneously broken local Supersymmetry*. Phys. Lett. B119:343, 1982.

[38] L. J. Hall, J. D. Lykken, S. Weinberg. *Supergravity as the messenger of Supersymmetry breaking*. Phys. Rev. D27:2359–2378, 1983.

[39] M. Dine, A. E. Nelson. *Dynamical Supersymmetry breaking at low energies*. Phys. Rev. D48:1277–1287, 1993. `hep-ph/9303230`.

[40] M. Dine, A. E. Nelson, Y. Shirman. *Low-energy dynamical Supersymmetry breaking simplified*. Phys. Rev. D51:1362–1370, 1995. `hep-ph/9408384`.

[41] M. Dine, A. E. Nelson, Y. Nir, Y. Shirman. *New tools for low-energy dynamical Supersymmetry breaking*. Phys. Rev. D53:2658–2669, 1996. `hep-ph/9507378`.

[42] G. F. Giudice, R. Rattazzi. *Theories with gauge-mediated Supersymmetry breaking*. Phys. Rept. 322:419–499, 1999. `hep-ph/9801271`.

[43] J. F. Gunion, H. E. Haber. *Higgs bosons in supersymmetric models 1*. Nucl. Phys. B272:1, 1986.

[44] J. F. Gunion, H. E. Haber. *Higgs bosons in supersymmetric models 2: Implications for phenomenology*. Nucl. Phys. B278:449, 1986.

[45] J. F. Gunion, H. E. Haber. *Higgs bosons in supersymmetric models 3: Decays into neutralinos and charginos*. Nucl. Phys. B307:445, 1988.

[46] A. Djouadi. *The Anatomy of Electro-weak Symmetry Breaking II: The Higgs Bosons in the Minimal Supersymmetric Model*, 2005. `hep-ph/0503173`.

[47] L. J. Hall, V. A. Kostelecky, S. Raby. *New flavor violations in supergravity models*. Nucl. Phys. B267:415, 1986.

[48] N. Cabibbo. *Unitary symmetry and leptonic decays*. Phys. Rev. Lett. 10:531–532, 1963.

[49] M. Kobayashi, T. Maskawa. *CP violation in the renormalizable theory of weak interaction*. Prog. Theor. Phys. 49:652–657, 1973.

[50] J. F. Donoghue, H. P. Nilles, D. Wyler. *Flavor changes in locally supersymmetric theories*. Phys. Lett. B128:55, 1983.

[51] M. J. Duncan. *Generalized Cabibbo angles in supersymmetric gauge theories*. Nucl. Phys. B221:285, 1983.

[52] A. Bouquet, J. Kaplan, C. A. Savoy. *On flavor mixing in broken supergravity*. Phys. Lett. B148:69, 1984.

[53] F. Borzumati, A. Masiero. *Large muon and electron number violations in supergravity theories*. Phys. Rev. Lett. 57:961, 1986.

[54] F. Gabbiani, A. Masiero. *FCNC in generalized supersymmetric theories*. Nucl. Phys. B322:235, 1989.

[55] F. Gabbiani, E. Gabrielli, A. Masiero, L. Silvestrini. *A complete analysis of FCNC and CP constraints in general SUSY extensions of the Standard Model*. Nucl. Phys. B477:321–352, 1996. `hep-ph/9604387`.

[56] F. del Aguila *et al.* *Collider aspects of flavour physics at high Q* , 2008. `arXiv:0801.1800`.

[57] J. R. Ellis, J. S. Hagelin, D. V. Nanopoulos, K. A. Olive, M. Srednicki. *Supersymmetric relics from the Big Bang*. Nucl. Phys. B238:453–476, 1984.

[58] U. Amaldi, W. de Boer, H. Fürstenau. *Comparison of grand unified theories with electroweak and strong coupling constants measured at LEP*. Phys. Lett. B260:447–455, 1991.

[59] U. Ellwanger, M. Rausch de Traubenberg, C. A. Savoy. *Particle spectrum in supersymmetric models with a gauge singlet*. Phys. Lett. B315:331–337, 1993. `hep-ph/9307322`.

[60] U. Ellwanger, M. Rausch de Traubenberg, C. A. Savoy. *Phenomenology of supersymmetric models with a singlet*. Nucl. Phys. B492:21–50, 1997. `hep-ph/9611251`.

[61] U. Ellwanger, C. C. Jean-Louis, A. M. Teixeira. *Phenomenology of the general NMSSM with gauge mediated Supersymmetry breaking*. JHEP 05:044, 2008. `arXiv:0803.2962`.

[62] T. Ibrahim, P. Nath. *CP violation from Standard Model to strings* , 2007. `arXiv:0705.2008`.

[63] R. Barbier *et al.* *R-parity violating Supersymmetry*. Phys. Rept. 420:1–202, 2005. `hep-ph/0406039`.

[64] W. M. Yao *et al.* (Particle Data Group). *Review of particle physics*. J. Phys. G33:1–1232, 2006.

[65] G. Bozzi, B. Fuks, B. Herrmann, M. Klasen. *Squark and gaugino hadroproduction and decays in non-minimal flavour violating Supersymmetry*. Nucl. Phys. B787:1–54, 2007. `arXiv:0704.1826`.

[66] B. Fuks, B. Herrmann, M. Klasen. *Flavour violation in gauge-mediated Supersymmetry breaking models: Experimental constraints and phenomenology at the LHC*, 2008. arXiv:0808.1104.

[67] M. Klasen, G. Pignol. *New results for light gravitinos at hadron colliders - Tevatron limits and LHC perspectives*. Phys. Rev. D75:115003, 2007. hep-ph/0610160.

[68] M. Ciuchini *et al.* *Soft SUSY breaking grand unification: Leptons vs. quarks on the flavor playground*. Nucl. Phys. B783:112–142, 2007. hep-ph/0702144.

[69] J. Foster, K.-i. Okumura, L. Roszkowski. *New constraints on SUSY flavour mixing in light of recent measurements at the Tevatron*. Phys. Lett. B641:452–460, 2006. hep-ph/0604121.

[70] T. Hahn, W. Hollik, J. I. Illana, S. Penaranda. *Interplay between $H \to b\bar{s}$ and $b \to s\gamma$ in the MSSM with non-minimal flavour violation*, 2005. hep-ph/0512315.

[71] E. Barberio *et al.* (Heavy Flavor Averaging Group (HFAG)). *Averages of B-hadron properties at the end of 2005*, 2006. hep-ex/0603003.

[72] A. L. Kagan, M. Neubert. *Direct CP violation in $B \to X_S\gamma$ decays as a signature of new physics*. Phys. Rev. D58:094012, 1998. hep-ph/9803368.

[73] S. Heinemeyer, W. Hollik, F. Merz, S. Penaranda. *Electroweak precision observables in the MSSM with non-minimal flavor violation*. Eur. Phys. J. C37:481–493, 2004. hep-ph/0403228.

[74] S. Heinemeyer, D. Stöckinger, G. Weiglein. *Two-loop SUSY corrections to the anomalous magnetic moment of the muon*. Nucl. Phys. B690:62–80, 2004. hep-ph/0312264.

[75] S. Heinemeyer, D. Stöckinger, G. Weiglein. *Electroweak and supersymmetric two-loop corrections to $(g-2)_\mu$*. Nucl. Phys. B699:103–123, 2004. hep-ph/0405255.

[76] T. Moroi. *The muon anomalous magnetic dipole moment in the Minimal Supersymmetric Standard Model*. Phys. Rev. D53:6565–6575, 1996. hep-ph/9512396.

[77] J. Hamann, S. Hannestad, M. S. Sloth, Y. Y. Y. Wong. *How robust are inflation model and dark matter constraints from cosmological data?* Phys. Rev. D75:023522, 2007. astro-ph/0611582.

[78] J. R. Ellis, K. A. Olive, Y. Santoso, V. C. Spanos. *Supersymmetric dark matter in light of WMAP*. Phys. Lett. B565:176–182, 2003. hep-ph/0303043.

[79] G. Bertone, D. Hooper, J. Silk. *Particle dark matter: Evidence, candidates and constraints*. Phys. Rept. 405:279–390, 2005. hep-ph/0404175.

[80] P. Gondolo, G. Gelmini. *Cosmic abundances of stable particles: Improved analysis*. Nucl. Phys. B360:145–179, 1991.

[81] J. Edsjo, P. Gondolo. *Neutralino relic density including coannihilations*. Phys. Rev. D56:1879–1894, 1997. hep-ph/9704361.

[82] G. Jungman, M. Kamionkowski, K. Griest. *Supersymmetric dark matter*. Phys. Rept. 267:195–373, 1996. hep-ph/9506380.

[83] P. Gondolo *et al.* *DarkSUSY: Computing supersymmetric dark matter properties numerically*. JCAP 0407:008, 2004. astro-ph/0406204.

[84] G. Bélanger, F. Boudjema, A. Pukhov, A. Semenov. *micrOMEGAs: A program for calculating the relic density in the MSSM*. Comput. Phys. Commun. 149:103–120, 2002. hep-ph/0112278.

[85] M. Bolz, A. Brandenburg, W. Buchmüller. *Thermal production of gravitinos*. Nucl. Phys. B606:518–544, 2001. hep-ph/0012052.

[86] J. Pradler, F. D. Steffen. *Thermal gravitino production and collider tests of leptogenesis*. Phys. Rev. D75:023509, 2007. hep-ph/0608344.

[87] V. S. Rychkov, A. Strumia. *Thermal production of gravitinos*. Phys. Rev. D75:075011, 2007. hep-ph/0701104.

[88] S. Davidson, E. Nardi, Y. Nir. *Leptogenesis*, 2008. arXiv:0802.2962.

[89] W. Buchmüller, P. Di Bari, M. Plümacher. *Leptogenesis for pedestrians*. Ann. Phys. 315:305–351, 2005. hep-ph/0401240.

[90] W. Porod. *SPheno, a program for calculating supersymmetric spectra, SUSY particle decays and SUSY particle production at e^+e^- colliders*. Comput. Phys. Commun. 153:275–315, 2003. hep-ph/0301101.

[91] S. Heinemeyer, W. Hollik, G. Weiglein. *FeynHiggs: A program for the calculation of the masses of the neutral CP-even Higgs bosons in the MSSM*. Comput. Phys. Commun. 124:76–89, 2000. hep-ph/9812320.

[92] B. C. Allanach *et al.* *The Snowmass Points and Slopes: Benchmarks for SUSY searches,* 2002. hep-ph/0202233.

[93] J. A. Aguilar-Saavedra *et al.* *Supersymmetry Parameter Analysis: SPA convention and project*. Eur. Phys. J. C46:43–60, 2006. hep-ph/0511344.

[94] M. Battaglia *et al.* *Updated post-WMAP benchmarks for Supersymmetry*. Eur. Phys. J. C33:273–296, 2004. hep-ph/0306219.

[95] B. Fuks, B. Herrmann, M. Klasen. *in preparation.*

[96] P. Gambino, U. Haisch, M. Misiak. *Determining the sign of the $b \to s\gamma$ amplitude*. Phys. Rev. Lett. 94:061803, 2005. hep-ph/0410155.

[97] K. Tobe, J. D. Wells, T. Yanagida. *Neutrino induced lepton flavor violation in gauge-mediated Supersymmetry breaking*. Phys. Rev. D69:035010, 2004. hep-ph/0310148.

[98] S. L. Dubovsky, D. S. Gorbunov. *Flavor violation and tanβ in gauge mediated models with messenger-matter mixing*. Nucl. Phys. B557:119–145, 1999. hep-ph/9807347.

[99] S. Heinemeyer, X. Miao, S. Su, G. Weiglein. *B-Physics observables and electroweak precision data in the CMSSM, mGMSB and mAMSB*, 2008. arXiv:0805.2359.

[100] B. Herrmann, M. Klasen. *SUSY-QCD corrections to dark matter annihilation in the Higgs funnel*. Phys. Rev. D76:117704, 2007. arXiv:0709.0043.

[101] M. S. Carena, M. Olechowski, S. Pokorski, C. E. M. Wagner. *Electroweak symmetry breaking and bottom – top Yukawa unification*. Nucl. Phys. B426:269–300, 1994. hep-ph/9402253.

[102] W. de Boer, C. Sander, V. Zhukov, A. V. Gladyshev, D. I. Kazakov. *EGRET excess of diffuse galactic gamma rays as tracer of dark matter*. Astron. Astrophys. 444:51, 2005. astro-ph/0508617.

[103] W. de Boer, C. Sander, V. Zhukov, A. V. Gladyshev, D. I. Kazakov. *The supersymmetric interpretation of the EGRET excess of diffuse galactic gamma rays*. Phys. Lett. B636:13–19, 2006. hep-ph/0511154.

[104] W. de Boer, C. Sander, V. Zhukov, A. V. Gladyshev, D. I. Kazakov. *EGRET excess of diffuse galactic gamma rays interpreted as a signal of dark matter annihilation*. Phys. Rev. Lett. 95:209001, 2005. astro-ph/0602325.

[105] L. Bergstrom, J. Edsjo, M. Gustafsson, P. Salati. *Is the dark matter interpretation of the EGRET gamma excess compatible with antiproton measurements?* JCAP 0605:006, 2006. astro-ph/0602632.

[106] S. Catani, S. Dittmaier, M. H. Seymour, Z. Trocsanyi. *The dipole formalism for next-to-leading order QCD calculations with massive partons*. Nucl. Phys. B627:189–265, 2002. hep-ph/0201036.

[107] M. Drees, K.-i. Hikasa. *Note on QCD corrections to hadronic Higgs decay*. Phys. Lett. B240:455, 1990.

[108] E. Braaten, J. P. Leveille. *Higgs boson decay and the running mass*. Phys. Rev. D22:715, 1980.

[109] K. G. Chetyrkin. *Correlator of the quark scalar currents and* $\Gamma_{tot}(H \to hadrons)$ *at* $\mathcal{O}(\alpha_s^3)$ *in pQCD*. Phys. Lett. B390:309–317, 1997. hep-ph/9608318.

[110] P. A. Baikov, K. G. Chetyrkin, J. H. Kühn. *Scalar correlator at* $O(\alpha^4(s))$*, Higgs decay into b-quarks and bounds on the light quark masses*. Phys. Rev. Lett. 96:012003, 2006. hep-ph/0511063.

[111] K. G. Chetyrkin, A. Kwiatkowski. *Second order QCD corrections to scalar and pseudoscalar Higgs decays into massive bottom quarks*. Nucl. Phys. B461:3–18, 1996. hep-ph/9505358.

[112] M. S. Carena, D. Garcia, U. Nierste, C. E. M. Wagner. *Effective Lagrangian for the* $\bar{t}bH+$ *interaction in the MSSM and charged Higgs phenomenology*. Nucl. Phys. B577:88–120, 2000. hep-ph/9912516.

[113] J. Guasch, P. Häfliger, M. Spira. *MSSM Higgs decays to bottom quark pairs revisited*. Phys. Rev. D68:115001, 2003. hep-ph/0305101.

[114] T. Moroi, Y. Sumino, A. Yotsuyanagi. *QCD correction to neutralino annihilation process and dark matter density in supersymmetric models*. Phys. Rev. D74:015016, 2006. hep-ph/0605181.

[115] B. C. Allanach, S. Kraml, W. Porod. *Theoretical uncertainties in sparticle mass predictions from computational tools*. JHEP 03:016, 2003. hep-ph/0302102.

[116] G. Bélanger, S. Kraml, A. Pukhov. *Comparison of SUSY spectrum calculations and impact on the relic density constraints from WMAP*. Phys. Rev. D72:015003, 2005. hep-ph/0502079.

[117] L. S. Stark, P. Häfliger, A. Biland, F. Pauss. *New allowed mSUGRA parameter space from variations of the trilinear scalar coupling A_0*. JHEP 08:059, 2005. hep-ph/0502197.

[118] A. Freitas. *Radiative corrections to co-annihilation processes*. Phys. Lett. B652:280–284, 2007. arXiv:0705.4027.

[119] B. Herrmann, M. Klasen, K. Kovařík. *to be published*.

[120] C. Amsler, et al (Particle Data Group). *Review of particle physics*. Phys. Lett. B 667:1, 2008.

[121] J. A. M. Vermaseren. *New features of FORM*, 2000. math-ph/0010025.

[122] T. Hahn. *Generating Feynman diagrams and amplitudes with FeynArts 3*. Comput. Phys. Commun. 140:418–431, 2001. hep-ph/0012260.

[123] T. Hahn, C. Schappacher. *The implementation of the minimal supersymmetric standard model in FeynArts and FormCalc*. Comput. Phys. Commun. 143:54–68, 2002. hep-ph/0105349.

[124] T. Hahn, M. Perez-Victoria. *Automatized one-loop calculations in four and D dimensions*. Comput. Phys. Commun. 118:153–165, 1999. hep-ph/9807565.

[125] T. Hahn, M. Rauch. *News from FormCalc and LoopTools*. Nucl. Phys. Proc. Suppl. 157:236–240, 2006. hep-ph/0601248.

[126] A. Denner. *Techniques for calculation of electroweak radiative corrections at the one loop level and results for W physics at LEP-200*. Fortschr. Phys. 41:307–420, 1993. 0709.1075.

[127] A. Denner, S. Dittmaier. *Reduction schemes for one-loop tensor integrals*. Nucl. Phys. B734:62–115, 2006. hep-ph/0509141.

[128] S. Catani, M. H. Seymour. *The dipole formalism for the calculation of QCD jet cross sections at next-to-leading order*. Phys. Lett. B378:287–301, 1996. hep-ph/9602277.

[129] H. Baer, J. Ferrandis, K. Melnikov, X. Tata. *Relating bottom quark mass in $\overline{DR}$ and $\overline{MS}$ regularization schemes*. Phys. Rev. D66:074007, 2002. hep-ph/0207126.

[130] L. V. Avdeev, M. Y. Kalmykov. *Pole masses of quarks in dimensional reduction*. Nucl. Phys. B502:419–435, 1997. hep-ph/9701308.

[131] T. Blažek. *private communication*.

[132] G. Bozzi, B. Fuks, M. Klasen. *Non-diagonal and mixed squark production at hadron colliders*. Phys. Rev. D72:035016, 2005. hep-ph/0507073.

[133] S. Dawson, E. Eichten, C. Quigg. *Search for supersymmetric particles in hadron – hadron collisions*. Phys. Rev. D31:1581, 1985.

[134] S. Y. Choi, A. Djouadi, H. S. Song, P. M. Zerwas. *Determining SUSY parameters in chargino pair-production in e^+e^- collisions*. Eur. Phys. J. C8:669–677, 1999. hep-ph/9812236.

[135] G. J. Gounaris, J. Layssac, P. I. Porfyriadis, F. M. Renard. *Neutralino pair production at LHC*. Phys. Rev. D70:033011, 2004. hep-ph/0404162.

[136] W. Beenakker *et al. The production of charginos/neutralinos and sleptons at hadron colliders*. Phys. Rev. Lett. 83:3780–3783, 1999. hep-ph/9906298.

[137] M. Spira. *Gaugino pair production at hadron colliders*. Nucl. Phys. Proc. Suppl. 89:222–227, 2000.

[138] P. Fayet. *Lower limit on the mass of a light gravitino from e^+e^- annihilation experiments*. Phys. Lett. B175:471, 1986.

[139] S. Ambrosanio, G. L. Kane, G. D. Kribs, S. P. Martin, S. Mrenna. *Supersymmetric analysis and predictions based on the CDF $ee\gamma\gamma + missing E_T$ event*. Phys. Rev. Lett. 76:3498–3501, 1996. hep-ph/9602239.

[140] J. Pumplin *et al. New generation of parton distributions with uncertainties from global QCD analysis*. JHEP 07:012, 2002. hep-ph/0201195.

[141] T. Falk, K. A. Olive, M. Srednicki. *Heavy sneutrinos as dark matter*. Phys. Lett. B339:248–251, 1994. hep-ph/9409270.

[142] S. Dimopoulos, G. F. Giudice, A. Pomarol. *Dark matter in theories of gauge-mediated supersymmetry breaking*. Phys. Lett. B389:37–42, 1996. hep-ph/9607225.

[143] D. Hooper, J. March-Russell. *Gauge mediated supersymmetry breaking and multi-TeV gamma-rays from the galactic center*. Phys. Lett. B608:17–23, 2005. hep-ph/0412048.

[144] M. Ibe, K. Tobe, T. Yanagida. *A gauge-mediation model with a light gravitino of mass O(10) eV and the messenger dark matter*. Phys. Lett. B615:120–126, 2005. hep-ph/0503098.

[145] E. Byckling, K. Kajantie. *Particle kinematics*. John Wiley & Sons, 1973.

Abstract

In absence of direct experimental evidence, it is essential to constrain the parameter space of the Minimal Supersymmetric Standard Model (MSSM) both at the Supersymmetry breaking and the electroweak scale. After a brief introduction to Supersymmetry (SUSY), we present an extensive analysis of electroweak, low energy, and cosmological constraints in minimal supergravity (mSUGRA) and gauge-mediated SUSY-breaking (GMSB) scenarios. We include the possibility of non-minimal flavour violation (NMFV) in the squark sector and define "collider-friendly" benchmark points based on detailed scans of the parameter space. We then consider neutralino pair annihilation into quark-antiquark pairs that dominates wide ranges of the mSUGRA parameter space. We present the corresponding full one-loop QCD and SUSY-QCD calculation and show numerically that the loop diagrams have an important impact on the annihilation cross section and, in consequence, in the prediction of the dark matter relic density, resulting in a modification of the preferred regions of the parameter space. We finally present analytical expressions and numerical predictions for squark, gaugino, and gravitino production cross sections at the LHC in GMSB with NMFV. We also discuss the phenomenology of flavour mixing and cosmological implications on the gravitino mass within this context.

Résumé

En l'absence d'évidence expérimentale directe de superpartenaires, il est essentiel de contraindre l'espace des paramètres du Modèle Standard Supersymétrique Minimal (MSSM) aux échelles de la brisure de la Supersymétrie et électrofaible. Après une brève introduction à la Supersymétrie (SUSY), nous présentons une analyse extensive des contraintes électrofaible, de basse énergie et cosmologiques dans des modèles de supergravité minimale (mSUGRA) et de brisure de Supersymétrie par médiation de jauge (GMSB). Nous incluons la possibilité de violation non-minimale de la saveur (NMFV) et définissons des scénarios "benchmark" basés sur des "scans" détaillés de l'espace des paramètres. Ensuite, nous considérons l'annihilation d'une paire de neutralinos en une paire de quark-antiquark qui domine dans de larges régions de l'espace des paramètres dans les modèles mSUGRA. Nous présentons le calcul complet incluant des corrections à une boucle en QCD et SUSY-QCD de ces processus et montrons numériquement que les diagrammes à une boucle ont un impact non négligeable sur la section efficace d'annihilation. En conséquence, la prédiction de densité relique de matière noire reçoit des corrections importantes, ce qui résulte en une modification de la région cosmologiquement favorisée dans l'espace des paramètres. Finalement, nous présentons des expressions analytiques et des prédictions numériques pour des sections efficaces de production de squarks, jauginos et gravitinos au LHC dans les modèles GMSB avec NMFV. Nous discutons également la phénoménologie du mélange de saveur et les implications cosmologiques sur la masse du gravitino dans ce contexte.

The electronic version of this document including fully coloured figures is available at `http://tel.archives-ouvertes.fr` *or* `http://www.arxiv.org`.